

Tailoring Fluoride/Fluorine Bond Activity for High-Energy Li and Li-ion Batteries

by

Haining Gao

Bachelor of Engineering, Materials Science and Engineering
Tsinghua University, 2017

SUBMITTED TO THE DEPARTMENT OF MATERIALS SCIENCE AND ENGINEERING
IN PARTIAL FULFILLMENT OF THE REQUIREMENTS FOR THE DEGREE OF

DOCTOR OF PHILOSOPHY IN MATERIALS SCIENCE AND ENGINEERING

at the

MASSACHUSETTS INSTITUTE OF TECHNOLOGY

May 2022

© 2022 Massachusetts Institute of Technology. All rights reserved.

Signature of Author: _____
Department of Materials Science and Engineering
May 13, 2022

Certified by: _____
Betar M. Gallant
Associate Professor of Mechanical Engineering
Thesis Supervisor

Yang Shao-Horn
JR East Professor of Engineering
Thesis Reader

Accepted by: _____
Frances M. Ross
Professor of Materials Science and Engineering
Chair, Departmental Committee on Graduate Studies

Tailoring Fluoride/Fluorine Bond Activity for High-Energy Li and Li-ion Batteries

By

Haining Gao

Submitted to the Department of Materials Science and Engineering
on May 13, 2022

in Partial Fulfillment of the Requirements for the Degree of
Doctor of Philosophy in Materials Science and Engineering

Abstract

Extending the classes of reactions that underlie electrochemical energy storage systems is of fundamental and practical importance to improving mobility, autonomy, medical devices and electronics. Most of the cathode materials developed so far are oxide-based: all commercial Li-ion cathodes utilize lithium transition metal oxides, while MnO_2 , SOCl_2 , and SO_2 are representative examples for Li primary cathodes. In contrast, fluoride-based cathodes are generally less investigated, with only several instances, but all with exceedingly high theoretical energy densities, such as carbon-monofluoride (CF_x), transition metal fluorides, and the recently developed perfluorinated gas cathodes (SF_6 and NF_3). This indicates the strong potential for fluoride-based cathodes to surpass the current energy density limit. Therefore, to expand the landscape of fluoride redox to provide a new degree of freedom for the design of high-energy cathodes, this thesis examines the controlling parameters for fluoride bond redox activities, and their implications for Li and Li-ion batteries.

The first part of this thesis targets sulfur–fluorine (S–F) bonds. Using Li– SF_6 battery as a platform, the dominating effect of the electrolyte solvent properties on lithium fluoride (LiF, one of the discharge products) nucleation and growth was demonstrated. The electrode passivation induced by LiF is mitigated via increasing the fluoride solvation strength of the solvents, resulting in improved Li– SF_6 cell rate capabilities. Strategies to tune the S–F bond redox activity at molecular structure level was investigated next using liquid phase pentafluorosulfanyl arenes (*R-Ph-SF₅*), where one of the F-ligands in the SF_6 molecule is replaced by an aromatic group (*R-Ph*). The ring structure facilitates electron transfer by increasing molecular polarity, while *R* functionality alters the S–F bond reduction potential by changing the electron distribution around the $-\text{SF}_5$ group. As a new family of Li primary catholytes, the *R-Ph-SF₅* reactants allow for full reactant defluorination and a total of up to $8 e^-$ transfer per molecule, yielding capacities of 861 $\text{mAh/g}_{\text{reactant}}$ and voltages up to $\sim 2.9 \text{ V}$ vs. Li/Li^+ . At a cell level, gravimetric energies of 1085 Wh/kg were attained at $50 \text{ }^\circ\text{C}$, exceeding all leading primary batteries based on electrode +

electrolyte (sub-stack) mass. Voltage compatibility of *R-Ph-SF₅* and CF_x solid cathodes further enabled design of a hybrid battery containing both fluorinated catholyte and cathode. The hybrid cells reach extraordinarily high cell active mass loading (~80%) and allow for significant boosting of sub-stack gravimetric energy of Li-CF_x cells by at least 20%.

The carbon-fluorine (C-F) bonds in perfluoroalkyl group (R_F) were investigated next. The effect of extrinsic factors was examined using liquid perfluoroalkyl iodides (CFIs) as an example system, where the polarizable iodine supports electrochemical reduction with concerted F⁻ ligand expulsion. C-F bond redox activity was found to be influenced significantly by multiple parameters, including reactant concentration, discharge rate, temperature, and solvent properties (e.g. catholyte viscosity). A maximum of 8 e⁻/C₆F₁₃I, or 8/13 available F, is accessible, but only at ideal conditions (low reactant concentration and rate). Increasing concentration or rate exacerbates premature cell termination caused by deactivation of intermediates, resulting in <2 e⁻/C₆F₁₃I. This challenge was addressed via molecular design. By replacing the I-ligand with an alkene linker connected to a conjugated system, close-to-full defluorination of R_F was achieved, yielding up to 15 e⁻ per molecule (or 15/17 available F), at voltages up to 2.6 V vs. Li/Li⁺. In addition to the ring structure and the *R* substitutional group, which facilitate charge transfer as that observed in *R-Ph-SF₅*, the alkene linker was found to be essential here for the reduction transformation propagating along the R_F tail.

Lastly, Mn-F bond was studied in the context of electrochemical fluorination of MnO, the product of which functions as rechargeable Li-ion cathodes. Previous studies showed that small MnO particle size (<10 nm) is necessary for MnO fluorination via LiF splitting reaction. We demonstrated that such limitation is originated from LiF instead of MnO. With electrochemically formed LiF, which is nano-crystallized and in intimate contact with MnO, high MnO utilization (~0.9 e⁻/MnO) is achievable even with large MnO particle size (~400 nm).

Overall, the central advance of this thesis is the identification of multiple new electrochemical conversion motifs. In addition to the development of novel classes of Li primary cathodes with extraordinary electrochemical performances, this work also constructs a map of handles to tune the fluoride bond activities, providing a new platform for the design of battery materials for different applications. For instance, in rechargeable batteries, LiF is suggested to play an important role in stabilizing reactive interfaces and improving cycling stability.

Thesis Supervisor: Betar M. Gallant

Title: Associate Professor of Mechanical Engineering

Acknowledgements

I express my deepest gratitude to many people who have guided, helped, and inspired me during this journey of acquiring my PhD degree. First and foremost, I would like to thank my advisor, Prof. Betar Gallant, for her invaluable mentorship and continued support over the past five years. With her creativity, intelligence, kindness, and perseverance, Betar has always been a role model for me, not only in research, but also in life beyond research. I cannot thank her enough for the supportive environment she created and fostered, where I am comfortable to be “stupid” and ask for help; for the detailed instructions and feedback on my writing and presentations, equipping me with essential tools to formulate and communicate ideas; for her boundless enthusiasm and bountiful ideas that motivated me to explore so many exciting paths; for the trust and understanding, which eased the stress along the way. Working with and learning from Betar has been such a great pleasure and an absolute honor.

I gratefully acknowledge my thesis committee members, Prof. Yang Shao-Horn and Prof. Yet-Ming Chiang, for their intellectual guidance. Their insightful comments and professional supports inspired me to consider problems from different angles, and allowed my work to be as comprehensive as it can be. I am also thankful to my collaborators, Dr. Kevin Tibbetts for the insightful discussions and help on battery testing; Prof. Timothy Swager and Dr. Kosuke Yoshinaga, for helping design and synthesize the fluorinated aromatics that led to the development of many innovative battery chemistries. I thank Dr. Simon Jones for providing valuable insights on practical-scale batteries and battery assembling. I feel extremely fortunate to have such great opportunities to learn from so many brilliant minds.

I would like to thank my former and current labmates, Dr. Aliza Khurram, Dr. Mingfu He, Dr. Sung Eun Jerng, Dr. Kyeong-Ho Kim, Dr. Graham Leverick, Aaron Melemed, Alejandro

Sevilla, Dhyllan Skiba, Elizabeth Bernhardt, Fang-Yu Kuo, Gustavo Hobold, Katherine Steinberg, and Kyle Jiang. I could not imagine a better team to work with: I have never thought twice before getting help from you whenever I needed it; I have greatly benefited from our discussions, which always sparked new ideas; I loved our inside jokes, everyone's distinct music lists, and creative ways to organize and decorate our lab and office; I really enjoyed us sitting around, sharing snacks, and chatting about random things besides our research, which always made my day and kept me afloat. Thank you all!

Lastly, I want to thank my family and friends for their unwavering support and for bringing me so much joy. I would like to thank my partner Qi Zheng for showing up at the right moment of my life, without whom I have no idea how I would have spent those long isolated time during Covid. Thank you for being my Grammarly, my Google, my Uber, my TripAdvisor, my Maps, my listener, and my supporter. I have so enjoyed the foods we've made, the places we've been, the "arts" we've created, the birds we've invited to our balcony, the games we've played, the movies we've watched, and more importantly, the time we've spent together. I also want to thank Qi's family for giving me another home to look forward to going back to. I am grateful to my parents, Shuhong Zhang and Zengbin Gao, and my grandparents for their unconditional love that permeates my entire life, for always believing in my choices and trying to help me no matter what. They make sure that I never need to worry about failing, because they have and will always back me up. Finally, I want to thank my friends at MIT and back home, especially the "battery team": Yuntong, Yiliang and Yimeng, for making graduate school so much more delightful and rewarding.

Table of Contents

Abstract.....	2
Acknowledgements.....	4
List of Figures.....	9
List of Tables.....	26
Chapter 1: Introduction.....	27
1.1 Executive Summary and Motivation.....	27
1.2 Lithium Primary Batteries.....	31
1.2.1 State-of-the-art primary battery chemistry.....	31
1.2.2 Fluorinated primary cathode: CF_x	35
1.3 Lithium-ion Batteries.....	37
1.3.1 State-of-the-art Li-ion battery chemistry.....	37
1.3.2 Fluoridation for Li-ion cathodes.....	41
1.4 Li-Gas Batteries.....	48
1.4.1 Li- O_2 batteries.....	48
1.4.2 Alternative oxide gas cathodes.....	56
1.4.3 Perfluorinated gas cathodes.....	60
Chapter 2: Controlling Electrolyte Solvation Properties for Fluorides to Improve Rate Capability in Li-SF₆ Batteries.....	65
2.1 Introduction.....	65
2.2 Experimental Methods.....	68
2.3 Results and Discussion.....	72
2.4 Conclusions.....	94
2.5 Appendix for Chapter 2.....	95
Chapter 3: Molecular Structural Design for Liquid S-F Bond Containing Reactants to Boost Lithium Primary Battery Energy.....	96
3.1 Introduction.....	96
3.2 Experimental Methods.....	99
3.3 Results and discussion.....	104

3.3.1	Intrinsic electroactivity and products of R-Ph-SF ₅ discharge.....	104
3.3.2	Discharge performance of Li-NO ₂ -Ph-SF ₅ cells.....	113
3.3.3	Hybrid solid-liquid cell design.....	119
3.3.4	Temperature effects	121
3.4	Conclusions.....	124
3.5	Appendix for Chapter 3	125
Chapter 4: Tuning C–F Bond Activity in Perfluoroalkylated Reactants to Enable Multi-		
Electron Carbon Reduction		
4.1	Introduction.....	132
4.2	Experimental Methods	135
4.3	Results and Discussion	137
4.3.1	Discharge of Li-fluorinated catholyte cells at 1 M concentration	137
4.3.2	Effect of rate and reactant concentration on Li-C ₆ F ₁₃ I cell discharge	144
4.3.3	Tuning solvent properties to tailor C ₆ F ₁₃ I reduction.....	149
4.4	Conclusion	157
Chapter 5: Molecular Structural Design for Liquid Perfluoroalkylated Reactants to		
Achieve Close-to-Full Defluorination.....		
5.1	Introduction.....	159
5.2	Experimental Methods	161
5.3	Results and Discussion	162
5.3.1	Design principles for fluoro-aromatic cathodes.....	162
5.3.2	Intrinsic electroactivity and products of fluoro-aromatic discharge	167
5.3.3	Concentration effect on <i>o</i> -NO ₂ -Ph-C ₆ discharge	172
5.4	Conclusion	175
Chapter 6: Tailoring Fluoride Morphology to Facilitate Electrochemical Fluoridation of		
MnO for Li-ion Cathodes.....		
6.1	Introduction.....	177
6.2	Experimental Methods	180
6.3	Results and discussions.....	183
6.3.1	Electrochemical formation and characterization of LiF coating on MnO	183

6.3.2	LiF splitting, MnO fluoridation and subsequent lithiation capacity	187
6.3.3	Rate capability of Mn-O-F derived from different fluorination sources	196
6.3.4	Trace SF ₆ as additive for improved cyclability.....	198
6.4	Conclusions.....	202
Chapter 7: Conclusions and Outlook.....		203
7.1	Conclusions.....	203
7.2	Outlook	206
References.....		214

List of Figures

- Figure 1-1** (a) Lattice structure of CF_x . Reproduced with permission from Ref. 42. (b) Galvanostatic discharge of $\text{Li}-\text{CF}_x$ cells with 1 M LiBF_4 in PC/DME as electrolyte. Cells were discharged at C/20 (red) and C/5 (green). Reproduced with permission from Ref. 38..... 36
- Figure 1-2** Lattice structures of intercalation cathodes: (a) layered (LiCoO_2), (b) Spinel (LiMn_2O_4), (c) olivine (LiFePO_4), and (d) disordered rock-salt. Part a–c reproduced with permission from Ref. 46; Part d reproduced with permission from Ref. 48..... 38
- Figure 1-3** Overall comparison of average discharge voltages and specific capacities for intercalation and conversion type materials. Reproduced with permission from Ref. 46. 39
- Figure 1-4** (a) XRD pattern, (b) cycle performance, and (c) galvanostatic charge/discharge curves in the 2nd and 50th cycles of non- and F-doped Li-rich NMC at the rate of 0.1 C. Reproduced with permission from Ref. 68..... 43
- Figure 1-5** (a) Charge–discharge curve for Li-Mn-O-F vs. lithium. First cycle is shown in the voltage range 2 V to 4.8 V at a rate of C/10 (22.4 mA/g). (b) Discharge capacity as a function of cycle number at progressively faster C-rates of C/10, C/2, and 1C. Reproduced with permission from Ref. 72..... 44
- Figure 1-6** (a) Schematic of the positive electrode material design strategy using metal monoxide (MO). After mechano-chemical mixing, LiF and MO exist without chemical reaction in the several nanometer scale. The crystal structure of all compounds is described by a polyhedral image. Red, O; grey, F; green, Li; purple, Mn; brown, Fe; blue, Co (b) First discharge and second charge profiles of LiF-MnO nanocomposites after the initial activating charge protocol. The cell was cycled between 1.5–4.8 V at a rate of 20 mA/g (0.03 mA/cm²). Reproduced with permission from Ref. 84..... 47

- Figure 1-7 (a)** Electrochemical cycling of MnO/C. The insets elucidate rate capability and cyclability of the activated composites. All the cells were in 1 M LiPF₆ in ethyl carbonate/dimethyl carbonate (EC/DMC; v/v = 1:1) electrolyte. **(b)** Schematic illustration of the in situ fluorination of MnO (by LiPF₆ decomposition) and subsequent cycling processes. Reproduced with permission from Ref. ⁸⁷. 48
- Figure 1-8 Performance of nonaqueous metal–gas batteries. (a)** Schematic of metal–gas batteries. **(b)** Voltage–capacity metrics (theoretical) of different metal–gas battery couples including select non-alkali, aqueous anode candidates (Al, Zn) for comparison. **(c)** Theoretical vs. attained specific energy (left axis) and voltage (right axis)..... 50
- Figure 1-9** Schematic of Li–oxygen battery discharge mechanisms: solution-localized (left) and surface-localized process (right)..... 53
- Figure 1-10** Morphology of solid products of Li–oxygen batteries, as indicated, obtained by Scanning Electron Microscopy. The inset in “solution reaction” was obtained at near-equilibrium growth conditions (10 mA/g_c)..... 54
- Figure 1-11** Galvanostatic cycle profile comparison for different Li–O₂(g) battery systems. 55
- Figure 1-13 (a)** Morphology of discharge products for Li–SO₂ / CO₂ / SF₆ / NF₃ gas cathodes, obtained by Scanning Electron Microscopy. **(b)** Experimental galvanostatic cycle profile comparison for Li–O₂, Li–SO₂, and Li–CO₂ batteries. **(c)** Galvanostatic discharge curve of Li–O₂/CO₂/SF₆/NF₃ series compared with commercial Li–primary batteries: Li–SOCl₂(l), Li–SO₂(l), and Li–MnO₂(s). **(d)** Rate capability comparison of Li–O₂ and Li–SF₆ batteries. 58
- Figure 2-1** Galvanostatic discharge profiles of Li–SF₆ cells in various solvents, as indicated, with a lower cutoff voltage of 1.6 V vs Li/Li⁺ on **(a)** Vulcan carbon or **(b)** gas diffusion layer (GDL) cathodes. Electrolytes contained 0.1 M LiClO₄ (TEGDME, DMSO, EC/DEC, PC and DMA) or 0.07 M LiClO₄ (diglyme). For GDL electrodes, capacity and current density are normalized to the GDL geometric area. 73

Figure 2-2 Galvanostatic discharge of Li–gas diffusion layer (Li–GDL) cells in different electrolyte solvents (PC, EC/DEC, TEGDME, diglyme, DMA and DMSO) under an argon headspace at a current density of $5 \mu\text{A}/\text{cm}^2$. The electrolyte was 0.1 M LiClO_4 (with the exception of 0.07 M in diglyme) and the cutoff voltage was 1.6 V vs. Li/Li^+ 74

Figure 2-3 (a) SEM images of cathodes discharged to a limited capacity of 0.05 mAh at $5 \mu\text{A}/\text{cm}^2$ in PC, EC/DEC, TEGDME, DMA, diglyme, and DMSO electrolyte. **(b)** Total achievable discharge capacity as a function of average particle size observed by SEM in different solvents at limited capacity ($0.05 \text{ mAh}/\text{cm}^2$). Average and error bars reflect statistics over at least 20 particles..... 76

Figure 2-4 X-ray diffraction (XRD) patterns of fully discharged Vulcan Carbon (VC) cathodes in different electrolyte solvents containing 0.1 M LiClO_4 (with the exception of 0.07 M in diglyme) at a current density of $75 \text{ mA}/\text{g}_\text{C}$ 77

Figure 2-5 (a) Galvanostatic discharge profiles of Li– SF_6 cells in DMSO electrolyte at current densities of 5, 20, 40, 80 and $120 \mu\text{A}/\text{cm}^2$. SEM image of cathodes discharged to **(b)** $0.1 \text{ mAh}/\text{cm}^2$ and **(c)** fully discharged at different current densities (as indicated) in DMSO..... 78

Figure 2-6 Rotating disk electrode (RDE) measurement of Li– SF_6 cells with DMSO electrolyte. The total integrated capacity of the 1st reduction cycle at various rotation speeds is shown in the inset. The scan rate is 100 mV/s, with a lower cutoff voltage of 1 V vs. Li/Li^+ . For all rotation rates investigated, negligible current can be detected after the 1st cycle in DMSO electrolyte. The argon background (at 1600 rpm, which was representative of all argon scans over different rotation rates) is shown in gray. 79

Figure 2-7 Nyquist plots of Li– SF_6 cells with 0.1 M $\text{LiClO}_4/\text{DMSO}$ electrolyte at different depths of discharge at **(a)** room temperature (RT), **(b)** $50 \text{ }^\circ\text{C}$, and **(c)** with 400 mM TPFPB additive at RT. The corresponding discharge states at which Electrochemical impedances were measured are indicated in the inset. 80

- Figure 2-8** Scanning electron microscopy (SEM) images of gas diffusion layer (GDL) cathodes in Li-SF₆ cells after full galvanostatic discharge in DMSO or DMA electrolyte (as indicated). The current density in both cases was 5 μA/cm² (capacity = 1.3 and 0.6 mAh/cm² for cells discharged with DMSO and DMA, respectively). 81
- Figure 2-9** Li-SF₆ cells at 50 °C. (a) Galvanostatic discharge profile of Li-SF₆ cells in 0.1 M LiClO₄/DMSO electrolyte with GDL electrodes at current densities from 40 to 500 μA/cm² (lower voltage cutoff of 1.9 V vs Li/Li⁺). (b) Comparison of discharge profiles at 50 °C and room temperature (RT) at current densities of 40 and 120 μA/cm². (c) SEM image of a GDL cathode fully discharged at 120 μA/cm² at 50 °C (lower) and RT (upper). (d) Discharge profile of Li-SF₆ cells in DMSO electrolyte with Vulcan carbon electrodes at RT and 50 °C. 82
- Figure 2-10** Galvanostatic discharge of Li/GDL cells at 50 °C in 0.1 M LiClO₄/DMSO electrolyte under an argon headspace and a current density of 40 μA/cm², with a cutoff voltage of 1.9 V vs. Li/Li⁺. 83
- Figure 2-11.** Scanning electron microscopy (SEM) images of GDL cathodes in Li-SF₆ cells fully discharged in DMSO electrolyte at 50 °C at current densities of 40, 80, 120 and 200 μA/cm² (capacity = 1.8, 1.0, 1.0, and 0.9 mAh/cm² respectively). The scale bar = 400 nm in all images. 84
- Figure 2-12 (a)** Schematic depicting the anion receptor, TPFPB, which promotes LiF solvation by forming a complex with F⁻ anions. Cyclic voltammetry traces and the total capacity (inset) of SF₆-saturated electrolyte containing (b) 0.1 M LiClO₄/DMSO, and (c) 0.1 M TPFPB with 0.1 M LiClO₄/DMSO at a scan rate of 100 mV/s. 85
- Figure 2-13. (a)** Cyclic voltammetry of 0.1 M LiClO₄/DMSO electrolyte containing 0.1 M TPFPB under an argon headspace at a scan rate of 100 mV/s. (b) Comparison of 1st scan in Figure 2-13a (as background measurement: TPFPB under Argon), Figure 2-12b (SF₆ in DMSO electrolyte without TPFPB), and Figure 2-12c (SF₆ in DMSO electrolyte with 0.1 M TPFPB). 86

Figure 2-14. (a) ^{19}F NMR of 400 mM TFPFB in 0.1M $\text{LiClO}_4/\text{DMSO}$ electrolyte with/without PC-stabilized Li soaked for six days. To avoid possible reaction between TFPFB and the reference (2,2,2-Trifluoroethanol, TFE), the measurements were conducted using coaxial NMR tubes. The inner tube was filled with 136 mM TFE in DMSO-d_6 with the outer tube containing the electrolyte. (b) Photograph of PC-stabilized Li after soaked in DMSO electrolyte containing 400 mM TFPFB for six days, showing negligible reactivity. 87

Figure 2-15 (a) Galvanostatic discharge profiles of Li-SF_6 cells at $40 \mu\text{A}/\text{cm}^2$. The electrolyte was 0.1 M $\text{LiClO}_4/\text{DMSO}$ containing 0, 50, 200 or 400 mM TFPFB. (b) Theoretical (dashed line) and observed (circles) average capacity gain at the corresponding TFPFB concentration. The averages and error bars represent statistics from more than three samples for each condition. (c) XRD pattern of the pristine GDL and cathodes fully discharged in electrolyte containing 50 and 400 mM TFPFB at $40 \mu\text{A}/\text{cm}^2$. (d) SEM images of cathodes fully discharged at $40 \mu\text{A}/\text{cm}^2$ in DMSO electrolyte with different TFPFB concentrations (as indicated)..... 89

Figure 2-16 Galvanostatic discharge of Li/GDL cells in 0.1 M $\text{LiClO}_4/\text{DMSO}$ electrolyte containing 0.4 M TFPFB under an argon headspace. The cutoff voltage was 1.9 V vs. Li/Li^+ 90

Figure 2-17 (a) Quantification of LiF formed after galvanostatic discharge at 50°C and RT with or without TFPFB additive, in 0.1 M $\text{LiClO}_4/\text{DMSO}$ electrolyte at $40 \mu\text{A}/\text{cm}^2$. Dashed lines indicate theoretical values of LiF formed per mAh of discharge capacity, which correspond to 28.0 and $37.3 \mu\text{mol}/\text{mAh}$ for $8 e^-$ transfer ($\text{Li} + \text{SF}_6 = \text{Li}_2\text{S} + \text{LiF}$) and $6 e^-$ transfer ($\text{Li} + \text{SF}_6 = \text{S} + \text{LiF}$) assumptions respectively. The averages and error bars represent statistics from more than three samples for each condition. (b) S 2p high-resolution XPS spectra of a fully discharged cathode (capacity = $3.0 \text{ mAh}/\text{cm}^2$) at $40 \mu\text{A}/\text{cm}^2$ in 0.1 M $\text{LiClO}_4/\text{DMSO}$ electrolyte with 400 mM TFPFB..... 91

Figure 2-18. Rate capability of Li-SF_6 cells with (a) 400 mM and (b) 200 mM of the TFPFB additive in 0.1 M $\text{LiClO}_4/\text{DMSO}$ electrolyte. Galvanostatic discharge was conducted

at a current density of 40, 80, or 120 $\mu\text{A}/\text{cm}^2$ with GDL electrodes and a cutoff voltage of 2.0 V vs. Li/Li⁺. The relatively large noise in the voltage profiles is caused by room temperature variation during discharge, as TPFPB was found to increase the thermal sensitivity of cells. We verified that all cells made at the same time showed exactly the same trend in voltage fluctuation, and that the noise could be eliminated if the test were performed in a constant temperature incubator. 92

Figure 2-19 Comparison of rate capability of Li-SF₆ cells at 50 °C and RT with or without TPFPB additive, obtained on GDL electrodes in 0.1 M LiClO₄/DMSO electrolyte at a cutoff voltage of 2.0 V vs. Li/Li⁺. The averages and error bars represent statistics from more than three samples for each condition. 93

Figure 3-1 Pentafluorosulfanyl arenes (*R-Ph-SF₅*) as a class of fluorinated catholytes. (a) Schematic depicting Li-*R-Ph-SF₅* batteries. (b) Molecular structures of *R-Ph-SF₅* reactants, with the corresponding discharge profiles shown in (c). All *R-Ph-SF₅* cells were discharged with 0.1 M *R-Ph-SF₅* / 0.1 M LiClO₄ / DMSO as catholyte, Ketjen black as cathode substrate, at 40 $\mu\text{A}/\text{cm}^2$ and 50 °C. Li-SF₆ discharge is included in c for comparison. 98

Figure 3-2 Electronic structure of pentafluorosulfanyl arenes. The bond length of the S-F and S-C bonds are as indicated. The aromatic group breaks the symmetry around the sulfur redox center with the F on the top octahedral vertex being closer to S than the four F that share the same plane. See **Section 3.5.1** for estimation of the sulfur oxidation state (OS)..... 104

Figure 3-3 Optical image of (a) 0.1 M *R-Ph-SF₅* / 0.1 M LiClO₄ / DMSO catholyte and (b) NO₂-Ph-SF₅ / 0.2 M LiClO₄ / DMSO catholyte with different NO₂-Ph-SF₅ concentrations. Generally, NO₂-Ph-SF₅ was found to be miscible with multiple common electrolyte solvents (*e.g.* PC, TEGDME, EC/DMC) in addition to DMSO. 105

Figure 3-4 Characterization of NO₂-Ph-SF₅ discharge products. (a) NO₂-Ph-SF₅ discharge profile under reactant-limited conditions with different cell termination voltages. (b) SEM of carbon cathodes from cells discharged to 2.38 or 1.90 V vs. Li/Li⁺. (c) High

resolution F 1s XPS spectra of discharged electrodes. The two C–F peaks at 688.4 and 686.4 eV are from the polyvinylidene difluoride (PVDF) binder. **(d)** XPS survey spectra (left) with corresponding F, O and S atomic percentage (right). **(e)** UV-vis spectra of extracted electrolyte from discharged cells (diluted in DMSO) as a function of termination voltage.^{228,229} **(f)** Corresponding photographs of samples in **e**. All cell conditions as in Figure 3-1. 108

Figure 3-5 XRD of discharged cathodes from Li–*R-Ph-SF₅* cells with 0.1 M *R-Ph-SF₅*, discharged at 40 μA/cm² and 50 °C. Cell discharge capacities: 0.93, 0.78, 0.73, and 0.70 mAh/cm², for *p*-Li–NO₂-Ph-SF₅, *m*-NO₂-Ph-SF₅, *p*-I-Ph-SF₅, and Ph-SF₅ cells, respectively. High voltage plateau capacities for Li–*p*-NO₂-Ph-SF₅, *m*-NO₂-Ph-SF₅ cells were 0.58 and 0.47 mAh/cm², respectively. 109

Figure 3-6 **(a)** S 2p and **(b)** N 1s high resolution XPS scans of discharged cathodes to the indicated voltages. Reference peaks: polysulfide: 162.9 eV;²³⁰ S₈: 164.0 eV;²³² oxidized sulfur: ~167.8 eV, *e.g.* SO_x²³³ or DMSO.²³⁴ The peaks at 399.4 and 405.0 eV can be attributed to –NO₂-containing organic compounds, while the N signal detected from pristine KB might be attributed to residual NMP.²³² Negligible Li₃N (~395.5 eV)²³⁵ was detected. **(c)** Atomic composition at different degrees of discharge from XPS quantification. **(d)** O 1s high resolution XPS scans of discharged cathodes to the indicated voltages. Reference peaks: Li₂CO₃: 531.4 eV; LiClO₄ (residual electrolyte salt): 532.9 eV.²³² **(e)** Raman spectra of discharged cathodes to the indicated voltages. Reference peaks: Li₂CO₃: 1080 cm⁻¹;²³⁶ –CH₂ stretching: 1464 cm⁻¹;^{237,238} 110

Figure 3-7 **(a)** Mass spectroscopy and **(b)** gas chromatography of the headspace gas from a fully-discharged Li–NO₂-Ph-SF₅ cell with 150 μL 0.1 M NO₂-Ph-SF₅ / 0.1 M LiClO₄ / DMSO electrolyte and KB electrode at 40 μA/cm². Background comparisons were conducted on the headspace gases from cells with the same electrolyte and cathode (without Li) after resting at 50 °C for 3 days. In part b, the peaks at 4.4–4.5 min and 8 min are due to valve switches. 111

Figure 3-8 Galvanostatic discharge of a Li–NO₂–Ph–SF₅ cell with 150 μL 0.1 M NO₂–Ph–SF₅ / 0.1 M LiClO₄ / DMSO as catholyte at 40 μA/cm² and 50 °C, with the corresponding cell pressure (blue symbols). The grey solid line is the projected pressure baseline, which is extrapolated from the linear fit of cell pressure profile during post-discharge resting (for 10 h). To provide a quantitative scale for these measurements, the yellow dashed line is the estimated cell pressure increase if 1 mol of gas were generated per 8 mol of electron transfer, e.g. one NO, NO₂, or SF_x gas molecule (e.g. SF₄). 112

Figure 3-9 Concentration and rate effects on Li–NO₂–Ph–SF₅ cell discharge. (a) Galvanostatic discharge of Li–NO₂–Ph–SF₅ cells as a function of NO₂–Ph–SF₅ concentration at 40 μA/cm². (b) SEM of carbon cathodes fully discharged with 3 M NO₂–Ph–SF₅ / 0.2 M LiClO₄ / DMSO cathode/electrolyte at 0.3 mA/cm². (c) Theoretical/attained capacities and attained gravimetric energies of Li–NO₂–Ph–SF₅ cells as a function of catholyte concentration. All cells were discharged at 0.1 mA/cm². Theoretical capacities correspond to 8 e⁻ per molecule (calculation details in the **Section 3.5.3**). (d) Rate capability of cells with 4 M NO₂–Ph–SF₅ / 0.2 M LiClO₄ / DMSO. Note that 1 C = ~490 mA/g_{sub-stack} = 24 mA/cm² at 4 M concentration. ‘Sub-stack’ weight denotes NO₂–Ph–SF₅ + electrolyte + carbon cathode + consumed Li. 113

Figure 3-10 Discharge of Li–NO₂–Ph–SF₅ cells as a function of reactant concentration at fixed total electrolyte volume (50 μL), normalized to cathode geometric area. The data are the same as Figure 3-9a. 114

Figure 3-11 Ionic conductivity of NO₂–Ph–SF₅-containing electrolytes as a function of NO₂–Ph–SF₅ concentration at 50 °C and at room temperature (RT). 115

Figure 3-12 Shelf-life tests for Li–NO₂–Ph–SF₅ cells with 4 M NO₂–Ph–SF₅ / 0.2 M LiClO₄ / DMSO. The cells were rested for different timespans after assembly and prior to discharge (upper) or after partial discharge (lower). 116

Figure 3-13 Discharge data of Li–CF_x cells at (a) 50 °C and (b) room temperature (RT). Sub-stack = CF_x + carbon + electrolyte + consumed Li. 117

Figure 3-14. Energy and power of primary Li batteries with fluorinated cathodes and catholytes. (a) Weight breakdown of cell components in Li-CF_x, Li-NO₂-Ph-SF₅, and hybrid cells. (b) Ragone plot comparing rate performance of the same cells. Average value and error bar (representing standard deviation) were based on three cells each. (c) Rate performance of hybrid cells using CF_x as solid cathode and 4 M NO₂-Ph-SF₅ / 0.2 M LiClO₄ / DMSO as catholyte. ‘Sub-stack’ for Li-CF_x denotes CF_x + electrolyte + carbon + consumed Li; for hybrid cells, the weight of NO₂-Ph-SF₅ is also included. (d) SEM of discharged cathodes from each cell type (0.3 mA/cm² for Li-NO₂-Ph-SF₅ and hybrid cells, 0.1 mA/cm² for Li-CF_x)...... 118

Figure 3-15 Rate performance of hybrid cells using CF_x as solid cathode and NO₂-Ph-SF₅ / 0.2 M LiClO₄ / DMSO as electrolyte. Cells were discharged with (a) 4 M NO₂-Ph-SF₅ at 50 °C, and (b) 3.5 M NO₂-Ph-SF₅ at 70 °C. 119

Figure 3-16 Projection of theoretical capacity of hybrid cells with different weight ratios (see **Section 3.5.6** for associated discussion and detailed calculations). The shaded region, where the weight of solid components (CF_x + C) is higher than that of liquids, is deemed as non-practical because it is difficult for electrolyte to sufficiently wet the electrode under this condition. The maximum attained capacity in Figure 3-14c (with 4 M NO₂-Ph-SF₅) is labeled as “attained”. 120

Figure 3-17 Low concentration discharge of NO₂-Ph-SF₅ at (a) 50 °C and (b) RT. All cells were discharged with 0.1 M NO₂-Ph-SF₅ / 0.1 M LiClO₄ / DMSO..... 121

Figure 3-18 Room temperature discharge of (a) Li-NO₂-Ph-SF₅ and (b) hybrid cells. Cells in a utilized 4 or 3 M NO₂-Ph-SF₅ / 0.2 M LiClO₄ / DMSO as catholyte, while cells in b utilized 3 M NO₂-Ph-SF₅ / 0.2 M LiClO₄ / DMSO. 122

Figure 3-19 Electrochemical impedance spectra evolution of (a) a Li|C cell and (b) a Li|Li half-cell after different resting times at 50 °C. Cells utilized 4 M NO₂-Ph-SF₅ / 0.2 M LiClO₄ / DMSO as catholyte. (c) SEM of a Li anode after resting at 50 °C in Li-NO₂-Ph-SF₅ (4 M) Swagelok cells with 50 μL electrolyte for 5 h or 1 week. (d) EDX mapping and elemental distribution of a Li anode after resting in Li-NO₂-Ph-SF₅ cells for 5 h at 50

°C. The SEM demonstrates conformal formation of a thin (~100 nm) LiF layer on the Li surface after 5-hour resting. EDX confirmed the layer to consist primarily of F (as LiF) with negligible amounts of other elements (*e.g.* no S or N; note that Li is too light to be detectable from EDX)..... 123

Figure 3-20 SEM image of a Li anode after resting at room temperature for one week in Li–NO₂–Ph–SF₅ cell (4 M reactant), showing sparser SEI formation..... 124

Figure 4-1 Discharge profile of a cell with 0.1 M LiClO₄ / DMSO electrolyte (*i.e.*, lacking CFI reactant) at 20 μA/cm² using 3 pieces of GDL as cathode substrate..... 138

Figure 4-2 Electrochemical discharge characteristics of perfluoroalkyl iodides (CFI) as Li primary battery catholytes. (a) Galvanostatic discharge profiles of various CFI reactants, with the corresponding reactant molecular structures shown in (b). Purple: iodine, blue: fluorine, gray: carbon atoms. All Li–CFI cells utilized 50 μL of 1 M CFI / 0.1 M LiClO₄ / DMSO as catholyte and Ketjen black (KB) as the cathode substrate and were discharged at 0.3 mA/cm² and room temperature (RT)..... 139

Figure 4-3 DFT-computed bond lengths of (a) the C–F bond adjacent to I (in the –CF₂I or –CFI– group) and in the terminal –CF₃ group, and (b) the C–I bond in examined CFI molecules. The initial discharge potential in **Figure 4-2** is plotted for comparison. 2-C₃F₇I and 1-C₃F₇I denote CF₃–CFI–CF₃ and CF₃–CF₂–CF₂I, respectively..... 140

Figure 4-4 Galvanostatic discharge profiles of various CFI reactants. All cells were discharged in Li cells using 150 μL of 1 M CFI / 0.1 M LiClO₄ / DMSO as catholyte and a single piece of gas diffusion layer (GDL) as the cathode substrate at 0.3 mA/cm²..... 142

Figure 4-5 (a) XRD of a gas diffusion layer (GDL) cathode from fully discharged Li–CFI cells ($Q = 3.1, 3.3, 3.2,$ and 3.2 mAh/cm² for CF₃–CF₂–CF₂I, CF₃–CFI–CF₃, C₄F₉I, and C₆F₁₃I, respectively). (b) SEM of the pristine (inset) and fully discharged GDL in Li–CFI cells ($Q = 3.0, 3.0, 3.4,$ and 3.4 mAh/cm² for CF₃–CF₂–CF₂I, CF₃–CFI–CF₃, C₄F₉I, and C₆F₁₃I, respectively). All cells used 150 μL of 1 M CFI / 0.1 M LiClO₄ /

DMSO as catholyte and GDL as the cathode substrate, and were discharged at 0.3 mA/cm ² and RT.	143
Figure 4-6 EDX spectrum of the fully discharged GDL in Li-CFI cells ($Q=3.0, 3.0, 3.4,$ and 3.4 mAh/cm ² for CF ₃ -CF ₂ -CF ₂ I, CF ₃ -CFI-CF ₃ , C ₄ F ₉ I, and C ₆ F ₁₃ I, respectively). All cells used 150 μL of 1 M CFI / 0.1 M LiClO ₄ / DMSO as catholyte and GDL as the cathode substrate, and were discharged at 0.3 mA/cm ²	144
Figure 4-7 Rate capability of Li-C ₆ F ₁₃ I cells with 50 μL of 1 M C ₆ F ₁₃ I / 0.1 M LiClO ₄ / DMSO catholyte and KB cathode substrates at RT.	145
Figure 4-8 Effects of reactant concentration. (a) Discharge profile of cells with 0.1 M C ₆ F ₁₃ I at 0.02 and 0.3 mA/cm ² . (b) Galvanostatic discharge of Li-C ₆ F ₁₃ I cells as a function of C ₆ F ₁₃ I concentration at 0.3 mA/cm ² , with the capacities normalized to number of electrons transfer per C ₆ F ₁₃ I molecule or (c) geometric area. All cells were discharged at RT with 3 pieces of GDL as the cathode substrate and 200 μL of catholyte (0.1 M LiClO ₄ / DMSO). (d) Catholyte ionic conductivities as a function of C ₆ F ₁₃ I concentration.	146
Figure 4-9 (a) SEM and EDX mapping with elemental distribution, and (b) XRD of the GDL cathode substrates extracted from the cell fully discharged at 0.02 mA/cm ² ($Q = 2.2$ mAh/cm ²) with 0.1 M C ₆ F ₁₃ I / 0.1 M LiClO ₄ / DMSO catholyte and 3 pieces of GDL as cathodes.	147
Figure 4-10 Discharge profiles of Li-C ₆ F ₁₃ I cells with 50 μL of 1 M C ₆ F ₁₃ I / 0.1 M LiClO ₄ / DMSO catholyte and KB cathode substrate, at 0.3 mA/cm ² and either 50 °C or room temperature (RT).	148
Figure 4-11 Galvanostatic discharge profiles of Li-C ₆ F ₁₃ I cells at 0.3 mA/cm ² and RT with different solvent species. All the cells utilized KB as cathode substrates, with 50 μL catholyte containing 1 M C ₆ F ₁₃ I and (a) 0.1 M LiClO ₄ or (c) 1 M LiTFSI. (b) Ionic conductivities of 1 M C ₆ F ₁₃ I catholytes in different co-solvent species, with 0.1 M LiClO ₄ or 1 M LiTFSI as electrolyte salt (as indicated). (d) C ₆ F ₁₃ I reduction potential	

($C_6F_{13}I_{(solution)} + Li^+ + e^-$) measured in different solvents, referenced to either Li/Li⁺ or Ag/Ag⁺..... 151

Figure 4-12 (a) Ionic conductivity as a function of DMC content for 0.1 M LiClO₄ / DMSO-DMC solution with or without 1 M C₆F₁₃I. (b) Kinematic viscosity of catholytes with 1 M C₆F₁₃I / 0.1 M LiClO₄ in DMSO, DMC, and/or DMSO-DMC (1:1 v/v) binary solvents. (c, d) Discharge profiles of Li–C₆F₁₃I cells with DMSO or DMSO-DMC (1:1 v/v) co-solvents. Cells contain (c) 200 μL catholyte with 0.1 M C₆F₁₃I / 0.1 M LiClO₄ and three GDL as the cathode substrate, and were measured at 20 μA/cm² and 50 °C, or (d) 50 μL of 1 M C₆F₁₃I / 0.1 M LiClO₄ and KB as cathode substrate, and were measured at 40 μA/cm² and RT. 153

Figure 4-13 Summary of measured defluorination extent of C₆F₁₃I. The intrinsic attained discharge capacity, normalized to number of electrons transferred per C₆F₁₃I molecule, is plotted as a function of C₆F₁₃I concentration at low (0.02 mA/cm², left panel) or high (0.3 mA/cm², right panel) discharge rate; in DMSO or DMSO-DMC (1:1, v/v) co-solvent; at different temperatures (RT and 50 °C); or with KB (square) or GDL (circle) cathode substrates..... 155

Figure 5-1 (a) Molecular structures of fluoro-aromatic reactants, with the corresponding galvanostatic discharge profiles shown in (b). For those molecules containing two substituents, the relative position of the two groups on the ring can be either *para* (*p*) or *ortho* (*o*). All cells were discharged at 50 °C and 40 μA/cm², with 0.1 M reactant in 0.1 M LiClO₄ / DMSO electrolyte, in Li cells with Ketjen black (KB) cathodes. The number of electrons transfer per molecule were calculated based on the capacities obtained..... 161

Figure 5-2 (a) Molecular structures of naphthalenes-based fluoro-aromatic reactants, with the corresponding galvanostatic discharge profiles shown in (b). All cells were at 50 °C and 40 μA/cm², with 0.1 M reactant in 0.1 M LiClO₄ / DMSO electrolyte, in Li cells with KB cathodes..... 166

- Figure 5-3** Galvanostatic discharge profiles of control group fluorinated reactants (as indicated) at 50 °C and 40 and 300 $\mu\text{A}/\text{cm}^2$, with 0.1 M reactant in 0.1 M LiClO_4 / DMSO electrolyte in Li cells with KB cathodes..... 167
- Figure 5-4** (a) XRD and (b) SEM of discharged cathodes from Li–fluoro-aromatics cells with 0.1 M reactant, discharged at 0.3 mA/cm^2 and 50 °C. Cell discharge capacities: 1.1, 1.5, and 1.5 mAh/cm^2 , for *o*- NO_2 -Ph-C6, *o*- NO_2 -Ph-C8, and *p*-CN-Ph-C8, respectively. 168
- Figure 5-5** SEM images of the KB electrodes after fully discharged in the Li–*p*-Ph-CN-C8 cells at 0.04, 0.3 and 0.5 mA/cm^2 (as indicated). All the cells were discharged at 50 °C. 169
- Figure 5-6** Galvanostatic discharge profiles of Li cells with 0.1 M fluoro-aromatic reactants: (a) *o*- NO_2 -Ph-C6, (b) *o*- NO_2 -Ph-C8, and (c) *p*-CN-Ph-C8 in 0.1 M LiClO_4 / DMSO supporting electrolyte, with KB cathode substrate at 50 °C..... 170
- Figure 5-7** Galvanostatic discharge profile of Li cells with 0.1 M fluoro-aromatic reactants: (a) *o*- NO_2 -Ph-C6 and (b) *o*- NO_2 -Ph-C8 in 0.1 M LiClO_4 /DMSO electrolyte, using KB electrodes at room temperature..... 171
- Figure 5-8** Galvanostatic discharge of Li– NO_2 -Ph-C6 cells as a function of NO_2 -Ph-C6 concentration in 0.1 M LiClO_4 / DMSO supporting electrolyte at 40 $\mu\text{A}/\text{cm}^2$ and 50 °C, with capacities normalized to (a) number of electron transfer per molecule, and (b) geometric area of carbon cathodes. 172
- Figure 5-9** Galvanostatic discharge of Li– NO_2 -Ph-C6 cells with 1 M NO_2 -Ph-C6 in 0.1 M LiClO_4 / DMSO supporting electrolyte at 0.3 mA/cm^2 and 50 °C, with three different sizes of carbon substrates: with 9, 12, and 15 mm diameter (total C: 3.2, 5.7, and 8.9 mg, respectively)..... 173
- Figure 5-10** Galvanostatic discharge of Li– NO_2 -Ph-C6 cells with 15 mm diameter carbon foam cathodes and 1 or 2 M NO_2 -Ph-C6 in 0.1 M LiClO_4 / DMSO catholytes, at 40 $\mu\text{A}/\text{cm}^2$

and 50 °C, with capacities normalized to (a) number of electron transfer per molecule, and (b) geometric area of carbon cathodes..... 174

Figure 6-1 Schematic depicting electrochemical fluoridation of MnO cathodes using SF₆ gas as an exemplar fluorination source. Step 1: Electrochemical nucleation and growth of LiF occurs on MnO upon cathodic SF₆ reduction. Step 2: MnO/LiF electrodes are charged to induce electrochemical splitting of LiF and concurrent MnO fluoridation; as depicted, this process initiates at the surface of MnO particles and can continue into the bulk as charging proceeds. Step 3: Subsequent cycling occurs between the nominal end phases Mn-O-F ↔ LiF-MnO..... 180

Figure 6-2 SEM of the ball-milled MnO and MnO/LiF powders (as indicated). Due to the large particle size of the as-received MnO (~0.25 μm), a short ball-mill of 3 h was conducted on MnO/Vulcan carbon (VC) mixture (MnO:VC=7:2 w/w) to reduce the particle size. The MnO/LiF composite (MnO:LiF = 1:1.2 m/m) contains 20 wt% of VC and was ball-milled for 48 h..... 184

Figure 6-3 (a) Galvanostatic discharge profiles of Li-SF₆ and Li-NF₃ cells using MnO/VC cathodes as the substrate at 100 mA/g_c (~65 mA/g_{MnO}) and 75 mA/g_c (~48 mA/g_{MnO}), respectively. (b) X-ray diffraction of a discharged electrode in the Li-NF₃ (*Q* = 1180 mAh/g_{MnO}) and Li-SF₆ (*Q* = 830 mAh/g_{MnO}) cells. (c) SEM images of pristine electrodes and of electrodes discharged to full capacity using fluorinated gas as indicated. (d) High-resolution F 1s XPS spectra of the discharged electrode of a Li-SF₆ cell. To avoid binder-induced F signal, a non-fluorinated binder, polyacrylonitrile (PAN), was used in the cathode instead of PVDF, thus the capacity (~310 mAh/g_{MnO}) is lower than in (a) for this particular cell. The C-F peak at 689.4 eV is from Toray paper..... 185

Figure 6-4 ¹⁹F Nuclear Magnetic Resonance (NMR) spectra of the discharged MnO cathode (under SF₆) after soaking in D₂O. 2, 2, 2-trifluoroethanol was added into the solvent as reference. 186

Figure 6-5. XPS survey scans of a pristine MnO/VC electrode, of LiF@MnO before first charge, and of LiF@MnO after first charge (LiF splitting) following either a constant current (CC) or constant current-constant voltage (CC-CV) protocol..... 187

Figure 6-6 Electrochemical profiles of the first charge (LiF splitting) and the subsequent first discharge of the (a) pristine MnO, (b) ball-milled MnO/LiF, (c) LiF@MnO (from fully-discharged Li-NF₃ cells), and (d) LiF@MnO (from partially and fully-discharged Li-SF₆ cells) with 1 M LiClO₄ EC/DMC electrolyte. All the cells were CC charged at 20 mA/g_{MnO} (~0.05 C) to 4.8 V, then CV charged with a cutoff of 10 mA/g_{MnO}, then CC discharged at 20 mA/g_{MnO} to 1.5 V. The total LiF amount relative to MnO are indicated in each panel, which was calculated based on either the LiF added (for ball-milled sample in part b, assuming 1 e⁻/LiF), or the discharge capacity of Li-SF₆ or NF₃ cell (for c and d). For the latter, each electron was assumed to produce 1 LiF for NF₃, or 6/8 LiF for SF₆. The theoretical capacity of MnO assuming Mn^{2+/3+} redox, 378 mAh/g_{MnO}, is indicated as a grey dashed line..... 188

Figure 6-7 SEM of MnO/VC cathodes in partially discharged Li-SF₆ cell, with a capacity of ~605 mAh/g_{MnO} (corresponding to LiF amount of 454 mAh/g_{MnO}). Two different morphologies were observed: the one on the left shows small discrete particles, which is the pristine (uncoated) morphology; while the one on the right shows larger particle sizes with film-like structure, indicating the presence of the coating layer..... 190

Figure 6-8 Differential capacity plot derived from the galvanostatic discharge profiles in Figure 6-6..... 192

Figure 6-9 (a) First charge (LiF splitting) and discharge (lithiation) profiles of LiF@MnO (from fully discharged Li-SF₆ cells; also used for part b-d) at 20 mA/g_{MnO} with different charge procedures: CC-CV charged to 4.8 V, CC-CV charged to 4.7 V, or CC charged to 4.8 V. Both CV charges were cut off at 10 mA/g_{MnO}. The lower voltage cutoff upon discharge was 1.5 V. (b) EELS of Mn L-edge and (c) Raman spectra for LiF@MnO before charge, and after CC or CC-CV charge as indicated. (d) High-resolution Li 1s and Mn 3p XPS spectra of the pristine MnO electrode and LiF@MnO at different

charge/discharge states. The XPS profile for pristine MnO, CC charged, CC-CV charged, and discharged electrodes are normalized by the Mn 3p peak integrated area. Binding energy reference peaks: LiF 55.7 eV, Mn₂O₃ 49.5 eV, Mn₃O₄ 49.1 eV, and MnO 48.1 eV.²³² To avoid binder-induced fluoridation, PAN binder was used in the cathode instead of PVDF. 193

Figure 6-10 Raman spectra of the pristine MnO/VC electrode, LiF@MnO (uncharged), and CC-CV charged MnO/VC (without LiF presence). Negligible change in Mn bonding environment can be observed. 194

Figure 6-11 High-resolution F 1s XPS spectra of the pristine MnO electrode and LiF@MnO at different charge states. Binding energy reference peaks: LiF 684.9 eV, covalent C–F 689.4 eV,²³² and F⁻ with oxidized Mn³⁺ 686.0 eV.⁸⁴ To avoid binder-induced fluoridation, PAN binder was used in the cathode instead of PVDF. The covalent C–F signal were from substrate Toray paper. Due to the weaker adhesion of PAN, some electrode powder was detached from the substrate after long cell testing and the underlying Toray paper became exposed, resulting in strong C–F signal. As a result, the ionic F signal is relatively weak. 195

Figure 6-12 (a) Rate capability of Mn-O-F. The discharge rate of 10, 20, 60, 100, 150 mA/g_{MnO} correspond to 0.025, 0.05, 0.15, 0.25, and 0.40 C, respectively. The Mn-O-F were derived from LiF@MnO (from fully discharged Li–SF₆ cells; also used for part b) by first CC charge at the corresponding rates to 4.8 V and then CV hold till current drop to half of the initial current. **(b)** Ragone plot comparing the electrochemical performance of LiF-MnO systems as Li-ion cathodes: Ball-milled MnO/LiF composite with an average particle size of ~8 nm (data from Ref. 84) or ~40 ± 25 nm (synthesized and measured in this study); LiF formed *via* LiPF₆ decomposition (data from Ref. 87); and electrochemically-formed LiF@MnO (this study). 197

Figure 6-13 (a) Discharge capacities as a function of cycle number of ball-milled MnO/LiF (~40 nm) cathodes and LiF@MnO cathodes (LiF formed from SF₆ discharge in 0.1 M LiClO₄ TEGDME electrolyte). **(b)** and **(c)** Electrochemical profiles of the first five

cycles of LiF@MnO (LiF formed from SF₆ reduction in 1 M LiClO₄ EC/DMC electrolyte). After LiF formation, **(b)** the cell was directly cycled under SF₆, or **(c)** purged with Ar, then cycled. **(d)** Discharge capacities as a function of cycle number of LiF@MnO cathodes in b and c, compared with the LiF@MnO with LiF formed in TEGDME electrolyte and cycled with no gas present (same data as LiF@MnO in part a). All cells were cycled with 1 M LiClO₄ in EC/DMC electrolyte at 20 mA/g_{MnO} (~0.05 C)..... 198

Figure 6-14 Galvanostatic discharge profile of Li-SF₆ cell with MnO/VC as cathode substrate and 1 M LiClO₄ EC/DMC as electrolyte at a rate of 100 mA/g_C..... 199

Figure 6-15 Galvanostatic discharge profile of Li-SF₆ cell with MnO/VC as cathode substrate and 1 M LiClO₄ EC/DMC as electrolyte at a rate of 20 mA/g_{MnO}..... 200

Figure 7-1 Motifs underlying molecular and solid-state reversibility. **(a)** Comparison of reactant gas cathode molecules, including electronic structures: molecular orbital (MO) diagram; highest occupied MO (HOMO)–lowest unoccupied MO (LUMO) gap. **(b)** Lattice structure of Li₂O₂, Li₂CO₃, Li₂C₂O₄, Li₂S₂O₄ (adapted from Na₂S₂O₄), LiF and LiS. Circles/arrows indicate moieties within the solid phases (O–O pairing in Li₂O₂ and LiO₂, SO₂ motifs within Li₂S₂O₄, and CO₂ motifs within Li₂C₂O₄) predictive of reversibility. Note that LiO₂ is rarely observed as a stable discharge phase but is included here for comparison. Likewise, Li₂C₂O₄ is not commonly observed in Li–CO₂ batteries where the primary product is the less-reversible Li₂CO₃, but is included here for comparison. 210

List of Tables

Table 1-1: Performance comparison of Li primary batteries.	32
Table 2-1: Donor Number (DN), acceptor number (AN) and reported LiF solubility (at room temperature, unless otherwise indicated) of different solvents.	75
Table 2-2. Calculation of TPFPB concentration from NMR result in Figure 2-14, from a nominal added concentration of 400 mM. (Integrals were normalized to that of reference peak. The volume ratio between outer and inner tube is 5.82.)* The case with ‘No Li’ is included to show the typical measurement error occurring without TPFPB present.	88
Table 3-1 Safety comparison of battery electrolytes *	106
Table 3-2: Performances of Li- <i>R-Ph-SF</i> ₅ batteries at 50 °C.....	118
Table 4-1. Solvent properties	150
Table 5-1. Substituent constants σ of <i>para</i> -substituted benzene rings ²²⁷	164
Table 5-2. Attained discharge performances of <i>o</i> -NO ₂ -Ph-C6, <i>o</i> -NO ₂ -Ph-C8, and <i>p</i> -CN-Ph-C8*	170

Chapter 1: Introduction

1.1 Executive Summary and Motivation

Sustained demand for high-energy-density electrochemical power and storage systems motivates continued improvement beyond today's battery chemistries. Driven by the need for better batteries to enable the transition to a more carbon-neutral society, either for grid storage or electric vehicles, rechargeable lithium-ion (Li-ion) batteries have received tremendous research focus in the past few decades. Commercialized Li-ion batteries rely on reversible electrochemical Li^+ insertion into oxide-based cathode materials, *i.e.* intercalation type cathodes, such as lithium cobalt oxide (LiCoO_2), lithium nickel-manganese-cobalt oxide (NMC), and lithium nickel-cobalt-aluminum oxide (NCA).^{1,2} These oxides utilized transition-metal (TM = Mn, Fe, Co, Ni) as active redox centers, which can accommodate 1–2 electrons (e^-) transfer per active-metal site. As a result, the gravimetric energy density of the current Li-ion batteries are relatively limited, with cell-level energy densities of 260 Wh/kg (700 Wh/L), fall short of U.S. Department of Energy targets (350 Wh/kg, 750 Wh/L) deemed necessary for mass-market EV adoption.^{3,4}

Primary Li batteries surpass the limits of Li-ion batteries by utilizing lighter electroactive units based on non-transition-metal redox centers such as carbon (C) or sulfur (S), which lessens the weight per electrical charge,⁵ and thus fill critical needs for applications where high energy, reliability, and portability are essential, such as medical implants, unmanned vehicles, and remote monitoring devices. The electrochemistry of these batteries is not reversible so they are not rechargeable. Examples of Li primary batteries including Li–carbon monofluoride (Li-CF_x), Li–thionyl chloride (Li-SOCl_2) and Li–sulfur dioxide (Li-SO_2), with energy densities ranging from 200–800 Wh/kg_{packaged} and 400–1160 Wh/L_{packaged}. Although these systems still face various challenges, such as rate performance, human health and fire risks, the Li-primary battery field is

deemed as quite mature, with very few fundamental innovations in cell chemistries in the past 40 years.^{6,7}

To widen the design space for advanced batteries, discovery of new electrochemical redox motifs is challenging yet critical. Most of the cathode materials investigated so far are oxide-based, providing deep understanding of various oxide bond properties. For example, common Li-ion cathodes (Li-TM-O) comprise metal–oxygen bonds, primary battery cathodes such as SO_2 and SOCl_2 contains S–O bonds. The currently under development Li–gas batteries utilized multi e^- transfer ($>1 e^-/\text{molecule}$) conversion reaction of the light-weight gas-phase molecules, such as oxygen (O_2),^{8,9} carbon dioxide (CO_2),¹⁰ yielding high theoretical energy densities (3460 and 1880 Wh/kg for Li– O_2 and Li– CO_2 battery, respectively). Despite the limited cyclability, these systems provide important platform to investigate the redox of O–O and C–O bonds. Fluoride-based cathodes, on the other hand, are relatively less investigated. The only instance of the fluoride-based material in commercial Li/Li-ion cathodes is CF_x , which has the highest theoretical energy density (2180 Wh/kg) in the battery market.⁵

Recently, fluorinated-cathodes exhibited strong potential to surpass the current energy density limit, emphasizing the attractiveness of fluoride bond as a new electrochemical redox motif. For intercalation type Li-ion cathodes, fluorine modification allows the retaining of the oxide lattice structure, and is capable of increasing the energy density and stability of the cathode materials. Such advantages can be attributed to the extraordinary electronegativity of F and exceptionally high free energy of formation of fluorides.^{11,12} Unlike intercalation materials, a host lattice for Li^+ is not necessary for conversion cathodes, and thus yielding high theoretical capacities. This led to the development of various fluoride-based conversion cathodes. For example, transition metal fluoride class (MF_y , $\text{M} = \text{Fe}, \text{Co}, \text{Ni}, \text{Cu}$, $y = 2$ or 3) cycles by the quasi-reversible reaction

$\text{MF}_y + y\text{Li} \rightarrow \text{M} + y\text{LiF}$ with high capacities (up to 700 mAh/g_{cathode}), but the cycle performance are limited by the insulating nature of LiF and electrolyte decomposition triggered by the formation of M.¹³ In 2018, our group developed Li–perfluorinated gas batteries, which utilized sulfur hexafluoride (SF₆)^{14,15} or nitrogen trifluoride (NF₃)¹⁶ as cathodes. During discharge, the SF₆ (or NF₃) undergo an 8 (or 3) e⁻ transfer reduction reaction, forming LiF and Li₂S (or N₂). Owing to the light weight of redox center (S or N) and multiple electron transfer per active site, the Li–perfluorinated gas batteries exhibit exceedingly high theoretical energy densities (3920 and 5070 Wh/kg, for Li–SF₆ and Li–NF₃, respectively). However, the multiple fluoride bonds cleavage makes it difficult to reconstruct those bonds on charge, and thus these cells are currently deemed as primary batteries.¹⁷

The goal of this thesis is to expand the landscape of fluoride redox motif to provide a new degree of freedom for the design of high performance batteries. Three different fluoride bonds are targeted: S–F (**Chapter 2 and 3**), C–F (**Chapter 4 and 5**), and Mn–F bonds (**Chapter 6**). Handles to tune the electrochemical activity of those bonds are investigated, including both intrinsic (e.g. molecular structures) and extrinsic (e.g. electrolyte solvent properties) parameters. Starting with Li–SF₆ batteries, in **Chapter 2**, the effect of solvent properties (e.g. donor number,¹⁸ LiF solubility) on the fluoride conversion reaction is investigated, and two strategies to improve Li–SF₆ cell rate capabilities by tuning the LiF nucleation and growth processes are reported. In **Chapter 3**, the effect of intrinsic molecular structures on S–F bond redox activities are examined, using pentafluorosulfanyl arenes, which contains a –SF₅ group, as an example system. We demonstrated that the aromatic structure can facilitate the charge transfer during discharge and affect the S–F bond reduction potential. Based on those understandings, a new type of catholyte is reported which can successfully boost the state-of-the-art Li primary battery energy by 20%.

Another path to surpass the energy limit of CF_x is to increase the F content x . However, this has been rarely investigated before, because those high F-content materials ($x > 2$) generally exhibit low conductivity and are electrochemically inactive. To address these challenges, in **Chapter 4**, strategies to unlock C–F bond reduction activity in high F-content fluorocarbon materials is investigated, using perfluoroalkyl halides ($\text{C}_6\text{F}_{13}\text{I}$, $\text{C}_4\text{F}_9\text{I}$, and $\text{C}_3\text{F}_7\text{I}$) as model liquid-phase reactants. The effect of extrinsic parameters on the C–F bond redox activity were analyzed, including co-solvent properties, reactant concentration, catholyte viscosity, temperature, surface area of substrate carbon, and discharge rate. A maximum of $8 \text{ e}^-/\text{C}_6\text{F}_{13}\text{I}$, or 8/13 available F, is accessible at ideal conditions (low reactant concentrations and rates). To achieve close-to-full defluorination of perfluoroalkyl groups, in **Chapter 5**, effect of molecular structure is studied. Design rationales are discussed for different structural components, including the perfluoroalkyl tail, the conjugated system, the alkene linker, and a ring substitutional functionality, providing multiple handles to tune the defluorination process at intrinsic molecular level.

Controlling parameters for electrochemical fluoridation of transition metal oxide is investigated in **Chapter 6**, using MnO as an example, which can function as rechargeable Li-ion cathodes after fluoridation. The electrochemical fluoridation is achieved by charging MnO/LiF mixture to trigger LiF splitting, and previous study showed that particle size $< 10 \text{ nm}$ was necessary for high MnO utilization. Using electrochemically formed LiF, we examined the effect of LiF morphology on MnO fluoridation, and demonstrated that such stringent particle size requirement is mainly governed by LiF instead of MnO. With nano-crystallized LiF, high MnO utilization ($\sim 0.9 \text{ e}^-/\text{MnO}$) is achievable with large MnO particle size ($\sim 400 \text{ nm}$).

These understandings offer a platform for the design of battery materials for different applications, either for high energy primary cathodes where multiple fluoride bonds breaking at

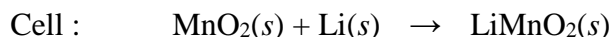
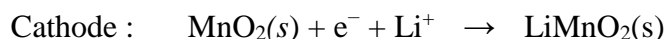
high voltages are critical;^{5,17} or for electrolyte/additive design for rechargeable batteries to improve the cathode or anode interface stability, where a uniform thin-layer of F-rich phase is more desirable, accompanied with additional voltage/kinetics requirements.^{2,19} Additionally, chemical advances in high energy density primary cathodes as described in this work, might contribute to advancements in rechargeable battery chemistry as well; for example, Li–O₂ and Li–SO₂ batteries, initially invented as primary batteries,^{20,21} were later found to be rechargeable following breakthroughs in their electrode and electrolyte formulations.^{22,23} Consequently, this work provides important tools for exploration of F-related chemical motifs across the battery field, and might substantially extend the boundaries of high-energy electrochemical storage.

1.2 Lithium Primary Batteries

1.2.1 State-of-the-art primary battery chemistry

Primary batteries, which represents > 20% of the battery market,²⁴ are critical for applications where high energy, reliability, and portability are essential, such as implantable and/or portable medical devices, undersea or aerial autonomous vehicles (UxVs), robots, military and space devices and their auxiliaries, sensors, consumer electronics, among others. Given the light weight, low standard reduction potential (–3.05 V vs. standard hydrogen electrode), high theoretical capacity (3860 mAh/g), and good conductivity, Li metal is the most attractive anode species for high-energy density electrochemical systems, and thus dominates the high-performance primary battery market.²⁵ Since 1970s, different Li primary battery chemistries have been developed, with sizes ranging from 5 mAh to 10000 Ah, and different cell formats, such as coin cells, cylindrical cells, and large prismatic cells.⁵

The state-of-the-art Li primary battery cathodes include manganese oxide (MnO₂), thionyl chloride (SOCl₂), sulfur dioxide (SO₂, in liquid phase), and carbon monofluoride (CF_x). The theoretical performances and the typical cell-level energy densities of these cathodes are summarized in **Table 1-1**. Li–MnO₂ battery, the first commercially available Li primary cell, was initially developed by Sanyo Electric Co. in 1975, and is now the most widely used Li primary battery given its high cell voltage (~3 V), good performance over a wide temperature range, and low cost. During discharge, MnO₂ serves as an intercalation host for Li⁺, with the Mn being redox-active (reduced from 4⁺ to 3⁺), compensating the charge transfer. The overall cell reaction is:²⁵



$$E^\circ = 3.5 \text{ V vs. Li/Li}^+, Q_{\text{theoretical}} = 286 \text{ mAh/g}, E_{\text{theoretical}} = 1005 \text{ Wh/kg}$$

The needs for oxide lattice host and the use of heavy transition metal (Mn) redox center makes it difficult to further lessen the weight per charge, and thus the cell performances fall short for applications where high gravimetric energy density is critical.

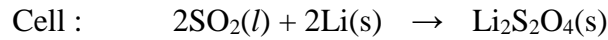
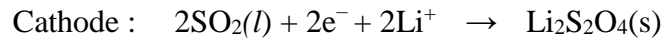
Table 1-1: Performance comparison of Li primary batteries.

Performances of state-of-the-art Li primary batteries at room temperature ⁵									
Cathode	State	Theoretical Capacity		Voltage (V)		Active Material Energy		Packaged Energy ⁵	
		Q (mAh·g ⁻¹)		Theoretical	Practical	Practical V × Theoretical Q ^b		Commercial cells	
		Cathode Active only	Cathode+Li Active only			Gravimetric (Wh·kg ⁻¹)	Volumetric (Wh·L ⁻¹)	Gravimetric (Wh·kg ⁻¹)	Volumetric (Wh·L ⁻¹)
MnO ₂	Solid	308	286	3.5	2.9	830	2560	230–270	545–620
SO ₂	Liquid	419	377	3.0	2.8	1055	1255	260	415
SOCl ₂	Liquid	450	403	3.65	3.6	1450	1950	480–590	950–1100
CF _x ^a	Solid	865	706	3.1	2.8/2.9	1980/2050	3065/3175	250–800	560–1160

^a Values measured at room temperature or 50 °C, following the format: room temperature/50 °C.

^b The *Theoretical Q* used to calculate the *Active Material Energy* is based on the weight of cathode + Li.

Li primary batteries that surpass the energy density of Li–MnO₂, exploited the electrochemical activity of lighter, non-transition-metal redox centers such as sulfur (S) or carbon (C). Primary Li–SO₂ battery was first developed in the 1960s,²⁰ and found commercial success in military and aerospace due to its long shelf life, good rate capability, and excellent low temperature performances (operating temperature window from –40 to 55 °C).⁵ Typical Li–SO₂ cell utilized carbon as cathode substrate, and catholyte consist of compressed, liquefied SO₂ (>3.4 atm) and an organic solvent (typically acetonitrile) or ionic liquid.²⁶ The overall cell reaction is:

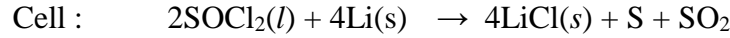
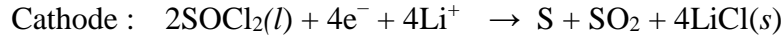


$$E^\circ = 3.1 \text{ V vs. Li/Li}^+, Q_{\text{theoretical}} = 377 \text{ mAh/g}, E_{\text{theoretical}} = 1170 \text{ Wh/kg}$$

Common Li–SO₂ cells are designed to be cathode limited, where the formation of passivating Li₂S₂O₄ on carbon surface is the major contribution to cell termination. In absence of SO₂, direct exothermic reaction between Li and acetonitrile could result in the formation of toxic and flammable products, such as lithium cyanide and methane, accompanied with cell venting or rupture due to high temperature. Therefore, balanced cell design with protective SO₂ remains in the electrolyte is currently more favorable.

Li–SOCl₂ battery, which also utilized the redox of S, has one of the highest attainable cell-level energy densities, with up to 590 Wh/kg and 1100 Wh/L achieved in practical cell systems. The extraordinary energy density is attributable to the exceedingly high cell voltage (nominal voltage 3.6 V) and the two e[–]/SOCl₂ reduction mechanism, which significantly lessens the weight per charge transferred. The Li–SOCl₂ cell utilized porous carbon as cathode substrate, SOCl₂ as

both the active material and the electrolyte solvent, and Li salt, such as lithium tetrachloroaluminate (LiAlCl_4) and lithium tetrachlorogallate (LiGaCl_4). The cell reaction is:²⁷



$$E^\circ = 3.65 \text{ V vs. Li/Li}^+, Q_{\text{theoretical}} = 403 \text{ mAh/g}, E_{\text{theoretical}} = 1470 \text{ Wh/kg}$$

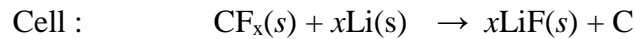
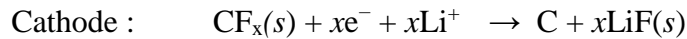
The reduction products, S and SO_2 , are soluble in SOCl_2 at initial discharge, and precipitate/release from the electrolyte as the SOCl_2 being consumed to the end of discharge. Insoluble LiCl and S passivates the carbon surface, blocking the cathode from further electron transfer, and triggering cell termination.

The two batteries with liquid cathodes, *i.e.* Li- SO_2 and Li- SOCl_2 cells, both exhibit excellent high rate performances and good shelf-life (5–20 years), the latter of which can be attributed to the stable passivating solid electrolyte interphase (SEI) formed on Li surface (mainly consists of $\text{Li}_2\text{S}_2\text{O}_4$ and LiCl for Li- SO_2 and Li- SOCl_2 cells, respectively). However, the high toxicity and corrosivity of these easily evaporated liquids raised significant safety concerns, and thus these cells are mainly limited to specialty applications.^{6,7,27}

Li- CF_x battery, with the highest theoretical energy density (2180 Wh/kg) among primary battery chemistries, addresses the safety challenges owing to the solid nature of CF_x cathode. For high-energy, low-rate applications, the packaged Li- CF_x cells can reach energy densities up to 800 Wh/kg.²⁸ However, the high power performances of this system is relatively limited, due to the low electronic conductivity of CF_x particles.^{29,30} Given its attractive theoretical performances, the Li- CF_x cell reaction mechanism and pathways to improve rate performances are introduced in detail in **Section 1.2.2**.

1.2.2 Fluorinated primary cathode: CF_x

The fluorine (F)-content x in CF_x ranges within $0 < x \leq 1.3$, with a typical value of $x \approx 1$ in commercial Li–CF_x batteries. CF_x are commonly synthesized by reacting fluorine (F₂) gas and graphite (or other carbon materials) at high temperatures (350–640 °C),^{31,32} and the resulting CF_x lattice structure is shown in **Figure 1-1a**. Commercial Li–CF_x cells utilize different electrolytes, such as 1 M lithium tetrafluoroborate (LiBF₄) in δ -butyrolactone, and 1 M LiBF₄ in propylene carbonate (PC) / 1,2-dimethoxyethane (DME) mixture. The cell reaction is:



$$E^\circ_{x=1} = 4.57 \text{ V vs. Li/Li}^+,^{33} E_{\text{OCV}} = 3.1 \text{ V vs. Li/Li}^+,^5$$

$$Q_{\text{theoretical}} = 706 \text{ mAh/g, } E_{\text{theoretical}} = 2180 \text{ Wh/kg}$$

Where the theoretical voltage E° based on thermodynamic data at $x = 1$ is 4.57 V vs. Li/Li⁺. However, in practice, the operating voltage of the cell is only ~2.5–2.7 V vs. Li/Li⁺ (**Figure 1-1b**), much lower than the theoretical value, indicating that the actual discharge mechanism is more complex and the single-step reduction assumed here failed to represent the actual voltage-determining reactions. Therefore, the open circuit voltage (OCV, 3.1 V vs. Li/Li⁺) is commonly used for the calculation of theoretical energy densities.

To understand the CF_x discharge process at a fundamental level, many first principles and experimental studies were conducted.^{11,34-41} To measure the theoretical voltage of Li–CF_x cells at near-equilibrium conditions, Leung et al. conducted galvanostatic intermittent titration technique (GITT) measurements, where the kinetic overpotentials are greatly minimized,³⁴ and reported CF_x discharge voltages below 3.1 V.³⁸ The origin of the overpotential was explained *via* solvent-

mediated and/or edge-propagation mechanisms. The solvent-mediated mechanism assumes a solvent (*S*)-coordinated Li^+ complex as intermediate phase: $\text{Li} + \text{CF} + y\text{S} \rightarrow (\text{CF}^-)(\text{Li}^+)(\text{S})_y$,^{11,35} providing a plausible explanation for the large overpotential and the solvent-dependent cell voltage.^{36,37} The edge-propagation mechanism, on the other hand, specifies that the reaction follows an edge-mediated pathway instead of a bulk-phase reaction, and thus the discharge properties are mainly determined by the local environment. This mechanism offers an explanation for the stable voltage plateau across the discharge, which is independent of the extent of the state-of-charge (**Figure 1-1b**).^{38,39}

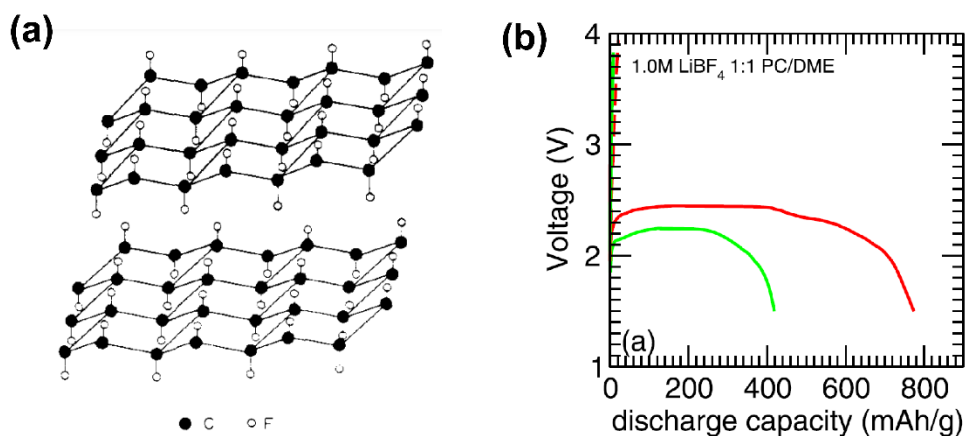


Figure 1-1 (a) Lattice structure of CF_x . Reproduced with permission from Ref. 42. (b) Galvanostatic discharge of $\text{Li}-\text{CF}_x$ cells with 1 M LiBF_4 in PC/DME as electrolyte. Cells were discharged at $C/20$ (red) and $C/5$ (green). Reproduced with permission from Ref. 38.

At a practical level, researchers have been focusing on optimizing cathode composition and/or structure to address the limitations induced by the low conductivity of CF_x , namely poor rate performances, voltage delay (at initial discharge), and heat generation during discharge.²⁹ One promising approach to improve high-power performance is by adding carbon nanotubes (CNTs) to form composites with CF_x , which can successfully increase both the cathode surface area and the electronic conductivity.³⁶ CNTs have also been used as the starting carbon material for CF_x

synthesis. The curvature of CNTs alters the C–F bonding nature and is beneficial for reducing the discharge overpotential.⁴³ Other efforts focused on synthesizing sub-fluorinated graphite with decreased F content ($0.33 < x < 0.66$), to induce some electronically conductive domains. However, lowering the F content directly decreased the theoretical energy density of the material, exhibiting a tradeoff between power and energy density.⁴⁴

Overall, the success of Li–CF_x batteries lies in the utilization of the light-weight C redox and high stability of the fluoride discharge product (LiF), the latter of which contributes to large Gibbs free energy change during reduction reactions. This energy-leading battery chemistry suggests the strong potential for fluoride-based cathodes to achieve exceedingly high energy densities.

1.3 Lithium-ion Batteries

1.3.1 State-of-the-art Li-ion battery chemistry

1.3.1.1 Intercalation cathodes

Rechargeable Li-ion batteries have greatly impacted the modern society ever since its first development in 1980s.^{1,45} Sustained demand for higher-energy rechargeable Li/Li-ion batteries that can reach U.S. Department of Energy targets (cell-level energy densities of 350 Wh/kg and 750 Wh/L, and pack-level costs <US\$125 kWh⁻¹) motivates continued improvement beyond today's Li-ion cathode chemistries, which is a key component that limit the battery performance.^{2,4} If the target is reached, enabling the mass market electric vehicle (EV) adoption, the greenhouse gas emission will be significantly reduced.⁴⁶ Therefore, development of novel cathodes with improved energy density, increased cycle life and safety, and lower cost, is of vital importance.⁴⁷

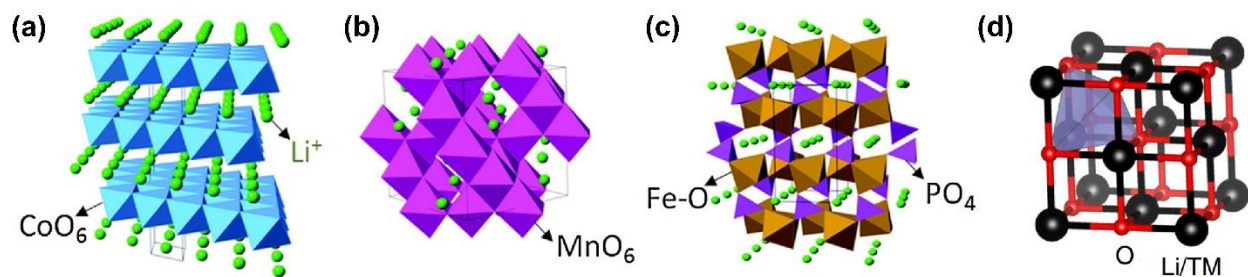


Figure 1-2 Lattice structures of intercalation cathodes: (a) layered (LiCoO₂), (b) Spinel (LiMn₂O₄), (c) olivine (LiFePO₄), and (d) disordered rock-salt. Part a–c reproduced with permission from Ref. 46; Part d reproduced with permission from Ref. 48.

Currently, all commercialized Li-ion battery cathodes belong to intercalation type oxide-based materials. These intercalation type cathode offers an oxide-lattice host, which allows reversible Li⁺ ion insertion/removal. The redox active sites, typical transition metal species (TM), compensating the additional charge *via* reversible valence change (by 1–2), and thus the bulk material remains charge neutral. The most popular cathode being used so far is lithium cobalt oxide (LiCoO₂), which has a layered lattice structure (**Figure 1-2a**) and can achieve a practical capacity of ~140 mAh/g in commercial lithium-ion batteries.⁴⁶ However, LiCoO₂ has known issues of poor thermal stability, and utilizes toxic and expensive Co.⁴⁹ Therefore, much effort has been focused on the development of alternative cathode materials where Co is fully or partially replaced, such as lithium nickel-manganese-cobalt oxide (NMC) and lithium nickel-cobalt-aluminum oxide (NCA). Particularly for NMC with a layered structure, a capacity higher than 200 mAh/g can be delivered, much higher than well-investigated spinel oxides (LiMn₂O₄, ~140 mAh/g, **Figure 1-2b**) and olivine oxides (LiFePO₄, ~170 mAh/g, **Figure 1-2c**).⁴⁶ Further optimization on NMC system has led to the development of Ni-rich⁵⁰ and Li-rich NMC⁵¹ system with enhanced capacity (>280 mAh/g). Another high-capacity oxide cathode currently under development is Li-rich disordered rock-salt phases (>300 mAh g⁻¹),⁵² where the Li and TM exhibit disordered arrangement on the

cation lattice sites (**Figure 1-2d**). However, those high-capacity systems rely on anionic redox, which triggers oxygen release along with transition metal dissolution during cycling, resulting in limited cyclability.⁵³⁻⁵⁵ Currently, commercialized Li-ion batteries emphasize the needs for cathodes with both high energy density and good cyclability.

1.3.1.2 Conversion cathodes

Reproduced in part with permission from Gao, H., & Gallant, B. M. (2020). Advances in the chemistry and applications of alkali-metal-gas batteries. Nat. Rev. Chem., 4, 566–583. Copyright 2020.

Seeking pathways to higher energy, there has been an impetus to re-consider the nature of charge storage in batteries. As an alternative to the intercalation cathodes, conversion reactions that involve bulk phase transformations such as solid–solid, liquid–solid, or gas–solid— have received significant attention.^{13,56,57} Conversion reactions are governed by physical phenomena distinct from intercalation reactions, including nucleation and growth of new phases, expressive volume change of electrodes, and unique and often more-complex reaction mechanisms. A general comparison of the voltages and capacities between intercalation and conversion cathodes is shown in **Figure 1-3**:

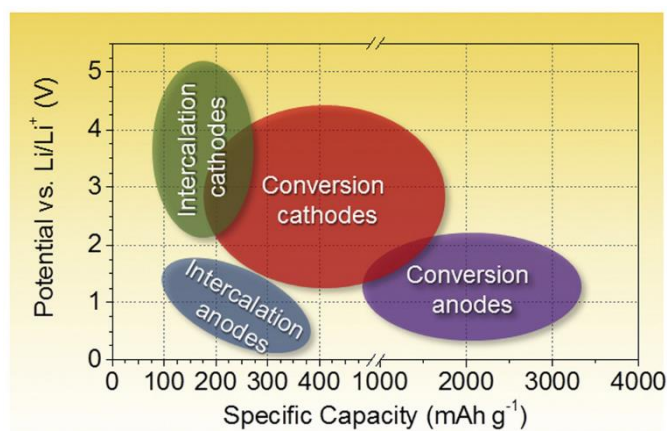


Figure 1-3 Overall comparison of average discharge voltages and specific capacities for intercalation and conversion type materials. Reproduced with permission from Ref. 46.

Depending on the full cell reaction mechanism, the conversion cathodes can generally be divided into two categories:^{13,46}



For Category A, an example of an established conversion technology is the sulfur (S) cathode in Li–S batteries, which cycles by solid(–liquid)–solid transition between $\text{S}_8(s)$ and $\text{Li}_2\text{S}(s)$ during discharge and charge with high theoretical capacity (1672 mAh/g_{sulfur} or 1165 mAh/g_{Li₂S}, ~2.2 V vs. Li/Li⁺).⁵⁸ S has received significant research interests because of its high theoretical capacity, low cost, and earth abundance. Practical Li–S batteries have faced challenges including the formation of soluble polysulfides (reduced S intermediates, S_n^{2-} , $n < 8$), which can create internal shuttles between cathode and the Li anode during conversion to the final insoluble Li_2S end product, and are still maturing.⁵⁹

An example for Category B is the transition metal fluoride class (MF_y , $\text{M} = \text{Fe}, \text{Co}, \text{Ni}, \text{Cu}$, $y = 2$ or 3) which cycle by the quasi-reversible reaction $\text{MF}_y + y\text{Li} \rightarrow \text{M} + y\text{LiF}$ with moderate voltages (~2.5–3.5 V vs. Li/Li⁺) and high capacities (up to 700 mAh/g_{cathode}). Charging and cycling are limited by poor electrical contact and slow kinetics upon re-conversion of two phase-separated solids (M and LiF) back to MF_y upon charge, leading to large voltage hysteresis (> 1 V) and rate limitations.¹³

Consequently, the search for better Li/Li-ion battery cathodes are proceeding in two different research directions: First is to optimize the current cathode chemistry at a fundamental level, for example, incorporating fluorine (F) into the oxide-based lattice to improve the attainable energy density or cycle stability (see **Section 1.3.2**); Another direction explores other high-energy conversion reactions with potential to achieve good cycleability. This led to a sharp re-focusing

on nonaqueous gas–solid—an alternative to solid–solid—electrochemistry around the beginning of the last decade (2010), which will be introduced in detail in **Section 1.4**.

1.3.2 Fluoridation for Li-ion cathodes

1.3.2.1 Fluorine substitution for intercalation oxide cathodes

For cathode oxides with intrinsic Li^+ -conduction pathway, F-substitution has been shown to be a promising approach to increase capacities. With F^- replace O^{2-} , the valence state of transition metal (TM) species in the oxides decreases, thus more charge can be compensated by TM redox during discharge. For example, with 6% of F substitution of O in $\text{Li}_{1.15}\text{Mn}_{1.7}\text{Co}_{0.15}\text{O}_4$ (spinel), the oxidation state of Mn changed from 3.76 to 3.62, accompanied with a capacity increase from only 77 mAh/g to 104 mAh/g.⁶⁰ F-induced capacity gain could also originate from novel redox reaction mechanism: with TM–F bonds partially substitute TM–O bonds, the electronic structure of TM ions is changed, which might trigger novel multi-electron redox reactions. This phenomenon has been observed in many oxides with disordered rock-salt structures. For example, Takeda et al. observed $\text{Mo}^{3+}/\text{Mo}^{5+}$ two-electron redox in $\text{Li}_2\text{MoO}_2\text{F}$, with a reversible capacity of over 300 mAh/g.⁶¹ Clément et al. suggest that in $\text{Li}_{1.15}\text{Ni}_{0.45}\text{Ti}_{0.3}\text{Mo}_{0.1}\text{O}_{1.85}\text{F}_{0.15}$, with F bonded with Ni, the oxidation from Ni^{2+} to Ni^{4+} occurs *via* the formation of Ni^{3+} intermediates instead of the direct valence increase by two, enabling a more complete $\text{Ni}^{2+}/\text{Ni}^{4+}$ redox.⁶²

In addition to higher capacities, F-substitution is also beneficial for improving cyclability. As for Mn-based oxides, due to the increased bond strength of Mn–F bond than Mn–O bond, F-substitution can increase the structural stability by suppressing Jahn-Teller distortion caused by Mn^{3+} ions, and /or by decreasing Mn dissolution. Okumura et al. demonstrated that in $\text{Li}_{1.1}\text{Mn}_{1.8}\text{Ni}_{0.1}\text{O}_{4-x}\text{F}_x$ ($x=0-0.18$) spinel, the capacity fade could be mitigated by the F^- ion substitution, possibly because the Mn–F bonds replace some of the Mn–O bonds, preventing the

MnO₆ octahedral distortion.⁶³ A similar stabilizing effect has also been observed by Windmüller et al. in fluorinated LiCoMnO₄ spinel. Improved capacities (up to 18%) and cycling stability (by ~20%) were achieved, compared to their non-fluorinated counterparts.⁶⁴

In NMC compounds, F-substitution is beneficial for protecting the oxides against side reaction with electrolyte, and thus to suppress the capacity fade. Yue et al. demonstrated that for LiNi_{0.8}Co_{0.1}Mn_{0.1}O₂, enhanced cyclability was achieved by only 2% F-doping: capacity retention of 94% after 100 cycles at 2 C was reached (that for un-doped sample is only 80%). Such enhancement might be attributed to strong metal–F bonding that protects the cathode surface from hydrogen fluoride (HF, a product of electrolyte decomposition) attack.⁶⁵ Wang et al. conducted fluorine surface modification for LiNi_{0.73}Co_{0.12}Mn_{0.15}O₂, where a partial phase transformation from a layered to a cubic rock-salt structure on the surface region was observed. As a result of the synergistic protection of this surface layer, side reactions between the active material and electrolyte was restrained and enhanced capacity retention (98% after 200 cycles) was observed.⁶⁶

In Li-excess oxides, F-substitution can improve the cyclability by decrease the capacity contribution from oxygen redox. Oxygen redox has been observed in Li-excess materials with layered structure and disordered rock-salt structure, where the excess Li occupied TM sites and resulted in the formation of some Li–O–Li configuration. O in such configuration pertains a higher energy state and thus oxygen redox becomes much easier to happen.⁵⁵ Oxygen redox contributes to excess capacity, but also triggers oxygen loss, resulting in substantial voltage and capacity fade.⁵⁴ Kang and Amine demonstrated that fluorine doping of 5% can enhance the cycle performance of Li-rich NMC (Li_{1.2}Mn_{0.55}Ni_{0.15}Co_{0.1}O₂).⁶⁷ Wang et al. revealed that F-substitution will not induce a drastic structural change (**Figure 1-4a**) but the lattice constant will decrease

slightly. The increased cyclability of the F-doped Li-rich NMC (**Figure 1-4b, c**) is attributable to the decreased capacity contribution from Li_2MnO_3 , which is a major source of oxygen redox.⁶⁸

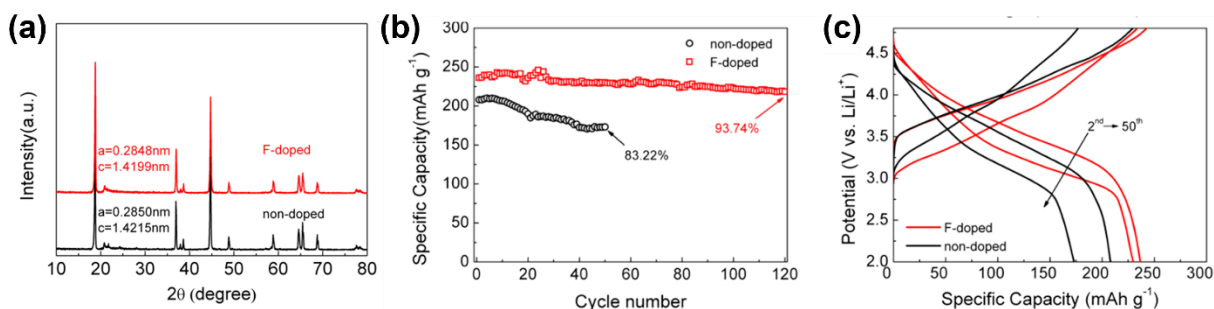


Figure 1-4 (a) XRD pattern, (b) cycle performance, and (c) galvanostatic charge/discharge curves in the 2nd and 50th cycles of non- and F-doped Li-rich NMC at the rate of 0.1 C. Reproduced with permission from Ref. 68.

Fluorinated oxides with disordered rock-salt (DRX) structures exhibit attractive electrochemical performance, while the mechanism of which still worth further investigation. In DRX, Li and TM species randomly occupy the lattice sites,⁶⁹ resulting in locally metal-poor / lithium-rich environments. Such environments exhibit high fluorine affinity, and thus, unlike classic well-ordered cathodes where fluorine is often present as a coating layer rather than incorporate into the bulk, DRX can achieve a high-degree of bulk fluoridation.⁷⁰ Experimentally, a high reversible capacity of 320 mAh/g with enhanced cyclability (>80% after 20 cycles at 1 C) has been achieved by F-substitution in disordered rock-salt $\text{Li}_2\text{VO}_2\text{F}$.⁷¹ Recently, House et al. demonstrated that relatively stable O-redox is achievable in an all-manganese oxyfluoride with disordered rock-salt structure. The charge/discharge profiles and the cycling performances are shown in **Figure 1-5**. $\text{Li}_{1.9}\text{Mn}_{0.95}\text{O}_{2.05}\text{F}_{0.95}$ exhibits a high capacity of 280 mAh/g (corresponding to 960 Wh/kg), half of which (130 mAh/g) arises from O-redox, while the rest is attributable to $\text{Mn}^{3+/4+}$ redox. Notably, there is little evidence of any O loss from the lattice.⁷²

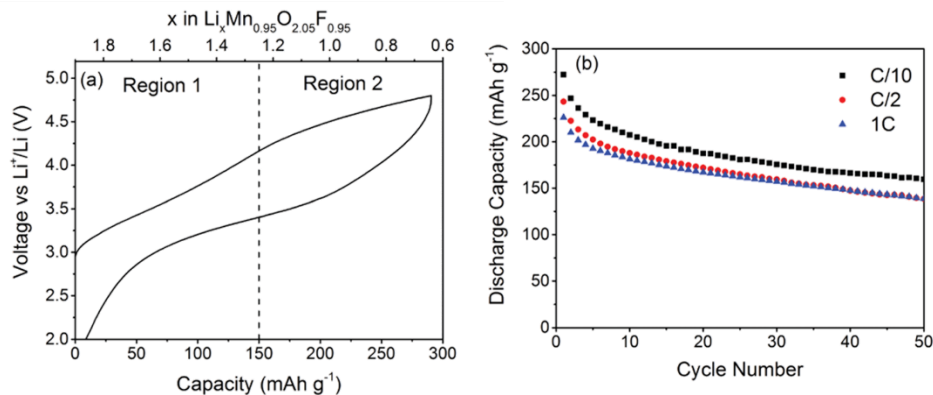


Figure 1-5 (a) Charge–discharge curve for Li-Mn-O-F vs. lithium. First cycle is shown in the voltage range 2 V to 4.8 V at a rate of C/10 (22.4 mA/g). (b) Discharge capacity as a function of cycle number at progressively faster C-rates of C/10, C/2, and 1C. Reproduced with permission from Ref. 72.

1.3.2.2 Fluorine substitution for conversion oxide cathodes

Simple binary oxides are attractive as a battery cathodes owing to their low-cost and high theoretical capacity. For such Li-free oxides to be used in practical batteries, they conventionally need to be coupled with Li metal or pre-lithiated anodes to make as-assembled charged-state lithium-ion batteries, which limits their use in Li-ion batteries.⁷³

Mixed-anion transition metal oxyfluorides offer the combined advantages of fluorides (high capacity and voltage) and the beneficial effects of oxide (increased conductivity when O replace F ions in lattice). Transition metal oxyfluorides can deliver a high discharge capacity, both theoretically and experimentally. For example, iron oxyfluoride (FeOF) exhibits a theoretical capacity of 885 mAh/g (assuming Fe^{3+/0} redox), higher than that for pure fluorides, which is 712 mAh/g for FeF₃ and 571 mAh/g for FeF₂.⁷³ Vanadium oxyfluoride (VO₂F, rhombohedral structure) undergoes phase transformation to disordered rock-salt structure upon cycling, yielding a high attained capacity of 350 mAh/g at 50 mA/g.⁷⁴ Oxyfluorides also tend to exhibit a high discharge

voltage, e.g. silver niobium oxyfluoride exhibits a discharge voltage >3 V vs. Li/Li⁺.⁷⁵ Increased conductivity has also been observed. For example, in molybdenum oxyfluoride, F-substitution leads to charge redistribution in MoO₃ lattice, contributing to conductivity increase from 4.4×10^{-9} to 1.8×10^{-6} S/cm, accompanied with improved capacity (from 120 mAh/g to 160 mAh/g).⁷⁶

However, the cyclability of the oxyfluorides is relatively limited, partially due to the the reaction between the electrolyte and the metallic phase formed from the conversion reaction. One possible approach to address this limitation is by tuning the concentration gradient within the oxyfluoride particles. In FeO_{0.7}F_{1.3}, the as-synthesized material had a rutile structure but was chemically heterogeneous, with a F-rich core and O-rich shell. Upon cycling, the O-rich shell transformed into a more stable rock-salt structure, which prevented the reaction between Fe and electrolyte. During cycling the O-rich shell went through intercalation reaction while the F-rich core experienced conversion reaction, resulting in a high capacity and good stability (with an initial capacity of 420 mAh/g, and capacity of 340 mAh/g after 20 cycles).^{77,78}

1.3.2.3 LiF-Coated Cathodes and Electrochemical Splitting of LiF

In addition to F-substitution, discrete LiF phase are also possible to be used as F source. LiF can present as a coating layer, or be mixed with cathode precursors (such as TM oxides). When used as the coating layer, despite that LiF is highly resistive to Li⁺ migration, it can act as a protection layer due to its wide stability window (from 0 to >6 V vs. Li/Li⁺),⁷⁹ yielding in an enhanced cyclability. Ménétrier et al. revealed (by ⁷Li and ¹⁹F MAS NMR) that in fluorinated NMC, a LiF coating layer is more preferred to form instead of bulk F-substitution.⁸⁰ The resulting LiF-coated NMC exhibited improved cyclability.⁸¹ This finding demonstrated that nanoscopic LiF can serve a beneficial role even if it's nominally passivating.

When mixed with cathode precursors, LiF can act as the built-in Li and F source, providing a possible approach to address the needs for pre-lithiation in Li-free cathodes. Kang et al. proposed that energy storage can be achieved in composites of a redox couple host (Li-free material) and a Li-ion host (LiF). The feasibility of this strategy was first demonstrated in FeF₂/LiF composites. FeF₂ was found to be electrochemically activated by LiF after the first charge via reaction $\text{FeF}_2 + \text{LiF} \rightarrow \text{FeF}_3 + \text{Li}^+ + \text{e}^- \leftrightarrow \text{LiFeF}_3$, yielding a reversible capacity of 190 mAh/g_{FeF₂+LiF} at 50 mA/g_{FeF₂+LiF}.⁸² A similar idea has also been applied to Mn-based compounds. Dimov et al. investigate the electrochemical performance of ball-milled LiF with MnF₂, MnO, Mn₃O₄, Mn₂O₃, and MnO₂. Unlike the FeF₂, the MnF₂/LiF composite was electrochemically inactive, which was attributed to the instability of MnF₃ making MnF₂ not suitable as F⁻ acceptor. In contrary, LiF splitting and substrate fluoridation was achieved with manganese oxides/LiF composites, and the lower the Mn valence, the better utilization of Mn redox. For example, MnO/LiF composites can deliver a capacity of 185 mAh/g_{MnO+LiF}, while that for LiF/MnO₂ was only 71 mAh/g_{MnO₂+LiF}.⁸³

Effect of TM species on the TM oxide fluoridation by LiF electrochemical splitting was investigated by Kang and co-workers. LiF-MnO, LiF-FeO and LiF-CoO nanocomposites with an average particle size of 8 nm were obtained through high energy ball-milling, exhibiting reversible capacities of 240, 310 and 206 mAh/g_{MO+LiF} at a rate of 20 mA/g_{MO+LiF}, respectively (**Figure 1-6**). The discharge performance is highly dependent on the composite particle size, for example, increasing the average particle size of Mn₃O₄/LiF composite from 6 to 20 nm, resulted in significant capacity decrease from 150 to 100 mAh/g_{MO+LiF}. Additionally, in contrast to LiF-MnO system, where the interaction between Mn- and F-ion was mainly surface-concentrated, in LiF-FeO system a substantial amount of F was found to be incorporated in the bulk-phase FeO particles, forming new FeO-F phase.^{84,85}

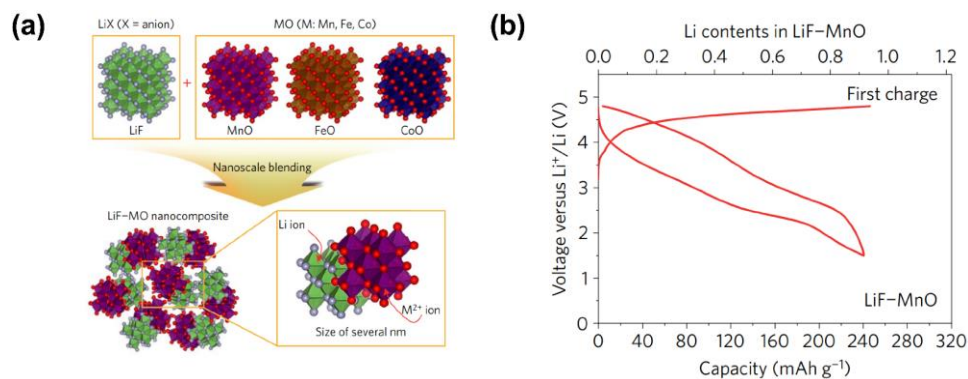


Figure 1-6 (a) Schematic of the positive electrode material design strategy using metal monoxide (MO). After mechano-chemical mixing, LiF and MO exist without chemical reaction in the several nanometer scale. The crystal structure of all compounds is described by a polyhedral image. Red, O; grey, F; green, Li; purple, Mn; brown, Fe; blue, Co **(b)** First discharge and second charge profiles of LiF-MnO nanocomposites after the initial activating charge protocol. The cell was cycled between 1.5–4.8 V at a rate of 20 mA/g (0.03 mA/cm²). Reproduced with permission from Ref. ⁸⁴.

Instead of directly adding into cathode, another source for LiF is electrolyte decomposition. LiPF₆, a commonly used electrolyte salt, was known to decompose at voltages > 4.5 V vs. Li/Li⁺ and forming LiF. Charging the cell Li-MnO cell to 4.8 V vs. Li/Li⁺ triggered *in situ* formation of LiF, which subsequently underwent electrochemical splitting and fluoridated the MnO substrate. Typical charge/discharge profiles are shown in **Figure 1-7a**, with reversible capacity over 300 mAh/g_{MnO} obtained.⁸⁶ Further investigation showed that MnO was fluoridated *via* a surface-induced activation process, forming highly disordered Mn-O-F phase, with an O-rich cubic-spinel-like core and a F-rich amorphous shell (**Figure 1-7b**).⁸⁷ Similar idea has also been applied in Na-ion battery system, with MnO as electrode, using the decomposition of NaPF₆ salt, a capacity of 145 mAh/g_{MnO} was achieved.⁸⁸

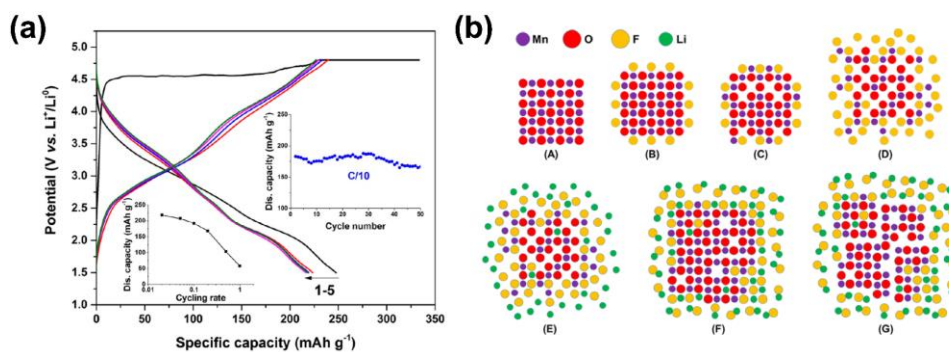


Figure 1-7 (a) Electrochemical cycling of MnO/C. The insets elucidate rate capability and cyclability of the activated composites. All the cells were in 1 M LiPF₆ in ethyl carbonate/dimethyl carbonate (EC/DMC; v/v = 1:1) electrolyte. (b) Schematic illustration of the in situ fluorination of MnO (by LiPF₆ decomposition) and subsequent cycling processes. Reproduced with permission from Ref. ⁸⁷.

Overall, these examples show that fluorinated cathodes, either from F-substitution, or LiF incorporation, have strong potential to achieve improved energy density and/or cycle stability that surpass the current Li-ion cathode chemistries. Therefore, gaining more understanding of the fluoride bond properties and handles to tune the redox activity, is critical for the development of advanced fluorinated cathode materials.

1.4 Li–Gas Batteries

Reproduced in part with permission from Gao, H., & Gallant, B. M. (2020). Advances in the chemistry and applications of alkali-metal–gas batteries. Nat. Rev. Chem., 4, 566–583. Copyright 2020.

1.4.1 Li–O₂ batteries

Batteries that employ gas cathodes and metal anodes have long been under development, given that the switch from transition metal redox to molecular (gas) redox significantly lessens

cell weight per amount of charge stored.⁸⁹ Early efforts explored aqueous metal–air batteries (with zinc as the prominent anode candidate), but had limited cycleability.²¹ The application viewpoint progressed in 1996, when K.M. Abraham and Z. Jiang reported the first rechargeable, nonaqueous Li–O₂ battery. The cell used a polymer electrolyte and cobalt phthalocyanine-catalyzed carbon electrode, which facilitated discharge of O₂(g) to form solid lithium peroxide (Li₂O₂) at 2.5 V vs. Li/Li⁺ (capacity of ~1600 mAh/g_{carbon}) and charged at 3.5–4 V vs. Li/Li⁺.²² Bruce et al. later showed that O₂(g) was evolved back on charge, confirming that electrochemical reversibility was indeed occurring.⁹⁰ It was not until several additional studies on the use of solid catalysts,^{91,92} which suggested the possibility of further lowering the charging voltage by several hundred millivolts, that the Li–O₂ field reached a tipping point and became one of the most hotly-researched battery topics in the 2010's.⁵⁷ Unfortunately, ensuing research led to a realization that intrinsic reactivity issues, involving O₂ redox in organic environments, prevent full electrochemical reversibility from being realized; today, commercially-viable charging voltages and cycle life have not yet been achieved.^{8,9}

The challenges faced by Li–O₂ batteries (introduced in detail below), led to great consternation but also newfound optimism in the prospect of developing novel cathode chemistries with the capability to broaden today's energy and power portfolio. To capitalize on successful aspects of Li–O₂, research pursuits diverged along two main paths. The first was a re-conception of the environment in which Li/O₂ redox occurs by changing either the electrolyte. Another approach has been to reconceive the gas cathode entirely through exploration of new reactants, including oxide and fluoride gases (**Figure 1-8a**). Together, this exploratory phase has led to a significant broadening of the combinatorial space for Li–gas battery design (**Figure 1-8b, c**).

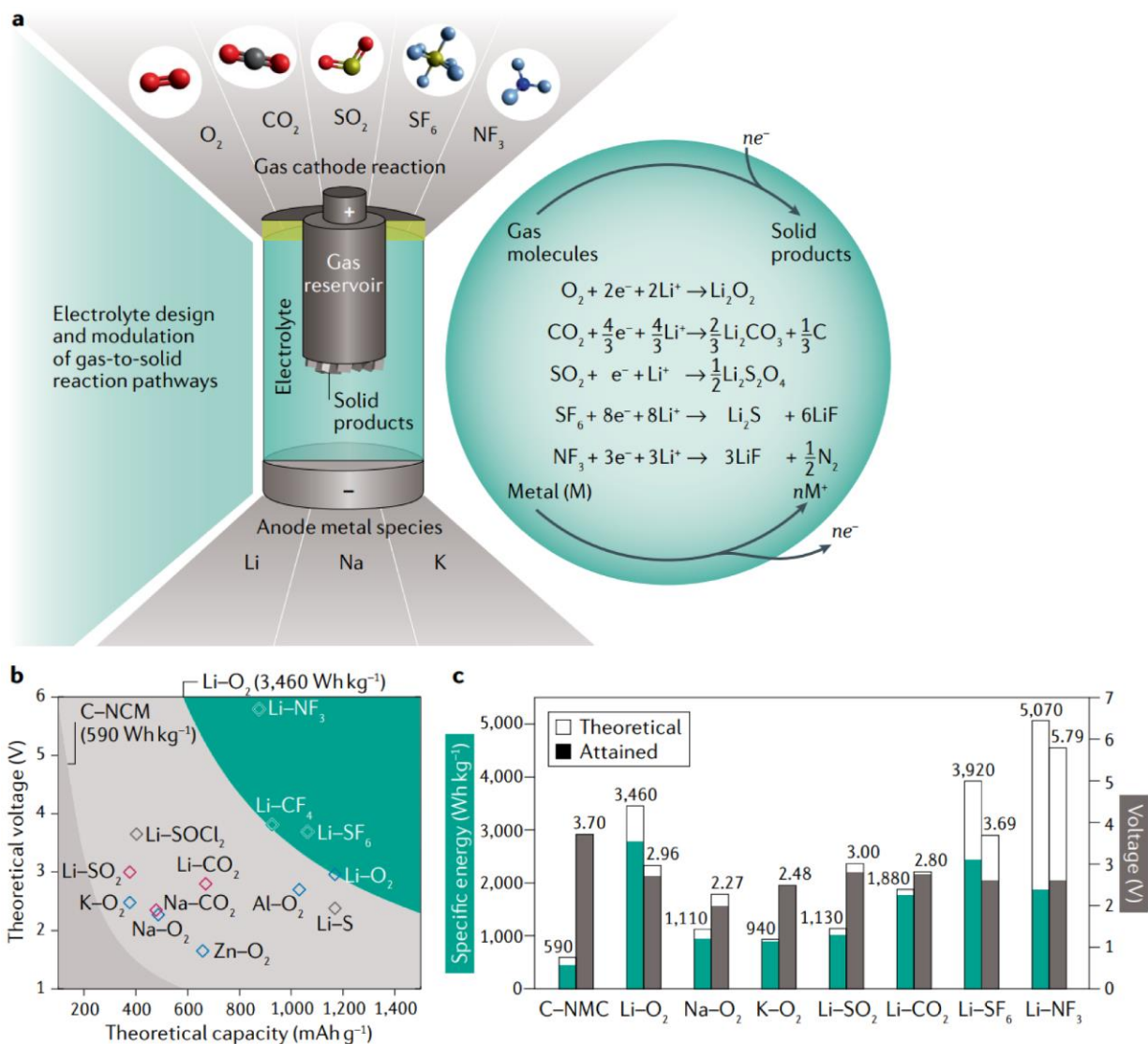
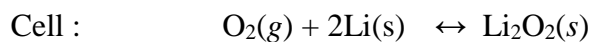
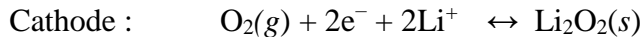


Figure 1-8 Performance of nonaqueous metal-gas batteries. (a) Schematic of metal-gas batteries. (b) Voltage-capacity metrics (theoretical) of different metal-gas battery couples including select non-alkali, aqueous anode candidates (Al, Zn) for comparison. (c) Theoretical vs. attained specific energy (left axis) and voltage (right axis).

The reaction mechanism of Li-O₂ battery is shown below, with the theoretical capacities and specific energies based on total weight of gas and anode metal consumed to form the stoichiometric solid-phase product:



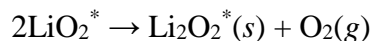
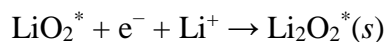
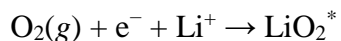
$$E^\circ = 2.96 \text{ V vs. Li/Li}^+, Q_{\text{theoretical}} = 1168 \text{ mAh/g}, E_{\text{theoretical}} = 3457 \text{ Wh/kg}$$

The cathode reaction proceeds on an electronically conductive surface, for example carbon, metals, conductive carbides or oxides,⁸ which may also function as electrocatalysts to enhance kinetics of discharge and charge. The reactant gas is introduced in the cell headspace and dissolved locally within the electrolyte in accordance with Henry's Law; typical solubilities are ~1-10 mM for O₂(g) at atmospheric pressure in nonaqueous electrolytes.^{93,94} Upon discharge, the solid phase nucleates and grows on the electrode surface and within the pore structure of the cathode.

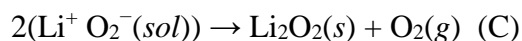
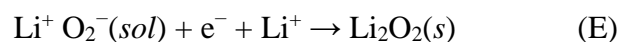
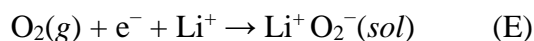
Early studies on Li-O₂ batteries utilized electrolytes containing organic carbonate solvents (such as propylene carbonate or ethylene carbonate/dimethyl carbonate), which were directly translated from Li-ion technology. Carbonate solvents, however, were later found to readily degrade in the presence of O₂ discharge intermediates. This reactivity led to formation of lithium carbonate (Li₂CO₃) rather than Li₂O₂, making the cell electrochemically irreversible (CO₂, rather than O₂, is released upon charge).⁹⁵⁻⁹⁷ Consequently, non-carbonate solvents such as ethers (glymes, tetrahydrofuran–THF) or dimethylsulfoxide (DMSO), among others, are nowadays utilized. In the search for viable, less-reactive solvents, it became clear that the electrolyte has a significant role to play in guiding the pathways of O₂ reactivity.

In non-carbonate solvents, O₂ reduction follows a step-wise reaction pathway that is strongly governed by solvent chemistry due to variable solubility of the principal discharge intermediate, superoxide (O₂⁻), in different environments.^{98,99} O₂ reduction branches between surface- or solution-localized processes (**Figure 1-9**, *–surface state, ‘sol’–dissolved species):

Surface reaction (cathode):



Solution reaction (cathode):



(E) denotes an electrochemical step whereas (C) denotes a chemical disproportionation step of two LiO_2 to form $\text{Li}_2\text{O}_2(s) + \text{O}_2(g)$.⁹⁹⁻¹⁰² Selectivity between solution and surface pathways is determined by availability of Li^+ to react with O_2^- (**Figure 1-9**). Larger Li^+ desolvation barriers (or stronger superoxide-solvent interactions) impede association of Li^+ and O_2^- , supporting higher O_2^- diffusivity farther from the cathode before LiO_2 and subsequently Li_2O_2 are formed. Solution-phase growth supports gentler precipitation of Li_2O_2 on existing Li_2O_2 nuclei, favoring large ‘toroid’-shaped particles (hundreds of nm to μm scale, **Figure 1-10**), rather than on the electrode substrate which instead supports film-like growth. Promotion of larger Li_2O_2 particles retains the cathode’s surface clear for continued reaction, extending the maximum capacities which are determined by the eventual passivation of the electrode surface.^{103,104} Electrolyte factors that decrease Li^+ activity and promote solution-mediated growth are several-fold. These include high Guttmann donor number (DN) solvents (*e.g.* DMSO);^{99,105} high anion acceptor number / ionic strength;^{106,107} additives that engineer enhanced O_2^- solubility (*e.g.* H_2O);^{107,108} and/or discharge redox mediators (RM) that can generate soluble complexes with reduced oxygen intermediates, which shuttle reduced oxygen through the electrolyte to Li_2O_2 nuclei, where they react with Li^+ and contribute to particle growth,¹⁰⁹ for example 2,5-di-*tert*-butyl-1,4-benzoquinone (DBBQ),^{110,111} combined DBBQ+ H_2O ,¹¹² and phenol.^{113,114} In addition to solvent properties, discharge rate (production rate of O_2^-) affects the supersaturation of electrolyte with O_2^- ,¹¹⁵ and can likewise distinguish between solution (lower rate) and surface (higher rate) mechanisms within

a given solvent.¹⁰⁷ Exceedingly high capacities have been achieved through electrolyte engineering (areal capacities >15 mAh/cm²).⁹

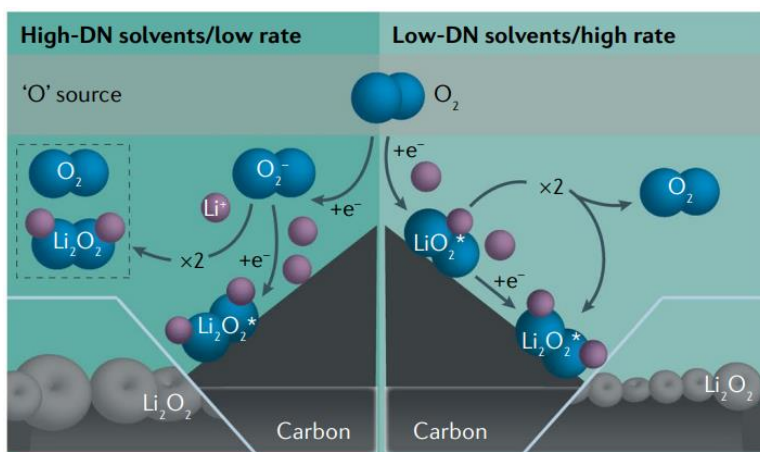


Figure 1-9 Schematic of Li–oxygen battery discharge mechanisms: solution-localized (left) and surface-localized process (right).

Unfortunately, oxygen reduction intermediates and products generated on discharge parasitically react with many cell components including electrolyte,^{116,117} carbon,¹¹⁸ and binder.¹¹⁹ Problematic species include strongly nucleophilic and basic O₂⁻/LiO₂, Li₂O₂,¹²⁰ and singlet oxygen (¹O₂) that forms during disproportionation.¹²¹⁻¹²³ (Superoxide and ¹O₂ are likewise generated during the charging reactions).¹²⁴ Critically, when O₂⁻ solubility is promoted, side reactions can become amplified in the same systems (such as high DN) that promote high capacities and best performance.¹²⁵ More drastically, reversibility of Li₂O₂ back to O₂ and Li on charge remains hindered by impractically high charging voltages of approximately 4 V vs. Li/Li⁺ and above (**Figure 1-11**). The high charging voltages arise from the resistive nature of parasitic products,¹²⁶ the insulating Li₂O₂ phase itself (bandgap of >5 eV for stoichiometric Li₂O₂),¹¹⁹ and possible intrinsic kinetic limitations of Li₂O₂ oxidation, which are still being elucidated.^{89,117,127}

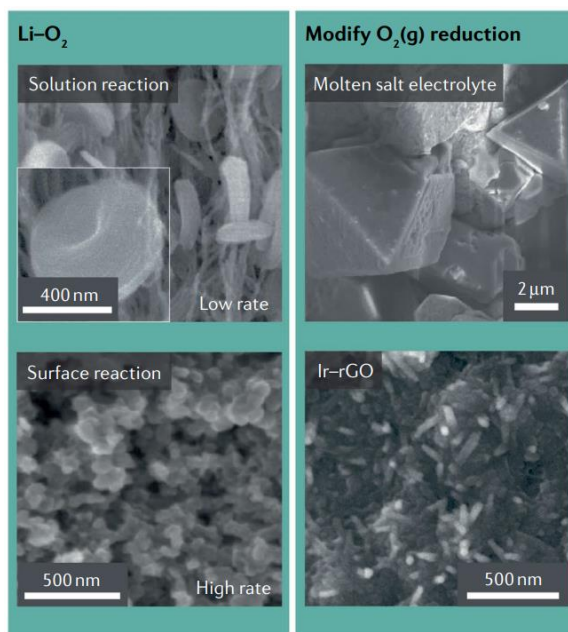


Figure 1-10 Morphology of solid products of Li–oxygen batteries, as indicated, obtained by Scanning Electron Microscopy. The inset in “solution reaction” was obtained at near-equilibrium growth conditions (10 mA/g_c).

Some strategies have been proposed to address chemical irreversibilities. These include use of non-carbon electrodes (*e.g.* gold),¹²⁸ conductive carbides (*e.g.* TiC),^{129,130} or oxides (*e.g.* Ti₄O₇),¹³¹ to minimize corrosion and side-product formation;^{128,129} solid catalysts to decrease charging voltages;¹³² and electrolyte-soluble redox mediators (*e.g.* tetrathiafulvalene, lithium iodide, and lithium bromide),¹³³⁻¹³⁵ which can facilitate Li₂O₂ decomposition on charge.^{134,136,137} The role of solid catalysts in lowering charging voltages has been debated, given the difficulties in disentangling the catalyst’s effect on Li₂O₂ discharge morphology and possible role in promoting other side-reactions.^{97,138,139} A major challenge in use of charge RM is their high solubility within the electrolyte and tendency to shuttle to the anode, where they can react with Li. Another challenge is incomplete O₂ recovery, which is compared stoichiometrically with the amount of Li₂O₂ formed on discharge, and tends to be below 95%.⁹ Consequently, the practicality

of engineering approaches (non-carbon electrodes, solid and soluble catalysts) from a weight, cost, and cell-level perspective remain uncertain, and in many instances introduce significant complexity into the cell.

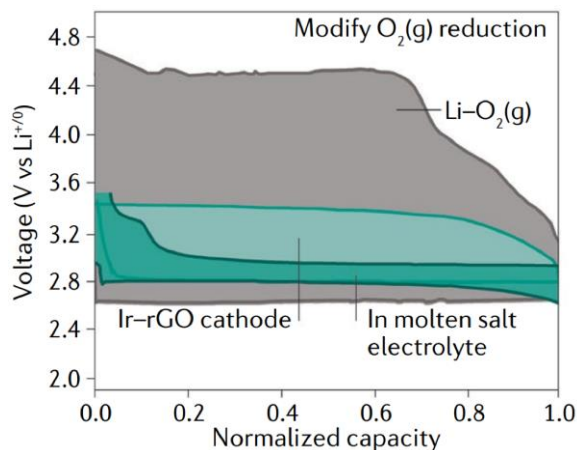


Figure 1-11 Galvanostatic cycle profile comparison for different Li–O₂(g) battery systems.

The above challenges spurred researchers to re-evaluate the fundamental nature of oxygen redox in Li batteries. One option to avoid high charge voltages associated with Li₂O₂ decomposition is to block full reduction of O₂ to Li₂O₂ upon discharge. Lopez and co-workers reported a proof-of-concept of using the electrolyte as the storage phase for the peroxide dianion (O₂²⁻) through complexation with hexacarboxamide cryptand during discharge, leading to reversible cycling of O₂ ⇌ O₂²⁻ in the presence of tetrabutylammonium perchlorate (TBAClO₄) in THF.¹⁴⁰ However, the practical performance with alkali salts have yet to be demonstrated. Certain electrode materials, such as iridium (Ir) supported on reduced graphene oxide (rGO), can promote surface stabilization of LiO₂ rather than Li₂O₂, which yielded improved reversibility with charging voltages <3.5 V vs. Li/Li⁺ (**Figure 1-10, Figure 1-11**).¹⁴¹ However, there has been debate about whether LiO₂ can truly be stabilized,^{142,143} as Raman shifts relied upon to identify LiO₂ exhibit overlap with binder degradation peaks.¹⁴³

A second approach to tackle the reactivity of reduced oxygen species is to move away from organic electrolytes in favor of less-reactive electrolyte environments. Li–O₂(g) batteries with molten salt electrolytes (LiNO₃–KNO₃–CsNO₃ eutectics), operating above the liquidus point (150 °C), exhibited significantly improved capacities (~1300 mAh/g_C vs. ~900 mAh/g_C with LiClO₄/DMSO), and were attributed to enhanced solubility of LiO₂/Li₂O₂ during discharge in the molten environment; dramatically lowered charging overpotentials (~50 mV at 80 mA/g_C) on carbon were also observed.¹⁴⁴ Building upon this concept, it was reported that Ni acts as an active catalyst for O₂ reduction and evolution in molten nitrate salt and can enable reversible, 4-electron reduction of O₂ to Li₂O at 150 °C, where Li₂O becomes thermodynamically favored over Li₂O₂.¹⁴⁵ Very high areal capacities (11 mAh/cm²) and charging below 3 V vs. Li/Li⁺ (**Figure 1-11**) were achieved at low rates (0.1 mA/cm²), with 150 reversible cycles.

1.4.2 Alternative oxide gas cathodes

1.4.2.1 Li–SO₂ batteries

The primary Li–SO₂ battery was first developed in the 1960s,²⁰ and found commercial success in military and aerospace application, as described in **Section 1.2.1**. Limited rechargeability (<15 cycles) of this system was first indicated by Maricle and Mohns in 1971.¹⁴⁶ At that time, it was believed that the reaction forming insoluble Li₂S₂O₄ was irreversible. In the following two decades, the rechargeability of the Li–SO₂(l) system was improved through alternative reaction pathways (such as those involving participation of the electrolyte salt). For example, LiAlCl₄ salt was shown to form a complex with SO₂ and carbon, thus the reduction products became LiCl and LiClAl(OSO-C)₃, which had a better reversibility (50 cycles).¹⁴⁷ Despite efforts made to identify optimized salts (*e.g.* Li₂B₁₀Cl₁₀ or LiGaCl₄), early rechargeable SO₂(l) prototypes still suffered from Li stability issues and limited cycles.¹⁴⁸ It was not until

recently that the Li–SO₂ system cell was shown to have compelling reversibility and cycle life when SO₂ is introduced into the cell as a gas (not liquid) with LiNTf₂ (1 M in tetraethylene glycol dimethyl ether (TEGDME)) as the electrolyte.²³ The reversible formation/decomposition of Li₂S₂O₄ (**Figure 1-12a**) followed the same reaction formula as the primary Li–SO₂ cells; attainable discharge voltages were slightly higher than that of Li–O₂, whereas charging voltages, which ranged from 3–4.2 V vs. Li/Li⁺, were significantly lower (**Figure 1-12b**). The success of this particular cell appears to lie in use of the glyme electrolyte, which may have also supported better Li reversibility than in previous rechargeability attempts. A soluble redox mediator, LiI, was found to lower the charging voltage even further to < 3.3 V vs. Li/Li⁺.²³ However, some side products (Li₂SO₃ and Li₂SO₄) were found in cycled electrodes.

Notably, unlike the Li–O₂ system, the reactivity of SO₂[−] against organic carbonate solvents is thermodynamically and kinetically unfavorable. The same group later demonstrated that it is also feasible to utilize carbonate solvent-based electrolytes for Li–SO₂ cycling, which are attractive due to their large stability window particularly on charge (in contrast to ethers) and to their high conductivity, resulting in improved performance. Using another soluble redox mediator, 5,10-dimethylphenazine, the Li–SO₂ cell could cycle for more than 450 cycles (0.5 mAh cutoff at 1 mA/cm²), with an overall polarization of only 0.2 V.¹⁴⁹ The formation of side products was somewhat mitigated, but accumulation of Li₂SO₄ could not be avoided.

Unfortunately, due to the toxicity of SO₂, widespread commercialization in EV applications is unlikely, even if better reversibility could be achieved without the use of soluble catalysts. Regardless, these interesting demonstrations-of-concept provide new insights into electrochemical and solid-phase motifs that support reversibility in gas-to-solid reactions.

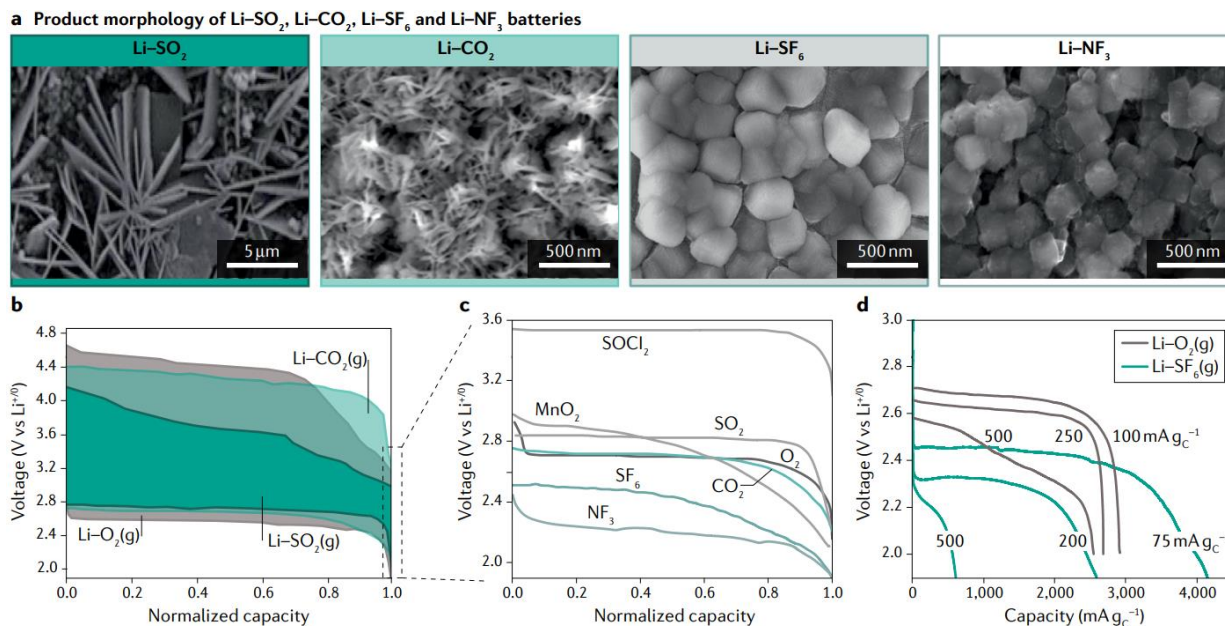
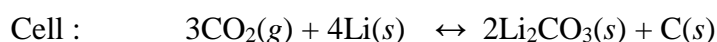
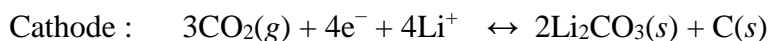


Figure 1-12 (a) Morphology of discharge products for Li-SO₂ / CO₂ / SF₆ / NF₃ gas cathodes, obtained by Scanning Electron Microscopy. (b) Experimental galvanostatic cycle profile comparison for Li-O₂, Li-SO₂, and Li-CO₂ batteries. (c) Galvanostatic discharge curve of Li-O₂/CO₂/SF₆/NF₃ series compared with commercial Li-primary batteries: Li-SOCl₂(l), Li-SO₂(l), and Li-MnO₂(s). (d) Rate capability comparison of Li-O₂ and Li-SF₆ batteries.

1.4.2.2 Li-CO₂ batteries

Another example of oxide gas batteries is Li-CO₂, which has been proposed as a technology of interest for potentially extracting end-of-life value from CO₂ emissions.¹⁰ Although a reaction forming carbon monoxide (CO) is theoretically possible on discharge,¹⁵⁰ the experimentally-observed reaction pathway forms only solid phases:



$$E^\circ = 2.80 \text{ V vs. Li/Li}^+, Q_{\text{theoretical}} = 670 \text{ mAh/g}, E_{\text{theoretical}} = 1880 \text{ Wh/kg}$$

Note that several elemental reaction pathways have been proposed that are consistent with this overall reaction, and are still under debate given challenges to verify the specific pathways experimentally.¹⁵¹⁻¹⁵³ Li–CO₂ electrochemistry was first studied in the context of mixed-gas Li–O₂/CO₂ batteries to investigate CO₂'s role in enhancing O₂ electrochemistry^{154,155} as well as its role as a possible contaminant in air-breathing O₂ cells.¹⁵⁶ In those systems, O₂ was shown to be the electro-active species due to more facile reduction kinetics, generating O₂[−] which chemically reacts with CO₂.¹⁵⁵ However, the formation of Li₂CO₃ in these mixed-gas systems is non-reversible, releasing no O₂ on charge.^{157,158} Later, CO₂ also became the focus of standalone gas cathode development. Archer's group reported the first primary Li–CO₂ battery based on an ionic liquid electrolyte operating at moderate temperature (60–100 °C) in 2013.¹⁵⁰ Subsequent efforts reported high attainable capacities in CO₂ cells at room temperature with select electrolytes. Glyme-based electrolytes are almost universally used in systems reporting high CO₂ activity and capacity with carbon electrodes; in contrast to Li–O₂ batteries, CO₂ has been observed to be largely inactive in DMSO electrolytes^{155,159} albeit with some exceptions.¹⁰ A reason for this was provided recently,¹⁵³ where it was found that the availability of Li⁺ is critical to activate CO₂ reduction intermediates and facilitate completion of the multi-electron reaction, which is favored in lower-DN solvents but precluded by higher-DN solvents. Though efforts have been made to gain insight into the complex step-wise CO₂ reduction process, the fundamental pathway is still under discussion.¹⁵⁴

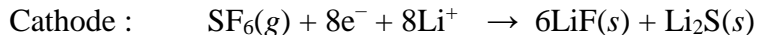
The Li–CO₂ system has limited reversibility. Although both C and Li₂CO₃ (**Figure 1-12a**) are formed on discharge, Li₂CO₃ decomposition has received the most interest when investigating the charging process. Li₂CO₃ oxidation can occur through two reaction pathways: reaction between Li₂CO₃ and C ($2\text{Li}_2\text{CO}_3 + \text{C} \rightarrow 3\text{CO}_2 + 4\text{Li}^+ + 4\text{e}^-$, $E^\circ = 2.80 \text{ V vs. Li/Li}^+$), the “true” reversible battery chemistry;¹⁶⁰ or decomposition of Li₂CO₃ only without involving carbon, nominally

forming O_2 ($2Li_2CO_3 \rightarrow 2CO_2 + O_2 + 4Li^+ + 4e^-$, $E^\circ = 3.82$ vs. Li/Li^+).¹⁶¹ Due to the high thermodynamic stability of Li_2CO_3 and large bandgap (8.8 eV compared to 4.9 eV for Li_2O_2),¹⁶² high charging overpotentials are needed ($E > 4.2$ V, **Figure 1-12b**).¹⁶³ These high voltages exacerbate cell degradation issues including electrolyte decomposition and carbon corrosion. Thus, most efforts have focused on identifying catalysts that can promote the desired reaction pathway,¹⁶¹ for example Mo_2C ,¹⁵² Ni ,¹⁶⁴ Mn_2O_3 ,¹⁶⁵ and Ru .¹⁶⁰ However, charging voltages still remain too high for practical use, and the degree of electrochemical reversibility upon cycling at high depth-of-discharge (rather than capacity-limited cycling, which is often utilized) remains unclear.

1.4.3 Perfluorinated gas cathodes

1.4.3.1 *Li-sulfur hexafluoride (Li-SF₆) batteries*

The gas cathodes presented so far achieve high capacities owing to low molecular weights, though only undergo up to 2 e^- /molecule redox on discharge/charge (O_2/Li_2O_2 : 2 e^- /molecule; $SO_2/Li_2S_2O_4$: 1 e^- /molecule; CO_2/Li_2CO_3 : 4/3 e^- /molecule). Thus, a prospective strategy to increase specific energy further is to seek gas reactants capable of higher electron-transfer numbers. Ideally, new chemistries can also provide alternatives to strongly oxidizing gases (O_2 and SO_2), which are often undesirable to transport and store in many applications, including military and space, for safety reasons. Our group demonstrated this concept with the $Li-SF_6$ battery in 2018. SF_6 , a gas that is widely used in the microelectronics industry, contains a central sulfur atom connected octahedrally to six fluoride (F^-) ligands (**Figure 1-8a**); sulfur is in its highest oxidation state (+6). It was recognized that full reduction of SF_6 can potentially accommodate up to 8 e^- /molecule by the reaction:



$$E^\circ = 3.69 \text{ V vs. Li/Li}^+, Q_{\text{theoretical}} = 1063 \text{ mAh/g}, E_{\text{theoretical}} = 3922 \text{ Wh/kg}$$

yielding a theoretical specific energy exceeding even that of Li–O₂ (**Figure 1-8b,c**). Interestingly, the Li–SF₆ reaction has been used in a separate context that reflects its capability for ultrahigh-energy: as a combustion reaction underlying the Mark 50 torpedo and other naval power uses, where the thermal energy released by injection of SF₆(g) into molten Li (~540 °C) was used to power a Rankine cycle for underwater propulsion.¹⁶⁶ However, an electrochemical analogue was not known. As a perfluorinated gas with spherical symmetry of the ligand shell, SF₆ is widely considered chemically inert (particularly at room temperature). This makes SF₆ a safe and non-toxic reactant; on the other hand, reactions usually have high activation energies.¹⁶⁶

Room-temperature reduction of SF₆ was first demonstrated in a Li–gas cell using carbon cathodes and glyme (TEGDME) electrolyte.¹⁴ Discharge coupled to pressure measurements, along with quantitative ¹⁹F NMR spectroscopy, confirmed 6 equivalents of LiF formed per SF₆ molecule reacted. Sulfur was also found in a reduced state (Li₂S) indicating that a large population of SF₆ can react fully to Li₂S, and indicating that up to 8 e⁻/molecule is achievable in practice. However, the presence of some less-reduced polysulfides in the cathode and electrolyte indicated that a population of partially-reduced SF_x (x<6) or Li_yS_z (y≤2) species are also formed and/or may react with Li₂S to yield more complex products.

The experimentally achievable discharge voltage of Li–SF₆, which was 2.2 V vs Li/Li⁺ in TEGDME electrolyte initially, was significantly lower than the theoretical value of 3.67 V vs. Li/Li⁺, and thus accounts for the major energy loss in the cell. The voltage could be increased

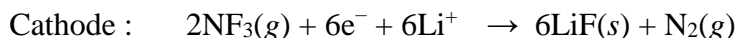
somewhat by changing the electrolyte to higher-DN solvents such as DMSO, reaching ~ 2.6 V vs Li/Li⁺ and 2550 Wh/kg at the active-materials level (**Figure 1-8c**). The voltage change (~ 300 mV at room temperature, **Figure 1-12c**) is consistent with the shift of the Li/Li⁺ redox potential between glyme (DME) and DMSO, and may not reflect significant change in the SF₆ reduction potential.¹⁶⁷ The fact that the Li⁺ solvation strength may alter the attainable cell voltages indicates that Li⁺ is likely not concerted in the cathode reduction reaction, but rather chemically precipitates the ejected F⁻ (SF₆ is known to decompose in the gas phase through anion ejection upon spark discharge activation),¹⁶⁸ such that it factors in the anode potential and does not cancel out in the cathode potential. The precise multi-step reduction mechanisms remain unclear as the highly complex branching over multiple electron-transfer steps evades experimental measurement to date.¹⁶⁹ However, the high discharge overpotential is believed to arise from sluggish activation kinetics of SF₆, which includes poor adsorption to typical carbon substrates. These kinetic limitations affect the rate capability and power of these cathodes significantly, similar to Li–O₂ systems (**Figure 1-12d**). It will be of interest to determine whether catalysts, which have been shown to activate SF₆ in homogeneous contexts,^{170,171} may be able to address the high overpotential issues.

As a result of the highly irreversible S–F bond cleavage, along with high stability and electronic resistivity of the products (LiF, Li₂S) formed upon discharge, it has not been possible to re-generate these fluorinated gases by charging the cell. Note that many partial sulfur fluorides are toxic gases (such as SF₄ and S₂F₁₀), and thus attempting to re-form SF₆ should be done while exercising extreme caution. This system is thus currently considered to be a primary battery. Further developments are needed to increase the accessible discharge voltage, improve rate capability, and tap into the intrinsically high energy densities before this metal–gas battery can

compete with commercial state-of-the-art including Li–SOCl₂ and Li–MnO₂, which benefit from higher discharge voltages (in the case of Li–SOCl₂, **Figure 1-12c**) and higher rate capabilities than the metal–gas systems at present.

1.4.3.2 Li–nitrogen trifluoride (Li–NF₃) batteries

A second model perfluorinated gas system was also investigated by the same group. NF₃ is another low-toxicity gas that is also commonly used in microelectronics processing, and can theoretically achieve a remarkably high voltage and specific energy upon discharge:



$$E^\circ = 5.70 \text{ V vs. Li/Li}^+, Q_{\text{theoretical}} = 876 \text{ mAh/g}, E_{\text{theoretical}} = 5072 \text{ Wh/kg}$$

The high specific energy density comes mainly from the exceedingly high theoretical voltage, which reflects the high e⁻/molecule transfer along with formation of highly stable N₂(g) and LiF as the products.¹⁶ In practice, the attainable voltage of Li–NF₃ was found to be remarkably lower than the theoretical, and, at ~2.3 V vs. Li/Li⁺ on carbon, was even slightly lower than that of Li–SF₆ (**Figure 1-12c**). The high voltage losses appear at present to be characteristic of the perfluorinated gases, although the precise reasons are not currently understood. Increasing the cell operating temperature was found to improve kinetics and thus the attainable voltage and capacity; the attainable energy could reach 1915 Wh/kg based on the weight of reactants (**Figure 1-8c**), which is however still well short of the theoretical value. Like SF₆, the Li–NF₃ battery is also irreversible. Thus the ability to unlock its intrinsically high specific energy, potentially through the use of catalysts, exploration of other electrolytes, higher cell pressures or operating

temperatures will be necessary to realize attractive and practical primary batteries based on this chemistry.

It should be noted that SF₆ and NF₃ are potent greenhouse gases, and thus they should be considered as model multi-electron systems at present, with possible niche applications for military and space if performance can be improved. However, the ability to realize 6-to-8 e⁻/molecule reactions can hopefully spur additional research into less environmentally-problematic reactants that capitalize on the high-oxidation states accessible to S, N, C, and other non-transition metal-containing molecules beyond that of O.

In conclusion, fluorinated cathode is a strong candidate for advanced battery systems for both primary Li batteries and secondary Li-ion batteries (and beyond), owing to their ability to unlock novel redox mechanisms that enable multiple electron transfer, and increased stability induced by strong fluoride bonds, which contributes to better cyclability. Considering the future trajectory of fluorinated cathode materials, two research paths can be defined, with different technology impacts: For rechargeable battery with either energy density or cyclability exceeding that of state-of-the-art Li-ion system; or, on the other hand, for new primary battery formulations with energies that exceed today's state-of-the-art. While the latter does not address clean energy needs, it represents an important space for electrochemical research as primary power systems are still in widespread demand for military (ground, naval and air), space exploration, medical, and emerging robotics applications among many others where portability is crucial. Ideally, it would be possible to identify systems that can achieve both ultrahigh energy and reversibility. Thus, it is critical to investigate various fluoride bonds redox behavior at fundamental level, mapping out the intrinsic properties and parameters to tune the bond activities.

Chapter 2: Controlling Electrolyte Solvation Properties for Fluorides to Improve Rate Capability in Li–SF₆ Batteries

Reproduced in part with permission from Gao, H., Li, Y., Guo, R., & Gallant, B. M. (2019). Controlling Fluoride-Forming Reactions for Improved Rate Capability in Lithium-Perfluorinated Gas Conversion Batteries. *Adv. Energy Mater.*, 9, 1900393. Copyright 2019.

2.1 Introduction

Continued demand for high-energy-density electrochemical power systems has drawn increasing attention to conversion-based systems,^{56,172} especially nonaqueous Li-gas batteries, which have theoretical energy densities substantially higher (>5x) than Li-ion batteries.^{98,132} While the majority of attention has focused on the Li-oxygen (Li–O₂) system due to its attractive energy density (3450 Wh/kg_{theoretical}, based on the weight of Li and O₂),¹¹⁰ and an earlier hope that it might be made rechargeable with continued development, significant challenges persist.^{89,173} Among these are impermissibly high overpotentials required on charge (> 1 V), even when catalysts are employed, and pervasive side reactions, which together limit the electrochemical and chemical reversibility of the battery (**Section 1.4.1**).

Inspired by the Li–O₂ system, different types of gas cathodes have been developed, as introduced in **Section 1.4.2 and 1.4.3**. Examples include oxide gases such as SO₂, which is currently a primary battery chemistry but exhibits potential to be made rechargeable;²³ CO₂-based batteries that attempt to extract end-of-life value from CO₂ while sequestering it in an electrochemical device;^{10,150,159} or fluoride gases such as sulfur hexafluoride (SF₆)¹⁴ or nitrogen trifluoride (NF₃)¹⁶ for use in primary batteries. Although such systems may not be suited *a priori* for reversible energy storage, exploring new chemistries provides significant opportunity to

develop new classes of high-capacity, high-energy conversion reactions, and to uncover new electrochemical mechanisms that may be employed in future primary or rechargeable batteries. In particular, perfluorinated gases, which are energy-dense, are typically stable or even inert in the reactant state,¹⁷⁴ and therefore offer additional advantages in terms of safety and storage compared to O₂.

Developing higher-energy electrochemical systems can be achieved by identifying high-potential or high-capacity reactions, or ideally both. Identifying new reaction with high capacities is non-trivial, given the inherent limitations in transition-metal redox (typically 1 e⁻/transition metal for conventional intercalation cathodes), or in oxygen molecular redox (typically a one- or two- electron transfer reaction at room temperature).¹⁷⁵⁻¹⁷⁷ In contrast, halogenated molecules, with a highly-oxidized central atoms such as carbon (*e.g.* CF₄), nitrogen (NF₃) or sulfur (SF₆), open up new opportunities in the design of lower-temperature multi-electron transfer reactions. High electron transfer numbers (>2) can be theoretically proposed, and scale proportionally with the number of fluoride ligands. Full reductions of two perfluorinated gases, NF₃ (to N₂(g) and LiF, nitrogen oxidation state change of 3)¹⁶ and SF₆ (to Li₂S/S and LiF, sulfur oxidation state change of 6 to 8),¹⁴ have been realized in Li-based cells at room temperature. Although high capacities were achieved (*e.g.* ~3600 mAh/g_C at 75 mA/g_C for SF₆), the discharge potentials were several hundred millivolts lower than typical Li–O₂ cell voltages, (~ 2.3 V vs. Li/Li⁺ compared to ~2.7 V vs. Li/Li⁺, respectively), and cells exhibited poor rate capability. Thus, the future attractiveness of such systems depends on the ability to improve the attainable energy density and increase the performance at higher rates. In this chapter, we demonstrate that such improvements are possible.

One of the major challenges currently limiting the attainable energy density in metal–gas systems in general is the eventual passivation of the electrode surface due to buildup of insulating

solids. In the Li–O₂ system, premature “sudden death” is mainly caused by coverage of active surfaces by Li₂O₂, an electronic insulator.^{103,178} Therefore, to enable higher capacities, a central strategy has been to increase the solubility of the reduction intermediate, the superoxide radical anion O₂^{•-}. This can be achieved intrinsically, either by utilizing electrolyte solvents with high Guttmann donor number (DN)⁹⁹ and/or acceptor number (AN);¹⁰⁷ or through incorporation of chemically-specific additives such as redox mediators,^{109,136} solution aggregation promoters such as molecular sieves,¹⁷⁹ or electrode functionalities that promote solution-phase Li₂O₂ growth.¹⁸⁰

In Li–fluorinated gas systems, a similar “sudden death” phenomenon occurs, caused by the buildup and eventual passivation of LiF. Whereas both SF₆ and NF₃ reduction reactions were found to exhibit high overpotentials (> 1 V) on discharge,^{14,16} the capacity was also dramatically curtailed at only moderate current densities (~100 mA/g_C), which represented the more severe contribution to poor rate capability. In this chapter, we focus on strategies to improve the rate performance by addressing the latter point, using the SF₆ conversion reaction as a model fluoride-forming system. In Li–SF₆ cells (SF₆ + 8Li → 6LiF + Li₂S), LiF is the majority product, formed at a 6-fold higher rate than sulfur-derived products, and thus is the species that we target for capacity improvements in the present study.

Herein, we report three strategies to improve the rate capability of Li–SF₆ batteries by modifying the electrolyte solvent and reaction conditions to promote LiF solubility. First, we explored the discharge performance of SF₆ in Li cells in a wide range of commonly-utilized battery solvents to identify trends that support high capacity. We find that DMSO with both a high DN and acceptor number (AN), showed good LiF solubility as well as stability against polysulfide species, in contrast to carbonates and ether-based solvents, both of which yield substantially lower capacities. Utilizing room-temperature DMSO cells as a benchmark, we investigated the Li–SF₆

discharge behavior at elevated temperatures of 50 °C to better understand the sensitivity of kinetics and/or solubility to thermal activation. Finally, we investigate the prospect of incorporating a commonly-utilized anion receptor, tris(pentafluorophenyl)borane (TPFPB), to promote LiF solubilization at high discharge rates. With TPFPB, a more than 25-fold increase in capacity can be achieved at high currents of 120 $\mu\text{A}/\text{cm}^2$.

2.2 Experimental Methods

Chemicals and Materials. All chemicals, electrodes and cell-making materials were thoroughly dried and stored in an argon-filled glovebox (H_2O content <1 ppm, O_2 content <1 ppm, MBRAUN). LiClO_4 (99.99% trace metals basis, Sigma-Aldrich) and TPFPB (>97%, Alfa Aesar) were dried for 24 hours at 70 °C and 90 °C, respectively, in a Buchi glass oven. Diethylene glycol dimethyl ether (diglyme (99.5%, Sigma-Aldrich), tetraethylene glycol dimethyl ether (TEGDME, 99%, Sigma-Aldrich), propylene carbonate (PC, 99.7%, Sigma-Aldrich), DMSO (> 99.9%, Sigma-Aldrich), ethylene carbonate (EC, 99%, Sigma-Aldrich), diethyl carbonate (DEC, > 99.9%, Sigma-Aldrich) and N,N-dimethylacetamide (DMA, 99.8%, Sigma-Aldrich) were dried over fresh molecular sieves (Type 3 Å, Sigma-Aldrich) inside the glovebox at room temperature for 24 hours prior to use. The molecular sieves and Whatman filter paper (Grade QM-A, 2.2 μm pore size, 450 μm in thickness, Sigma Aldrich) were dried overnight at 120 °C under active vacuum in a glass oven (Buchi).

Carbon Cathode Preparation. The Vulcan carbon (VC) cathodes were fabricated in-house by uniformly coating sonicated inks composed of VC (XC-72, Cabot Corporation), isopropanol, and lithiated Nafion (LITHion dispersion, Ion Power, with a Nafion/VC weight ratio of 1:2) onto a sheet of Celgard separator (Celgard 2325, 25 μm thickness, MTI Corporation). The obtained VC-

coated Celgard was dried at room temperature before being punched into circular disks (12 mm diameter), with a typical VC loading of $0.27 \pm 0.08 \text{ mg}_C/\text{cm}^2$ (error bar represents four measurements). The as-received gas diffusion layer (GDL, Freudenberg H23, FuelCellStore) was also punched into 12 mm diameter discs. The VC and GDL cathodes were subsequently dried under active vacuum in a glass oven (Buchi) overnight at 70 °C and 120 °C, respectively.

Galvanostatic Discharge. Two-electrode Swagelok-type Li-SF₆ cells were constructed in an argon glovebox, with VC or GDL as cathode and a 9 mm diameter disk of Li metal as anode (0.75 mm thick, 99.9% metals basis, Alfa Aesar), which was prestabilized by soaking in 0.1 M LiClO₄ in PC for more than three days before use.¹²⁸ The separator (13 mm diameter glass fiber filter paper) was impregnated with 150 μL electrolyte solution. The LiClO₄ concentration in DMSO, TEGDME EC/DEC (50/50 v/v), PC and DMA electrolytes were 0.1 M, while the only exception was diglyme, where the concentration was 70 mM owing to a lower salt solubility limit. SF₆ gas (Airgas, 99.999% purity) was introduced into cells following their assembly by purging SF₆ into the cell headspace within the glovebox for approximately 3 min, pressurizing it to ~1.6 bar, and then sealing the cell for subsequent measurement outside the glovebox.

Li-SF₆ cells were rested at open circuit voltage (OCV) for 15 hours prior to testing. Typical open circuit voltage (OCV) values of assembled cells ranged from 2.7–3.3 V (vs. Li/Li⁺). The subsequent galvanostatic discharge measurements were carried out (BioLogic VMP3 potentiostat or MPG2 workstation) at the specified current density with a voltage window ranging from open circuit to a lower cutoff voltage of 1.6–2.0 V vs Li/Li⁺ (as indicated). The lower cutoff voltage was varied in different measurements to avoid the decomposition of electrolyte, particularly when the anion receptor, TFPFB, was added. Results (current density and capacity) were normalized to the geometric area of GDL or the weight of VC used. For galvanostatic discharge at 50 °C, the

cells were placed inside an incubator (Mettler GmbH + Co. KG). For cells using DMA electrolyte, due to its reactivity with Li, pre-oxidized LiFePO₄ (LFP) was used as anode. The LFP electrode (9 mm diameter, single-side coated on Al foil, MTI Corporation, 7.63 mg) was first charged at a current density of 0.2 C for 15 min in a Li-LFP Swagelok-type cell with 1 M LiPF₆ in EC/DEC electrolyte (v/v = 1/1, battery grade, Sigma-Aldrich). After pre-delithiation, the electrode was extracted from the cell and rinsed before used in LFP–SF₆ cells. The LFP–SF₆ cell voltage was converted to Li/Li⁺ scale by adding the measured oxidation potential of LFP (3.44 V vs. Li/Li⁺). The capacity of LFP–SF₆ DMA cells was in all cases < 1 mAh, below the capacity remaining in the LFP electrodes (~1.23 mAh).

Rotating Disk Electrode (RDE) Measurements. Three-electrode electrochemical measurements were carried out in an argon-filled glovebox. All the electrodes and glass cells were purchased from Pine Research Instruments. The reference electrode was constructed by immersing a silver wire into a ceramic-fritted glass tube filled with 0.01 M AgNO₃ and 0.1 M TBAClO₄ in acetonitrile. For the counter electrode, a Pt wire was inserted in a fritted glass compartment that was filled with working electrolyte. A glassy carbon (GC) disk (0.196 cm²) was used as working electrode. Prior to each measurement, the GC electrode was polished using de-ionized water-wetted polishing papers (Thorlabs) in a sequence of 5, 3, 1, and 0.3 μm until a mirror finish was obtained, followed by a rinsing step with de-ionized water, and was dried under active vacuum in a glass oven (Buchi) at 70 °C overnight. The electrode was transferred into glovebox directly without exposure to air.

To determine the potential of reference electrode versus Li/Li⁺, a piece of Li foil was inserted into the electrolyte solution and its potential relative to Ag/Ag⁺ was measured until stabilization. The obtained value were: $0 V_{Li} = -3.65 V$ vs. Ag/Ag⁺ in 0.1 M LiClO₄ in DMSO; 0

$V_{\text{Li}} = -3.64 \text{ V}$ vs. Ag/Ag^+ in 0.1 M TFPFB / 0.1 M LiClO_4 in DMSO. After the Li/Li^+ potential was established, the working electrode was then immersed in the electrolyte and repeatedly cycled at 100 mV/s with a passive argon headspace between 3 V and 1 V (vs. Li/Li^+) until a stable capacitive background current was obtained. The GC electrode was then replaced with a freshly-polished electrode, and SF_6 was bubbled into the electrolyte for at least 5 min prior to cyclic voltammetry (CV) measurements. For rotating disk electrode measurements, the rotation rate of GC electrode was controlled by a Modulated Speed Rotator (Pine).

Scanning Electron Microscopy (SEM). After discharge, the Li- SF_6 cell was disassembled inside the glovebox and the cathode was extracted, rinsed with 1,2-dimethoxyethane (DME) and dried in the argon glovebox prior to SEM characterization. The sample, which was sealed in a glass vial in the glovebox, was then quickly transferred into the SEM chamber for the measurement to minimize exposure to ambient. All the SEM characterizations were conducted on a Zeiss Merlin High-resolution SEM operating at an accelerating voltage of 5 kV and beam current of 100 pA.

X-ray Diffraction (XRD). The pristine and rinsed discharged cathodes were all stored inside the glovebox. Prior to XRD measurements, the samples were sealed in an air-sensitive sample holder in the glovebox to minimize atmospheric contamination. XRD patterns were collected on a PANalytical X'Pert Pro multipurpose diffractometer with a copper anode ($\text{Cu K}\alpha$). All scans for cathode characterization were performed from $5^\circ < 2\theta < 90^\circ$ at a typical scan speed of $0.5^\circ/\text{min}$. Reference data for LiF : space group: $Fm\bar{3}m$, JCPDS: 00-004-0857.

Spectroscopic Measurements. ^{19}F Nuclear Magnetic Resonance (NMR) measurements were performed using a Bruker Advance Neo 400 MHz NMR spectrometer. Samples dissolved in deuterated solvents (D_2O (Sigma-Aldrich) or DMSO-d_6 (Sigma-Aldrich)) with 2,2,2-

trifluoroethanol (TFE, Sigma-Aldrich) or trifluoroacetic acid (TFA, Sigma-Aldrich) as reference. Samples were then transferred into capped NMR tubes (Wilmad, 528-PP-7) or coaxial tubes (Wilmad, 517-complete) for NMR analysis. X-ray photoelectron spectroscopy (XPS) analysis was conducted on a PHI VersaProbe II X-ray Photoelectron Spectrometer. The samples were transferred to XPS with minimum exposure to the air. The binding energies were calibrated by F 1s peak of LiF at 685.0 eV.

Electrochemical impedance spectroscopy (EIS). EIS analysis was conducted on two-electrode Swagelok cells. A potential perturbation of 5 mV was applied in a frequency range from 1 MHz to 100 mHz at open circuit voltage.

Quantification of LiF yield. The amount of LiF generated after discharge was determined using the following procedure: the cathode and separator of the discharged cell were extracted and soaked in 3 mL D₂O overnight to dissolve solid LiF. A portion of this solution was transferred into a capped NMR tube with 136 mM 2,2,2-trifluoroethanol (TFE) added as an internal reference. The concentration of LiF was obtained by comparing the integrated peak area of TFE and LiF in the ¹⁹F NMR spectrum.

2.3 Results and Discussion

We hypothesized that, analogous to Li–O₂ systems, the electrolyte solvent might influence the solubility of SF₆ reduction intermediates (lower fluorides of SF₆, F⁻, or LiF) and thus the growth of LiF crystallites during discharge. To investigate this, the discharge behavior of Li–SF₆ cells was first examined in six typical solvents: DMSO, N,N-dimethylacetamide (DMA), diethylene glycol dimethyl ether (diglyme), tetraethylene glycol dimethyl ether (TEGDME), ethylene carbonate/diethyl carbonate (EC/DEC), and propylene carbonate (PC). Lithium

perchlorate (LiClO_4) was chosen as the salt to avoid a possible additional fluoride source. To avoid possible reaction between Li and electrolyte solvents, Li metal was stabilized in PC electrolyte before being used as the anode.¹²⁸ Trends were first examined on porous Vulcan carbon (VC, $\sim 100 \text{ m}^2/\text{g}$)¹⁸¹ electrodes, comparable to those used previously. As shown in **Figure 2-1**, the solvent had a strong effect on the discharge behavior. At $75 \text{ mA}/\text{g}_\text{C}$, the carbonates PC and EC/DEC exhibited limited capacities of 630 and 735 $\text{mAh}/\text{g}_\text{C}$, respectively, and had low voltage plateaus of $\sim 1.9 \text{ V}$ vs. Li/Li^+ (**Figure 2-1a**). These relatively low capacities can be attributed in part to the known reactivity of polysulfides with carbonate-based electrolytes, which likely forms passivating decomposition products on the electrode.^{182,183} Meanwhile, ether-based electrolytes yielded significantly higher capacities ($\sim 1345 \text{ mAh}/\text{g}_\text{C}$ for diglyme and $\sim 1170 \text{ mAh}/\text{g}_\text{C}$ for

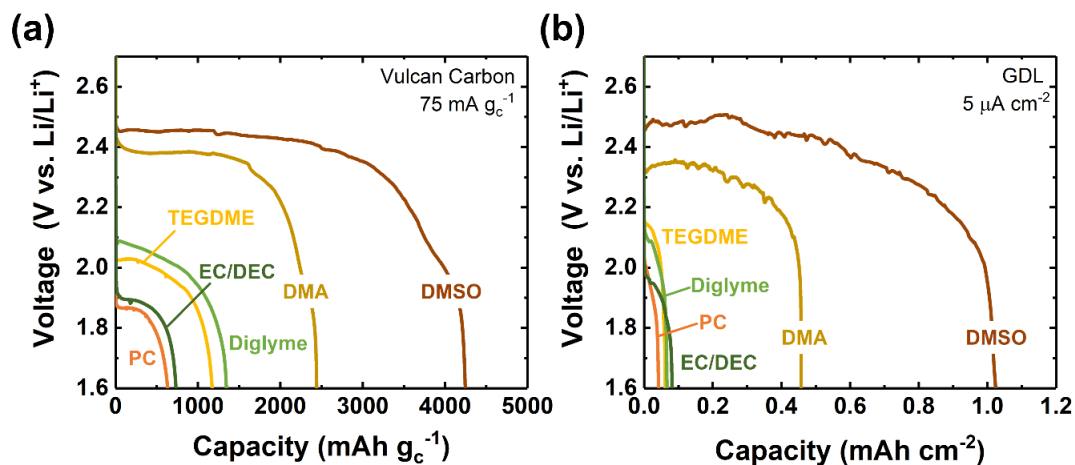


Figure 2-1 Galvanostatic discharge profiles of Li– SF_6 cells in various solvents, as indicated, with a lower cutoff voltage of 1.6 V vs Li/Li^+ on (a) Vulcan carbon or (b) gas diffusion layer (GDL) cathodes. Electrolytes contained 0.1 M LiClO_4 (TEGDME, DMSO, EC/DEC, PC and DMA) or 0.07 M LiClO_4 (diglyme). For GDL electrodes, capacity and current density are normalized to the GDL geometric area.

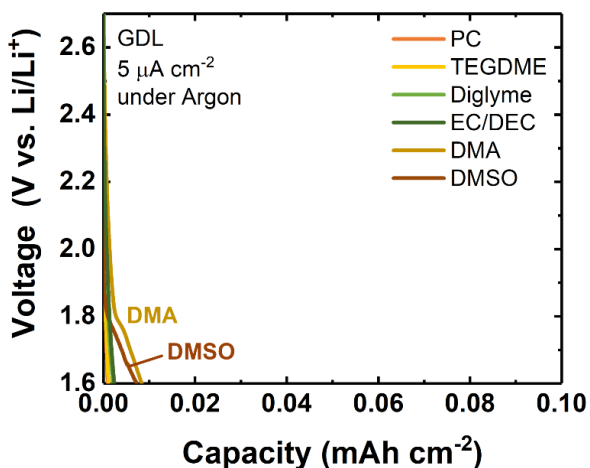


Figure 2-2 Galvanostatic discharge of Li–gas diffusion layer (Li–GDL) cells in different electrolyte solvents (PC, EC/DEC, TEGDME, diglyme, DMA and DMSO) under an argon headspace at a current density of $5 \mu\text{A}/\text{cm}^2$. The electrolyte was 0.1 M LiClO_4 (with the exception of 0.07 M in diglyme) and the cutoff voltage was $1.6 \text{ V vs. Li/Li}^+$.

TEGDME), and the discharge voltages were also found to be approximately 100 mV higher, at $\sim 2.0 - 2.1 \text{ V vs. Li/Li}^+$. A more dramatic improvement in both capacity and voltage was observed with both DMA (2445 mAh/g_C at $\sim 2.40 \text{ V vs. Li/Li}^+$) and DMSO (4250 mAh/g_C at $\sim 2.45 \text{ V vs. Li/Li}^+$). This trend was also well-reproduced on gas diffusion layer (GDL) electrodes discharged at comparable low rates of $5 \mu\text{A}/\text{cm}^2$ (**Figure 2-1b**; all corresponding argon backgrounds exhibited negligible capacity, **Figure 2-2**). Although GDL has relatively low surface area ($\sim 1 \text{ m}^2/\text{g}$)¹⁸⁴ and is not optimized for practical batteries, in this study, GDL is valuable for standardizing the electrode porosity and surface area from cell to cell and providing suitable visual contrast to examine the discharge product morphology (discussed later in the text). Thus, GDL electrodes are utilized (unless otherwise noted) in the remainder of the study.

Table 2-1: Donor Number (DN), acceptor number (AN) and reported LiF solubility (at room temperature, unless otherwise indicated) of different solvents.

Solvent	DN ^{18,185}	AN ¹⁸⁵	LiF solubility(g/L)
PC	15.1	18.3	0.13 ¹⁸⁶
EC	16.4	22.2	5.52 ¹⁸⁶ (40 °C)
DEC	16	6.2	<0.01 ¹⁸⁷
Diglyme	18 ¹⁸⁸	9.9	
TEGDME	16.6	10.5 ¹⁸⁹	
DMA	27.8	13.6	
DMSO	29.8	19.3	0.37 ¹⁹⁰

We considered three parameters to explain the performance trends of the solvents studied herein: LiF solubility; solvent acceptor number (AN); and donor number (DN). However, as LiF is only slightly soluble in water (1.33 g/L at 291 K),¹⁹¹ and is considered virtually insoluble in organic solvents,¹⁹² the solubility in organic electrolytes has not been consistently reported (although it is known to be higher in DMSO, 0.37 g/L,¹⁹⁰ compared to e.g. PC or DEC; see **Table 2-1**). Meanwhile, whereas LiF solubility is descriptive of the intrinsic ability of a solvent to stabilize both F⁻ and Li⁺, donor and acceptor number reflect the individual strength of solvent interaction with Lewis acids (*e.g.* Li⁺) or bases (*e.g.* F⁻), respectively. Although the elemental electrochemical steps of SF₆ reduction are not currently known, SF₆ has been reported to decompose by rapid fluoride ion rejection¹⁷¹ and our previous study of the perfluorinated gas analogue, NF₃, showed electron-coupled fluoride expulsion to be the likely conversion mechanism.¹⁶ Thus, it is probable that “lone” metastable F⁻ may be generated during discharge, with finite lifetimes in the electrolyte before complexation with Li⁺ and subsequent precipitation. Indeed, a strong correlation between DN and total achievable capacity was observed: ethers, having relatively low DN (16 for TEGDME and 18 for diglyme), showed lower SF₆ discharge capacity, whereas DMSO (DN = 29.8) and DMA (DN = 27.8) delivered the highest. For solvents

with comparable DN, higher AN (DMA = 13.6, DMSO = 19.3) also supported higher capacity. Such trends are similar to those observed in Li–O₂ batteries, where high DN solvents such as DMSO promote solution-phase growth of Li₂O₂ by strongly solvating Li⁺ and limiting its rate of reaction with superoxide.^{99,193} Thus, we conclude that similar effects govern the growth of LiF and lead to higher capacities in the SF₆ system. Higher DN solvents have also been reported to increase polysulfide solubility in Li–sulfur batteries, which may aid here as a secondary effect against S/Li₂S passivation.¹⁹⁴ As DN and AN are more widely reported and experimentally accessible than LiF bulk solubility, these metrics may aid in future prediction of additional solvents that support high-capacity SF₆ discharge.

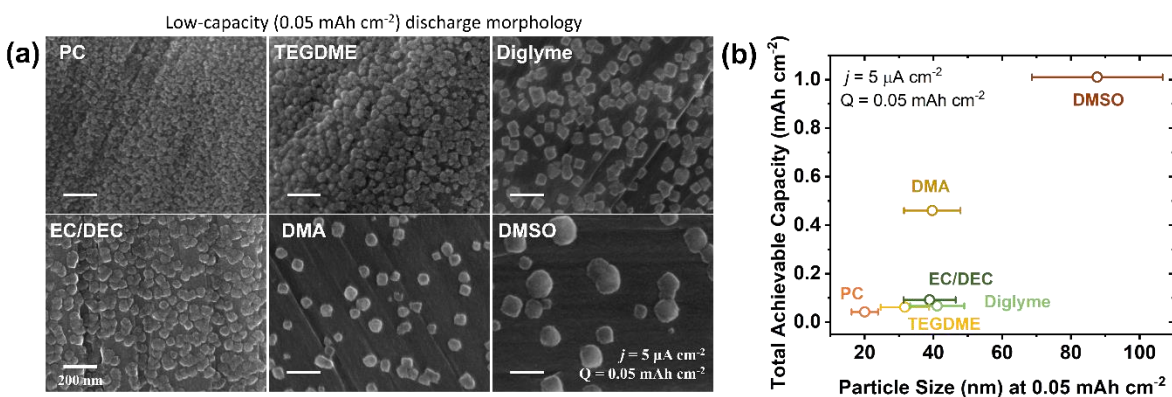


Figure 2-3 (a) SEM images of cathodes discharged to a limited capacity of 0.05 mAh at 5 $\mu\text{A}/\text{cm}^2$ in PC, EC/DEC, TEGDME, DMA, diglyme, and DMSO electrolyte. (b) Total achievable discharge capacity as a function of average particle size observed by SEM in different solvents at limited capacity (0.05 mAh/cm²). Average and error bars reflect statistics over at least 20 particles.

Comparisons of discharged electrodes were made to investigate whether the solvent modulated the discharge product morphology. **Figure 2-3a** shows scanning electron microscopy (SEM) images of cathodes discharged to a limited capacity of 0.05 mAh/cm², which is low enough to be reached in all solvents, at 5 $\mu\text{A}/\text{cm}^2$. X-ray diffraction (XRD) performed on electrodes

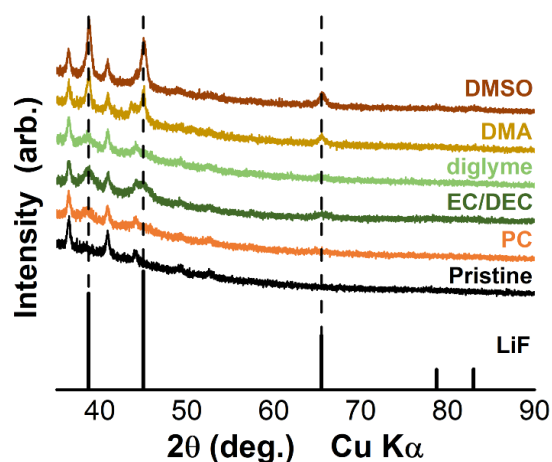


Figure 2-4 X-ray diffraction (XRD) patterns of fully discharged Vulcan Carbon (VC) cathodes in different electrolyte solvents containing 0.1 M LiClO₄ (with the exception of 0.07 M in diglyme) at a current density of 75 mA/gc.

discharged in all five solvents (**Figure 2-4**) confirmed that LiF was the only detectable crystalline product, and therefore, in the following, we interpret the morphologies as being predominantly reflective of LiF. From the images, it is evident that the cathodes for solvents that exhibit low discharge capacity, *i.e.* rapid electrode passivation (EC/DEC, PC, diglyme, and TEGDME), generally showed uniform LiF coverage consisting of many small LiF particles. In contrast, the cathode in high DN solvents (DMSO and DMA) exhibited sparser particles with more available carbon surface area, consistent with the ability to continue discharge to much higher capacities. The variation of average particle size in different electrolytes is quantified in **Figure 2-3b**. A general trend of increasing particle size with achievable discharge capacity is observed, which reflects the ability to form more microscopically three-dimensional and thus less passivating particles in DMA and DMSO. DMSO, which gave the highest capacity, showed significantly larger average particle size (~90 nm) compared to all others (< 40 nm). Overall, it is evident that

the LiF nuclei at low capacity vary dramatically in different solvents, and their nanoscale morphologies underlie the ability to undergo continued discharge to high capacities. Given the apparently unique ability of DMSO to promote high capacities, we select it as the solvent for continued study.

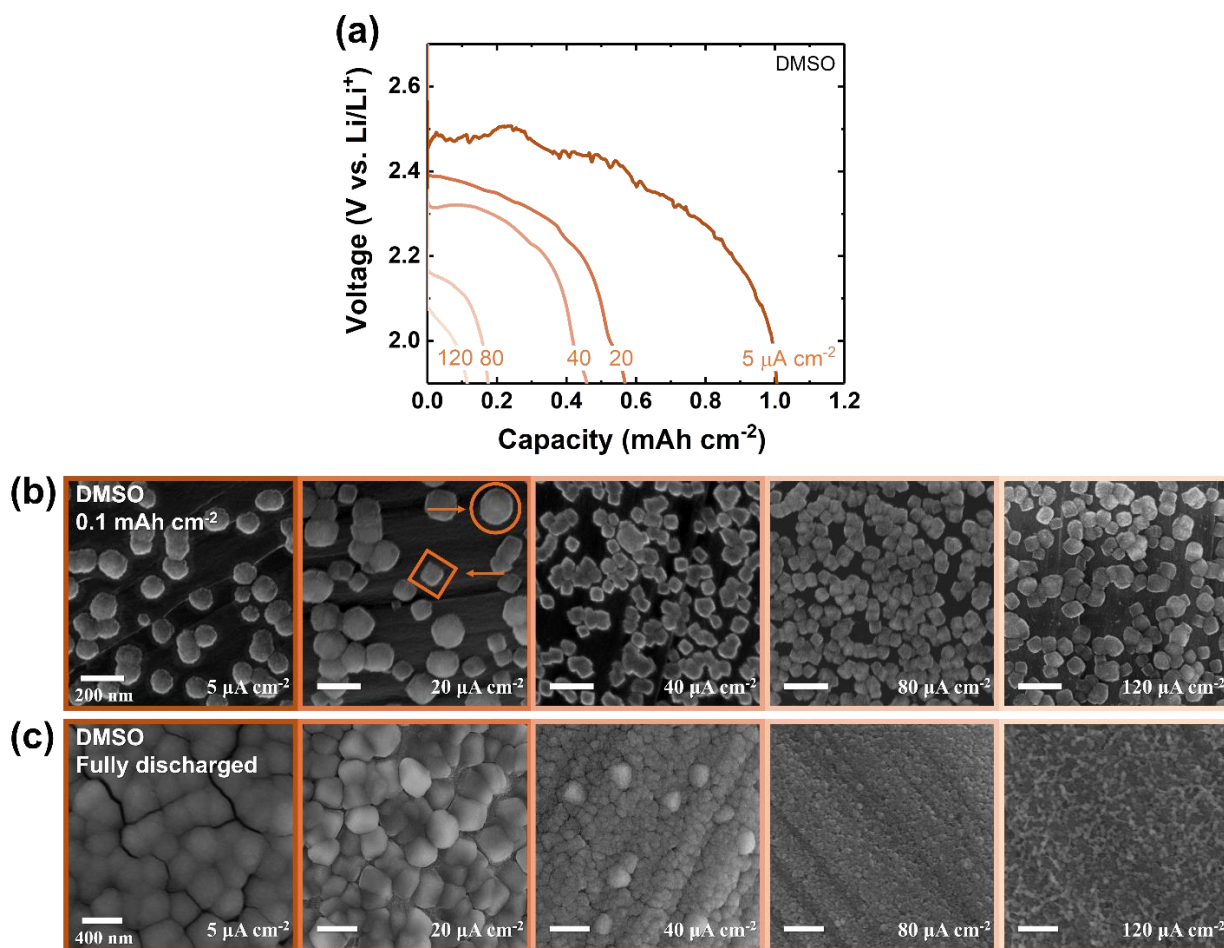


Figure 2-5 (a) Galvanostatic discharge profiles of Li-SF₆ cells in DMSO electrolyte at current densities of 5, 20, 40, 80 and 120 μA/cm². SEM image of cathodes discharged to (b) 0.1 mAh/cm² and (c) fully discharged at different current densities (as indicated) in DMSO.

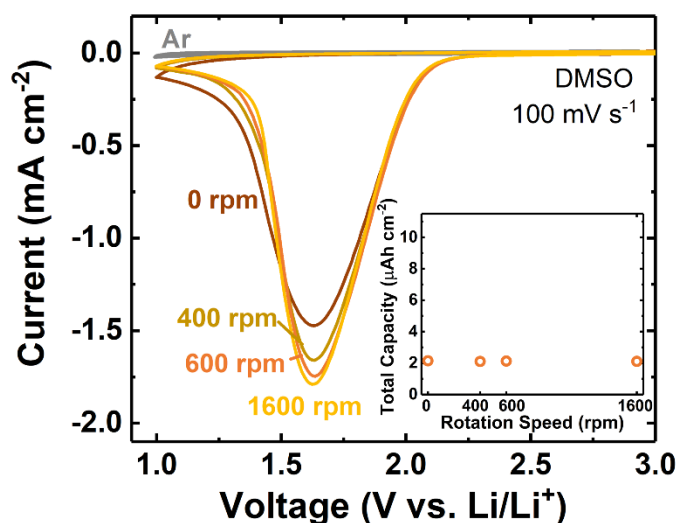


Figure 2-6 Rotating disk electrode (RDE) measurement of Li-SF₆ cells with DMSO electrolyte. The total integrated capacity of the 1st reduction cycle at various rotation speeds is shown in the inset. The scan rate is 100 mV/s, with a lower cutoff voltage of 1 V vs. Li/Li⁺. For all rotation rates investigated, negligible current can be detected after the 1st cycle in DMSO electrolyte. The argon background (at 1600 rpm, which was representative of all argon scans over different rotation rates) is shown in gray.

The rate capability at full capacity was next investigated in DMSO on GDL over a range of current densities, as shown in **Figure 2-5a**. Between 5 and 120 μA/cm², the discharge capacity decreased by almost an order of magnitude, from approximately 1.0 to 0.1 mAh/cm², and was accompanied by a decrease in discharge potential of around 0.4 V, from 2.5 to 2.1 V vs. Li/Li⁺. The high sensitivity of voltage to discharge rate is comparable with other metal-gas batteries discharged on non-catalyzed carbon electrodes.¹⁹⁵ To confirm that the capacity was limited by LiF passivation and not transport in DMSO, Rotating Disk Electrode (RDE) measurements were conducted in SF₆-saturated DMSO electrolyte using glassy carbon (GC) as working electrode

(**Figure 2-6**). Even at a rotation speed of 1600 rpm, limiting current behavior could not be reached under cyclic voltammetry conditions at 100 mV/s, and a comparable total reduction capacity of 2.1 $\mu\text{Ah}/\text{cm}^2$ was obtained in all cases regardless of rotation rate, due to rapid passivation once the onset of SF_6 reduction began. Negligible anodic current was detected on the forward scan, indicating the non-rechargeability of the Li-SF_6 system, in agreement with that observed in our previous study.¹⁴ Furthermore, significant impedance increase detected during discharge (**Figure 2-7a**) also provided evidence for electrode passivation. We therefore concluded that the reactions under given electrochemical conditions (galvanostatic or cyclic voltammetry) are always limited by LiF passivation, even though higher capacities are achievable in DMSO compared to other solvents.

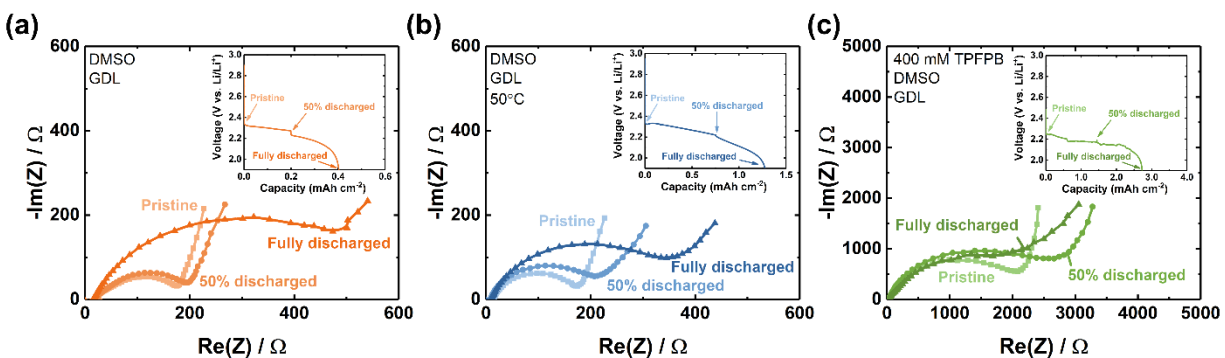


Figure 2-7 Nyquist plots of Li-SF_6 cells with 0.1 M $\text{LiClO}_4/\text{DMSO}$ electrolyte at different depths of discharge at (a) room temperature (RT), (b) 50 °C, and (c) with 400 mM TFPFB additive at RT. The corresponding discharge states at which Electrochemical impedances were measured are indicated in the inset.

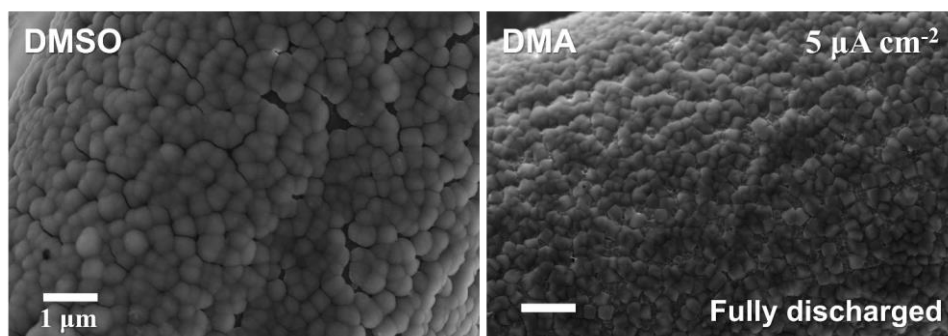


Figure 2-8 Scanning electron microscopy (SEM) images of gas diffusion layer (GDL) cathodes in Li-SF₆ cells after full galvanostatic discharge in DMSO or DMA electrolyte (as indicated). The current density in both cases was 5 μA/cm² (capacity = 1.3 and 0.6 mAh/cm² for cells discharged with DMSO and DMA, respectively).

The structure of the LiF particles, in addition to being solvent-dependent, was also highly rate-dependent. Limited-capacity morphologies at 0.1 mAh/cm² are shown in **Figure 2-5b** for current densities up to 120 μA/cm². At low rates of 5 μA/cm², sparser and rounder nuclei (~110 nm) were observed at 0.1 mAh/cm²; these gradually became more cube-shaped and smaller (~60 nm) at increasing current densities. At an intermediate current density of 20 μA/cm², a mix of spheres and cubes was seen, indicating a transition between the two morphologies. These distinct morphologies were retained up to full discharge capacities (**Figure 2-5c**). We note that similar results were observed in DMA, *i.e.* the surface was fully passivated by larger, although less spherical, LiF particles at full capacity (**Figure 2-8**). However, the LiF particles were smaller in DMA than in DMSO, consistent with a larger population of active nuclei and more rapid passivation in DMA.

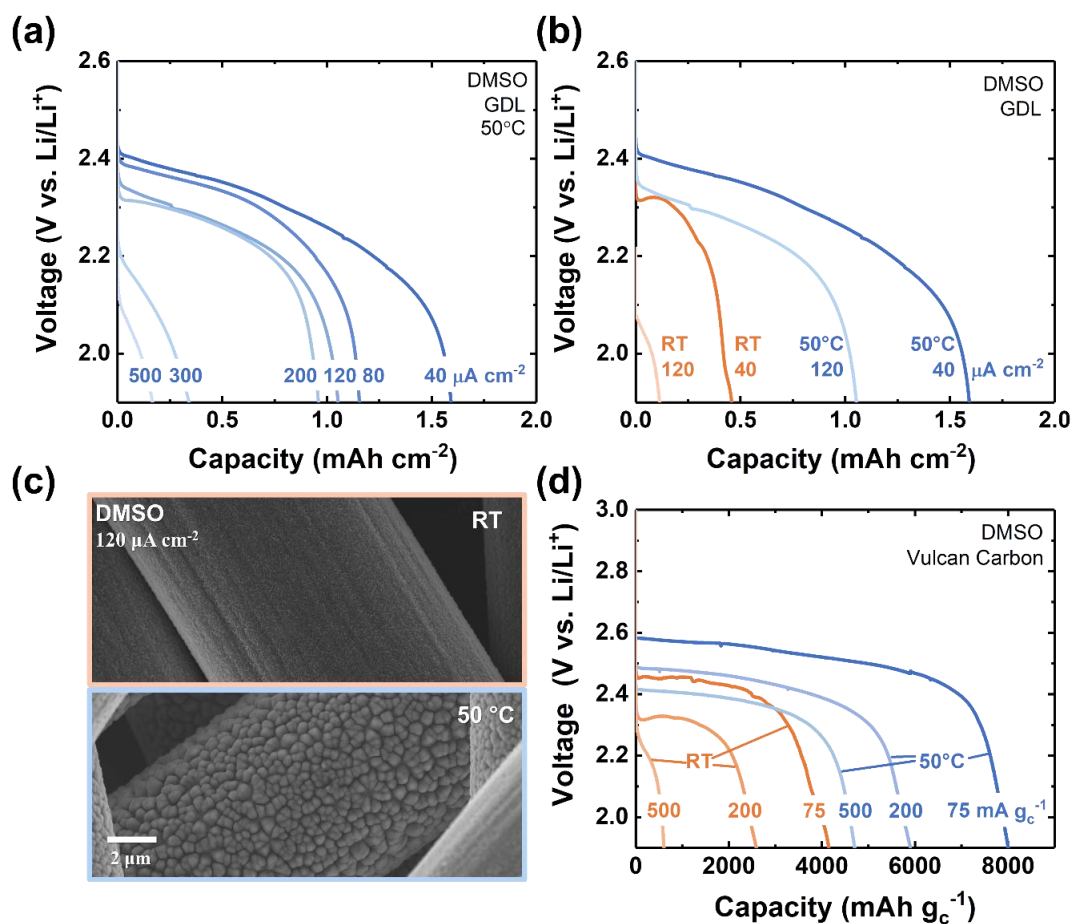


Figure 2-9 Li-SF₆ cells at 50 °C. (a) Galvanostatic discharge profile of Li-SF₆ cells in 0.1 M LiClO₄/DMSO electrolyte with GDL electrodes at current densities from 40 to 500 μA/cm² (lower voltage cutoff of 1.9 V vs Li/Li⁺). (b) Comparison of discharge profiles at 50 °C and room temperature (RT) at current densities of 40 and 120 μA/cm². (c) SEM image of a GDL cathode fully discharged at 120 μA/cm² at 50 °C (lower) and RT (upper). (d) Discharge profile of Li-SF₆ cells in DMSO electrolyte with Vulcan carbon electrodes at RT and 50 °C.

Given the central role of the spherical LiF deposits in supporting higher capacities, we investigated whether thermal effects can promote enhanced formation of this desired morphology. Discharge performance of Li-SF₆ cells was evaluated at a moderately higher temperature of 50 °C, as shown in **Figure 2-9a**, for current densities ranging from 40 to 500 μA/cm². We confirmed that

the higher temperature did not modify the background currents under argon, as indicated in **Figure 2-10**. The corresponding rate capability of Li-SF₆ cells with DMSO electrolyte at room temperature (RT) and 50 °C are compared in **Figure 2-9b**. At a relatively low current density of 40 μA/cm², the discharge capacity at 50 °C reached 1.8 mAh/cm², more than four times higher than the capacity observed at room temperature (~0.4 mAh/cm²). Meanwhile, at a higher current density of 120 μA/cm², whereas severe performance loss was already observed under room temperature conditions (discharge voltage < 2.1 V vs. Li/Li⁺ and only ~ 0.1 mAh/cm²), at 50 °C the cell could retain a capacity above 1.0 mAh/cm² and a voltage of 2.3 V vs. Li/Li⁺. Severe performance loss was only observed at rates higher than 300 μA/cm². Note that a trend of increasing temperature yielding higher capacity and potential was also previously observed in Li-O₂ and Li-NF₃ batteries.^{16,196} In the Li-SF₆ system, the improvement at higher temperature is related both to increased solubility of LiF and, to likely lesser effect, lithium sulfide or polysulfide, as indicated by the modified morphologies; but also to improved kinetics, as reflected in the higher

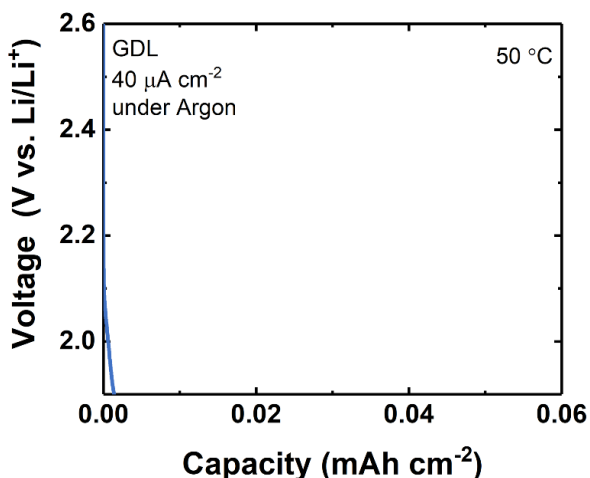


Figure 2-10 Galvanostatic discharge of Li/GDL cells at 50 °C in 0.1 M LiClO₄/DMSO electrolyte under an argon headspace and a current density of 40 μA/cm², with a cutoff voltage of 1.9 V vs. Li/Li⁺.

average discharge potentials. These higher voltages achieved at elevated temperature help to support the selective activation of fewer nucleation sites while promoting their growth to substantially larger sizes (~ 350 nm, compared to ~ 50 nm at room temperature; **Figure 2-9c** and **Figure 2-11**). A temperature increase from 25 °C to 45 °C was found in a separate study to increase LiF solubility by nearly a factor of two, from 0.37 g/L to 0.60 g/L in DMSO,¹⁹⁰ in agreement with the electrochemical and morphological results observed here.

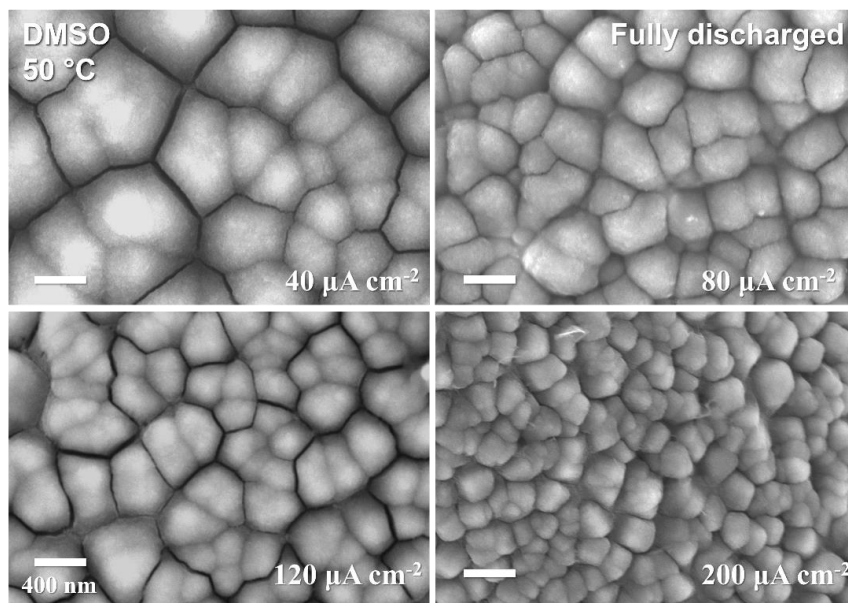


Figure 2-11. Scanning electron microscopy (SEM) images of GDL cathodes in Li-SF₆ cells fully discharged in DMSO electrolyte at 50 °C at current densities of 40 , 80 , 120 and 200 $\mu\text{A}/\text{cm}^2$ (capacity = 1.8 , 1.0 , 1.0 , and 0.9 mAh/cm^2 respectively). The scale bar = 400 nm in all images.

Figure 2-9d shows that these substantial performance gains, obtained on GDL, could also be translated to the more practical Vulcan carbon electrodes. A nearly two-fold increase in capacity (~ 8000 $\text{mAh}/\text{g}_\text{C}$ at 50 °C), as well as a ~ 0.1 V increase in discharge potential (from less than 2.5 V to ~ 2.6 V vs. Li/Li⁺) was observed at moderate currents of 75 $\text{mA}/\text{g}_\text{C}$. Moreover, capacities remained greater than ~ 4500 $\text{mAh}/\text{g}_\text{C}$ at 500 $\text{mA}/\text{g}_\text{C}$. Overall, the results indicate that moderate

temperature increases can dramatically alter the LiF nucleation and growth process, resulting in sizeable gains in performance and enabling high-rate performance. However, LiF passivation is still ultimately the limiting factor, which is supported by the SEM images at full discharge along with electrochemical impedance measurements, which show significantly larger resistances as depth of discharge increased (**Figure 2-7b**). Thus, we next investigated an additional strategy to further improve the capacity at room temperature based on chemically-specific promotion of LiF solubility.

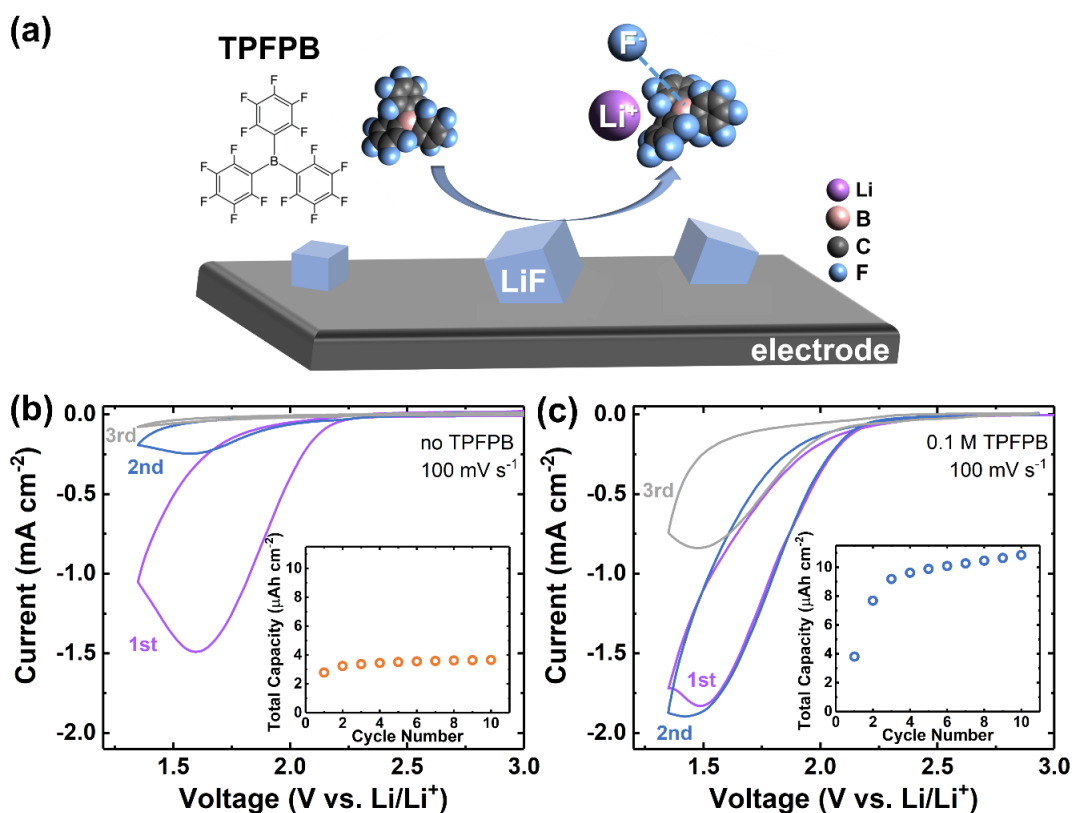


Figure 2-12 (a) Schematic depicting the anion receptor, TFPFB, which promotes LiF solvation by forming a complex with F⁻ anions. Cyclic voltammetry traces and the total capacity (inset) of SF₆-saturated electrolyte containing (b) 0.1 M LiClO₄/DMSO, and (c) 0.1 M TFPFB with 0.1 M LiClO₄/DMSO at a scan rate of 100 mV/s.

Tris(pentafluorophenyl)borane (TPFPB), with a molecular structure as shown in **Figure 2-12a**,^{197,198} is among the family of borate-based anion receptors that contain electron-deficient Lewis acid centers effective for binding F^- and promoting LiF solubilization.^{199,200} Thus, it has been used previously as an additive in Li-ion batteries at low concentrations (typically < 0.1 M) to increase the solubility of LiF formed from parasitic decomposition of fluorine-containing electrolyte salts,^{201,202} or to promote silicon²⁰³ or graphite²⁰⁴ anode stability. More recently, TFPFB has been used in Li–O₂ batteries to catalyze superoxide disproportionation.^{205,206} However, to the best of our knowledge, TFPFB has not been used previously in large concentrations as a participant in a bulk fluoride-forming reaction. Thus, we began by exploring the feasibility of using TFPFB at the high fluoride-forming rates in Li–SF₆ systems. To do so, passivation was initially exacerbated by using the low-surface area, “planar” GC electrode in the RDE configuration, where passivation effects can be readily detected as early as the first scan, as discussed previously.

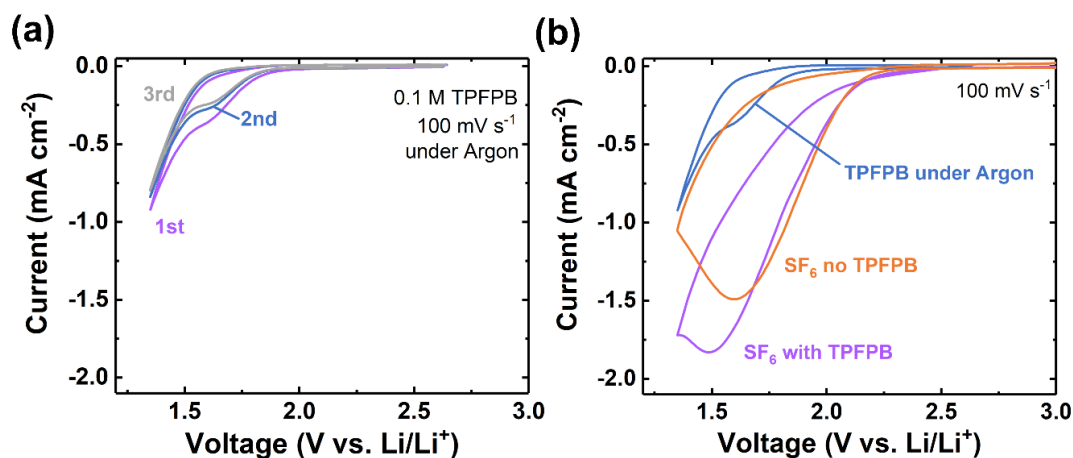


Figure 2-13. (a) Cyclic voltammetry of 0.1 M LiClO₄/DMSO electrolyte containing 0.1 M TFPFB under an argon headspace at a scan rate of 100 mV/s. (b) Comparison of 1st scan in Figure 2-13a (as background measurement: TFPFB under Argon), Figure 2-12b (SF₆ in DMSO electrolyte without TFPFB), and Figure 2-12c (SF₆ in DMSO electrolyte with 0.1 M TFPFB).

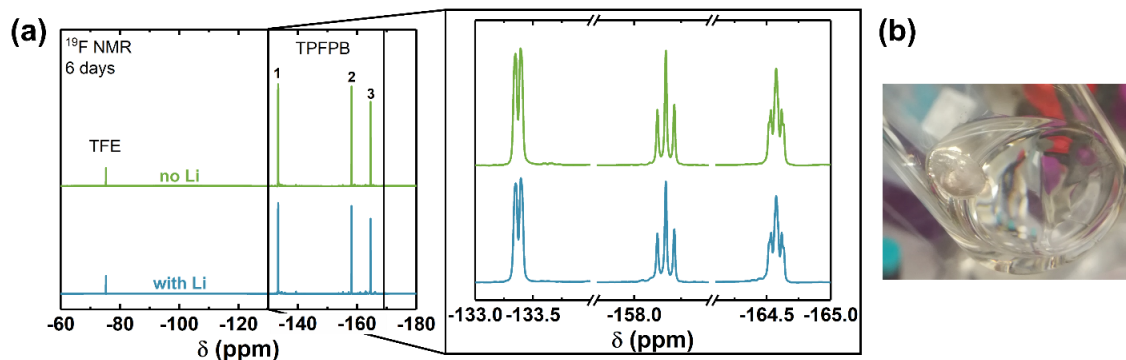


Figure 2-14. (a) ^{19}F NMR of 400 mM TFPFB in 0.1M $\text{LiClO}_4/\text{DMSO}$ electrolyte with/without PC-stabilized Li soaked for six days. To avoid possible reaction between TFPFB and the reference (2,2,2-Trifluoroethanol, TFE), the measurements were conducted using coaxial NMR tubes. The inner tube was filled with 136 mM TFE in DMSO-d_6 with the outer tube containing the electrolyte. (b) Photograph of PC-stabilized Li after soaked in DMSO electrolyte containing 400 mM TFPFB for six days, showing negligible reactivity.

Figure 2-12b,c shows the first three CV scans in DMSO electrolyte at a fast scan rate of 100 mV/s, without and with TFPFB additive at a concentration of 0.1 M. Note that when TFPFB was used, the lower voltage cutoff was set as 1.35 V vs. Li/Li^+ (instead of 1.0 V vs. Li/Li^+ , as in **Figure 2-6**) to avoid parasitic reduction of TFPFB, which was found to be significant below ~ 1.3 V vs. Li/Li^+ (**Figure 2-13**). Without TFPFB (**Figure 2-12b**), the carbon electrode was nearly passivated on the second scan, and the integrated reduction capacity (figure inset) reached a rapid plateau after the 2nd cycle, at $< 4 \mu\text{Ah}/\text{cm}^2$. With TFPFB present, however, the peak current reached on the first scan was modestly higher ($\sim 1.9 \text{ mA}/\text{cm}^2$ vs. $\sim 1.5 \text{ mA}/\text{cm}^2$) and nearly comparable currents were retained on the second scan. Continued cycling was still possible after that, albeit with passivation becoming more predominant. Consequently, the integrated reduction capacity (figure inset, **Figure 2-12c**) increased rapidly and reached a higher steady-state value greater than $10 \mu\text{Ah}/\text{cm}^2$. Note that these gains were achieved at a relatively high scan rate of 100 mV/s, and

are expected to be even more pronounced at lower rates. Thus, having established the feasibility of using TPFPB to dissolve passivation-scale amounts of LiF during SF₆ reduction, we further investigated its effect under more practical galvanostatic conditions in Swagelok cells with GDL electrodes.

Table 2-2. Calculation of TPFPB concentration from NMR result in Figure 2-14, from a nominal added concentration of 400 mM. (Integrals were normalized to that of reference peak. The volume ratio between outer and inner tube is 5.82.)* The case with ‘No Li’ is included to show the typical measurement error occurring without TPFPB present.

	Integral				TPFPB concentration (mM)
	Peak 1	Peak 2	Peak 3	Total	
No Li	35.13	15.40	32.72	83.25	389
With Li	35.59	15.96	33.33	84.88	396

* The volume ratio was calibrated by using two different references with known concentration: 136 mM TFE and 129 mM trifluoroacetic acid (TFA) in DMSO-d₆, in inner and outer tubes respectively.

The capacity of Li-SF₆ cells was found to depend sensitively on the concentration of TPFPB. Cells were characterized at a typical current density of 40 μA/cm², which corresponds to an intermediate F⁻ generation rate (assuming 8 e⁻/SF₆) of 4.7×10⁻¹⁰ mol/s or 3.1 μM/s (based on the electrolyte volume of 150 μL). Prior to discharge experiments, we confirmed that the Li, pre-stabilized by soaking in PC electrolyte, was chemically stable against TPFPB by performing ¹⁹F NMR analysis of electrolytes in contact with Li over long soaking times (six days), which indicated negligible reactivity and no loss of TPFPB (**Figure 2-14** and **Table 2-2**). As shown in **Figure 2-15a**, the attainable capacity scaled monotonically with TPFPB concentration up to 3.0 mAh/cm² at 400 mM, indicating the strong contribution from TPFPB in solubilizing LiF (discharge under argon headspace with TPFPB yielded negligible capacity, **Figure 2-16**). Meanwhile, higher TPFPB concentrations yielded slightly lower discharge potentials (by ~50 mV) at 400 mM, due to increased viscosity at higher concentrations. The capacity improvement, defined as the difference

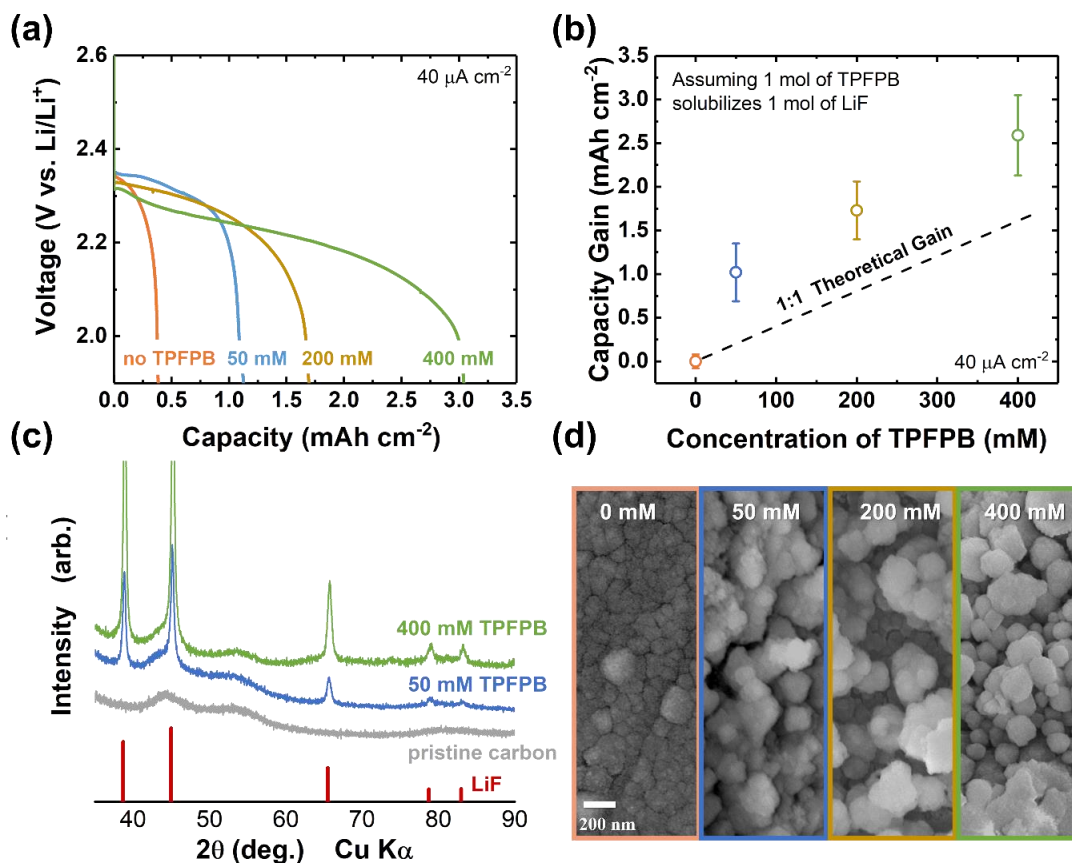


Figure 2-15 (a) Galvanostatic discharge profiles of Li-SF₆ cells at 40 μA/cm². The electrolyte was 0.1 M LiClO₄/DMSO containing 0, 50, 200 or 400 mM TPFPB. (b) Theoretical (dashed line) and observed (circles) average capacity gain at the corresponding TPFPB concentration. The averages and error bars represent statistics from more than three samples for each condition. (c) XRD pattern of the pristine GDL and cathodes fully discharged in electrolyte containing 50 and 400 mM TPFPB at 40 μA/cm². (d) SEM images of cathodes fully discharged at 40 μA/cm² in DMSO electrolyte with different TPFPB concentrations (as indicated).

with and without TPFPB at each current density, was calculated and compared to the theoretical capacity gain assuming that each TPFPB molecule dissolves only one molecule of LiF, as might be expected if the TPFPB becomes saturated after reaction (see **Section 2.5** for calculation details).

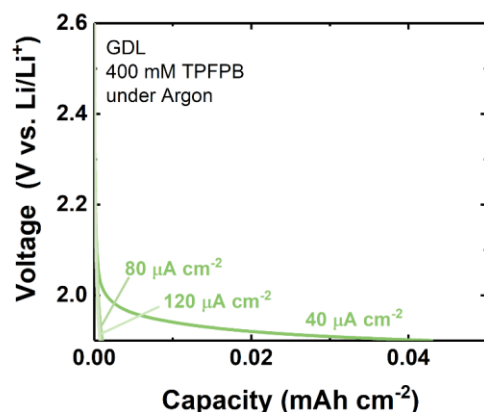


Figure 2-16 Galvanostatic discharge of Li/GDL cells in 0.1 M LiClO₄/DMSO electrolyte containing 0.4 M TFPFB under an argon headspace. The cutoff voltage was 1.9 V vs. Li/Li⁺.

As shown in **Figure 2-15b**, the actual capacity gain is significantly larger than this theoretical value at all currents. This greater-than-predicted capacity improvement suggests that some amount of F⁻ turnover occurs, or in other words, that each molecule of TFPFB dissolves more than one LiF, perhaps by facilitating its deposition in more energy-favorable sites *via* a solution-precipitation route that frees TFPFB for solubilization of additional LiF. Assuming this mechanism, the turnover rate of TFPFB at concentrations of 50, 200 and 400 mM could be calculated as 5.1, 2.2 and 1.6, respectively. This indicates that the gains in capacity decreased with increasing TFPFB concentration, especially at higher concentrations of 200 and 400 mM, where viscosity was significant and may have impeded precipitation and turnover of TFPFB. We note that higher viscosity was also reflected in impedance measurements, which indicated an order-of-magnitude increase in charge-transfer resistance when 400 mM TFPFB was added to the electrolyte (**Figure 2-7c**, compared with **Figure 2-7a**). We note that the major crystalline discharge product in the discharged cathodes spanning the range of additive concentrations used was confirmed to still be

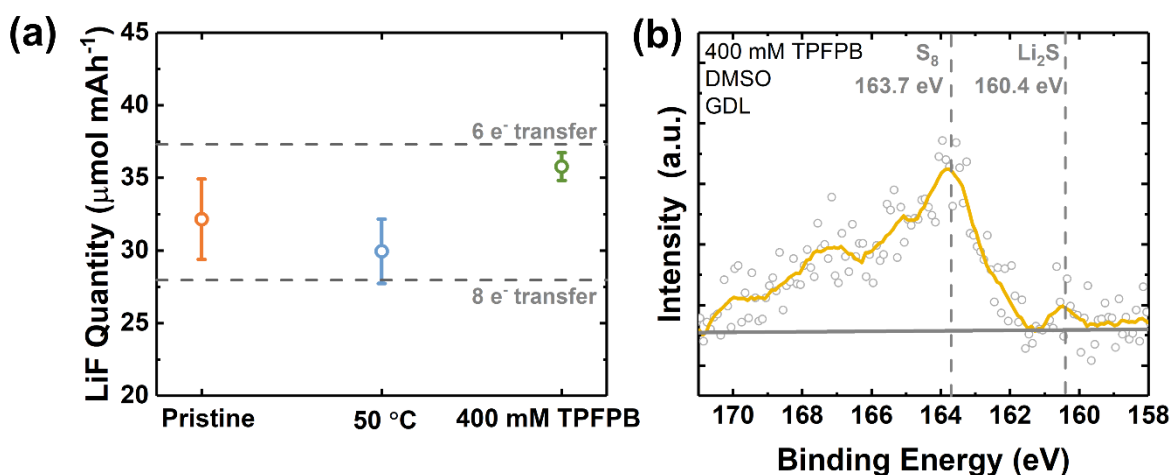


Figure 2-17 (a) Quantification of LiF formed after galvanostatic discharge at 50 °C and RT with or without TFPFB additive, in 0.1 M LiClO₄/DMSO electrolyte at 40 μA/cm². Dashed lines indicate theoretical values of LiF formed per mAh of discharge capacity, which correspond to 28.0 and 37.3 μmol/mAh for 8 e⁻ transfer (Li + SF₆ = Li₂S + LiF) and 6 e⁻ transfer (Li + SF₆ = S + LiF) assumptions respectively. The averages and error bars represent statistics from more than three samples for each condition. **(b)** S 2p high-resolution XPS spectra of a fully discharged cathode (capacity = 3.0 mAh/cm²) at 40 μA/cm² in 0.1 M LiClO₄/DMSO electrolyte with 400 mM TFPFB.

LiF, as indicated by XRD (**Figure 2-15c**). Consistent with the above picture, the LiF formed in the presence of TFPFB was substantially more three-dimensional and porous compared to the TFPFB-free case, as revealed in SEM images (**Figure 2-15d**). At higher concentrations of 400 mM, the particles were still three-dimensional in appearance, yet had smaller diameters than at 50 or 200 mM. We again attribute this to the high viscosity at 400 mM, which may limit transport of bulky TFPFB from the electrode surface, resulting in more rapid precipitation and smaller LiF particle growth. Interestingly, the inclusion of TFPFB appeared to alter the discharge state of sulfur, which was predominantly present in reduced form in previous work.¹⁴ Through quantitative ¹⁹F NMR analysis, the total amount of fluoride formed can be compared with that expected, based on

either a 6- or 8-electron transfer reaction (**Figure 2-17a**). Whereas both room-temperature and 50 °C discharge in DMSO quantitatively produced LiF consistent with a predominantly 8-electron transfer reaction, slightly higher amounts of LiF were present with TFPFB with respect to the number of electrons transferred, corresponding to a ~6-electron process. This could be confirmed by X-ray photoelectron spectroscopy measurements post-discharge with TFPFB (**Figure 2-17b**), in which S₈ was the major S-containing species present in the electrode, in contrast to our previous work.¹⁴ The detailed elementary reaction steps require future efforts to elucidate in full and a future study is planned dedicated to the influence of electrolyte on sulfur redox processes near the end of discharge.

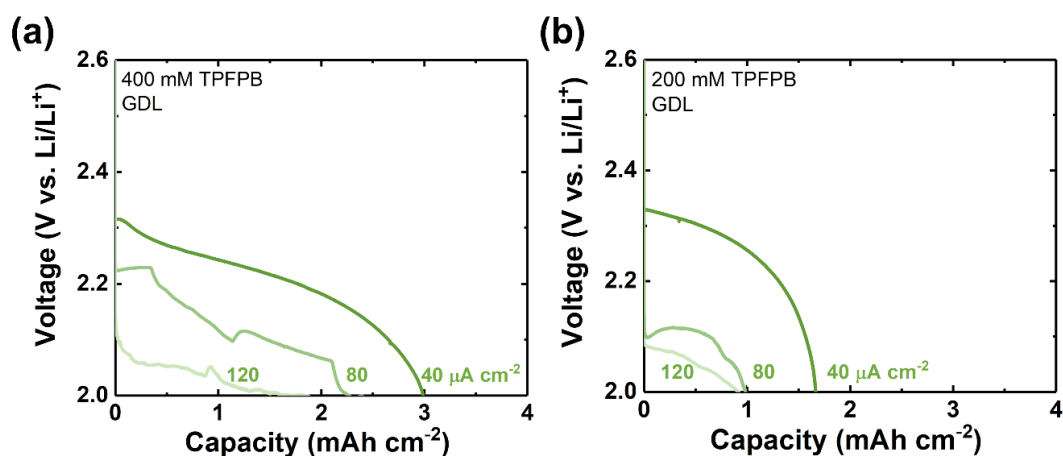


Figure 2-18. Rate capability of Li-SF₆ cells with (a) 400 mM and (b) 200 mM of the TFPFB additive in 0.1 M LiClO₄/DMSO electrolyte. Galvanostatic discharge was conducted at a current density of 40, 80, or 120 μA/cm² with GDL electrodes and a cutoff voltage of 2.0 V vs. Li/Li⁺. The relatively large noise in the voltage profiles is caused by room temperature variation during discharge, as TFPFB was found to increase the thermal sensitivity of cells. We verified that all cells made at the same time showed exactly the same trend in voltage fluctuation, and that the noise could be eliminated if the test were performed in a constant temperature incubator.

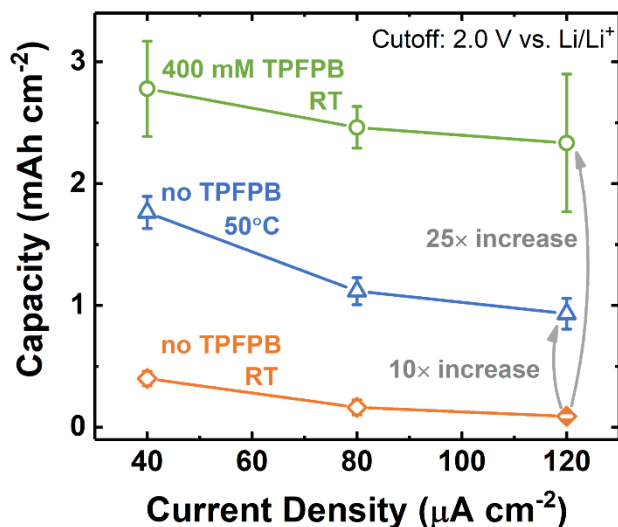


Figure 2-19 Comparison of rate capability of Li–SF₆ cells at 50 °C and RT with or without TPFPB additive, obtained on GDL electrodes in 0.1 M LiClO₄/DMSO electrolyte at a cutoff voltage of 2.0 V vs. Li/Li⁺. The averages and error bars represent statistics from more than three samples for each condition.

The rate capability improvements attainable with 400 mM TPFPB from 40 – 120 $\mu\text{A/cm}^2$ are summarized and compared with the other two systems in this work. The individual rate capability profiles of cells with 400 and 200 mM TPFPB are given in **Figure 2-18**. As shown in **Figure 2-19**, at moderate rates (40 $\mu\text{A/cm}^2$), higher temperature increased the discharge capacity by approximately five-fold, from 0.4 to 1.8 mAh/cm^2 . Meanwhile, TPFPB increased the capacity by a factor of seven (to 2.8 mAh/cm^2). The capacity gains were even larger at higher currents. For example, at 120 $\mu\text{A/cm}^2$, the capacity increased by an order of magnitude by elevating the cell temperature to 50 °C, and by a factor of 25 when adding TPFPB. Although we did not explore combining these two effects (higher temperature and TPFPB), it is likely that even higher capacities could be obtained by capitalizing on both effects; however, special care will be needed to ensure TPFPB stability at higher temperatures. Overall, these results indicate that tailoring the

LiF solubility presents a promising route to dramatically increase the energy density attainable at higher rates, a key limitation in our original study. We note that TFPFB is not necessarily an optimized choice among the many different choices of anion receptor available commercially,²⁰² and therefore, further gains in improvement may be achievable, particularly if less-bulky anion receptors can be identified to minimize viscosity increases at higher concentrations. Overall, these improvements open the door for further development of bulk solid-forming reactions for sustained power delivery in halogenated-molecular conversion reactions.

2.4 Conclusions

We have reported viable strategies to dramatically improve the attainable capacity, and thus the energy density, in Li-SF₆ cells undergoing bulk fluoride-forming reactions. Both approaches explored herein target the intrinsically low solubility of LiF, either by operating at moderately elevated temperatures of 50 °C to improve solubility and favor sparser and larger LiF nuclei in the initial stages of growth; or through more aggressive chemical modification of the electrolyte to incorporate an anion receptor additive (TFPFB) that dissolves LiF. Both strategies can significantly increase the achievable capacity by a factor of 10 and 25 respectively, at a high current density of 120 μA/cm². Use of anion receptors, in particular, appears promising for applications where operating at higher temperature may not be an option. Combining this approach with future efforts to increase the discharge voltage, for instance by altering the electrode material to promote specific SF₆ adsorption and/or catalyze its reduction, may lead to even closer realization of the high theoretical energy densities intrinsic to the Li-SF₆ system.

2.5 Appendix for Chapter 2

Calculation of TPFPB-induced theoretical capacity gain:

Total mole of TPFPB (n_{TPFPB}) in a volume V [L] of electrolyte ($V = 150 \times 10^{-6}$ L) at a concentration of c [M]: $n_{\text{TPFPB}} = c \times V$

Total mole of LiF (n_{LiF}) dissolved by TPFPB (assuming each TPFPB molecule dissolves only one molecule of LiF): $n_{\text{LiF}} = n_{\text{TPFPB}}$

The solubilization of each LiF molecule corresponds to one electron transferred during discharge, so the total additional charge transfer (Q , [C]) corresponding to n_{LiF} mol of LiF: $Q = F \times n_{\text{LiF}}$ (F denotes Faraday constant, 96485 C mol^{-1}).

Thus the theoretical capacity gain is: $Q = F \times c \times V \div 3.6$ [C/mAh]

For example, at concentration of $c = 0.05 \text{ M}$, $Q = \left(96485 \frac{\text{C}}{\text{mol}}\right) \times (0.05 \text{ M}) \times (150 \times 10^{-6} \text{ L}) \div 3.6 \text{ (C/mAh)} = 0.20 \text{ (mAh)}$.

Chapter 3: Molecular Structural Design for Liquid S–F Bond Containing Reactants to Boost Lithium Primary Battery Energy

Reproduced in part with permission from Gao, H., Sevilla, A., Hobold, G. M., Melemed, A., Guo, R., Jones, S. C., & Gallant, B. M. (2022). Fluoro-Organosulfur Catholytes to Boost Lithium Primary Battery Energy. *Submitted*. 2022.

3.1 Introduction

To widen the design space for advanced batteries, developing new electrochemical conversion reactions is challenging yet critical. Primary Li batteries have the highest energy densities among all battery technologies, owing to the successful exploitation of light-weight non-transition-metal redox centers, and thus represent exemplar systems for maximizing energy storage in chemical bonds.⁵ Such commercial batteries, as introduced in **Section 1.2**, include Li–carbon monofluoride (Li–CF_x), Li–thionyl chloride (Li–SOCl₂) and Li–sulfur dioxide (SO₂), with energy densities ranging from 200–800 Wh/kg_{packaged} and 400–1160 Wh/L_{packaged} (**Table 1-1**). Li–CF_x has the highest energy, reaching up to 800 Wh/kg_{packaged} in low-rate, high-energy cells and offers good safety and storage characteristics due to the solid nature of the CF_x cathode. However, Li–CF_x has limited performance at higher discharge rates.³⁰ Alternatively, Li–SOCl₂ and Li–SO₂ offer a broader range of operation for high delivered energy, but these cells incorporate corrosive and easily vaporized sulfur-based catholytes and are limited to specialty applications due to the associated safety concerns. The Li-primary battery field is quite mature, with very few fundamental innovations in cell chemistries in the past 40 years.^{6,7}

The redox centers of carbon (+4 to -4), nitrogen (+3 to -5), sulfur (+6 to -2), or phosphorus (+3 to -5) are of particular interest to exploit for advanced battery formulations given their light weight and large theoretically-accessible electron transfer numbers. Sulfur (S)-based redox has

received particular focus given the reversibility of its lowest oxidation states (0 to -2) as exploited in rechargeable Li-S batteries^{57,58}. The higher range of sulfur's oxidation states have been realized in commercial primary chemistries based on (halo)oxides, *viz.* Li-SOCl₂ (S oxidation state: +4 to 0),²⁷ Li-SO₂ (+4 to +3),^{148,207} and in Li-SO₂Cl₂ (+6 to +4).²⁰⁸ Li-SF₆ batteries (**Section 1.4.3** and **Chapter 2**) successfully exploits the full oxidation-state range of sulfur (+6 to -2). In spite of unrivaled high theoretical energy densities of 3920 Wh/kg_{Li+SF₆} based on weight of reactants, Li-SF₆ cells exhibited sluggish discharge reactions in practice associated with low gas solubilities (~1-5 mM) and hindered activation of symmetric SF₆ in which octahedrally-coordinated F⁻ ligands shield the redox-active S⁶⁺ center¹⁷, making this first generation of S-F redox systems of scientific interest but unable to fully realize the intrinsically high energy density.

Here we demonstrate that these challenges can be overcome through design of liquid catholytes that extensively exploit S-F bond electroactivity (**Figure 3-1a**), providing high delivered energy with facile kinetics. We examined the family of pentafluorosulfanyl arenes^{209,210} with the formula *R-Ph-SF₅*, where *Ph* is a phenyl ring and *R* is an electron-withdrawing group. When used as a catholyte in Li-carbon cells, *R-Ph-SF₅* reactants are found to undergo complete defluorination (corresponding to 5-e⁻, or 1-e⁻ per fluoride) with additional reduction possible up to a total of 8-e⁻ transfer per molecule, yielding competitive gravimetric energies up to 1845 Wh/kg_{Li+R-Ph-SF₅} and excellent rate capability. Inspection of the discharge pathways illuminates a coupling of S-F bond cleavage with further S-based redox that is highly sensitive to the reactant structure and *R*-group functionality, providing multiple motifs for design and manipulation of electrochemical defluorination reactions as an emerging class of high-capacity and energy-dense storage vectors. Practically, voltage compatibility of *R-Ph-SF₅* and solid CF_x cathodes further

enables design of a hybrid battery that achieves remarkably high active mass loading in the cell, boosting the attainable gravimetric energy of Li–CF_x batteries by a minimum of 20%.

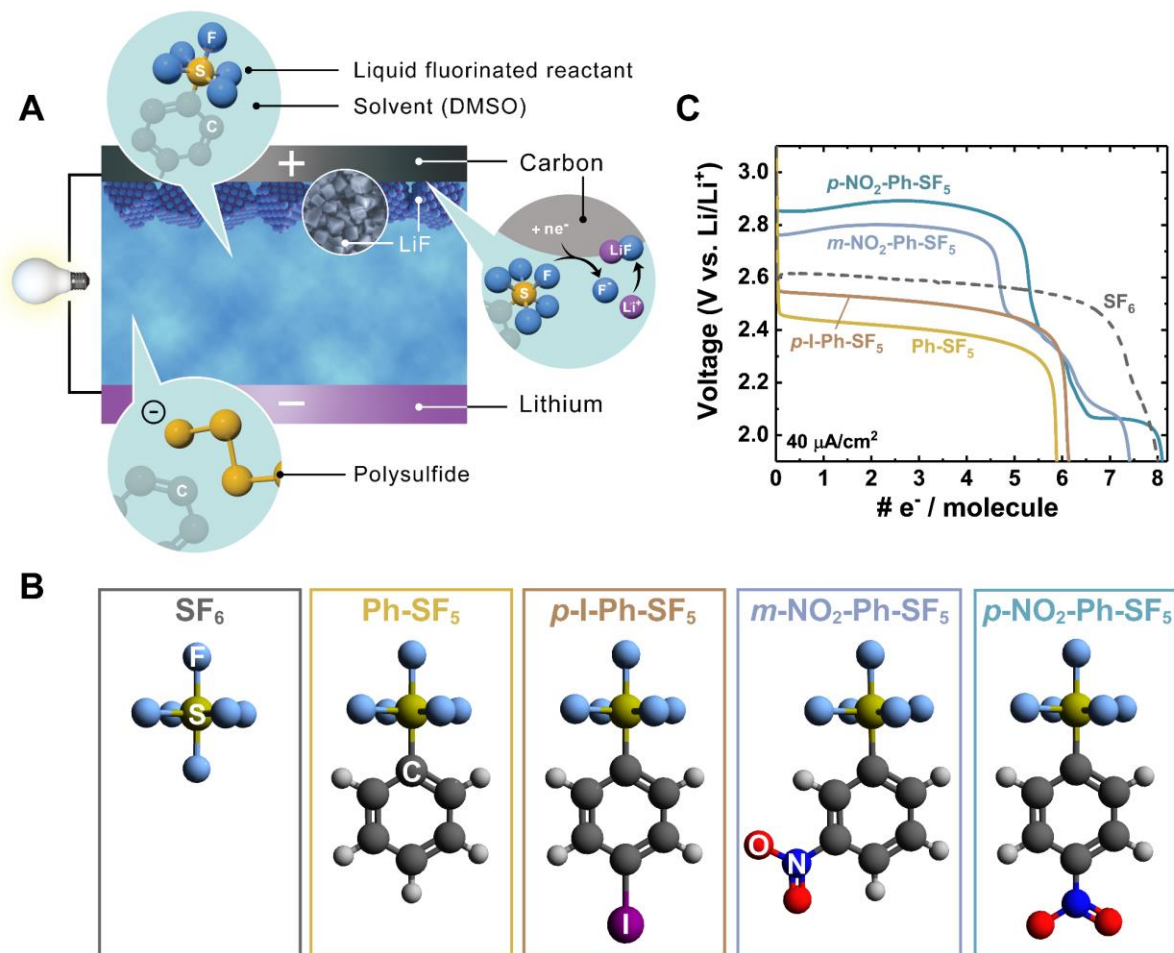


Figure 3-1 Pentafluorosulfanyl arenes (*R-Ph-SF₅*) as a class of fluorinated catholytes. (a) Schematic depicting Li-*R-Ph-SF₅* batteries. (b) Molecular structures of *R-Ph-SF₅* reactants, with the corresponding discharge profiles shown in (c). All *R-Ph-SF₅* cells were discharged with 0.1 M *R-Ph-SF₅* / 0.1 M LiClO₄ / DMSO as catholyte, Ketjen black as cathode substrate, at 40 μA/cm² and 50 °C. Li-SF₆ discharge is included in c for comparison.

3.2 Experimental Methods

Chemicals and Materials. 4-nitrophenylsulfur pentafluoride ($p\text{-NO}_2\text{-Ph-SF}_5$, >96%, TCI), 4-iodophenylsulfur pentafluoride ($p\text{-I-Ph-SF}_5(p)$, >94%, TCI), phenylsulfur pentafluoride (Ph-SF_5 , >98%, TCI), 3-nitrophenylsulfur pentafluoride ($m\text{-NO}_2\text{-Ph-SF}_5$, Synquest) were stored inside the argon-filled glovebox (MBRAUN). The density of $p\text{-NO}_2\text{-Ph-SF}_5$ in the liquid state is 1.60 ± 0.04 g/mL, which was determined by measuring the weight of 1 mL $p\text{-NO}_2\text{-Ph-SF}_5$ liquid upon heating to just above the melting temperature (30–40 °C).

Cathode Preparation. All electrodes were dried under active vacuum in a glass oven (Buchi) overnight at 90 °C and stored in an Ar glovebox. Ketjen black (KB) electrodes were fabricated in-house by uniformly coating sonicated inks composed of KB powder (AzkoNobel), N-methyl-2-pyrrolidone (NMP), and polyvinylidene difluoride (PVDF) binder (weight ratio of KB:PVDF = 80:20) onto a sheet of Toray paper (TGP-H-030, 5% wet proofing, Fuel Cell Earth). The resulting carbon loading was 0.6 ± 0.1 mg/cm² (average and error bar based on ten measurements). The obtained coated Toray paper was dried at room temperature and then punched into circular disks (12 mm diameter) prior to further drying as indicated above. Carbon foam cathodes (gas diffusion layer coated with a microporous layer, EQ-bcgdl-1400S-LD, MTI Corp.) has a carbon loading reported as 5 mg/cm². The as-received carbon foam was punched into 15 mm-diameter disks and dried as above. The CF_x powder mix has a CF_x (ARC 1000)/carbon/polytetrafluoroethylene (PTFE) ratio of 85/10/5. The as-received powder mix was rolled into a film and punched into circular disks with a diameter of 15 mm before drying. The typical CF_x loading of the obtained electrode is 11.5 ± 1.3 mg/cm² (based on ten measurements).

Galvanostatic Discharge. All the cells were constructed in the argon glovebox. For low reactant concentration (0.1 M) Li-*R-Ph-SF*₅ tests, two-electrode Swagelok cells were used as they are easy to disassemble and thus most suitable for cathode retrieval for subsequent *ex situ* analysis. The cells were constructed in the argon glovebox and consisted of KB as the cathode substrate and a 9 mm diameter disk of Li metal as the anode (0.75 mm thick, 99.9% metals basis, Alfa Aesar) which was placed on a stainless steel plunger. A 12 mm diameter stainless steel mesh (McMaster) was used as the cathode current collector. The separator (13 mm diameter Whatman filter paper) was impregnated with 50 μ L of electrolyte solution (0.1 M *R-Ph-SF*₅/0.1 M LiClO₄ / DMSO). For high concentration Li-NO₂-Ph-SF₅ cells (≥ 0.5 M, based on total volume of NO₂-Ph-SF₅ and DMSO), Li-CF_x cells, and hybrid cells, two-electrode coin cells were used to provide better sealing over long testing times (up to one month) given the large proportion of reactants. Cells were constructed inside the Ar glovebox using a 15 mm diameter cathode substrate (carbon foam or CF_x electrode), a 16 mm diameter Whatman separator, a 15 mm diameter Li anode, two stainless steel disks (MTI Corp.) as anode and cathode current collectors, and 50 μ L electrolyte. All coin cells were assembled using an electric crimper (MSK-160E, MTI Corp.) with a constant mass loading of 0.82 tons. All cells were rested at open circuit voltage (OCV) for 5 h before initiating galvanostatic discharge. All discharge tests (BioLogic VMP3 potentiostat or MPG2 workstation) were conducted at the indicated current density with a voltage window ranging from OCV (typically ~ 2.9 (Li-CF_x), ~ 3.0 (Li-*m*-NO₂-Ph-SF₅), ~ 3.2 (Li-*p*-NO₂-Ph-SF₅), ~ 3.3 (Li-*p*-I-Ph-SF₅), ~ 3.4 (Li-Ph-SF₅) V vs. Li/Li⁺) to a lower voltage cutoff of 1.9 V vs Li/Li⁺. For galvanostatic discharge at 50 or 70 °C, cells were placed inside an incubator (Mettler GmbH + Co. KG).

Raman spectroscopy. Raman spectroscopy measurement was performed on the rinsed/dried discharged cathodes using a Renishaw Invia Reflex Raman Confocal Microscope.

The samples were sealed under Ar inside the glovebox using a Linkam FTIR600 stage (quartz window, sealed ports) and remained sealed throughout the measurements. A 785 nm bar laser at an operating power of 100 mW was used as the excitation source with a 1200 l/mm grating and 10% at 50 cm⁻¹ shift Rayleigh filter. Accumulations of spectra were obtained to improve the signal to noise ratio.

X-ray photoelectron spectroscopy (XPS). Discharged cathode substrates were harvested from cells inside the glovebox and dried under vacuum overnight at room temperature. XPS analysis was conducted on a PHI VersaProbe II X-ray Photoelectron Spectrometer. The binding energies were calibrated by the LiF peak at 684.90 eV, except for the pristine carbon sample without LiF, in which case energies were calibrated to the C–F binder peak at 688.40 eV. High-resolution spectra were deconvoluted using CasaXPS software with a Shirley-type background and a 70% Gaussian/30% Lorentzian line shape.

Ultraviolet-visible (UV-vis) spectroscopy. UV-vis measurements were conducted using an Agilent Cary 60 UV-vis spectrometer. To prepare samples, the separator was harvested from the discharged cell inside the glovebox and soaked in 1 mL DMSO. The resulting solution was then diluted by ~20x for UV-vis measurements inside the glovebox, and 1 mL of this diluted solution was transferred to a cuvette and sealed under Ar. A typical UV-vis measurement (including scan time) takes around 10 minutes.

Gas chromatography/mass spectroscopy (GC/MS). For GC/MS and GC-only experiments, custom-designed gas-tight two-electrode cells with a headspace of ~6 mL were used. Before each experiment, the cells were purged with clean Ar and pressurized to ~30 psi. Gases evolved during rest/discharge accumulated in the closed headspace of the cell. After rest/discharge, 2.5 mL gas

samples were extracted from the headspace of the cell with a gas-tight syringe, and then immediately injected into the appropriate instrument for gas characterization. GC/MS samples were manually injected into a GC instrument (Agilent 7890B) fitted with a MS detector (Agilent 5977B) capable of detecting species in the 10–200 Da range. The final ionization mass spectra were obtained by integrating the signal intensity over all scans. GC-only samples were manually injected into a GC instrument (Agilent 7890B) fitted with flame ionization (FID) and thermal conductivity (TCD) detectors.

Operando Pressure Measurement. A custom built electrochemical cell coupled with a pressure transducer (PX309, OMEGA Engineering, Inc.) was used for *operando* pressure measurements. Detailed cell design can be found in Ref. 16. After assembling, the cell was pressurized with Ar to ~18 psi, sealed and placed in the 50 °C incubator. After resting at OCV (~3.1 V vs. Li/Li⁺) for 5 h, galvanostatic discharge was conducted from OCV to 1.9 V vs. Li/Li⁺, with 150 μL 0.1 M NO₂-Ph-SF₅ / 0.1 M LiClO₄ / DMSO as catholyte at 40 μA/cm². In the meantime, the pressure transducer (powered by a regulated DC power supply, Digi-Key) was connected to the same potentiostat via a DB9 connector, and the voltage output of the transducer was recorded and converted to the pressure based on a calibrated factory specification. Additional resting for 10 h was conducted after cell discharge to establish the pressure baseline (linear fit of pressure as a function of time). To calculate the projected cell pressure with the assumption that 1 mol of gas (*e.g.* NO or NO₂) is generated per 8 mol of e⁻ transfer, the ideal gas law was applied to calculate the pressure increase (in psi, where 1 psi = 6894.76 Pa) by equation –

$$\Delta P = \frac{\Delta nRT}{V} = \frac{RT}{V} \left(\frac{Q \times 3.6}{F \times 8} \right) / 6894.76, \text{ where } V \text{ is the headspace volume, which was measured to}$$

be 4.77×10⁻⁶ m³ (4.77 mL); *T* is temperature (323 K); *R* is universal gas constant (8.314 J/(mol·K);

Q is discharge capacity (in mAh); F is the Faraday constant (96485 C/mol). The projected cell pressure is then $P_{projected} = P_{baseline} + \Delta P$, where $P_{baseline}$ is the baseline pressure.

Electrolyte Ionic Conductivity Measurements. Ionic conductivity measurements were performed inside the glovebox using an Oakton CON 700 benchtop meter equipped with a conductivity probe. The probe has a cell constant $K=L/A=1$ (L is the distance between the probe's electrodes; A is the effective surface area of the electrodes). To measure ionic conductivity at temperature, the vial containing the electrolyte was placed in a heating block on a hot plate set at 50 °C. Ionic conductivity was measured by immersing the probe in 3 mL of the electrolyte solution until a steady reading was obtained. The measurement was repeated three times for each solution, from which an average value was determined.

Density Functional Theory (DFT) Calculations. All calculations were carried out using the Gaussian 03 program.²¹¹ To obtain HOMO and LUMO structures, molecular geometries in the gas phase were optimized to minimized energy at the B3LYP/6-31G+ level for SF₆ and all *R-Ph-SF₅* molecules, except for *p-I-Ph-SF₅*, where B3LYP/3-21G was used so that the basis set is suitable for iodine. The atoms-in-molecules (AIM) analysis and localized orbital bonding analysis (LOBA)²¹² were performed on Multiwfn 3.8 software²¹³ using the optimized structure obtained from Gaussian 03.

Note that experimental details for all other testing and analysis techniques used in this chapter have already been provided in earlier chapters. Additional chemical and materials, experimental procedures for SEM and XRD characterizations can be found in **0**.

3.3 Results and discussion

3.3.1 Intrinsic electroactivity and products of R-Ph-SF₅ discharge

The reactant structures and their incorporation into a Li primary battery are shown in **Figure 3-1**. *R*-Ph-SF₅ reactants exhibit multiple design handles, including the nature of the

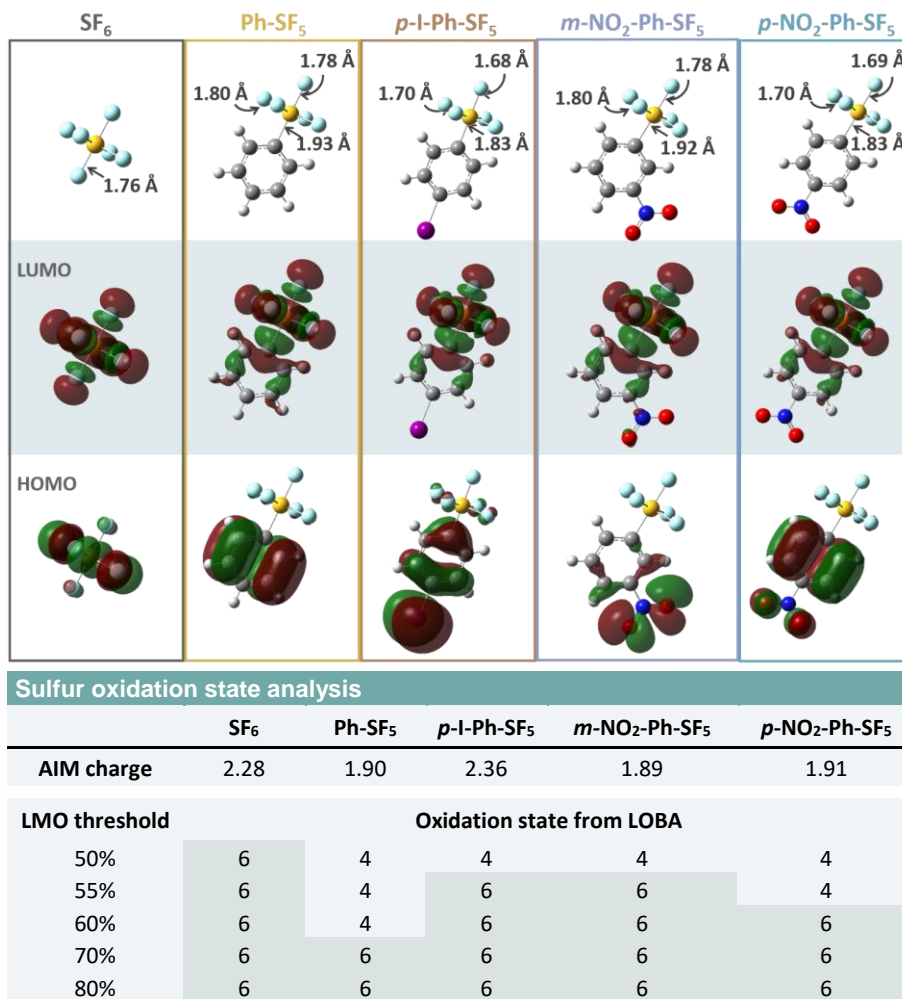


Figure 3-2 Electronic structure of pentafluorosulfanyl arenes. The bond length of the S–F and S–C bonds are as indicated. The aromatic group breaks the symmetry around the sulfur redox center with the F on the top octahedral vertex being closer to S than the four F that share the same plane. See **Section 3.5.1** for estimation of the sulfur oxidation state (OS).

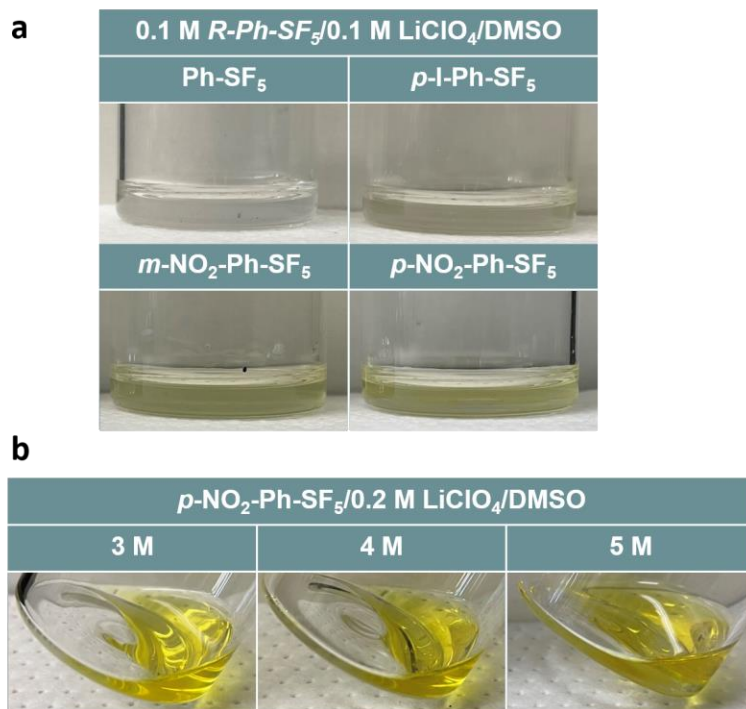










Figure 3-3 Optical image of (a) 0.1 M *R-Ph-SF₅* / 0.1 M LiClO₄ / DMSO catholyte and (b) NO₂-Ph-SF₅ / 0.2 M LiClO₄ / DMSO catholyte with different NO₂-Ph-SF₅ concentrations. Generally, NO₂-Ph-SF₅ was found to be miscible with multiple common electrolyte solvents (*e.g.* PC, TEGDME, EC/DMC) in addition to DMSO.

aromatic group, R-group composition and position (**Figure 3-1b**). Compared to SF₆(g), molecular structure and lowest unoccupied molecular orbital (LUMO) calculations (**Figure 3-2**) show that the aromatic group of *R-Ph-SF₅* breaks the S–F symmetry while retaining a similar electronic structure around the sulfur redox center. The aromatic group also imparts miscibility with organic solvents up to 5 M concentration (**Figure 3-3**). Notably, *R-Ph-SF₅*-class reactants have safety ratings favorable to both SOCl₂ and typical Li-ion electrolyte formulations due to low corrosivity, low flammability, high boiling point and high chemical stability (**Table 3-1**). Cells (**Figure 3-1a**) were assembled with a Li metal anode, a carbon cathode substrate (Ketjen black or carbon foam), and a catholyte comprising *R-Ph-SF₅* (0.1–5 M) with LiClO₄ salt and dimethyl sulfoxide (DMSO)

solvent. LiClO₄ was used to avoid additional sources of F for characterization purposes whereas the use of additional DMSO solvent was necessary to dissolve Li-salt. In addition, DMSO was shown previously to support high capacities of fluoride conversion cathodes given the ability to partially solubilize LiF.¹⁷

Table 3-1 Safety comparison of battery electrolytes*

	SOCl ₂ ²¹⁴	LIB electrolyte ^b ₂₁₅	CF _x electrolyte ^d	Ph-SF ₅ ²¹⁶	<i>p</i> -I-Ph-SF ₅ ²¹⁷	<i>m</i> -NO ₂ -Ph-SF ₅ ²¹⁸	<i>p</i> -NO ₂ -Ph-SF ₅ ²¹⁹		
State at RT	liquid	liquid	liquid	liquid	solid	liquid	solid		
Boiling point	79 °C	~100 °C ^c	--	≥148 °C	~220 °C ^e	~273 °C ^f	~197 °C ^g		
Category 1–5, with <u>1</u> the most hazardous									
Acute toxicity ^a		LiPF ₆	EC	LiBF ₄ ²²⁰	DME ²²¹				
Oral	4	3	4	4	--	--	4	4	3
Dermal	--	--	--	4	--	--	--	4	3
Inhalation	3	--	--	4	4	--	--	4	3
Category 1–3, subcategory A–C, with <u>1A</u> the most corrosive.									
Skin irritation ^a	1A	1A	1B	2	2	2	2	2	
Eye irritation ^a	1	1	1	2	2A	2A	2A	2A	
Hazard rating 0–4, with <u>4</u> the most hazardous									
NFPA rating ^h									
Health	4	3	3	2	3	3	3	3	
Fire	0	3	0	3	2	0	0	1	
Reactivity	2	0	1	0	0	0	0	0	

^a Toxicity and irritation categories are reported following the globally harmonized system (GHS) classification.

^b 1 M LiPF₆ in ethylene carbonate/ethyl methyl carbonate (EC/EMC, 3:7), a commonly used electrolyte for Li-ion batteries (LIB).

^c The boiling point for 1 M LiPF₆ EC/EMC (3:7) is not available, thus the data for 1 M LiPF₆ EC/EMC (1:1) is used here, from Ref.²²².

^d Commonly used electrolyte in Li–CF_x batteries is LiBF₄ or LiClO₄ in PC/DME^{223,224}.

^e Converted to 1 atm based on the reported value of 50 °C @ 0.75 mmHg (conversion based on Ref.²²⁵. Same for note f and g).

^f Converted to 1 atm based on the reported value of 106 °C @ 2 mmHg.

^g Converted to 1 atm based on the reported value of 76-77 °C @ 12 mmHg.

^h NFPA: National Fire Protection Association. **W** means the material reacts violently or explosively with water.

* The major risk for SOCl₂ is its high corrosivity and low stability (high reactivity). Specifically, it reacts with water (*e.g.* in air) to release SO₂ and HCl. The relatively low boiling point increases the risk of vapor

inhalation. In addition, during battery use, Li–SOCl₂ cells face risk of thermal runaway due to heat generation, or explosion due to internal cell pressure increase (due to evolution of SO₂ gas, a major product, during discharge²⁷).

A major risk for commercial Li-ion battery electrolytes based on carbonate solvents, which are also used in Li–CF_x batteries, is high flammability. Note that these electrolytes also cause severe skin or eye damage if in contact.

In contrast, *R-Ph-SF₅* reactants are thermally and chemically stable, less corrosive, have relatively low flammability (1 vs. 3 on the NFPA and HMIS ratings), and high boiling points (typically >150 °C, e.g. *m-NO₂-Ph-SF₅*: 273 °C at 1 atm). The use of solvent might increase the flammability of the electrolyte (e.g. DMSO has a flammability rating of 2 in NFPA and HMIS systems²²⁶), but noting that the solvent volume will be minimized in a practical cell to maximize the reactant concentration, safety concerns are expected to be less severe than in a dilute DMSO-based electrolyte.

To examine the intrinsic redox behavior, **Figure 3-1c** shows discharge of cells containing 0.1 M *R-Ph-SF₅* at 40 μA/cm² as a function of electrons reacted per molecule (calculation details in **Section 3.5.2**). Cells were tested at 50 °C to maximize capacity; temperature effects are revisited later. Unsubstituted *Ph-SF₅* and *Ph-I-SF₅* exhibited modest voltages of ~2.5 V vs. Li/Li⁺ over a single plateau. Increasing the Hammett coefficient of the electron-withdrawing functionality to –NO₂ in the meta (*m*) or para (*p*) position (0.71 or 0.78, vs. 0.18 for –I at para)²²⁷ led to higher discharge voltages. The highest cell voltage was obtained with –NO₂ in the para (*p*) position and yielded a three-stage discharge profile with plateaus at 2.9, 2.3 and 2.1 V vs. Li/Li⁺ with a total capacity of 8 e[–]/molecule (861 mAh/g_{R-Ph-SF₅}, identical to the theoretical capacity). Given its leading performance, all subsequent studies utilize *p-NO₂-Ph-SF₅* with the ‘*p*’ henceforth omitted.

To examine the conversion process in detail, 0.1 M NO₂-Ph-SF₅ was discharged to varying terminal voltages (**Figure 3-4a**) after which cathodes and/or electrolyte were extracted for analysis. At 2.54–2.38 V vs. Li/Li⁺, the cathodes consisted of cubic crystallites of ~270 ± 50 nm in **Figure 3-4b**, confirmed to be LiF (rocksalt, *Fm* $\bar{3}$ *m*) from X-ray diffraction (**Figure 3-5**) and in the XPS F 1s spectrum (684.9 eV, **Figure 3-4c**). Given the electronically insulating nature of LiF, the energy-minimized structure and large particle size suggests that LiF particles grow *via* a solution-

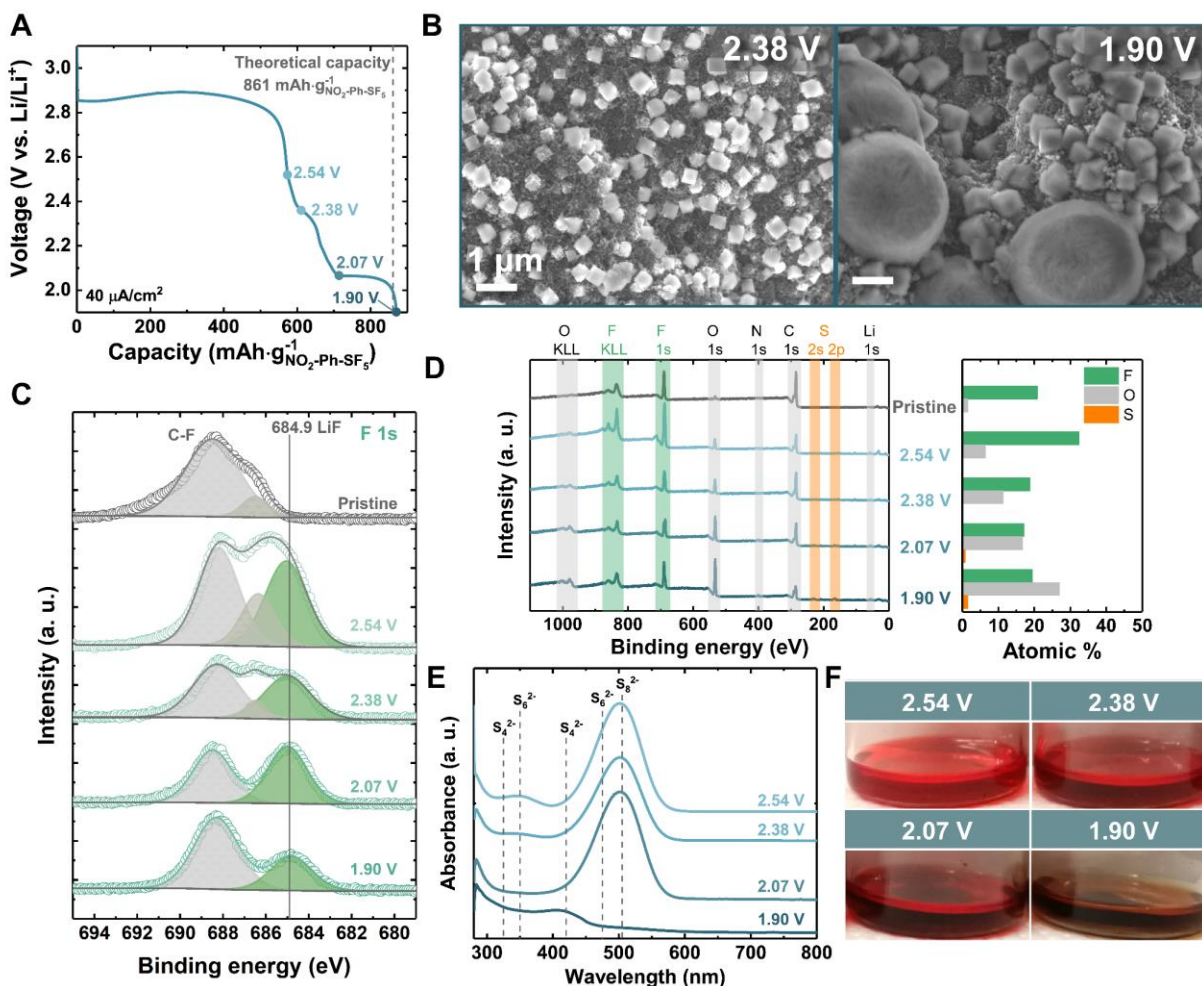


Figure 3-4 Characterization of $\text{NO}_2\text{-Ph-SF}_5$ discharge products. (a) $\text{NO}_2\text{-Ph-SF}_5$ discharge profile under reactant-limited conditions with different cell termination voltages. (b) SEM of carbon cathodes from cells discharged to 2.38 or 1.90 V vs. Li/Li^+ . (c) High resolution F 1s XPS spectra of discharged electrodes. The two C-F peaks at 688.4 and 686.4 eV are from the polyvinylidene difluoride (PVDF) binder. (d) XPS survey spectra (left) with corresponding F, O and S atomic percentage (right). (e) UV-vis spectra of extracted electrolyte from discharged cells (diluted in DMSO) as a function of termination voltage.^{228,229} (f) Corresponding photographs of samples in e. All cell conditions as in Figure 3-1.

mediated process^{17,99}. The amount of solid sulfur products in the cathode S 2p spectra was negligible (< 0.1 at. %, **Figure 3-4d** and **Figure 3-6a**)²³⁰ after the high-voltage plateau, however, ultraviolet-visible (UV-vis) spectroscopy and visual analysis confirmed that most of the sulfur was present in solution as polysulfides, with S_8^{2-} predominant (**Figure 3-4e, f**). The data collectively indicate that the high-voltage plateau corresponds to near-stoichiometric defluorination of all 5 F ligands in NO_2 -Ph-SF₅, a process that liberates S intermediates from the parent molecule which then undergo polymerization reactions in solution. Polysulfide generation continued upon further discharge to 2.07 V vs. Li/Li⁺ ($\sim 1 e^-$), with a slight increase in cathode S content (to ~ 0.8 at. %, **Figure 3-4d**).

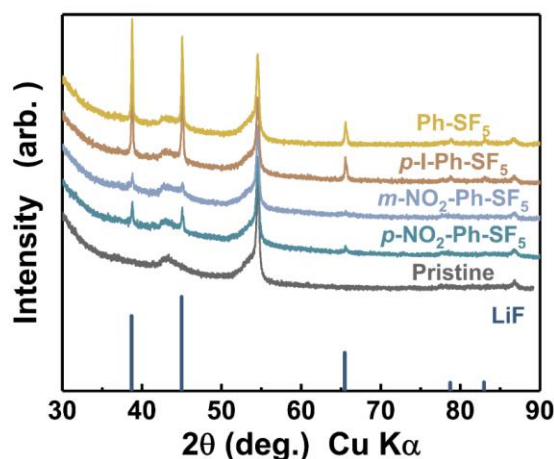


Figure 3-5 XRD of discharged cathodes from Li-*R-Ph-SF*₅ cells with 0.1 M *R-Ph-SF*₅, discharged at 40 $\mu A/cm^2$ and 50 °C. Cell discharge capacities: 0.93, 0.78, 0.73, and 0.70 mAh/cm², for *p*-Li-NO₂-Ph-SF₅, *m*-NO₂-Ph-SF₅, *p*-I-Ph-SF₅, and Ph-SF₅ cells, respectively. High voltage plateau capacities for Li-*p*-NO₂-Ph-SF₅, *m*-NO₂-Ph-SF₅ cells were 0.58 and 0.47 mAh/cm², respectively.

Full discharge to 1.90 V vs. Li/Li⁺ led to near-complete disappearance of any species detected by UV-vis²³¹ (**Figure 3-4e**) and XPS indicated a modest increase in the cathode's S and N content (to ~ 1.5 and 1.3 at.%, respectively, **Figure 3-4d** and **Figure 3-6a-c**). Prior studies have

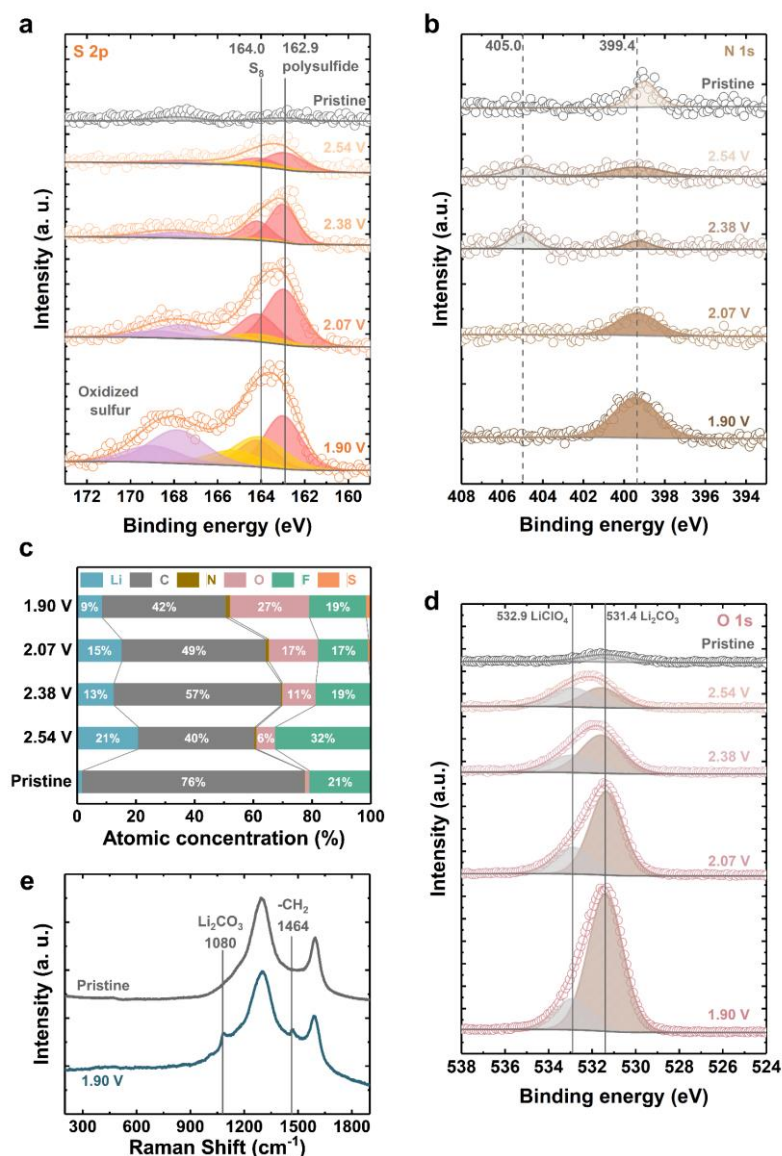


Figure 3-6 (a) S 2p and (b) N 1s high resolution XPS scans of discharged cathodes to the indicated voltages. Reference peaks: polysulfide: 162.9 eV;²³⁰ S₈: 164.0 eV;²³² oxidized sulfur: ~167.8 eV, *e.g.* SO_x²³³ or DMSO.²³⁴ The peaks at 399.4 and 405.0 eV can be attributed to –NO₂-containing organic compounds, while the N signal detected from pristine KB might be attributed to residual NMP.²³² Negligible Li₃N (~395.5 eV)²³⁵ was detected. (c) Atomic composition at different degrees of discharge from XPS quantification. (d) O 1s high resolution XPS scans of discharged cathodes to the indicated voltages. Reference peaks: Li₂CO₃: 531.4 eV; LiClO₄ (residual electrolyte salt): 532.9 eV.²³² (e) Raman spectra of discharged cathodes to the indicated voltages. Reference peaks: Li₂CO₃: 1080 cm⁻¹,²³⁶ –CH₂ stretching: 1464 cm⁻¹,^{237,238}

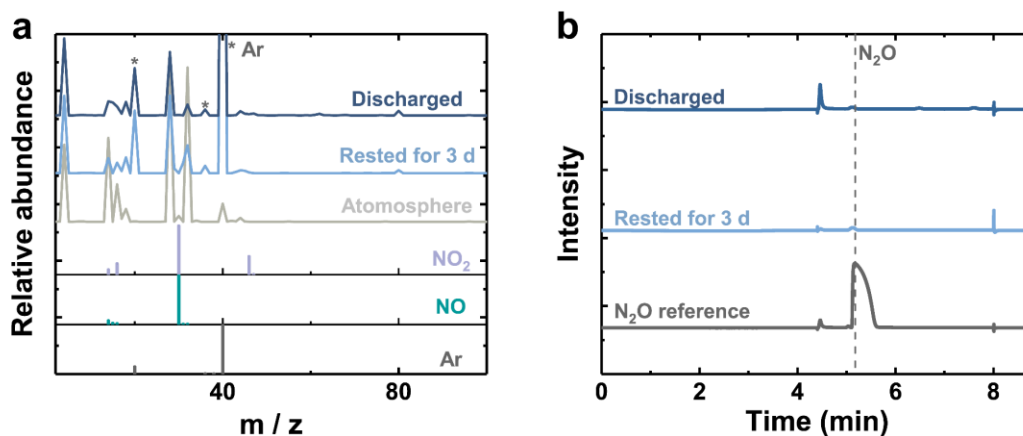


Figure 3-7 (a) Mass spectroscopy and (b) gas chromatography of the headspace gas from a fully-discharged Li-NO₂-Ph-SF₅ cell with 150 μ L 0.1 M NO₂-Ph-SF₅ / 0.1 M LiClO₄ / DMSO electrolyte and KB electrode at 40 μ A/cm². Background comparisons were conducted on the headspace gases from cells with the same electrolyte and cathode (without Li) after resting at 50 °C for 3 days. In part b, the peaks at 4.4–4.5 min and 8 min are due to valve switches.

reported the tendency of nitro-functionalized aromatics to react with short-chain (S₂²⁻) polysulfides in DMSO and undergo a ring thiol substitution with NO₂⁻ as a leaving group,²³⁹ – a possible mechanism that could account for S-poor solid phases in discharged cathodes and retention of reduced S in the liquid phase, along with minor increases in N. O content in the cathode also increased from 16.8 to 27.0 at.% between 2.07 and 1.90 V vs. Li/Li⁺ (**Figure 3-4d** and **Figure 3-6c**), while corresponding SEM images indicated nucleation of a new phase with spherical morphology (**Figure 3-4b**), confirmed to be O-rich and N, F, S-poor by energy-dispersive X-ray analysis. The XPS O 1s (**Figure 3-6d**) and Raman spectrum (**Figure 3-6e**) indicated this phase to be Li₂CO₃, which might arise from –NO₂-derived interactions with DMSO or prior formation of Li₂O, a plausible reduction product of the nitro group that could react further with electrolyte or trace CO₂ to yield Li₂CO₃. These spherical particles formed only with –NO₂ containing reactants and regardless of salt, excluding the possibility that they originate from LiClO₄. Significantly, cell

headspace analysis by gas chromatography and mass spectroscopy (**Figure 3-7**) ruled out formation of NO, NO₂, or N₂O, and cells discharged with a pressure transducer showed negligible gas evolution (**Figure 3-8**) of any kind. While the precise mechanism of multi-electron NO₂-Ph-SF₅ reduction is complex, the overall mechanism indicates extensive S-F, S-S, C-S, and N-O bond activation and reduction, yielding solid and liquid products that accumulate throughout the cell.

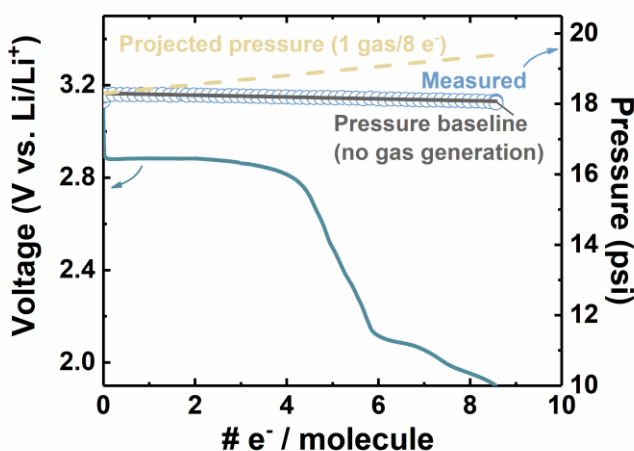


Figure 3-8 Galvanostatic discharge of a Li-NO₂-Ph-SF₅ cell with 150 μL 0.1 M NO₂-Ph-SF₅ / 0.1 M LiClO₄ / DMSO as catholyte at 40 μA/cm² and 50 °C, with the corresponding cell pressure (blue symbols). The grey solid line is the projected pressure baseline, which is extrapolated from the linear fit of cell pressure profile during post-discharge resting (for 10 h). To provide a quantitative scale for these measurements, the yellow dashed line is the estimated cell pressure increase if 1 mol of gas were generated per 8 mol of electron transfer, e.g. one NO, NO₂, or SF_x gas molecule (e.g. SF₄).

3.3.2 Discharge performance of Li-NO₂-Ph-SF₅ cells

The electrochemical performance was examined as a function of reactant concentration to evaluate feasibility as a high-concentration catholyte. **Figure 3-9a** shows galvanostatic discharge

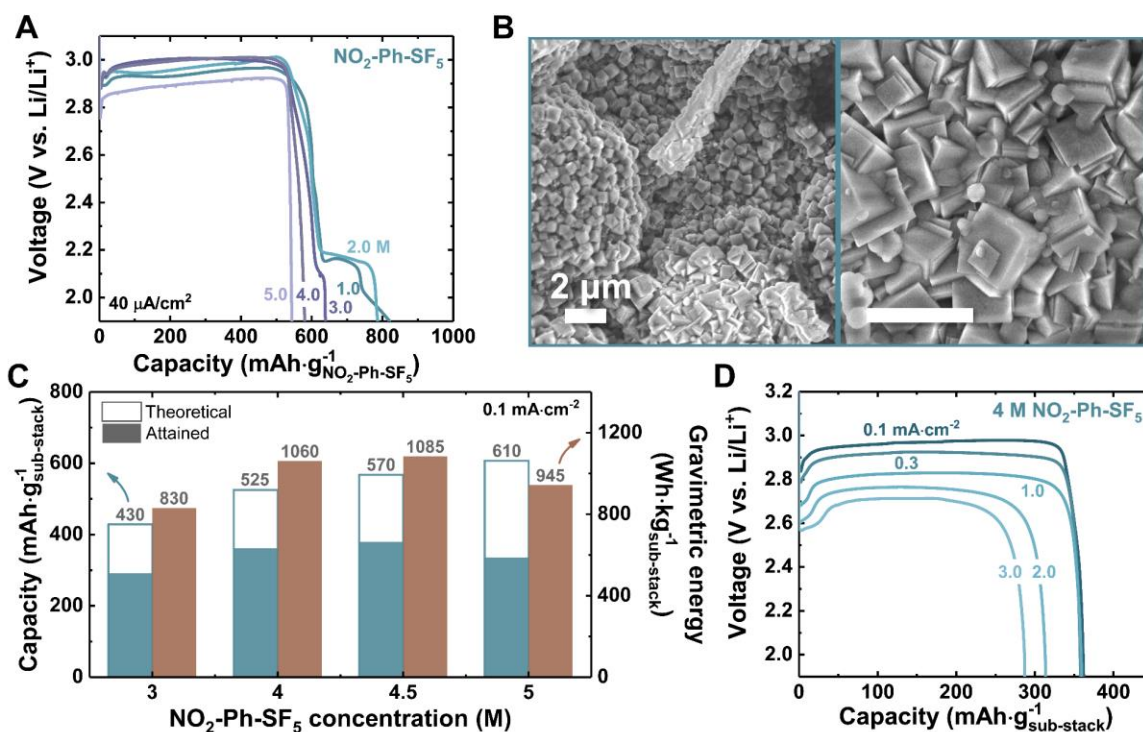


Figure 3-9 Concentration and rate effects on Li-NO₂-Ph-SF₅ cell discharge. (a) Galvanostatic discharge of Li-NO₂-Ph-SF₅ cells as a function of NO₂-Ph-SF₅ concentration at 40 μA/cm². (b) SEM of carbon cathodes fully discharged with 3 M NO₂-Ph-SF₅ / 0.2 M LiClO₄ / DMSO cathode/electrolyte at 0.3 mA/cm². (c) Theoretical/attained capacities and attained gravimetric energies of Li-NO₂-Ph-SF₅ cells as a function of catholyte concentration. All cells were discharged at 0.1 mA/cm². Theoretical capacities correspond to 8 e⁻ per molecule (calculation details in the **Section 3.5.3**). (d) Rate capability of cells with 4 M NO₂-Ph-SF₅ / 0.2 M LiClO₄ / DMSO. Note that 1 C = ~490 mA/g_{sub-stack} = 24 mA/cm² at 4 M concentration. ‘Sub-stack’ weight denotes NO₂-Ph-SF₅ + electrolyte + carbon cathode + consumed Li.

at concentrations of 1–5 M at $40 \mu\text{A}/\text{cm}^2$, where capacities are here normalized to the weight of $\text{NO}_2\text{-Ph-SF}_5$ as an intrinsic measure of reactant utilization. Discharge at concentrations of 1.0–2.0 M led to attainable capacities of 818 and 786 $\text{mAh}/\text{g}_{\text{NO}_2\text{-Ph-SF}_5}$ respectively, with retention of a similar discharge profile. Further increasing concentration (≥ 3 M) saw disappearance of the lower-voltage plateau at ~ 2.1 V vs. Li/Li^+ , with capacities of 544 $\text{mAh}/\text{g}_{\text{NO}_2\text{-Ph-SF}_5}$ attained at 5.0 M. The loss of the lower-voltage plateau indicates that the carbon cathode surface became passivated by LiF at high potentials before $\text{NO}_2\text{-Ph-SF}_5$ could be fully reduced, *i.e.*, cells switched from being reactant-limited to surface passivation-limited. This was confirmed by SEM of discharged cathodes showing extensive crystallization of cubic LiF particles and no visible carbon substrate remaining (**Figure 3-9b** vs. **Figure 3-4b**).

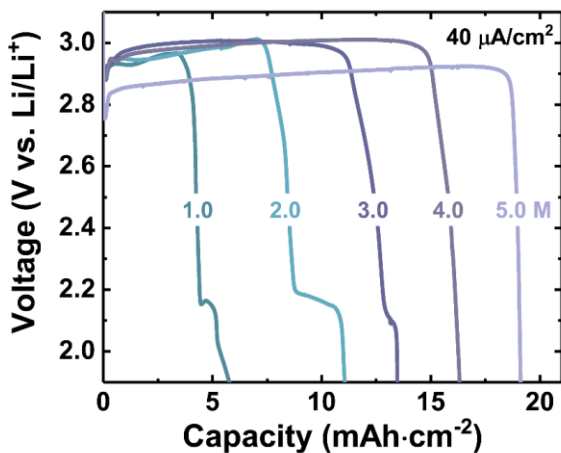


Figure 3-10 Discharge of $\text{Li-NO}_2\text{-Ph-SF}_5$ cells as a function of reactant concentration at fixed total electrolyte volume ($50 \mu\text{L}$), normalized to cathode geometric area. The data are the same as **Figure 3-9a**.

In spite of lower per-molecule utilization, increasing the concentration enables improved cell-level metrics. **Figure 3-10** plots the same data in **Figure 3-9a** at $40 \mu\text{A}/\text{cm}^2$ in units of areal capacity, showing a monotonic increase from 5.8–19.1 mAh/cm^2 between 1.0 and 5.0 M. To

accurately represent the cell performance on a gravimetric basis, normalization was additionally conducted based on the weight of all cell materials (*i.e.* NO₂-Ph-SF₅ + electrolyte + carbon cathode + consumed Li) excluding only the current collectors, separator, binder, and cell housing,²⁴⁰ henceforth denoted as “sub-stack”. **Figure 3-9c** shows these sub-stack capacities and gravimetric energies at a slightly higher current of 0.1 mA/cm². Capacities increased from 292 to 362 mAh/g_{sub-stack} as concentration increased from 3 M to 4 M, beyond which further gains were negligible. The maximum gravimetric energy of 1085 Wh/kg_{sub-stack} was obtained at 4.5 M. Capacity and energy decreased with concentrations exceeding 4.5 M due to diminishing supporting solvent (DMSO, ~16 wt% of the catholyte at 5 M) which led to significant decline in ionic conductivity from 6.4 to 0.6 mS/cm from 0.1 M to 5 M (**Figure 3-11**). Additionally, low DMSO content decreases the ability to solubilize LiF, making electrode passivation effects more severe. The rate capability of cells at 4.0 M concentration is shown in **Figure 3-9d**. Capacities remained constant at ~362 mAh/g_{sub-stack} from 0.3 – 1.0 mA/cm² (0.01 C – 0.04 C-rate; calculation in **Section 3.5.5**) and

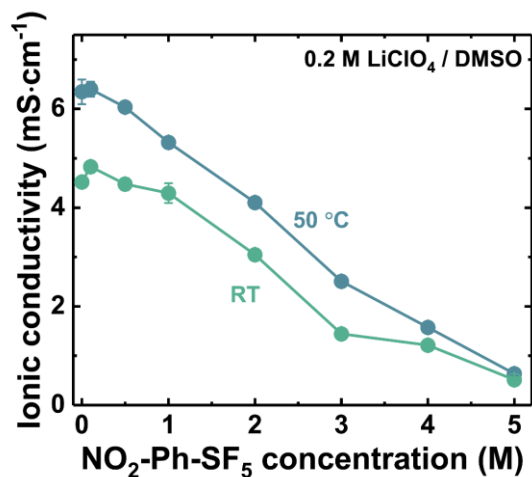


Figure 3-11 Ionic conductivity of NO₂-Ph-SF₅-containing electrolytes as a function of NO₂-Ph-SF₅ concentration at 50 °C and at room temperature (RT).

decreased moderately thereafter up to 3 mA/cm² (0.12 C), indicating excellent rate capability. Critically for primary battery applications, **Figure 3-12** shows that as-assembled Li–NO₂–Ph–SF₅ cells rested for 30 days at 50 °C exhibited no capacity loss upon subsequent discharge, and cells also exhibited negligible voltage fade upon interruption at partial depth-of-discharge and resting for 10–30 days, indicating good shelf-life characteristics.

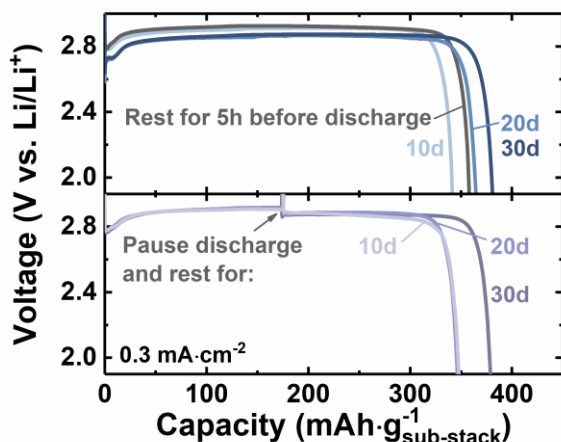


Figure 3-12 Shelf-life tests for Li–NO₂–Ph–SF₅ cells with 4 M NO₂–Ph–SF₅ / 0.2 M LiClO₄ / DMSO. The cells were rested for different timespans after assembly and prior to discharge (upper) or after partial discharge (lower).

To compare performance with state-of-the-art primary batteries, Li–CF_x cells were assembled and tested (**Figure 3-13**). The breakdown of the cell masses is shown in **Figure 3-14a**. Typical electrolyte-to-active solid mass fractions in commercial cells range from 0.7–1.3,^{241,242} a lean electrolyte loading that is challenging to achieve in-house. Consequently, Li–CF_x cells (20.4 ± 2.3 mg of CF_x, 11.5 ± 1.3 mg/cm² loading) were tested in a flooded electrolyte configuration but normalized assuming a 1:1 electrolyte:cathode mass ratio dictated by commercial standards. In Li–NO₂–Ph–SF₅ cells, the active material is in the liquid phase, hence design considerations favor

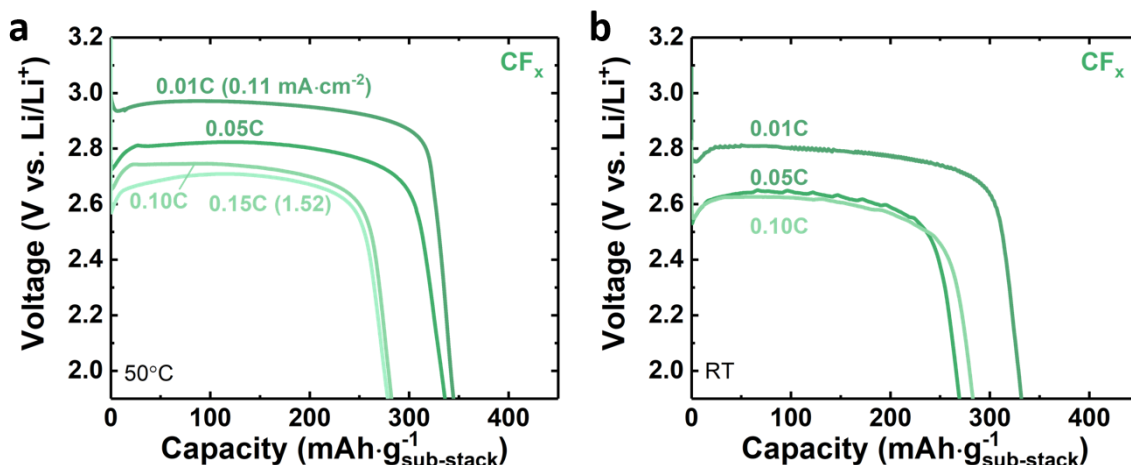


Figure 3-13 Discharge data of Li-CF_x cells at (a) 50 °C and (b) room temperature (RT). Sub-stack = CF_x + carbon + electrolyte + consumed Li.

a substantially larger electrolyte-to-solid ratio (carbon being electrochemically inactive) of ~8:1 w/w, with 5 mg/cm² of carbon and ~28 mg/cm² of NO₂-Ph-SF₅ for 4 M concentration. A Ragone plot in **Figure 3-14b** shows that Li-NO₂-Ph-SF₅ cells attain comparable sub-stack level performance to Li-CF_x cells at low power (~1000 Wh/kg_{sub-stack} at ~15 W/kg_{sub-stack}). These values compare to active-mass theoretical values of 1845 Wh/kg_{active} (Li-NO₂-Ph-SF₅) and 2050 Wh/kg_{active} (Li-CF_x), which, in contrast to sub-stack metrics, omit inactive electrolyte/carbon (**Table 1-1** and **Table 3-2**). The numbers indicate the following: First, both cell formulations, as expected, exhibit significant decreases in gravimetric energy when inactive masses (electrolyte + carbon) are accounted for on the more-realistic sub-stack basis. Second, Li-NO₂-Ph-SF₅ cells with liquid reactants exhibit proportionally higher active mass utilization, which in turn enables comparable or higher cell energies in practice. This gain arises from the ability to minimize dead weight of electrolyte compared to Li-CF_x (both cells utilize comparable inactive C). Moreover, Li-NO₂-Ph-SF₅ cells show advantages over Li-CF_x at moderate powers (50–100 W/kg_{sub-stack}) which is attributed to facile kinetics in the liquid phase. These gains diminish at higher powers

(>150 W/kg_{sub-stack}) for this particular formulation due to limitations of ionic conductivity of NO₂-Ph-SF₅-based electrolytes, which will require future studies to engineer and optimize.

Table 3-2: Performances of Li-*R-Ph-SF*₅ batteries at 50 °C

Cathode	# e ⁻ / reactant	Theoretical Capacity Q (mAh/g)		Voltage (V)	Active Material Energy <i>Practical V × Theoretical Q</i>	
		Cathode <i>Active only</i>	Cathode+Li <i>Active only</i>		Gravimetric (Wh/kg)	Volumetric (Wh/L)
<i>p</i> -NO ₂ -Ph-SF ₅ ^a	8	646/215/861	553/204/704	2.9/2.1/2.6	1605/430/1845	1995/620/2165
<i>m</i> -NO ₂ -Ph-SF ₅ ^a	8	646/215/861	553/204/704	2.8/2.2/2.6	1550/450/1830	1925/650/2145
<i>p</i> -I-Ph-SF ₅	6	487	433	2.5	1075	1680
Ph-SF ₅	6	788	654	2.8	1565	1790

^a Due to multiple voltage plateaus observed from NO₂-Ph-SF₅ discharge, performances are reported separately for high voltage (OCV-2.54 V), low voltage (2.54 V-1.9 V), and overall discharge (OCV-1.9 V) following the format: high voltage/low voltage/overall discharge.

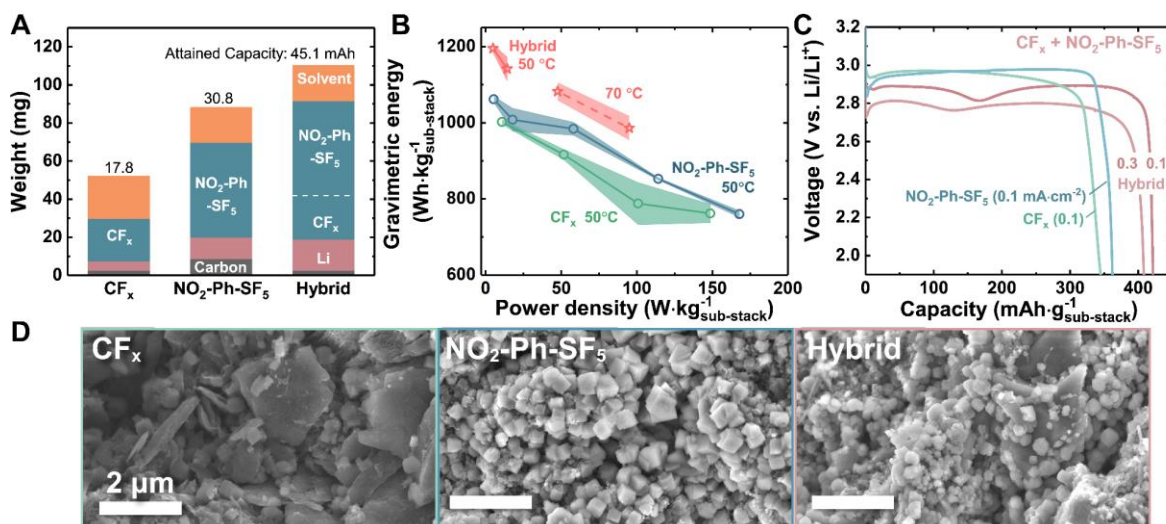


Figure 3-14. Energy and power of primary Li batteries with fluorinated cathodes and catholytes. (a) Weight breakdown of cell components in Li-CF_x, Li-NO₂-Ph-SF₅, and hybrid cells. **(b)** Ragone plot comparing rate performance of the same cells. Average value and error bar (representing standard deviation) were based on three cells each. **(c)** Rate performance of hybrid cells using CF_x as solid cathode and 4 M NO₂-Ph-SF₅ / 0.2 M LiClO₄ / DMSO as catholyte. ‘Sub-stack’ for Li-CF_x denotes CF_x + electrolyte + carbon + consumed Li; for hybrid cells, the weight of NO₂-Ph-SF₅ is also included. **(d)** SEM of discharged cathodes from each cell type (0.3 mA/cm² for Li-NO₂-Ph-SF₅ and hybrid cells, 0.1 mA/cm² for Li-CF_x).

3.3.3 Hybrid solid-liquid cell design

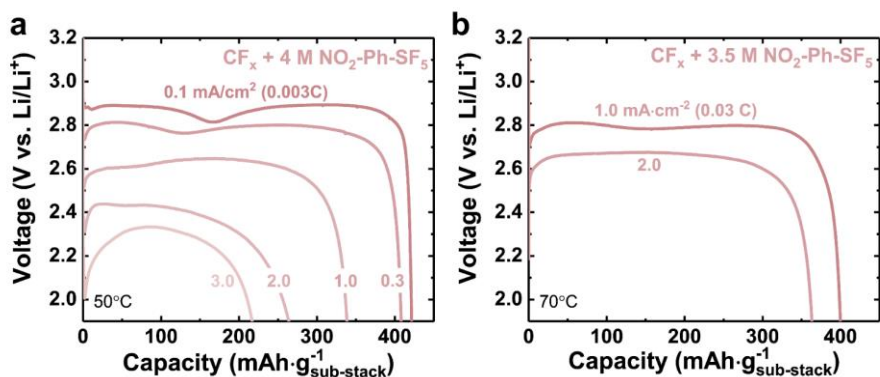


Figure 3-15 Rate performance of hybrid cells using CF_x as solid cathode and $\text{NO}_2\text{-Ph-SF}_5 / 0.2 \text{ M LiClO}_4 / \text{DMSO}$ as electrolyte. Cells were discharged with (a) $4 \text{ M NO}_2\text{-Ph-SF}_5$ at 50°C , and (b) $3.5 \text{ M NO}_2\text{-Ph-SF}_5$ at 70°C .

The chemical compatibility and voltage matching of $\text{Li-NO}_2\text{-Ph-SF}_5$ and Li-CF_x creates new possibilities to design hybrid cell concepts that surpass the gravimetric energy of any known formulation.^{243,244} To demonstrate this, we designed cells containing a $\text{NO}_2\text{-Ph-SF}_5\text{:CF}_x$ mass ratio of $\sim 2\text{:}1$ (**Figure 3-14a**). The total sub-stack percentage of active materials was $\sim 80\%$, compared to the Li-CF_x ($\sim 50\%$) or $\text{Li-NO}_2\text{-Ph-SF}_5$ cells ($\sim 70\%$). A gravimetric capacity of $421 \text{ mAh/g}_{\text{sub-stack}}$ was obtained at 0.1 mA/cm^2 with the hybrid cell, significantly higher than the respective individual cells ($\leq 362 \text{ mAh/g}_{\text{sub-stack}}$, **Figure 3-14c**). The gravimetric energy, reaching $1195 \text{ Wh/kg}_{\text{sub-stack}}$ at $5 \text{ W/kg}_{\text{sub-stack}}$, represents a $\sim 20\%$ improvement over Li-CF_x at the sub-stack level (**Figure 3-14b**). SEM images (**Figure 3-14d**) of discharged cells showed formation of LiF crystallites on CF_x graphite flakes that were not present in CF_x -only cells, further confirming utilization of both solid and liquid capacities. We note that the hybrid cell utilized a commercial CF_x powder blend optimized for conventional cell performance and does not necessarily provide optimal surface area to accommodate $\text{NO}_2\text{-Ph-SF}_5$ discharge, which may be improved through

future development. Indeed, higher rates in the hybrid cell configuration led to decreasing capacity due to premature passivation by LiF (**Figure 3-15a**). Thus, as a second example of hybrid cell design for higher power, reactant concentrations were lowered to 3.5 M and temperatures were increased to 70 °C. At 2.0 mA/cm², a capacity of 363 mAh/g_{sub-stack} was obtained, corresponding to a 38% capacity increase than that obtained at 50 °C with 4 M NO₂-Ph-SF₅ (**Figure 3-15**).

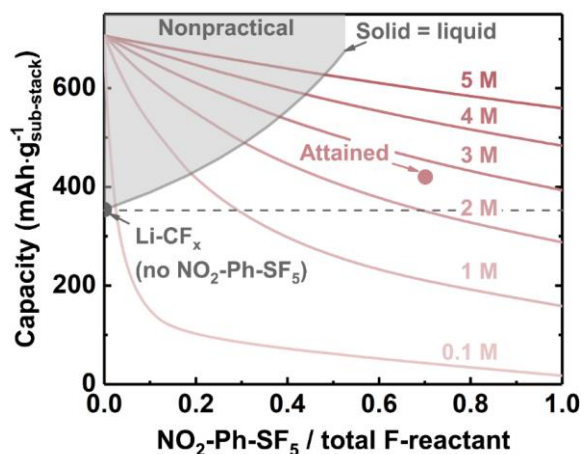


Figure 3-16 Projection of theoretical capacity of hybrid cells with different weight ratios (see **Section 3.5.6** for associated discussion and detailed calculations). The shaded region, where the weight of solid components (CF_x + C) is higher than that of liquids, is deemed as non-practical because it is difficult for electrolyte to sufficiently wet the electrode under this condition. The maximum attained capacity in Figure 3-14c (with 4 M NO₂-Ph-SF₅) is labeled as “attained”.

We emphasize that these metrics, which demonstrate several pathways to exceed performance of commercial CF_x at mild temperature (50–70 °C), were tested in cells subjected to limited optimization. Further improvements in cell performance are envisioned possible with continued development, including cell conditions that can finely-tune electrolyte-to-solid ratios. The theoretical expected energy of a hybrid cell is computed in **Figure 3-16** and indicates that

maximum performance for 5 M reactant occurs around a $\text{NO}_2\text{-Ph-SF}_5\text{:CF}_x$ mass ratio of 1:1.1 and $627 \text{ mAh/g}_{\text{sub-stack}}$, a $\sim 50\%$ increase compared to the above numbers attained in practice so far.

3.3.4 Temperature effects

Additional efforts are needed to realize competitive operation of fluorinated liquid cathode batteries at room temperatures. Without heating, the high-voltage discharge plateau exhibits truncation and capacities that are 15–20% lower (**Figure 3-17**). Rate effects are also more severe (**Figure 3-18**), which may result from hindered transport, *e.g.* decreased diffusivity of reactant or LiF product solubility, noting that ionic Li conductivities were not strongly sensitive to temperature (**Figure 3-11**). Future improvements lie with all aspects of electrolyte engineering, including reactant, solvent, and salt to balance the demands for high reactant solubility, high salt solubility, and low viscosities throughout discharge. Second, cathode engineering to tailor active surface and

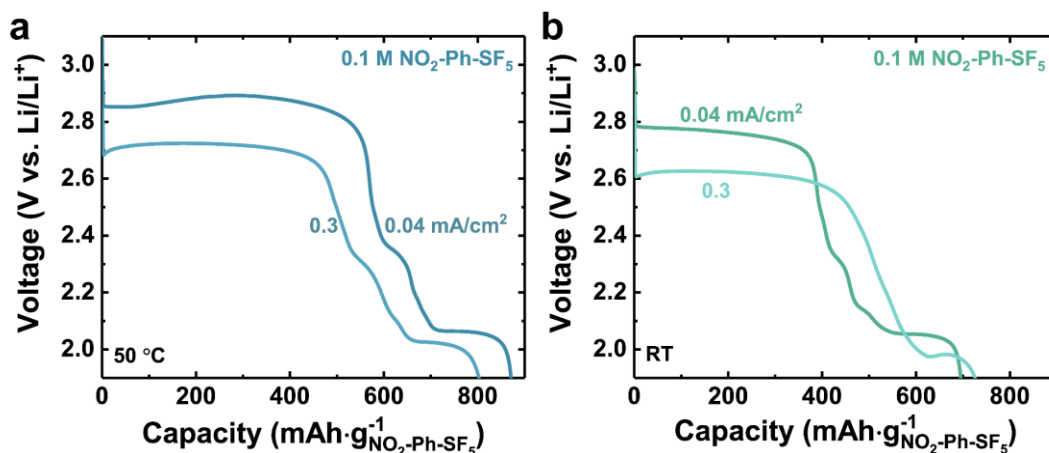


Figure 3-17 Low concentration discharge of $\text{NO}_2\text{-Ph-SF}_5$ at (a) 50°C and (b) RT. All cells were discharged with $0.1 \text{ M NO}_2\text{-Ph-SF}_5 / 0.1 \text{ M LiClO}_4 / \text{DMSO}$.

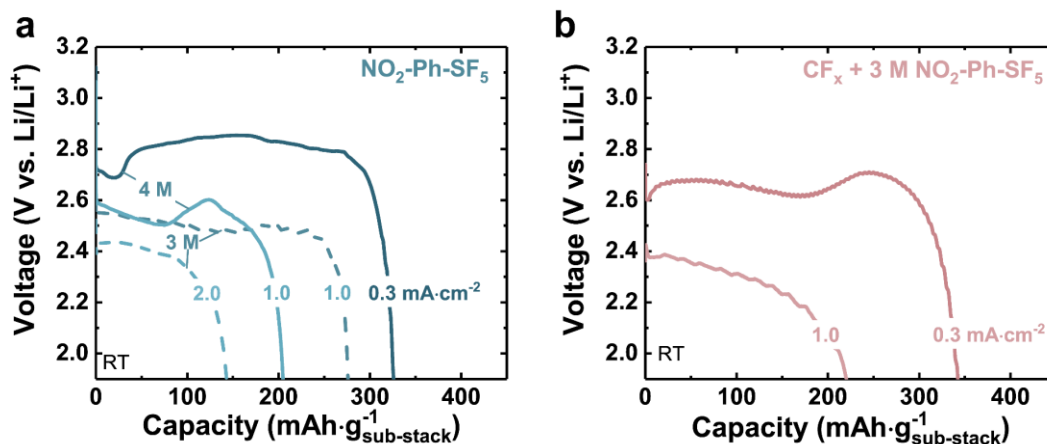


Figure 3-18 Room temperature discharge of (a) Li-NO₂-Ph-SF₅ and (b) hybrid cells. Cells in a utilized 4 or 3 M NO₂-Ph-SF₅ / 0.2 M LiClO₄ / DMSO as catholyte, while cells in b utilized 3 M NO₂-Ph-SF₅ / 0.2 M LiClO₄ / DMSO.

pore sizes may help to accommodate larger amounts of LiF prior to passivation, allowing improved performance at lower temperatures. Temperature effects on the Li anode should also not be overlooked: at 50 °C, Li anodes from Li-NO₂-Ph-SF₅ cells rested for one week showed, *via* SEM and electrochemical impedance spectroscopy, growth and stabilization of a ~200 nm thick solid electrolyte interphase (SEI) consisting primarily of LiF (**Figure 3-19**). This SEI can effectively protect the Li anode against sustained parasitic reactivity. Note that a 200 nm thick interface, assuming it to consist entirely of LiF, corresponds to ~0.72 μmol reactant consumed (assuming 5 F⁻/reactant), *i.e.* 0.36% of total reactant or 0.15 mAh capacity lost. At room temperature, LiF particles on Li were sparser and smaller, even after resting for one week (**Figure 3-20**). The results suggest that Li anode engineering to favor optimal SEI growth is a compelling future direction.

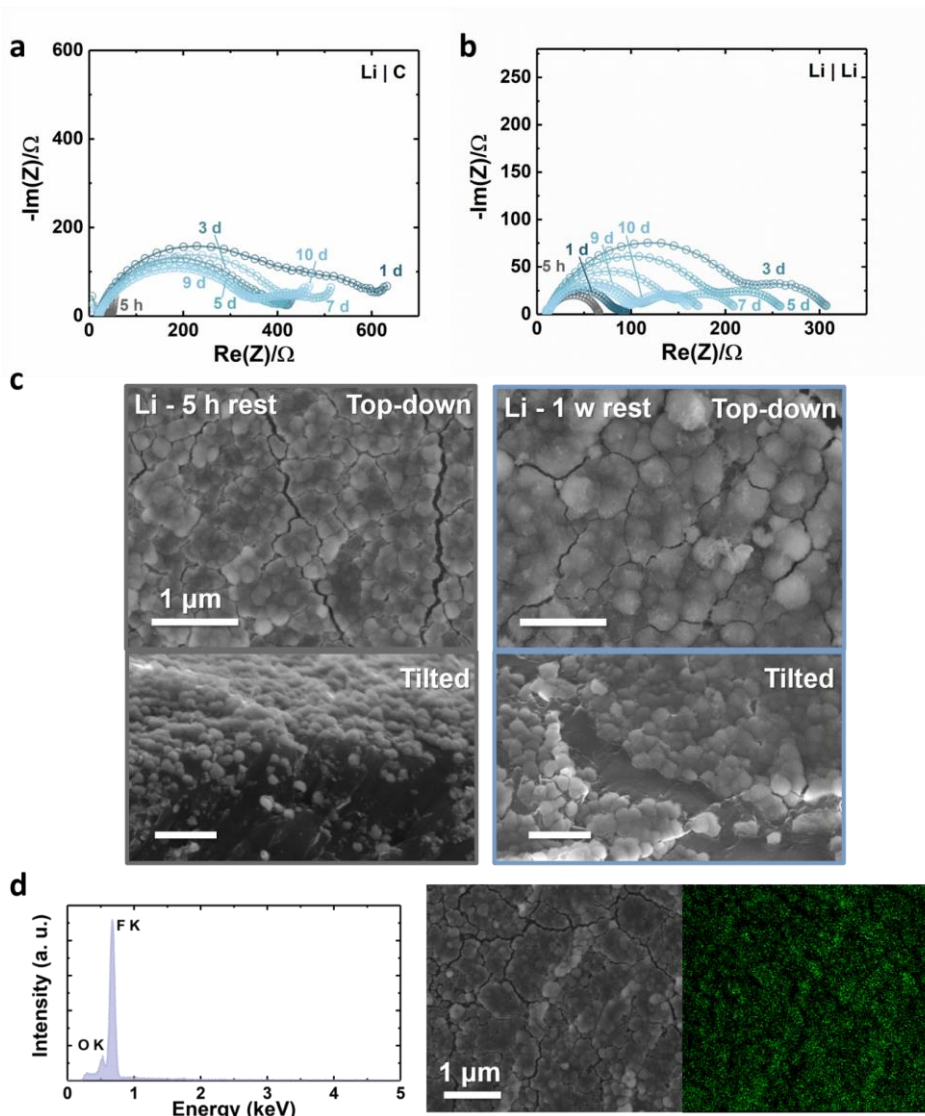


Figure 3-19 Electrochemical impedance spectra evolution of (a) a Li|C cell and (b) a Li|Li half-cell after different resting times at 50 °C. Cells utilized 4 M NO₂-Ph-SF₅ / 0.2 M LiClO₄ / DMSO as catholyte. (c) SEM of a Li anode after resting at 50 °C in Li-NO₂-Ph-SF₅ (4 M) Swagelok cells with 50 μL electrolyte for 5 h or 1 week. (d) EDX mapping and elemental distribution of a Li anode after resting in Li-NO₂-Ph-SF₅ cells for 5 h at 50 °C. The SEM demonstrates conformal formation of a thin (~100 nm) LiF layer on the Li surface after 5-hour resting. EDX confirmed the layer to consist primarily of F (as LiF) with negligible amounts of other elements (*e.g.* no S or N; note that Li is too light to be detectable from EDX).

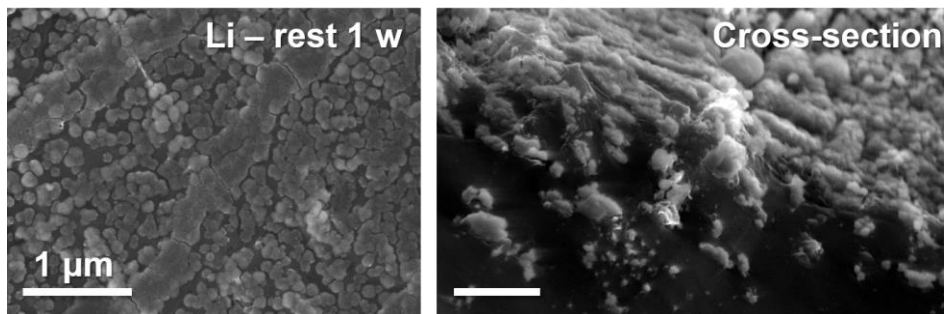


Figure 3-20 SEM image of a Li anode after resting at room temperature for one week in Li-NO₂-Ph-SF₅ cell (4 M reactant), showing sparser SEI formation.

3.4 Conclusions

Through molecular design, advanced catholytes have been developed that successfully exploit the wide oxidation state window of S in non-metal-containing, lightweight reactants. These catholytes yield high capacities and permit high cell active mass loadings, enabling the gravimetric energy of all known Li primary batteries to be exceeded at a sub-stack level. Handles to further tailor capacity, voltage, and kinetics in fluorosulfur catholytes at a fundamental level include number and positioning of fluoride/halide ligands, chemical and electronic structure of the aromatic group, its linker to the -SF₅ moiety, and R-group functionality. At the cell level, the wide landscape for electrolyte design and solid-liquid balancing highlight significant remaining room for improvement. Although lowering the temperature requirements is attractive, many battery technologies operate at mildly elevated temperatures either intrinsically (due to operation requirements)⁵ or reach such temperatures due to self-heating;²⁴⁵ there is no intrinsic limitation identified at present to prevent competitive metrics at room temperature if key challenges can be addressed. Looking ahead, learning how to adapt S-based molecular redox to achieve both large oxidation state changes and reversibility is tantalizing and remains a grand challenge for future high-energy battery development.

3.5 Appendix for Chapter 3

3.5.1 Estimation of S oxidation state in *R-Ph-SF₅*

To estimate the oxidation state (OS) of sulfur, the localized orbital bonding analysis (LOBA) method was utilized with different localized molecular orbital (LMO) thresholds as indicated in the table. If the atomic contribution to one LMO is higher than the selected threshold, electrons in the LMO are treated as originating from the atom (here, S). Typically, a threshold of 50% or 60% is used.²¹² The OS of S in *R-Ph-SF₅* is found to be around 4–6 and is relatively sensitive to the LMO threshold, which can be attributed to the complex bonding nature (mixed ionic and covalent). Consequently, LOBA analysis provides an estimate of electronic structure although is not precise here for determining OS of S in *R-Ph-SF₅*.²⁴⁶

3.5.2 Calculation for electron transfer number

The average number of electrons transferred per molecule (n_e) was calculated following equation:

$$n_e = \frac{Q * 3.6 / F}{V \times 10^{-6} \times c}$$

In which:

V —total electrolyte volume (μL); typical electrolyte volume was 50 μL .

c —concentration of reactant molecule (M)

Q —discharge capacity (mAh)

F —Faraday constant (96485 C/mol)

The calculation assumes all electrons are consumed by reduction of the liquid fluorinated reactant.

3.5.3 Calculation for theoretical capacities in Figure 3-9c

The sub-stack level theoretical capacities of NO₂-Ph-SF₅ ($Q_{theo}^{sub-stack}$, units of mAh/g) listed in Figure 3-9c are calculated using the following equation:

$$Q_{theo}^{sub-stack} = \frac{c \times n_e \times F / 3.6 \times 10^{-3}}{\rho_{electrolyte} + c \times n_e \times M_{Li} \times 10^{-3}}$$

In which:

c —concentration of reactant molecule (M)

n_e —number of electron transfer per molecule (assumed to be 8)

F —Faraday constant (96485 C/mol)

M_{Li} —Molar mass of Li (6.9 g/mol)

$\rho_{electrolyte}$ —density of electrolyte (g/mL). This is calculated using the density of DMSO (ρ_{DMSO} , 1.1 g/mL)²²⁶ and NO₂-Ph-SF₅ ($\rho_{NO_2-Ph-SF_5}$, 1.6 g/mL measured in the liquid state, see **Section 3.2**) using the equation below (where $V_{component}$ is the volume of the indicated component (mL), and M_m is the molar mass of NO₂-Ph-SF₅, 249.16 g/mol):

$$\begin{cases} \text{Electrolyte mass: } m_{electrolyte} = \rho_{electrolyte} \times V_{electrolyte} = \rho_{NO_2-Ph-SF_5} \times V_{NO_2-Ph-SF_5} + \rho_{DMSO} \times V_{DMSO} \\ \text{NO}_2\text{-Ph-SF}_5 \text{ mass: } m_{NO_2-Ph-SF_5} = \rho_{NO_2-Ph-SF_5} \times V_{NO_2-Ph-SF_5} = c \times V_{electrolyte} \times 10^{-3} \times M_{NO_2-Ph-SF_5} \\ V_{electrolyte} = V_{NO_2-Ph-SF_5} + V_{DMSO} \end{cases}$$

$$\Rightarrow \rho_{electrolyte} = c \times M_{NO_2-Ph-SF_5} \times 10^{-3} + \rho_{DMSO} \times (1 - c \times M_{NO_2-Ph-SF_5} \times 10^{-3} / \rho_{NO_2-Ph-SF_5})$$

The electrolyte salt (LiClO₄) has negligible influence on the electrolyte density (<2 wt% of total electrolyte), thus is not included in the calculation.

Calculation examples are shown below:

c (M)	$\rho_{electrolyte}$ (g/mL)	NO ₂ -Ph-SF ₅ weight ratio in electrolyte (α) ^a	n_e	Theoretical capacity $Q_{theo}^{sub-stack}$ (mAh/g _{sub-stack}) ^b
0.1	1.11	2%	8	19
1.0	1.18	21%	8	174
2.0	1.26	40%	8	314
3.0	1.33	56%	8	429
4.0	1.41	71%	8	526
4.5	1.45	77%	8	568
5.0	1.49	84%	8	607
6.4	1.60	100%	8	703

$$^a \alpha = c \times M_{NO_2-Ph-SF_5} \times 10^{-3} / \rho_{electrolyte}$$

^b The unit mAh·g_{sub-stack}⁻¹ represents mAh/g_{NO₂-Ph-SF₅+electrolyte+C+Li}. The weight of carbon is assumed to be 0, because it is not intrinsic to the theoretical performance.

3.5.4 Comment on electrolyte-to-cathode weight ratio

For Li-CF_x and Li-NO₂-Ph-SF₅ cells fabricated in house, in the absence of optimized vacuum filling to enhance pore-infiltration of electrolyte, 50 μ L was found to be the minimum electrolyte volume needed to ensure sufficient wetting of the electrodes. Further reducing the electrolyte amount resulted in decreased utilization of active materials. The weight of 50 μ L electrolyte, depending on the NO₂-Ph-SF₅ concentration, ranges from ~55 mg to ~75 mg (from 0 M to 5 M).

To form a fair comparison with the Li-NO₂-Ph-SF₅ cell (with 4 M reactant, typical attained capacity of ~17 mAh/cm²), comparable cell capacities are ideal, meaning a CF_x loading of ~ 20 mg/cm² is ideal. However, given the electrolyte pore filling issue mentioned above, and the limited control over pressing pressure when fabricating CF_x cathodes in-house, an average CF_x loading of

11.5±1.3 mg/cm² was used as CF_x cathodes with higher loading exhibit less active material utilization (<90% of the theoretical capacity), and thus underestimate CF_x performance. The CF_x performance values reported in this manuscript are therefore conservative as they will overestimate performance obtainable with higher mass loadings commensurate with NO₂-Ph-SF₅ loading.

3.5.5 C rate calculation

Theoretical capacity of NO₂-Ph-SF₅. The theoretical capacity of NO₂-Ph-SF₅ reactant $Q_{theo}^{NO_2-Ph-SF_5}$ is calculated by the following equation:

$$Q_{theo}^{NO_2-Ph-SF_5} = \frac{n_e \times F / 3.6}{M_{NO_2-Ph-SF_5}} = \frac{8 \times 96485 / 3.6}{249.16} = 861 \text{ mAh} \cdot \text{g}_{NO_2-Ph-SF_5}^{-1}$$

where n_e is the number of electron transfer per NO₂-Ph-SF₅ and is assumed to be 8; $M_{NO_2-Ph-SF_5}$ is the molar mass of NO₂-Ph-SF₅ (249.16 g/mol); F is Faraday constant (96485 C/mol).

Theoretical capacity of CF_x. The theoretical capacity of CF_x ($Q_{theo}^{CF_x}$) can be calculated using same method with x assumed to be 1 (*i.e.* CF₁), as equation:

$$Q_{theo}^{CF_x} = \frac{n_e \times F / 3.6}{M_{CF_1}} = \frac{1 \times 96485 / 3.6}{31} = 865 \text{ mAh} \cdot \text{g}_{CF_x}^{-1}$$

where n_e is for CF_x is 1, and the molar mass of CF_x (or CF₁, M_{CF_1}) is 31 g/mol.

C rate calculation. The C rate is calculated by equation:

$$\text{C rate} = \frac{I}{m_{NO_2-Ph-SF_5} \cdot Q_{theo}^{NO_2-Ph-SF_5} + m_{CF_x} \cdot Q_{theo}^{CF_x}}$$

where:

I – discharge current (mA)

$m_{NO_2-Ph-SF_5}$ – weight of NO₂-Ph-SF₅ in cell (g)

m_{CF_x} – weight of CF_x in cell (g)

Calculation examples are shown below:

Cell type	$m_{NO_2-Ph-SF_5}$ (g)	m_{CF_x} (g)	Total theoretical capacity (mAh)	Current I (mA)	Areal current (mA·cm ⁻²)	C rate
4 M NO_2 -Ph- SF_5 (Figure 3-9)	0.050	0	42.9	0.07	0.04	0.002
	0.050	0	42.9	0.18	0.1	0.004
	0.050	0	42.9	0.53	0.3	0.012
	0.050	0	42.9	1.77	1	0.041
	0.050	0	42.9	3.54	2	0.083
	0.050	0	42.9	5.31	3	0.124
CF_x (Figure 3-13)	0	0.022	18.7	0.19	0.11	0.010
	0	0.017	15.0	0.75	0.42	0.050
	0	0.022	19.4	1.94	1.10	0.100
	0	0.017	14.6	2.18	1.23	0.150
4 M NO_2 -Ph- SF_5 + CF_x (Figure 3-14)	0.050	0.022	61.9	0.18	0.1	0.003
	0.050	0.017	57.8	0.53	0.3	0.009
3.5 M NO_2 -Ph- SF_5 + CF_x (Figure 3-15)	0.044	0.022	56.7	1.77	1	0.031
	0.044	0.020	54.5	3.54	2	0.065

3.5.6 Calculation for capacity projection for hybrid cells (Figure 3-16)

The projected sub-stack capacity Q_{hybrid} (mAh·g $_{NO_2-Ph-SF_5+CF_x+electrolyte+C}^{-1}$) of the hybrid cell was calculated following equation:

$$Q_{hybrid} = \frac{Q_{theo}^{NO_2-Ph-SF_5} \cdot m_{NO_2-Ph-SF_5} + Q_{theo}^{CF_x} \cdot m_{CF_x}}{m_{NO_2-Ph-SF_5} + m_{CF_x} + m_{DMSO} + m_C + m_{Li}}$$

where:

$m_{NO_2-Ph-SF_5}$ – weight of NO_2 -Ph- SF_5 in cell (g)

m_{CF_x} – weight of CF_x in cell (g)

$$Q_{theo}^{NO_2-Ph-SF_5} = 861 \text{ mAh/g}_{NO_2-Ph-SF_5}$$

$$Q_{theo}^{CF_x} = 865 \text{ mAh/g}_{CF_x}$$

m_{DMSO} – weight of DMSO (g); When $NO_2-Ph-SF_5$ concentration >0 , m_{DMSO} is related with $m_{NO_2-Ph-SF_5}$, following: the total weight of liquid = $m_{NO_2-Ph-SF_5} + m_{DMSO} = m_{NO_2-Ph-SF_5} / \alpha$ (α is the $NO_2-Ph-SF_5$ weight ratio in electrolyte, with exact values listed in **Section 3.5.3**). Therefore, $m_{DMSO} = (1/\alpha - 1)m_{NO_2-Ph-SF_5}$

m_c – weight of carbon, fixed at 10% of total weight of liquid (catholyte or, for CF_x -only cells, electrolyte) in all experiments and calculations. The inclusion of carbon is to ensure basic electronic conductivity and sufficient active surface for LiF growth.

m_{Li} – weight of Li, which is determined by the total theoretical capacity:

$$m_{Li} = (Q_{theo}^{NO_2-Ph-SF_5} \cdot m_{NO_2-Ph-SF_5} + Q_{theo}^{CF_x} \cdot m_{CF_x}) \times \frac{3.6 \times M_{Li}}{F}, \text{ (molar mass of Li } (M_{Li})=6.9 \text{ g/mol).}$$

Set x to be the weight ratio of $NO_2-Ph-SF_5$ /total F-reactant (*i.e.* $x = \frac{m_{NO_2-Ph-SF_5}}{m_{NO_2-Ph-SF_5} + m_{CF_x}}$ or

$m_{CF_x} = \frac{1-x}{x} m_{NO_2-Ph-SF_5}$), then Q_{hybrid} can be expressed as:

$$Q_{hybrid} = \frac{Q_{theo}^{NO_2-Ph-SF_5} \cdot m_{NO_2-Ph-SF_5} + Q_{theo}^{CF_x} \cdot \frac{1-x}{x} m_{NO_2-Ph-SF_5}}{m_{NO_2-Ph-SF_5} + \frac{1-x}{x} m_{NO_2-Ph-SF_5} + \left(\frac{1}{\alpha} - 1\right) m_{NO_2-Ph-SF_5} + 0.1 \cdot \frac{m_{NO_2-Ph-SF_5}}{\alpha} + m_{Li}}$$

Therefore,

$$Q_{hybrid} = \frac{Q_{theo}^{NO_2-Ph-SF_5} + Q_{theo}^{CF_x} \cdot \frac{1-x}{x}}{\frac{1-x}{x} + \frac{1.1}{\alpha} + \left(Q_{theo}^{NO_2-Ph-SF_5} + Q_{theo}^{CF_x} \cdot \frac{1-x}{x}\right) \frac{3.6 \times M_{Li}}{F}}$$

For each NO₂-Ph-SF₅ concentration (>0), α is determined, and Q_{hybrid} as a function of x is plotted (**Figure 3-16**).

A constraint was assumed to limit practical cell assembly, namely that the mass of liquid in the cell cannot be substantially lower than the mass of solids given poor wetting and thus decreasing solid utilization at low liquid amounts. For this boundary condition where solid mass = liquid mass, i.e. $m_{CF_x} + m_C = m_{NO_2-Ph-SF_5} + m_{DMSO}$, the value of α can be expressed as a function of x , following:

$$\frac{1-x}{x} m_{NO_2-Ph-SF_5} + 0.1 \cdot \frac{m_{NO_2-Ph-SF_5}}{\alpha} = m_{NO_2-Ph-SF_5} + \left(\frac{1}{\alpha} - 1\right) m_{NO_2-Ph-SF_5}$$

$$\frac{1-x}{x} = \frac{1-0.1}{\alpha}$$

$$\alpha = \frac{0.9x}{1-x}$$

For Li-CF_x cells with no NO₂-Ph-SF₅, the boundary condition solid=liquid is still applicable with $\alpha = x = 0$. In this case: $m_{CF_x} + m_C = m_{DMSO}$, and $m_C = 0.1 \cdot m_{DMSO}$, thus

$$m_{DMSO} = m_{CF_x} / 0.9.$$

Thus, Q_{hybrid} can be expressed as:

$$Q_{hybrid} = \frac{Q_{theo}^{CF_x} \cdot m_{CF_x}}{m_{CF_x} + m_{DMSO} + 0.1 \cdot m_{DMSO} + m_{Li}} = \frac{Q_{theo}^{CF_x} \cdot m_{CF_x}}{m_{CF_x} + 1.1/0.9 \cdot m_{CF_x} + Q_{theo}^{CF_x} \cdot m_{CF_x} \frac{3.6M_{Li}}{F}}$$

$$Q_{hybrid} = \frac{Q_{theo}^{CF_x}}{1 + \frac{1.1}{0.9} + \frac{Q_{theo}^{CF_x} \times 3.6 \times M_{Li}}{F}} = 354 \text{ mAh} \cdot \text{g}^{-1}_{\text{sub-stack}}$$

Chapter 4: Tuning C–F Bond Activity in Perfluoroalkylated Reactants to Enable Multi-Electron Carbon Reduction

Reproduced in part with permission from Gao, H., Sevilla, A., & Gallant, B. M. (2022). Lithium Primary Batteries Employing Multi-Electron Carbon-Fluorine Bond Cleavage in Perfluoroalkylated Reactants. *J. Electrochem. Soc.*, 169, 030535, Copyright 2022.

4.1 Introduction

Lithium–carbon monofluoride (Li-CF_x) primary batteries have the highest theoretical energy densities ($2180 \text{ Wh/kg}_{\text{active material}}$)²⁴⁷ among all battery chemistries, and exhibit gravimetric energy densities up to 800 Wh/kg in packaged cells.²⁸ As introduced in **Section 1.2.2**, the solid-state nature of CF_x ($0 < x \leq 1.3$) particles provides excellent safety and shelf stability, but also contributes to limited rate performance given low electronic conductivity.²⁹ To improve high-power performance, efforts have focused on optimizing the cathode architecture, for example by adding carbon nanotubes (CNTs) to form composites with CF_x that increase the surface area and electronic conductivity.³⁶ At a fundamental level, first principles and experimental studies were conducted to understand the CF_x discharge process,^{40,41} and the origin of the overpotential was explained *via* solvent-mediated³⁵ and/or edge-propagation mechanisms.^{38,39} Other efforts focused on sub-fluorinated graphite with decreased F content ($0.33 < x < 0.66$), to induce some electronically conductive domains, trading energy density for power.⁴⁴

Increasing the F content, on the other hand, is an appealing approach to surpass the present energy density of CF_x materials by widening the accessible oxidation states of carbon (*i.e.* > 1 electron transfer per carbon). However, the electrochemical performance of super-stoichiometric CF_x ($x > 1$) remains underexplored due to synthetic difficulties (requiring temperatures $> 600 \text{ }^\circ\text{C}$)⁴² and limited electronic conductivity of such materials: as x increases, C–F bond length decreases

from ~0.3 nm to ~0.14 nm, when x reaches 1, where the material becomes highly insulating.²⁴⁸ Therefore, although x can synthetically reach as high as 1.3 while still retaining a layered lattice structure of the underlying graphite,²⁴⁹ x in commercial Li-CF_x batteries is limited to ~1 (theoretical capacity = 865 mAh/g) or below.²⁵⁰

Further increase in F content, *e.g.* to 2 or higher, has in general been considered nonviable due to a combination of the material becoming exceedingly electronically insulating and electrochemically inert. A common example is Teflon (C₂F₄)_n, which is known for its chemical and electrochemical stability owing to the high C-F bond energy in covalent perfluoroalkyl groups (R_F = C_nF_{2n+1}, 485 kJ/mol).¹² Electrochemical reduction of covalent C-F bonds occurs in relatively rare circumstances such as in specially substituted acetanilides (such as C₆H₅NHCOCF₃ in 0.1 M tetraethylammonium chloride/ethanol electrolyte)²⁵¹ and polymers (such as polytetrafluoroethylene in tetrabutylammonium tetrafluoroborate / dimethylformamide electrolyte)²⁵² at very low potentials (approximately -2.1 or -2.0 V vs. saturated calomel electrode, respectively). Another example is the reduction of C-F bond in fluoroethylene carbonate (FEC), which occurs at ~0.8 V vs. Li/Li⁺ and thus has been used as the electrolyte in rechargeable Li metal batteries to facilitate the formation of F-rich solid electrolyte interphase.^{253,254} The electrochemical activity of some perfluoroalkyl iodides and bromides (R_FX, X = Br, I), common building blocks for fluorinated chemical synthesis,²⁵⁵ have also been previously investigated *via* cyclic voltammetry in common aprotic solvents, including dimethylformamide, dimethyl sulfoxide (DMSO), acetonitrile, and benzonitrile with tetraalkylammonium or (more rarely) Li⁺-containing salts, but bonds within R_F are generally believed to be stable upon reduction within the electrolyte stability window. Consequently, only C-X bond cleavage was reported, leading to R_F[·] (radical) and I⁻ or Br⁻ as leaving groups.²⁵⁶⁻²⁵⁸

Herein, the electrochemical characteristics of these perfluoroalkyl iodides (termed ‘CFI’) were investigated in the context of Li cells as a first step to examine possible strategies for tailoring the defluorination of $R_F X$ reactants having F/C ratios exceeding 1. Although such high fluorination degrees correspond to electronically insulating materials in solid CF_x as discussed, the reactants examined herein are liquids, thus they provide a framework of interest to test whether F/C ratio limitations are intrinsic or can be overcome at a molecular scale. Assuming electron transfer proportional to the sum total of F and non-F halogen atoms,²⁵⁹ the theoretical capacities of the reactants approach (though do not exceed) the theoretical capacity of CF_x at $x = 1$: *e.g.* 841 mAh/g ($C_6F_{13}I$, 14 e^- transfer); 775 mAh/g (C_4F_9I , 10 e^- transfer); and 724 mAh/g (C_3F_7I : 8 e^- transfer), with the higher gravimetric capacities corresponding to longer fluoroalkyl tails. The relatively lower capacities than CF_x are due to the additional weight of I. Thus, they are of potential interest for use as standalone catholytes in Li cells with carbon cathodes, particularly if high discharge rates can be achieved; or for cell hybridization, *i.e.* as catholytes for use with solid CF_x cathodes, to attain higher energy densities than CF_x alone can achieve. Determining the realistically accessible capacity of CFI reactants under both non-aggressive (low reactant concentration, low rate) and more realistic cell discharge conditions (higher concentration and rate) was a core objective of this work. The role of additional parameters, such as solvent properties and discharge temperature, are also examined. Under ideal conditions (0.1 M reactant, 0.02 mA/cm²), a high degree (>60%) of R_F defluorination is possible with attractive discharge voltages starting at a maximum of ~2.9 V vs. Li/Li⁺, but capacity decreases when either rate or reactant concentration are increased. Possible limiting mechanisms are discussed. The results indicate future directions to tune C–F bond activity through intrinsic tailoring of reactant structures and defluorination pathways.

4.2 Experimental Methods

Chemicals and Materials. All chemicals, electrodes and cell-making materials were stored in the argon-filled glovebox (MBRAUN) after being dried. Dimethyl carbonate (DMC, >99.9%, Sigma-Aldrich), methyl(2,2,2-trifluoroethyl) carbonate (FEMC, >98%, TCI), C₆F₁₃I (99%, Sigma-Aldrich), C₄F₉I (98%, Sigma-Aldrich), CF₃-CFI-CF₃ (98%, Sigma-Aldrich), CF₃-CF₂-CF₂I (98%, Alfa Aesar), and C₆F₁₃Br (98%, Sigma-Aldrich) were used as received and stored inside the glovebox. Industrial synthesis routes to CFIs are listed in Ref. 260.

Galvanostatic Discharge. Two-electrode Swagelok-type Li-CFI cells were constructed in an argon glovebox, with the dried carbon cathodes and a 9 mm diameter disk of Li metal as anode (0.75 mm thick, 99.9% metals basis, Alfa Aesar), which was pre-stabilized by soaking in pure C₆F₁₃I at room temperature for at least three days prior to use. The separator (13 mm diameter glass fiber filter paper) was impregnated with 50–200 μ L electrolyte solution as indicated in the text. Cells were rested at open circuit voltage (OCV) for 5 h prior to galvanostatic discharge tests, which were carried out (BioLogic VMP3 potentiostat or MPG2 workstation) at the specified current density with a voltage window ranging from OCV (typically 3.2–3.4 V vs. Li/Li⁺) to a lower cutoff voltage of 1.9 V vs Li/Li⁺. For galvanostatic discharge at 50 °C, cells were placed inside an incubator (Mettler GmbH + Co. KG).

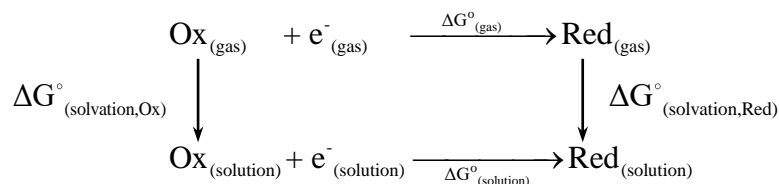
Li potential measurement. Measurements of the Li⁰/Li⁺ potential vs. a Ag/Ag⁺ reference were conducted in an argon-filled glovebox using a glass cell setup (Pine Research Instruments). The reference electrode consisted of a silver wire immersed in a ceramic-fritted glass tube filled with 0.01 M AgNO₃ and 0.1 M TBAClO₄ in acetonitrile. A piece of Li foil was inserted into the catholyte solution and its potential relative to Ag/Ag⁺ was measured until stabilization. The

standard potential of Ag/Ag⁺ reference is reported as 0.54 V vs. standard hydrogen electrode (SHE).²⁶¹ The intrinsic C₆F₁₃I reduction potential was obtained by converting the initial discharge potential obtained in **Figure 4-11c** (vs. Li/Li⁺) to the Ag/Ag⁺ basis. The C₆F₁₃I reduction potential was not directly measured in the 3-electrode cell because the glass cell requires large volume (~10 mL) of electrolyte, and thus requires significant amount of C₆F₁₃I (>2 mL for each measurement) and is not practical for FEMC.

Kinematic viscosity measurements. An Ubbelohde type suspended-level capillary viscometer (size 0B, Cannon Instrument) was used for the kinematic viscosity measurements at room temperature. Approximately 11 mL of electrolyte with varying amounts of solvent ratios was prepared, and measurements of the falling-time t_{fall} (s) of the liquid was measured using a stopwatch. The experiments were repeated multiple times to obtain an average and standard deviation (the relative standard deviations (RSD) of all measurements are very small, < 2%). Prior to use, the calibration constant κ was confirmed to be $(5.4 \pm 0.04) \times 10^{-3} \text{ mm}^2/\text{s}^2$ using the known kinematic viscosity of liquid water at room temperature (1.0 mm²/s). The kinematic viscosity ν (mm²/s) of the electrolytes was then obtained by the following equation: $\nu = \kappa \cdot t_{fall}$.

Density functional theory (DFT) calculations. All calculations were carried out using the Gaussian 03²¹¹ and Gaussian 09 program.²⁶² To obtain bond lengths, molecular geometries in the gas phase were optimized to minimized energy at the B3LYP/3-21G level for all CFI molecules. The calculation for theoretical defluorination potential of C₆F₁₃I was conducted on Gaussian 09 program²⁶² at the WB97XD/LANL2DZ level. The molecular geometries of the reactants and products (in reaction equations below) were optimized in the gas phase. Solvation calculations were conducted using the optimized geometries in gas phase with polarizable continuum model

(PCM). To calculate the Gibbs free energy change of the reaction in solution phase ($\Delta G^\circ_{(\text{solution})}$), Born-Haber cycle shown in the figure below was used:²⁶³



where $\Delta G^\circ_{(\text{gas})}$ is the Gibbs free energy change in gas phase, and $\Delta G^\circ_{(\text{solvation, Ox})}/\Delta G^\circ_{(\text{solvation, Red})}$ are the solvation energy of the reactants/products, respectively. The defluorination product (in addition to LiF) was assumed to be $\text{C}_6\text{F}_{12}\text{I}$, with the C–F bond adjacent to the C–I being reduced. Two different states of LiF were considered: (1) LiF dissolved in electrolyte solution as contact ion-pair: $\text{C}_6\text{F}_{13}\text{I}_{(\text{solution})} + \text{Li}^+_{(\text{solution})} + \text{e}^- \rightarrow \text{C}_6\text{F}_{12}\text{I}_{(\text{solution})} + \text{LiF}_{(\text{solution})}$, $E^\circ = 3.0 \text{ V vs. Li/Li}^+$; (2) LiF in solid phase, where experimental data for LiF formation was utilized:²⁶⁴ $\text{C}_6\text{F}_{13}\text{I}_{(\text{solution})} + \text{Li}_{(\text{solid})} \rightarrow \text{C}_6\text{F}_{12}\text{I}_{(\text{solution})} + \text{LiF}_{(\text{solid})}$, $E^\circ = 3.3 \text{ V vs. Li/Li}^+$.

Note that experimental details for all other testing and analysis techniques used in this chapter have already been provided in earlier chapters. Additional chemicals and materials, experimental procedures for SEM and XRD characterizations can be found in **0**, whereas those for KB cathode preparation, Ionic conductivity measurements can be found in **Chapter 3**.

4.3 Results and Discussion

4.3.1 Discharge of Li–fluorinated catholyte cells at 1 M concentration

The discharge behavior of a set of CFI reactants having variable molecular structure was investigated in cells with Li metal foil as the anode and carbon as the cathode substrate, with the latter comprising Ketjen black (KB) except where noted. A co-solvent, dimethylsulfoxide (DMSO)

unless specified otherwise, was used to co-dissolve electrolyte salt and CFI, since salt is not directly soluble in the latter. DMSO was chosen as the initial solvent because it was shown previously to promote high discharge capacities in Li-SF₆ metal-gas cells, which also undergo a discharge conversion reaction to generate LiF and exhibit strongly beneficial capacity and voltage sensitivity to solvent.^{15,17} Unless otherwise noted, a non-fluorinated salt, lithium perchlorate (LiClO₄), was used to avoid introduction of a secondary fluorine source for purposes of discharge product characterization. Cells with 0.1 M LiClO₄ / DMSO only (without fluorinated reactant) showed negligible activity (**Figure 4-1**).

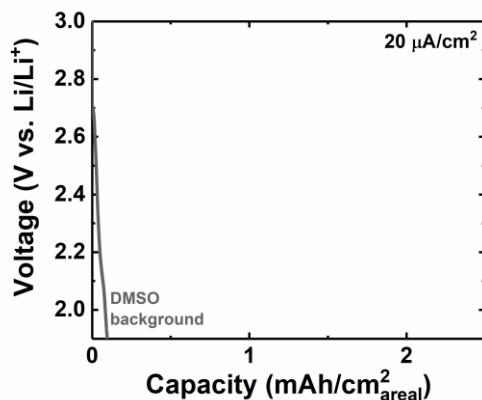


Figure 4-1 Discharge profile of a cell with 0.1 M LiClO₄ / DMSO electrolyte (*i.e.*, lacking CFI reactant) at 20 μA/cm² using 3 pieces of GDL as cathode substrate.

Figure 4-2a shows the discharge profiles of cells containing 1 M CFI in DMSO at a discharge rate of 0.3 mA/cm², with the corresponding molecular structures shown in **Figure 4-2b**. To investigate the influence of the reactant structure, three R_F chain lengths were examined: C₃F₇I, C₄F₉I, C₆F₁₃I; for the shortest-chain reactants (C₃F₇I), two isomers were tested, either with the I functionality bonded to the carbon at position 1 (1-iodoheptafluoropropane, CF₃-CF₂-CF₂I) or at position 2 (2-iodoheptafluoropropane, CF₃-CFI-CF₃). For the shortest-chain reactants (C₃F₇I), the position of the iodine was found to significantly affect discharge voltage, with CF₃-CFI-CF₃

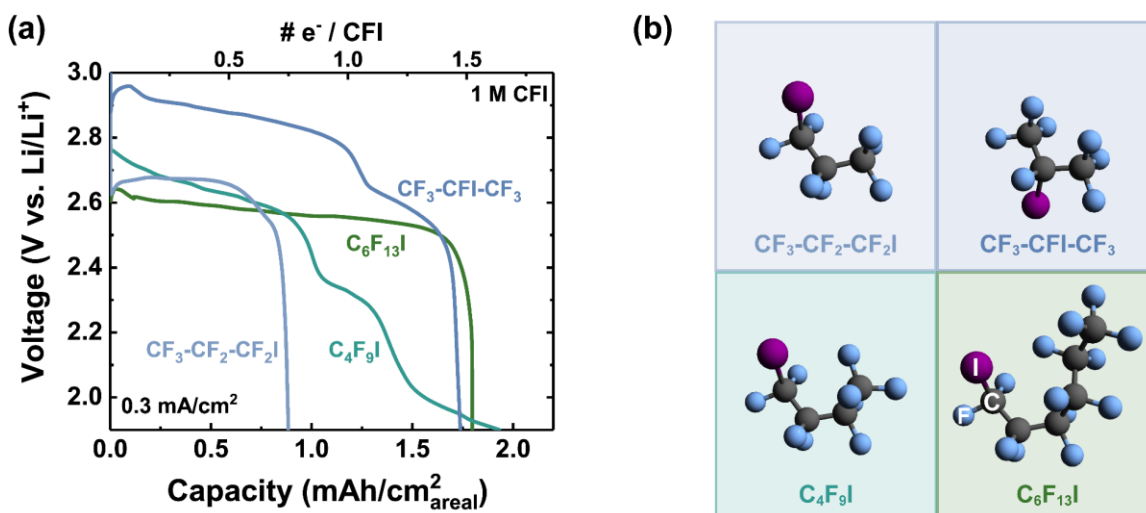


Figure 4-2 Electrochemical discharge characteristics of perfluoroalkyl iodides (CFI) as Li primary battery catholytes. **(a)** Galvanostatic discharge profiles of various CFI reactants, with the corresponding reactant molecular structures shown in **(b)**. Purple: iodine, blue: fluorine, gray: carbon atoms. All Li–CFI cells utilized 50 μ L of 1 M CFI / 0.1 M LiClO₄ / DMSO as catholyte and Ketjen black (KB) as the cathode substrate and were discharged at 0.3 mA/cm² and room temperature (RT).

exhibiting the highest initial discharge voltage at \sim 2.9 V vs. Li/Li⁺ of all reactants, with a sloping, two-stage discharge profile up to a total capacity of 1.5 e⁻/CFI (1.7 mAh/cm²). Changing the I to the terminal position in the CF₃-CF₂-CF₂I isomer resulted in a drop in discharge voltage by about 200 mV to \sim 2.7 V vs. Li/Li⁺; a mainly flat voltage profile; and the lowest capacity of all reactants (0.7 e⁻/CFI and 0.9 mAh/cm²). Among all reactants with the I at position 1, increasing the chain length further led to only moderate changes in average discharge voltage: \sim 2.7 V vs. Li/Li⁺ for C₄F₉I (comparable to CF₃-CF₂-CF₂I) and \sim 2.6 V vs. Li/Li⁺ for C₆F₁₃I, indicating a slight decrease with increasing chain length. Taking C₆F₁₃I as an example, we calculated its initial defluorination potential using density functional theory (DFT) as 3.3 V vs. Li/Li⁺, assuming C₆F₁₂I and LiF_(solid)

as products (calculation details in **Section 4.2**). However, we note that $C_6F_{12}I$ might not be the actual discharge intermediate, and thus this calculation is only a very rough estimation of the theoretical potential. With the exception of $CF_3-CF_2-CF_2I$, the intrinsic capacity was similar ($1.5 e^-/CFI$) regardless of chain length. Note that, to promote chemical stability, $CF_3-CF_2-CF_2I$ contains stabilizer (copper particles), the residue of which might be included in the electrolyte and affect the discharge process and Faradaic quantification, leading to somewhat lower numbers than the other reactants. Attempts were made to also examine the bromide analogue of CFI, perfluorohexyl bromide ($C_6F_{13}Br$), however, the discharge performance is not included here because 1 M $C_6F_{13}Br$ is immiscible with DMSO. In general, the $> 1 e^-$ /molecule transfer for most CFI reactants suggests that at least a minor degree of C–F bond activation occurs, even if possible electron transfer ($1 e^-$) to the I terminal group is assumed to occur, which is examined in further detail later.

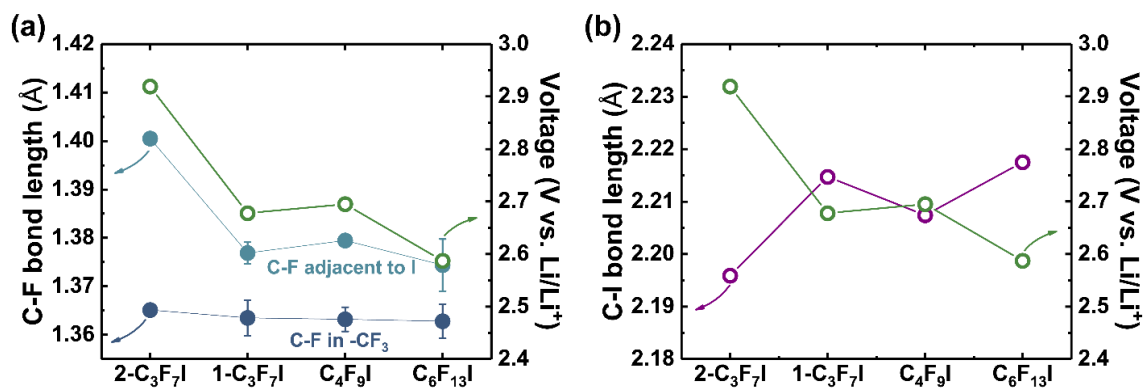


Figure 4-3 DFT-computed bond lengths of (a) the C–F bond adjacent to I (in the $-CF_2I$ or $-CFI-$ group) and in the terminal $-CF_3$ group, and (b) the C–I bond in examined CFI molecules. The initial discharge potential in **Figure 4-2** is plotted for comparison. 2- C_3F_7I and 1- C_3F_7I denote $CF_3-CFI-CF_3$ and $CF_3-CF_2-CF_2I$, respectively.

Following the observation that shorter C–F alkyl chain lengths correlate with higher discharge potentials and that the iodine position strongly affects the discharge voltage, DFT calculation was conducted to examine bond lengths in the four CFI molecules. **Figure 4-3a** shows C–F bond lengths adjacent to the I (in the –CF₂I or –CFI– group) and in the –CF₃ group (farthest from I), while that for the C–I bond is shown in **Figure 4-3b**. All C–F bond lengths fall within the range of 0.136–0.140 nm, consistent with covalent bonding.²⁴⁸ Additionally, a correlation between CFI discharge voltage and C–F bond length adjacent to the I is observed, whereas CFI discharge potential is instead inversely correlated with C–I bond length: *e.g.*, CF₃-CFI-CF₃ (2.9 V vs. Li/Li⁺) has the longest C–F bond adjacent to I (1.40 Å) but shortest C–I bond (2.20 Å). Meanwhile, in accordance with the lower discharge potentials (~2.7 V vs. Li/Li⁺), C₄F₉I and CF₃-CF₂-CF₂I have shorter C–F bonds (1.38 Å) and longer C–I bonds (2.21 Å). C₆F₁₃I, with a discharge voltage of ~2.6 V vs. Li/Li⁺, had the shortest C–F bond length (1.37 Å), together with the longest C–I bond (2.22 Å). In contrast, the length of C–F bonds in the opposing trifluoromethyl (–CF₃) terminal group are similar across all four reactants (~1.36 Å), indicating that these C–F bonds see much weaker electronic effects from the iodine. These correlations, along with the > 1 e⁻/molecule transfer noted previously, show that the iodine terminal group exhibits varying degrees of electronic hybridization with neighboring C–F bonds, with more covalent (shortened) C–I bonds leading to greater weakening (lengthening) of nearby C–F bonds and thus less reducing potentials (lower electron energies) required during electron transfer. We ascribe this to the generally low electronegativity and higher polarizability of I compared to F, which enables a shift in the electron distribution towards the adjacent F depending on R_F. However, no clear correlation of F⁻ utilization (e⁻/CFI) could be observed given the similar capacities of ~1.5 e⁻/CFI for most reactants,

indicating that other factors beyond electronic structure influence capacity under these conditions, as examined further in this study.

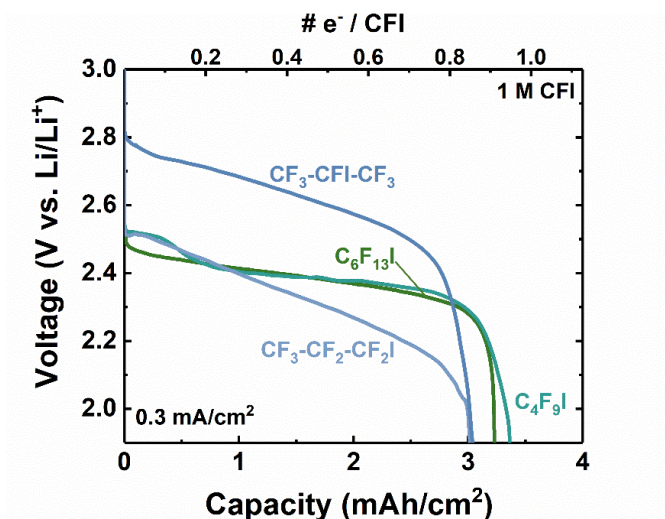


Figure 4-4 Galvanostatic discharge profiles of various CFI reactants. All cells were discharged in Li cells using 150 μL of 1 M CFI / 0.1 M LiClO_4 / DMSO as catholyte and a single piece of gas diffusion layer (GDL) as the cathode substrate at 0.3 mA/cm^2 .

In search of direct evidence of C–F bond activation, the solid discharge products formed on the carbon substrate were characterized. Here, Li–CFI cells were discharged with GDL, which lacks hydrophobic treatment and binder, and thus does not contain additional F. Notably, the lower surface area of GDL (1 m^2/g ,¹⁸⁴ vs. 1300 m^2/g for KB¹⁶⁹) results in ~ 0.1 V decrease in cell voltage and lower capacities (to < 1 e^-/CFI at 1 M), but no drastic effect on the qualitative reduction behavior of CFI, with the previously observed voltage trend remaining (**Figure 4-4**). As shown in **Figure 4-5a**, for all four Li–CFI cells, even at < 1 e^-/CFI , LiF was readily detected as the only crystalline discharge product by X-ray diffraction (XRD) with negligible evidence of LiI. The slightly weaker peak intensity observed for $\text{CF}_3\text{-CF}_2\text{-CF}_2\text{I}$ might be attributed to the lower LiF crystallinity as well as smaller areal capacity. From scanning electron microscopy (SEM), cubic

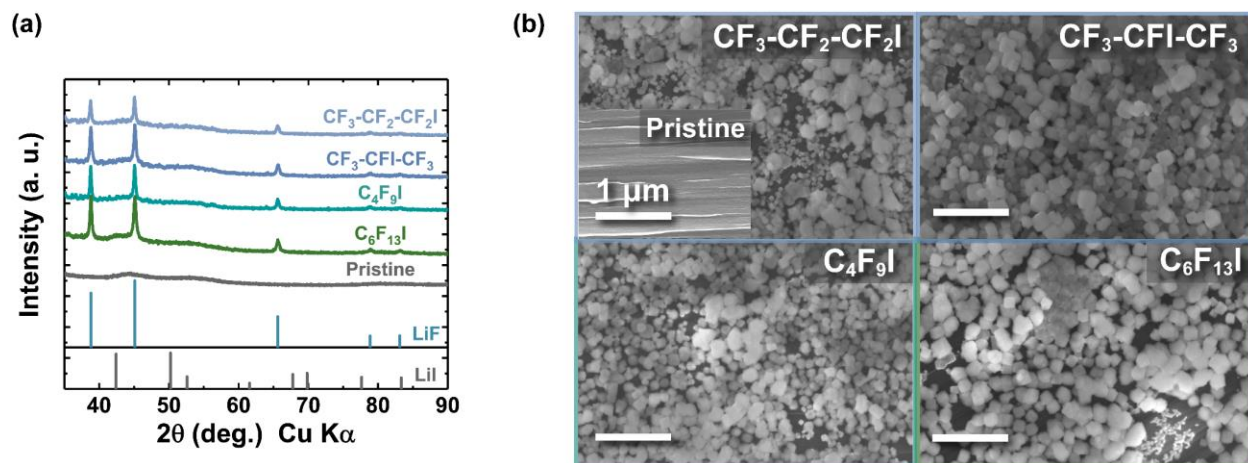


Figure 4-5 (a) XRD of a gas diffusion layer (GDL) cathode from fully discharged Li-CFI cells ($Q = 3.1, 3.3, 3.2,$ and 3.2 mAh/cm² for CF₃-CF₂-CF₂I, CF₃-CFI-CF₃, C₄F₉I, and C₆F₁₃I, respectively). (b) SEM of the pristine (inset) and fully discharged GDL in Li-CFI cells ($Q = 3.0, 3.0, 3.4,$ and 3.4 mAh/cm² for CF₃-CF₂-CF₂I, CF₃-CFI-CF₃, C₄F₉I, and C₆F₁₃I, respectively). All cells used 150 μL of 1 M CFI / 0.1 M LiClO₄ / DMSO as catholyte and GDL as the cathode substrate, and were discharged at 0.3 mA/cm² and RT.

LiF particles were observed on the discharged GDL with comparable particle sizes: $70 \pm 40, 100 \pm 30$ nm, $80 \pm 30,$ and 100 ± 30 nm, for CF₃-CF₂-CF₂I, CF₃-CFI-CF₃, C₄F₉I, and C₆F₁₃I, respectively (**Figure 4-5b**). The three-dimensional distribution of electronically insulating LiF suggests that the particles grow *via* a solution-mediated pathway^{8,9,99} involving generation of solvated fluoride anions and subsequent LiF precipitation from a supersaturated solution. Energy-dispersive X-ray analysis (EDX) indicated that the discharged electrodes contained mainly C and F, with trace amounts of O that might be induced during sample transfer or related to trace solvent reaction, and negligible I (at ~ 4 keV) (**Figure 4-6**). In total, these findings confirm that C-F bond cleavage occurs extensively during the first e⁻ transfer of CFI reduction, with negligible formation of I-containing precipitates. Given its suitable discharge characteristics, highest theoretical

capacity, and highest boiling point (116–119 °C vs. <66 °C for C₄F₉I and C₃F₇I) making it less volatile and thus better suited for battery applications than the higher-voltage C₃F₇I, C₆F₁₃I was used in all subsequent studies.

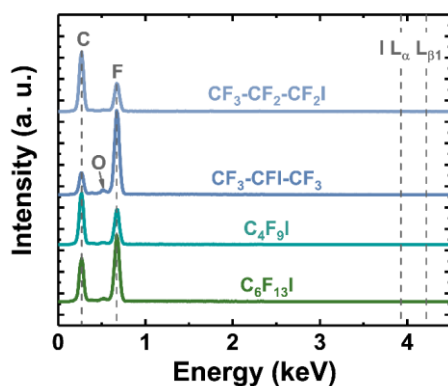


Figure 4-6 EDX spectrum of the fully discharged GDL in Li-CFI cells ($Q=3.0, 3.0, 3.4,$ and 3.4 mAh/cm² for CF₃-CF₂-CF₂I, CF₃-CFI-CF₃, C₄F₉I, and C₆F₁₃I, respectively). All cells used 150 μL of 1 M CFI / 0.1 M LiClO₄ / DMSO as catholyte and GDL as the cathode substrate, and were discharged at 0.3 mA/cm².

4.3.2 Effect of rate and reactant concentration on Li-C₆F₁₃I cell discharge

The rate capability of 1 M Li-C₆F₁₃I cell was further investigated in detail with KB cathode substrates in **Figure 4-7**. At a low discharge rate of 0.02 mA/cm², a two-stage discharge profile with a total capacity of 2.5 e⁻/C₆F₁₃I emerged. The higher capacity was fully attributed to the emergence of a lower-voltage plateau below 2.6 V vs. Li/Li⁺, as the higher-voltage plateau at 2.9–2.75 V vs. Li/Li⁺ exhibited nearly identical capacity to that at 0.12–0.3 mA/cm², which lacked the lower-voltage process as did all higher rates. Given that the lower-voltage process occurs only rarely and after the higher-voltage plateau appears to have fully completed, there is inevitably a large degree of LiF already present on the cathode. This makes it difficult to distinguish limiting

factors of the lower-voltage process, which may include sluggish kinetics with more extensive C–F activation, electronic passivation, and/or mass transport (of reactants or intermediates) as the reaction progresses. High rates in excess of 1 mA/cm² led to increasingly severe voltage polarization and lower capacity, although a degree of discharge was possible to rates as high as 3.9 mA/cm².

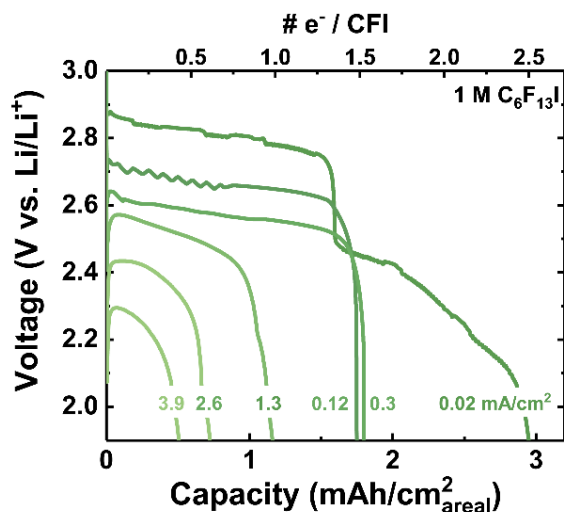


Figure 4-7 Rate capability of Li–C₆F₁₃I cells with 50 μ L of 1 M C₆F₁₃I / 0.1 M LiClO₄ / DMSO catholyte and KB cathode substrates at RT.

To more fundamentally examine the intrinsic redox properties of C₆F₁₃I, a lower reactant concentration (0.1 M) was next used to minimize contributions of LiF passivation. Considering that the total reactant amount was greatly reduced (by 10x), which might exacerbate the effect of potential measurement errors (*e.g.* reactant and catholyte volume, capacity, and Faradaic quantification), the catholyte volume for these experiments was increased from 50 to 200 μ L and three stacked pieces of GDL were used to accommodate the increased amount of electrolyte and provide excess surface area. The discharge profiles of Li–C₆F₁₃I cells at low and intermediate rate are shown in **Figure 4-8a**. Under low-concentration conditions, C₆F₁₃I reduction yielded a much

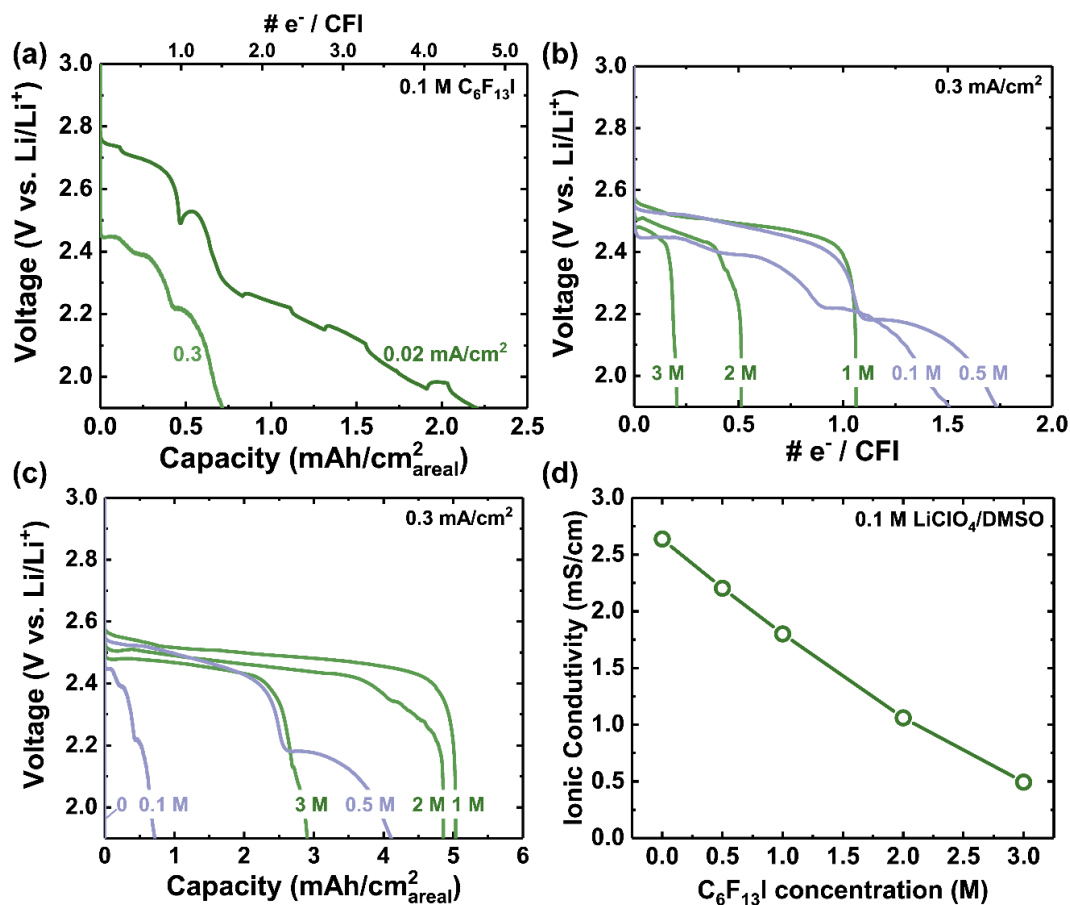


Figure 4-8 Effects of reactant concentration. (a) Discharge profile of cells with 0.1 M $C_6F_{13}I$ at 0.02 and 0.3 mA/cm^2 . (b) Galvanostatic discharge of $Li-C_6F_{13}I$ cells as a function of $C_6F_{13}I$ concentration at 0.3 mA/cm^2 , with the capacities normalized to number of electrons transfer per $C_6F_{13}I$ molecule or (c) geometric area. All cells were discharged at RT with 3 pieces of GDL as the cathode substrate and 200 μL of catholyte (0.1 M $LiClO_4 / DMSO$). (d) Catholyte ionic conductivities as a function of $C_6F_{13}I$ concentration.

more strongly sloping profile than observed previously, with distinct voltage regions initiating at ~ 2.7 , 2.5 , and 2.2 V vs. Li/Li^+ , corresponding to partial capacities of ~ 1.0 , 0.5 , and $3.2 e^-/C_6F_{13}I$ each, for a total of $4.7 e^-/C_6F_{13}I$ ($\sim 280 mAh/g_{CFI}$). The staged nature of discharge is consistent with occurrence of distinct redox processes as observed previously, *i.e.* activation of C–F bonds having

different bond energies, as is also consistent with the higher electron-transfer numbers. The periodic voltage fluctuation at < 2.2 V vs. Li/Li^+ is due to variations in ambient temperature. SEM/EDX and XRD again confirmed formation of three-dimensional LiF particles and no discernible LiI (**Figure 4-9**). Increasing the discharge rate to $0.3 \text{ mA}/\text{cm}^2$ at this concentration led to retention of distinct discharge stages with a polarization of 0.3 V, *i.e.* discharge initiated at ~ 2.4 V vs. Li/Li^+ , but the capacity rapidly decreased to $\sim 1.5 \text{ e}^-/\text{C}_6\text{F}_{13}\text{I}$.

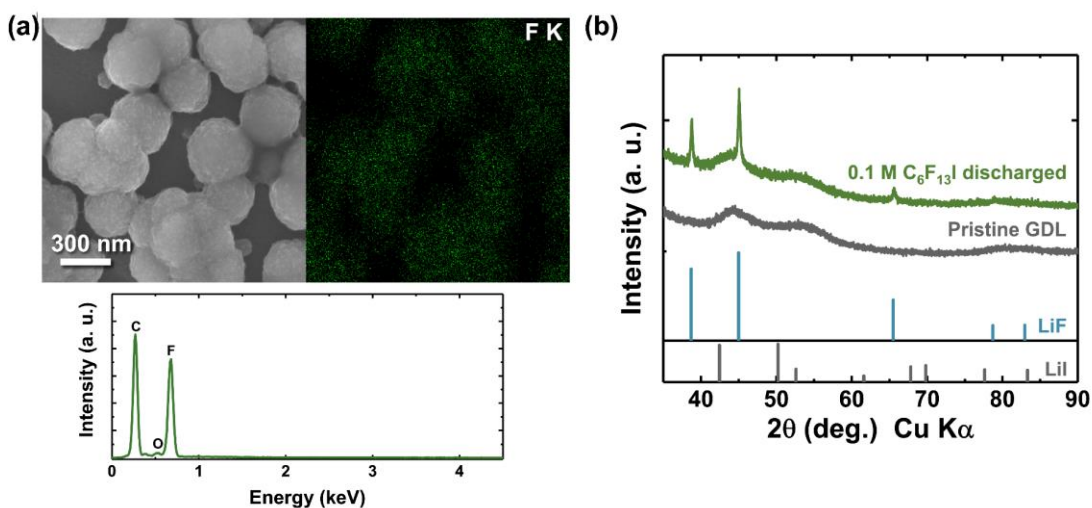


Figure 4-9 (a) SEM and EDX mapping with elemental distribution, and (b) XRD of the GDL cathode substrates extracted from the cell fully discharged at $0.02 \text{ mA}/\text{cm}^2$ ($Q = 2.2 \text{ mAh}/\text{cm}^2$) with $0.1 \text{ M C}_6\text{F}_{13}\text{I} / 0.1 \text{ M LiClO}_4 / \text{DMSO}$ catholyte and 3 pieces of GDL as cathodes.

To further investigate concentration effects, the discharge behavior of $\text{C}_6\text{F}_{13}\text{I}$ catholyte was examined from $0.1 - 3 \text{ M}$ at $0.3 \text{ mA}/\text{cm}^2$ (**Figure 4-8b-c**), with capacities normalized to the number of electrons transferred per $\text{C}_6\text{F}_{13}\text{I}$ and electrode geometric area, respectively. Consistent with the results so far, a two-stage discharge process was only observed up to 0.5 M , and the F utilization ($\text{e}^-/\text{C}_6\text{F}_{13}\text{I}$) decreased significantly and monotonically beyond 0.5 M (**Figure 4-8b**). However, decreasing F utilization was counterbalanced between $0.1 - 1 \text{ M}$ by the increasing

concentration, leading to an increase in areal capacity up to a maximum of 5.0 mAh/cm² (at 1 M), before decreasing further at higher concentration (**Figure 4-8c**). LiF passivation effects are expected to be exacerbated at concentrations beyond 1 M, where the lower DMSO content (*e.g.*, 66 vs. 22 wt% at 1 vs. 3 M) may hinder LiF solubility, resulting in faster electrode passivation. Higher concentrations may also hinder catholyte transport, including ionic conductivity, which was indeed found to rapidly decrease with increasing concentration (**Figure 4-8d**).

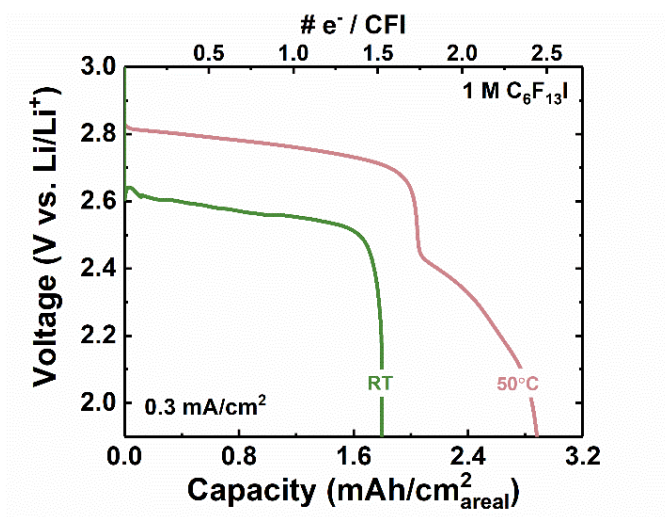


Figure 4-10 Discharge profiles of Li–C₆F₁₃I cells with 50 μ L of 1 M C₆F₁₃I / 0.1 M LiClO₄ / DMSO catholyte and KB cathode substrate, at 0.3 mA/cm² and either 50 °C or room temperature (RT).

To examine whether the two-stage profile, *i.e.* ~ 2 or more e⁻/C₆F₁₃I, could be recovered at the higher concentration of 1 M, cells were discharged at increased temperature with KB cathode substrates (50 °C, **Figure 4-10**). Compared with room temperature (RT) discharge, elevated temperature increased the voltage of the first plateau by ~ 0.2 V to 2.8 V vs. Li/Li⁺. Additionally, the cells at high temperature exhibit a second discharge step starting at 2.4 V vs. Li/Li⁺, with a capacity of 0.7 e⁻/C₆F₁₃I (~ 0.8 mAh/cm²), yielding a total capacity of 2.5 e⁻/C₆F₁₃I. The explicit

role of higher temperature is uncertain at present and may relate to improved reactant transport to the cathode, higher LiF solubility, or more facile kinetics of C–F bond activation.

In summary, so far, $>4 e^-/C_6F_{13}I$ is only accessible with low reactant concentration (0.1 M) at low rate (0.02 mA/cm^2), while for higher reactant concentration (1 M) or rate (0.3 mA/cm^2), the maximum $C_6F_{13}I$ utilization attained is $\sim 2.5 e^-/C_6F_{13}I$ via a two-stage voltage profile with optimized cathode structure at elevated temperature. Given the C–F bond lengthening occurring closest to the iodine, we suggest that that fluorine is most likely to be electrochemically accessible and result in LiF formation; iodine may also participate in electron transfer, but we have been unable to ascertain its product state so far in the electrolyte, having ruled out its presence in discharged cathodes. A majority of C–F bonds within $C_6F_{13}I$ remain inaccessible in purely DMSO electrolyte.

4.3.3 Tuning solvent properties to tailor $C_6F_{13}I$ reduction

To further examine the previously-raised hypothesis regarding mass transport limitations in CFI reactions, we next investigated the $C_6F_{13}I$ reduction behavior in different solvation environments. The concentration was selected as 1 M, given limitations associated with higher concentration as previously discussed, and KB electrodes were used henceforth for all comparisons given their higher surface area and support of higher voltages. Common electrolyte solvents were tested, including propylene carbonate (PC), ethylene carbonate (EC), dimethyl carbonate (DMC), dimethoxyethane (DME), tetraethylene glycol dimethyl ether (TEGDME), N,N-dimethylacetamide (DMA), and a fluorinated solvent, methyl (2,2,2-trifluoroethyl) carbonate (FEMC). Solvent properties, including donor number (DN) and dielectric constant (ϵ), are summarized in **Table 4-1**. Given the largely nonpolar nature of $C_6F_{13}I$, a first consideration in

electrolyte design is the mutual solubility of reactant and solvent, which was found to decrease, as expected, with increasing solvent dielectric constant. Specifically, for solvents with $\epsilon > 60$ (PC and EC), only < 0.1 M $C_6F_{13}I$ is miscible, compared to up to 3 M of $C_6F_{13}I$ in DMSO ($\epsilon = 46.7$). Therefore, DMC, FEMC, and TEGDME, ($\epsilon = 3.1, 7.0,$ and 7.9 respectively)^{185,265} were selected for further detailed investigation and comparison with DMSO. In addition to a wide range of dielectric constant, these solvents also span a range of DN: 17.2, 16.6 and 29.8 for DMC, TEGDME, and DMSO, respectively.^{18,185} The DN is considered here because it reflects the solvation strength of Li^+ , and high DN solvents (*e.g.* DMSO and DMA) were previously shown to promote the formation of large LiF particles and alleviate electrode surface passivation.¹⁵

Table 4-1. Solvent properties

Solvent	DN ^{18,185}	AN ^{185,266}	ϵ ¹⁸⁵	0.1 M salt ^a		1 M salt ^b	
				σ (μ S/cm)	Comments	σ (μ S/cm)	Comments
PC	15.1	18.3	64.9		Limited miscibility with CFI		
EC	16.4	22.2	89.8				
DMC	17.2	--	3.1	1.6	Low conductivity	3273	Active
FEMC	--	--	~ 7.0 ²⁶⁵	4.3		655.0	
DME	20.0	10	7.2	171.6	Active		--
TEGDME	16.6	10.5	7.9	142.7		2227	Active
DMA	27.8	13.6	37.8		Unstable with Li	--	High activity
DMSO	29.8	19.3	46.7	1747	High activity	6080	High activity

^a 0.1 M $LiClO_4$ was used for low salt concentration measurements.

^b 1 M $LiTFSI$ was used for high salt concentration measurements, except for DMA, where $LiNO_3$ was used to ensure Li anode stability.

Galvanostatic discharge profiles of 1 M $C_6F_{13}I$ in the four different solvents with 0.1 M $LiClO_4$ at 0.3 mA/cm² are shown in **Figure 4-11a**. A higher cutoff voltage was used for DMSO (1.9 V vs. Li/Li^+) compared to the other solvents (1.6 V vs. Li/Li^+) due to the relatively limited

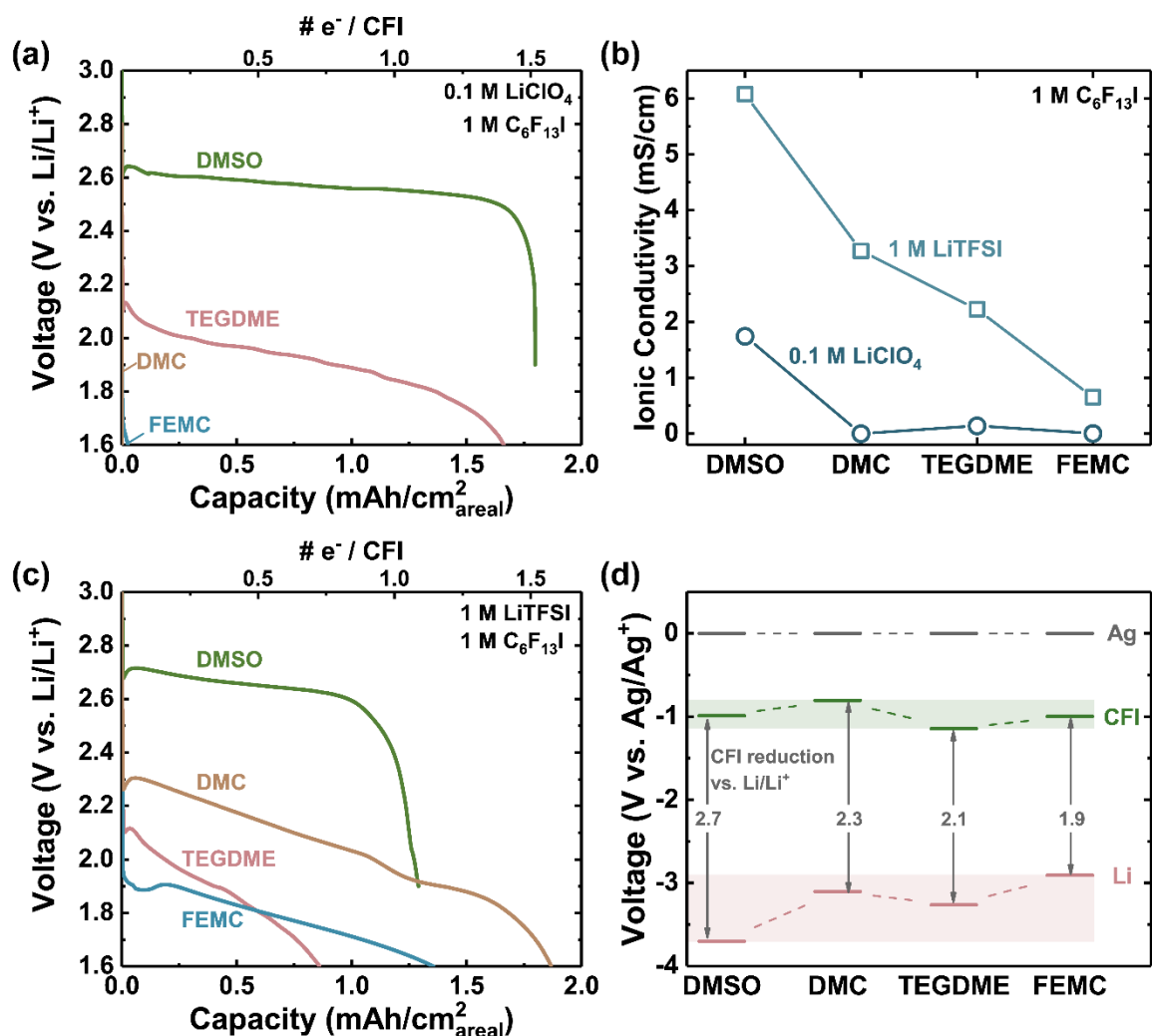


Figure 4-11 Galvanostatic discharge profiles of Li–C₆F₁₃I cells at 0.3 mA/cm² and RT with different solvent species. All the cells utilized KB as cathode substrates, with 50 μ L catholyte containing 1 M C₆F₁₃I and (a) 0.1 M LiClO₄ or (c) 1 M LiTFSI. (b) Ionic conductivities of 1 M C₆F₁₃I catholytes in different co-solvent species, with 0.1 M LiClO₄ or 1 M LiTFSI as electrolyte salt (as indicated). (d) C₆F₁₃I reduction potential (C₆F₁₃I_(solution) + Li⁺ + e⁻) measured in different solvents, referenced to either Li/Li⁺ or Ag/Ag⁺.

stability of DMSO at lower potentials. The DMSO-based cell exhibited the highest discharge voltage at 2.6 V, which was ~0.6 V higher than that with TEGDME, while the capacities of the

two cells were similar ($\sim 1.7\text{--}1.8\text{ mAh/cm}^2$). In contrast, cells with DMC and FEMC exhibited negligible discharge capacities in spite of suitable reactant solubility. We hypothesized that this was due to the limited catholyte ionic conductivities ($<5\text{ }\mu\text{S/cm}$ for both, vs. 1.7 mS/cm for that with DMSO, **Figure 4-11b**). To test this hypothesis, the salt concentration in the catholyte was increased to 1 M , necessitating that the salt species be changed to lithium bis(trifluoromethanesulfonyl)imide (LiTFSI) given difficulties dissolving LiClO_4 at a similar concentration. This change significantly increased the conductivity of DMC and FEMC catholytes by 2–3 orders of magnitude, to 3.3 and 0.7 mS/cm respectively (**Figure 4-11b**). Consequently, discharge activity was observed with DMC and FEMC with high capacities of 1.9 and 1.4 mAh/cm^2 , with sloping discharge profiles initiating at 2.3 and 1.9 V vs. Li/Li^+ respectively (**Figure 4-11c**).

Notably, the $\text{C}_6\text{F}_{13}\text{I}$ discharge voltage was highly sensitive to the DN of co-solvent, *i.e.* the DN decreased in the order of DMSO, DMC and TEGDME, in accordance with decreasing voltage: ~ 2.7 , 2.3 , and 2.1 V vs. Li/Li^+ , respectively. Among all four solvents tested, FEMC had the lowest voltage (initiating at $\sim 1.9\text{ V vs. Li/Li}^+$). In contrast, the cell capacity is less dependent on the solvent DN, indicating that LiF passivation might not be the dominating factor for cell termination here. To further examine the origin of this cell voltage change, the CFI reduction and Li potentials were independently measured vs. a nonaqueous Ag/Ag^+ reference electrode. Interestingly, the $\text{C}_6\text{F}_{13}\text{I}$ reduction potential varies significantly across all four solvents, *e.g.* -1.1 , -1.0 , -1.0 , and $-0.8\text{ V vs. Ag/Ag}^+$ for TEGDME, FEMC, DMSO, and DMC, respectively (**Figure 4-11d**). Changes in the Li^0/Li^+ redox potential were, however, even more extensive: -3.7 , -3.3 , -3.1 and $-2.9\text{ V vs. Ag/Ag}^+$, for DMSO, TEGDME, DMC and FEMC, respectively. The results indicate that the choice of solvent has a moderate effect on the intrinsic $\text{C}_6\text{F}_{13}\text{I}$ reduction potential, which

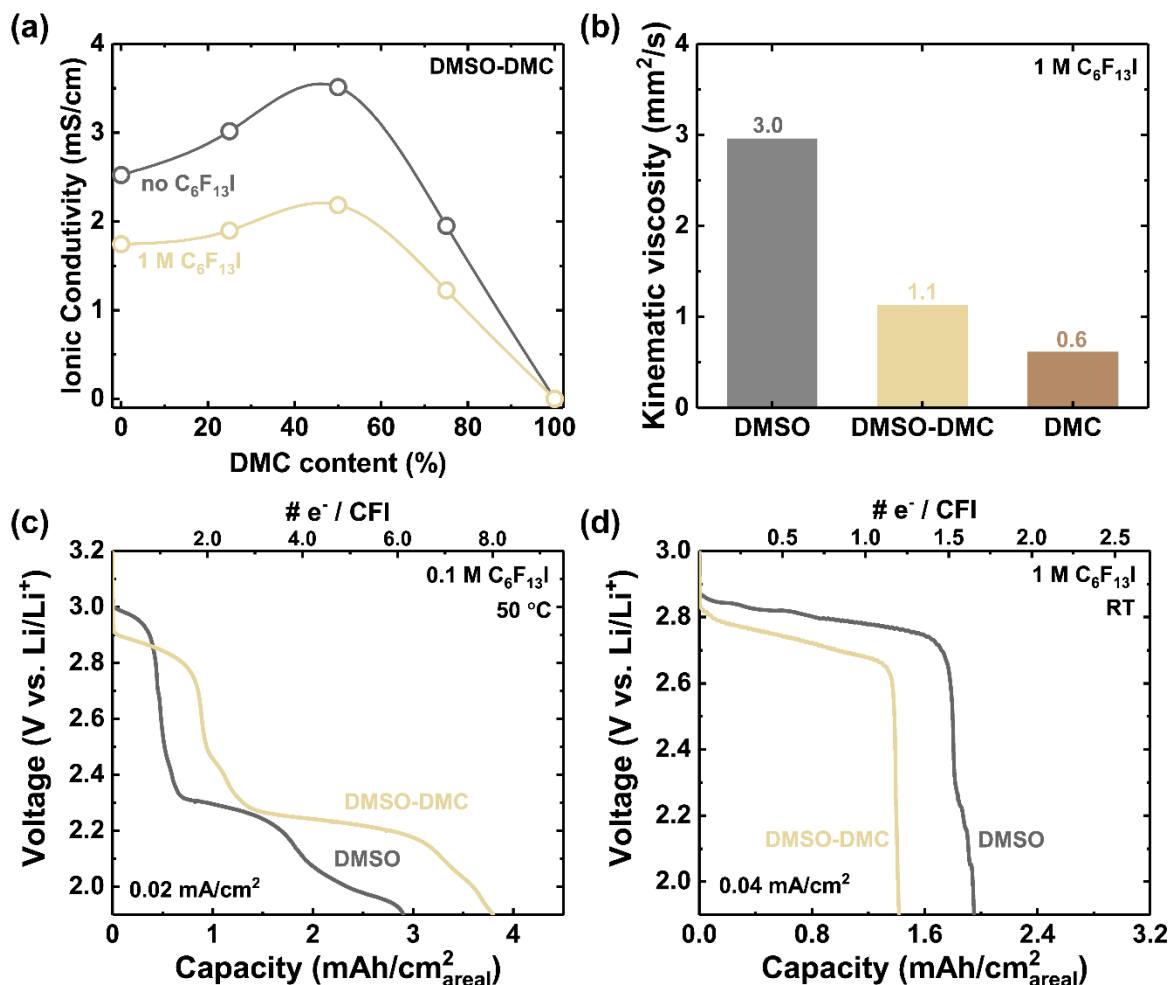


Figure 4-12 (a) Ionic conductivity as a function of DMC content for 0.1 M LiClO₄ / DMSO-DMC solution with or without 1 M C₆F₁₃I. (b) Kinematic viscosity of catholytes with 1 M C₆F₁₃I / 0.1 M LiClO₄ in DMSO, DMC, and/or DMSO-DMC (1:1 v/v) binary solvents. (c, d) Discharge profiles of Li-C₆F₁₃I cells with DMSO or DMSO-DMC (1:1 v/v) co-solvents. Cells contain (c) 200 μ L catholyte with 0.1 M C₆F₁₃I / 0.1 M LiClO₄ and three GDL as the cathode substrate, and were measured at 20 μ A/cm² and 50 °C, or (d) 50 μ L of 1 M C₆F₁₃I / 0.1 M LiClO₄ and KB as cathode substrate, and were measured at 40 μ A/cm² and RT.

may reflect changes in F^- solvation as it is generated electrochemically, or incomplete Li^+ desolvation upon LiF formation, as has been reported with $Li-CF_x$ batteries where solvent can significantly affect discharge voltage.^{36,37} However, the major contribution to the changing in $Li-C_6F_{13}I$ cell voltages in two-electrode cells is the substantial degree of drift in the Li^0/Li^+ potential (by ~ 0.8 V).¹⁶⁷ The results make clear that electrolyte engineering is critical to maximize cell voltage as one important component of energy density in these systems.

Given that DMSO and DMC – a lower viscosity solvent – have distinct transport and solvation properties and that both are viable for $C_6F_{13}I$ discharge, we next examined whether combining these two solvents could be beneficial for C–F utilization. The ionic conductivity of 1 M $C_6F_{13}I$ catholyte with DMSO/DMC at varying proportions, as shown in **Figure 4-12a**, was moderately improved as the DMC volume content increased up to 50% (from 1.7 to 2.2 mS/cm), and then decreased when the DMC ratio was further increased (to <5 μ S/cm for pure DMC). On the other hand, the inclusion of DMC up to a 1:1 v/v ratio led to decreased viscosity (1.1 mm²/s) compared to that with DMSO (3.0 mm²/s, **Figure 4-12b**). To examine maximum attainable capacity, following our previous studies, low $C_6F_{13}I$ concentration (0.1 M), elevated temperature (50 °C) and low rate (0.02 mA/cm²) were first used. As shown in **Figure 4-12c**, inclusion of DMC led to a slight decrease in the higher voltage plateau from 3.0 to 2.9 V vs. Li/Li^+ , while the lower voltage plateau was largely unchanged. Meanwhile, the total capacity increased significantly, from approximately 6 e⁻/ $C_6F_{13}I$ (in DMSO only) to 8 e⁻/ $C_6F_{13}I$ in the blended solvent. This suggests that improving transport properties can facilitate higher C–F utilization in the low concentration regime, where LiF passivation effect is less dominating. Unfortunately, for more practical cells tested at RT and 1 M $C_6F_{13}I$ concentration, the binary solvent was less favorable compared to DMSO, with ~ 0.1 V lower voltage and a lower capacity (**Figure 4-12d**). We interpret this to mean

that decreasing viscosity has potential to aid performance at low reactant concentrations but that other contributors we have been unable to directly control, such as LiF solubility, are dominant at 1 M and above.

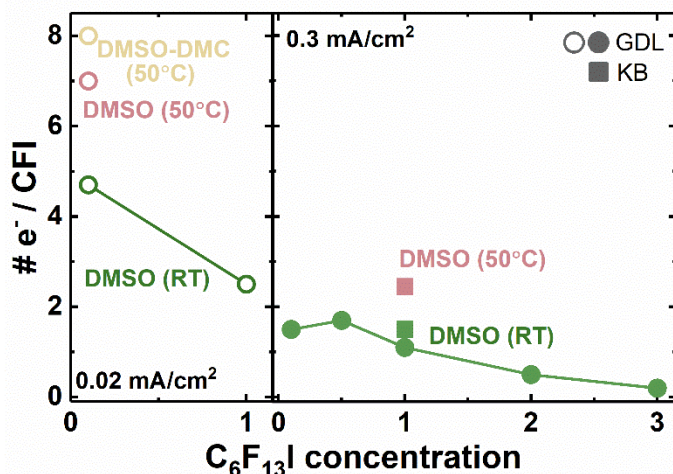


Figure 4-13 Summary of measured defluorination extent of $C_6F_{13}I$. The intrinsic attained discharge capacity, normalized to number of electrons transferred per $C_6F_{13}I$ molecule, is plotted as a function of $C_6F_{13}I$ concentration at low (0.02 mA/cm^2 , left panel) or high (0.3 mA/cm^2 , right panel) discharge rate; in DMSO or DMSO-DMC (1:1, v/v) co-solvent; at different temperatures (RT and 50°C); or with KB (square) or GDL (circle) cathode substrates.

The governing factors for $C_6F_{13}I$ reduction, including discharge rate, reactant concentration, temperature, and catholyte viscosity are summarized in **Figure 4-13**. While our results show that up to $8 e^-$ transfers are possible (out of a total speculated 14 for this reactant), in most cases, only a very limited number of C–F bonds are accessed in practice. We hypothesized previously that the premature cell termination is related to mass transport of CFI and/or its reduction intermediates, and as expected, higher numbers of e^- transfer per molecule is favored by conditions that maximize

transport in general, including low reactant concentration, low current density, and decreased catholyte viscosity. In addition, a previous study has suggested that a potential reduction intermediate, the $C_6F_{13}\cdot$ radical (a product of only a single-electron transfer and loss of I), can become electrochemically deactivated *via* either dimerization (forming insoluble $C_{12}F_{26}$) or H-atom abstraction (from solvent),²⁵⁶ either of which would render the reactant electrochemically inaccessible for further electron transfer. Dimerization reactions, in particular, would be favored by higher reactant concentrations and rate (generating higher local concentrations of the $C_6F_{13}\cdot$ radical); we therefore tentatively propose that this reaction may underlie early cell terminations (prior to LiF passivation) in regimes tested herein. Interestingly, if such a pathway occurs, the average e^-/CFI for some molecules would exceed the maximum average value (8) measured herein. Decreased viscosity might delay such a deactivation reaction by lowering the local concentration of problematic intermediates, a plausible explanation for the improved C–F utilization upon discharge observed with DMSO-DMC binary solvent (at 0.1 M $C_6F_{13}I$ concentration and 50 °C, **Figure 4-12c**). It is harder to rationalize how H-atom abstraction might be concentration- or rate-dependent, though the pathway cannot be ruled out. To gain more understanding of the cell termination mechanism, in the future studies, the reduced carbon species need to be characterized, which might require non-carbon cathode substrates (for solid products) or isotope-labeled solvents (for liquid products).

Unfortunately, the inability to utilize higher reactant concentrations is antithetical to realizing high gravimetric and volumetric energy densities in Li cells, unless capacities can be substantially improved by suppressing this pathway. Possible paths forward include molecular engineering of the terminal halogen beyond I to suppress the reactivity of the radicals generated,

alteration of the reactant tail structure to promote high diffusivity in electrolyte, or further electrolyte engineering to disfavor radical deactivation reactions.

The up to $8 e^-/C_6F_{13}I$ attained corresponds to $>1.3 e^-$ per C, which exceeds that achieved in CF_x materials, making the reactants of scientific interest for study and design of multi-electron fluorocarbon materials. The attained gravimetric capacity and energy of Li- $C_6F_{13}I$ cells reached 480 mAh/g_{CFI} and 1135 Wh/kg_{CFI}, higher than the theoretical value for MnO₂ (310 mAh/g_{MnO2} and 1080 Wh/kg_{MnO2}), a common commercial Li primary battery cathode.⁵ The compatible discharge voltage of CFI and CF_x (~ 2.7 V vs. Li/Li⁺) may provide opportunities for combining the two active materials in hybrid batteries in the future, particularly if key issues identified herein can be improved upon.

4.4 Conclusion

This study investigated electrolyte engineering strategies to unlock C-F bond reduction activity in high F-content fluorocarbon materials, using perfluoroalkyl halides ($C_6F_{13}I$, C_4F_9I , and C_3F_7I) as model liquid-phase reactants. The reduction of highly stable C-F bonds in R_F groups could be demonstrated at potentials starting at ~ 2.8 V vs. Li/Li⁺ and up to $8 e^-/C_6F_{13}I$ ($>1.3 e^-$ per C), with the I playing an important role in both enabling reactant solubility in nonaqueous solvents and as an electronic activator of nearby C-F bonds. Handles for tuning the C-F bond activity were analyzed in depth, including co-solvent properties, reactant concentration, catholyte viscosity, temperature, surface area of substrate carbon, and discharge rate. Lower reactant concentration, current density, and catholyte viscosity promote higher numbers of e^- transfer per molecule, suggested to suppress the deactivation reaction of reduction intermediates. Such insights open up new opportunities for the design of fluorinated materials (*e.g.* electrolytes, additives) in primary

batteries and potentially in rechargeable batteries alike, where LiF is suggested to play an important role in stabilizing reactive interfaces and improving cycling stability.

Chapter 5: Molecular Structural Design for Liquid Perfluoroalkylated Reactants to Achieve Close-to-Full Defluorination

5.1 Introduction

Lithium–carbon monofluoride (Li-CF_x , $0 < x \leq 1.3$) batteries, with a theoretical energy density of 2180 Wh/kg_{active material} (assuming $x=1$), is the current energy leader in the primary battery market (see discussion in **Section 1.2.2**).^{247,249} One approach to surpass the theoretical energy limit of CF_x cathodes is to increase the F content x . However, high F content is generally associated with decreased electronic conductivity,²⁹ and thus such materials are typically deemed less viable as battery cathodes. Particularly, when F content x reaches 2 or higher, the material will become exceedingly electronically insulating and electrochemically inert, owing to the high C–F bond energy in covalent perfluoroalkyl groups ($\text{R}_F = \text{C}_n\text{F}_{2n+1}$, 485 kJ/mol).¹² Therefore, x in commercial Li-CF_x batteries is limited to ~ 1 (theoretical capacity = 865 mAh/g) or below.²⁵⁰

In **Chapter 4**, the electrochemical characteristics of high fluorine content material ($x > 2$) were investigated using liquid perfluoroalkyl iodides (termed ‘CFI’) as an exemplar system. Two categories of parameters to tailor the CFI discharge properties were examined, including the intrinsic parameters, such as length of fluoroalkyl tails and location of I ligand; and the extrinsic parameters, such as solvent properties, CFI concentration, discharge rate, and temperature. A high degree (>60%) of perfluoroalkyl group (R_F) defluorination was obtained at low reactant concentration (0.1 M) and low rate (0.02 mA/cm²), enlightening the possibility of using high F-content C–F bond containing materials to enable multi-electron reduction of carbon. However, the defluorination degree decreases significantly to only 1–2 e⁻/CFI when either rate or reactant

concentration is increased, which might be attributed to the deactivation of reaction intermediates, *e.g.* dimerization reaction of the partially defluorinated- R_F radicals.

Herein, we demonstrate that close-to-full defluorination of R_F group can be realized through molecular structural design, by replacing the I-ligand in CFI with an alkene group connected to an aromatic structure. The resulting fluoro-aromatics are termed as *R-Ph(or Py)-C6 (or C8)* (**Figure 5-1a**), where *R* is an electron-withdrawing group; *Ph* and *Py* are the aromatic groups, representing a phenyl or pyridine ring, respectively; *C6* and *C8* are R_F groups with different chain length, with *C6* stands for $-C_6F_{13}$ and *C8* for $-C_8F_{17}$. There are three main considerations for this structural design: (1) R_F group as the main redox-active component, and the length of which affects the theoretical energy density and the reactant miscibility with supporting electrolytes; (2) the aromatic structure (*Ph* or *Py*) with an alkene linker to facilitate charge transfer and improve reactant solubility; and (3) the *R* functionality that allows for voltage and electrochemical activity of the C–F bond to be tailored. When coupled with Li metal anodes, the fluoro-aromatic cathodes were found to undergo reduction reactions up to 11 e^- (out of 13 available F) or 15 e^- (out of 17 available F) transfer per molecule, yielding attractive gravimetric energies of up to 1785 Wh/kg_{Li+R-Ph-C8}, at high potentials (up to 2.6 V vs. Li/Li⁺). Future research efforts will be focusing on improving battery performances at more practical conditions, namely at high reactant concentrations (up to 2 M), which is currently limited by the extensive LiF passivation on carbon. Some possible approaches to address this challenge include optimizing carbon cathode pore size and surface area, identifying supporting solvents with improved fluoride solvation properties, and tuning *R* functionality to have a stronger Li⁺ affinity. Overall, this new class of R_F -containing catholytes opens up new opportunities to further tailor the C–F bond activity and defluorination reaction pathways.

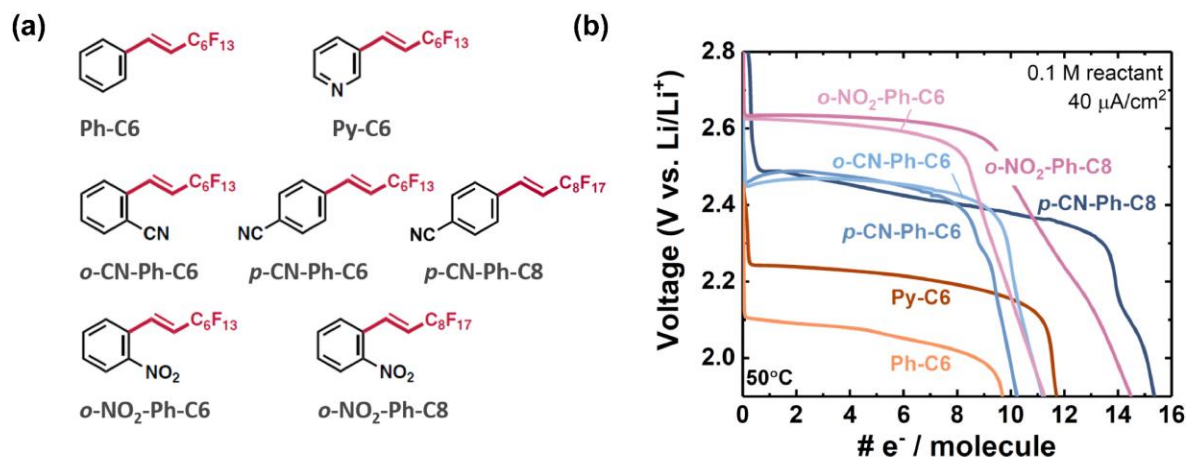


Figure 5-1 (a) Molecular structures of fluoro-aromatic reactants, with the corresponding galvanostatic discharge profiles shown in (b). For those molecules containing two substituents, the relative position of the two groups on the ring can be either *para* (*p*) or *ortho* (*o*). All cells were discharged at 50 °C and 40 μA/cm², with 0.1 M reactant in 0.1 M LiClO₄ / DMSO electrolyte, in Li cells with Ketjen black (KB) cathodes. The number of electrons transfer per molecule were calculated based on the capacities obtained.

5.2 Experimental Methods

Chemicals and Materials: All electrodes and cell-making materials were stored in the argon-filled glovebox (MBRAUN) after dried. The fluoro-aromatic reactants were synthesized with high yield from chemical reactions in one step from commercial starting materials. The detailed synthesis methods are described in Ref. 267.

Galvanostatic Discharge: Two-electrode Swagelok-type Li cells were constructed in an argon glovebox, with the dried Ketjen black (KB) cathode and a 9 mm diameter disk of Li metal as anode (0.75 mm thick, 99.9% metals basis, Alfa Aesar). The separator (13 mm diameter glass fiber filter paper) was impregnated with 50 μL fluoro-aromatic-containing solution (as indicated

in text). For cells with 15-mm diameter carbon cathodes, two-electrode coin cells were used. Cells were constructed inside the Ar glovebox with a 16 mm diameter Whatman separator, a 15 mm diameter Li anode, two stainless steel disks (MTI Corp.) as anode and cathode current collectors, and 50 μ L electrolyte. All coin cells were assembled using an electric crimper (MSK-160E, MTI Corp.) with a constant mass loading of 0.82 mg. All cells were rested at open circuit voltage (OCV) for 5 h before initiating galvanostatic discharge. All discharge tests (BioLogic VMP3 potentiostat or MPG2 workstation) were conducted at the indicated current density with a voltage window ranging from OCV to a lower voltage cutoff of 1.9 V vs Li/Li⁺. For galvanostatic discharge conducted at 50 °C, the cells were placed in an incubator (Mettler GmbH + Co. KG) after assembling.

Note that experimental details for all other testing and analysis techniques used in this chapter have already been provided in earlier chapters. Additional chemicals and materials, experimental procedures for SEM and XRD characterizations can be found in **0**, whereas those for KB cathode preparation can be found in **Chapter 3**.

5.3 Results and Discussion

5.3.1 Design principles for fluoro-aromatic cathodes

The key to the success of defluorination of R_F in CFIs is the I-ligand, which increases the molecular polarization by breaking the symmetry of R_F structure, and thus facilitates charge transfers (see details in **Chapter 4**). Upon electron transfer, the loosely-bonded I-ligand becomes a leaving group,²⁵⁶⁻²⁵⁸ resulting in the formation of (partially-defluorinated) R_F radicals, which are highly vulnerable for side reactions with other radicals or supporting solvents. Therefore, to avoid the early cell termination triggered by deactivation of those reduction intermediates, we replaced

the terminal C–I bond with a stronger but still polarizable bonding environment: a conjugated system (*i.e.* aromatic group) connected to an alkene linker. We hypothesized that, the aromatic unit could help the reactant to accept electrons on discharge (similar to that observed with *R-Ph-SF₅* in **Chapter 3**), while the alkene group, *e.g.* carbon-carbon double bonds, is the essential elements for facilitating the reductive transformation propagating along the R_F tail. The fluoro-aromatics, *i.e.* *R-Ph(or Py)-C₆ (or C₈)* (**Figure 5-1a**), can be synthesized follow an one step chemical reaction from commercial starting materials.²⁶⁷ Note that even for those reactants that are in the liquid state at room temperature (*e.g.* *o*-NO₂-Ph-C₆), no common lithium salt can be dissolved in the neat form, making it necessary to use a co-solvent to help with the salt solvation. The fluoro-aromatic cells were assembled with a Li metal foil anode, a carbon cathode substrate, and a catholyte comprising dissolved fluoro-aromatic reactants with LiClO₄ salt and dimethyl sulfoxide (DMSO) solvent. LiClO₄ was used to avoid additional sources of F for characterization purposes whereas the use of additional DMSO solvent was necessary to dissolve Li-salt. In addition, DMSO was shown previously to support high capacities of fluoride conversion cathodes given the ability to partially solubilize LiF.¹⁷

To examine the intrinsic redox behavior, **Figure 5-1b** shows discharge profiles of Li cells containing 0.1 M fluoro-aromatic reactants at 40 $\mu\text{A}/\text{cm}^2$ as a function of electron transfer per molecule (following the similar calculation methods in **Section 3.5.2**). Due to the limited solubility of long alkyl chain molecules at room temperature (RT), *e.g.* *p*-CN-Ph-C₈, unless otherwise noted, cells were all tested at 50 °C. Temperature effects are revisited later. All the fluoro-aromatics exhibited single voltage plateau during discharge, with voltages ranging from 2.1 to 2.6 V vs. Li/Li⁺. The molecular structure induced voltage and capacity variances are examined in detail below.

The effect of the R_F group chain length is probed by comparing the discharge profiles of *o*-NO₂-Ph-C6 vs. *o*-NO₂-Ph-C8, or *p*-CN-Ph-C6 vs. *p*-CN-Ph-C8. As shown in **Figure 5-1b**, up to 11 e⁻ or 15 e⁻ transfer per molecule (calculated based on capacities) can be obtained during discharge for C6 or C8 containing reactants that contain 13 or 17 C–F bonds per molecule, respectively. This indicates that, assuming all the e⁻ transfer are induced by C–F bond reduction, nearly full defluorination of the R_F can be achieved, with only two C–F bonds remained unreacted. Molecules with longer alkyl chains tend to exhibit better F utilization (11/13 vs. 15/17 for C6 vs. C8), and thus higher gravimetric capacities, *e.g.* the attained capacities of the two nitro (–NO₂) substituted reactants, *o*-NO₂-Ph-C6 and *o*-NO₂-Ph-C8, are 642 and 681 mAh/g_{reactant}, respectively. However, increased R_F chain length inevitably decreases the solubility of the reactants in DMSO. For example, *p*-CN-Ph-C6 is liquid and miscible with DMSO at room temperature (RT), but its C8 counterpart is solid at RT and can only be solubilized at elevated temperatures (*e.g.* 50 °C). This suggests a trade-off between intrinsic capacity and active material loading (*i.e.* reactant concentration), which might be overcome by tuning *R* group properties or supporting solvent species.

Table 5-1. Substituent constants σ of *para*-substituted benzene rings²²⁷

Substituent	Label	σ
None	–H	0.00
Trifluoromethyl	–CF ₃	+0.54
Cyano	–CN	+0.66
Nitro	–NO ₂	+0.78

Next, we examined the effect of the functional group species and their positions on phenyl ring. To compare across different functional species, substituent constant σ in Hammett equation is considered, which is an indicator of the electron-withdrawing strength of the functional groups. The σ of the substituents investigated (at *para* position) is shown in **Table 5-1**. Since Hammett

equation does not give optimally linear relationships with *ortho* substituents,²⁶⁸ the reduction behavior change caused by the different substituent positions (*para* vs. *ortho*) was first probed prior to other analysis. As shown in **Figure 5-1b**, the discharge potentials and capacities of *o*-CN-Ph-C6 and *p*-CN-Ph-C6 showed negligible differences, indicating that the substituents at *para* and *ortho* positions have relatively similar effects on the reduction of R_F, and thus it is reasonable (in this context) to consider σ as a rough representative for the electron-withdrawing strength of *R* substituents at *ortho* positions. Based on this assumption, a general trend that increasing the σ of the *R* group resulting in higher reduction potential can be observed: Ph-C6, *o*-CN-Ph-C6, and *o*-NO₂-Ph-C6, with increased σ value (0, 0.66, 0.78, 0.66, respectively), exhibited improved initial discharge voltages (2.1 V, 2.5 V and 2.6 V vs. Li/Li⁺, respectively).

In addition to reduction potential, the *R* functional group species also directly influence the miscibility/solubility of the reactants in 0.1 M LiClO₄/DMSO supporting electrolyte. Unlike *p*-CN-Ph-C8 which is not soluble at room temperature and faces a solubility limit of 0.8 M at 50 °C, *o*-NO₂-Ph-C8 can reach a concentration of 2 M at room temperature. For trifluoromethyl group (-CF₃) substituted reactants, both *o*-CF₃-Ph-C6 and *p*-CF₃-Ph-C6 showed negligible miscibility with 0.1 M LiClO₄/DMSO even at 50 °C, thus the electrochemical properties of these molecules were not investigated herein.

The effect of ring structure was elucidated from comparison between the two unsubstituted (no *R* group) reactants, Ph-C6 and Py-C6. Changing the aromatic unit from benzene to pyridine, resulting in the increased discharge potential by ~ 0.1 V. This suggests that using pyridine as the underlying ring structure, with similar substituent modifications, substantially higher cell voltage (higher than 2.6 V vs. Li/Li⁺, as was obtained with *o*-NO₂-Ph-C6) could be achieved. However, changing the aromatic component is slightly more drastic than varying *R* functionality or R_F length,

which will require more efforts on synthesis process, and thus is out of the scope of this current study.

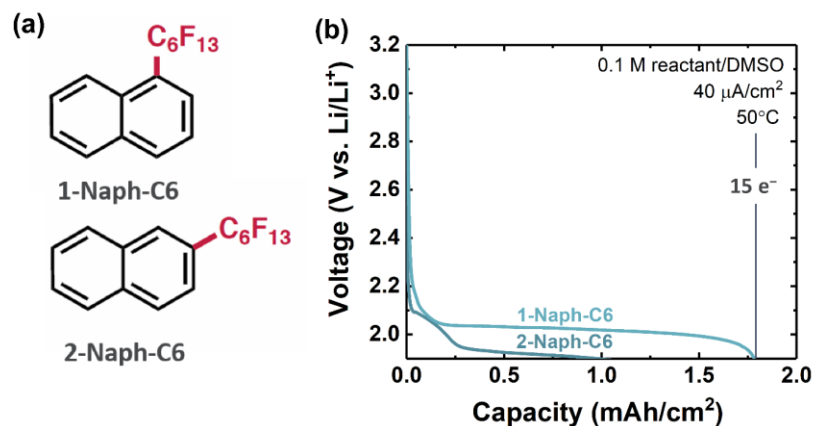


Figure 5-2 (a) Molecular structures of naphthalenes-based fluoro-aromatic reactants, with the corresponding galvanostatic discharge profiles shown in (b). All cells were at 50 °C and 40 μA/cm², with 0.1 M reactant in 0.1 M LiClO₄ / DMSO electrolyte, in Li cells with KB cathodes.

In conclusion, the design principles for the fluoro-aromatic cathodes can be expressed as: a conjugated system + an alkene linker + a R_F, with another optional substitution functionality *R* on the conjugated system as an additional handle to further tune the C–F bond redox activity. We note that the molecular structures following this rationale is not limited to those listed in **Figure 5-1a**. One example is the naphthalenes, which can also be treated as a combination of a conjugated system + an alkene linker. As a proof of concept, naphthalenes-based fluoro aromatics (**Figure 5-2a**) were synthesized and their galvanostatic discharge profiles are shown in (**Figure 5-2b**), with up to 15 e⁻ transfer per molecule obtained for 1-Naph-C6, corresponding to 900 mAh/g_{1-Naph-C6}. The detailed redox mechanism beyond the R_F reduction (13 available F in total) is worth investigating in the future, and might be attributable to the redox of the ring structures.

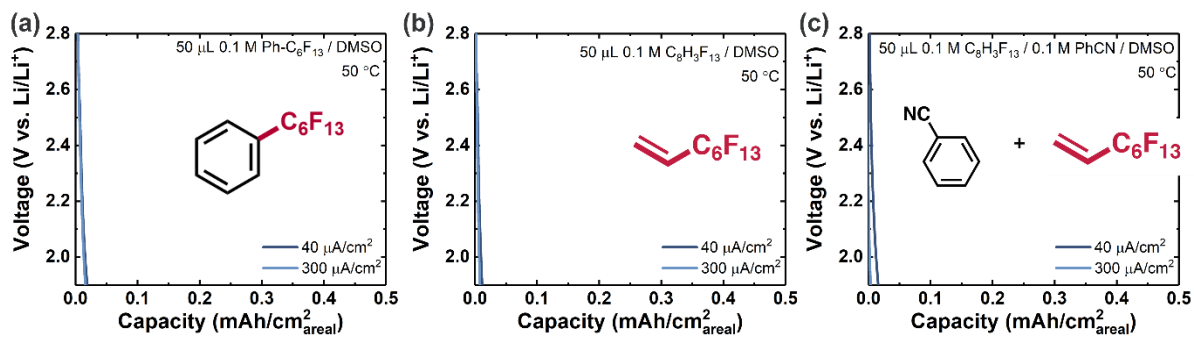


Figure 5-3 Galvanostatic discharge profiles of control group fluorinated reactants (as indicated) at 50 °C and 40 and 300 $\mu\text{A}/\text{cm}^2$, with 0.1 M reactant in 0.1 M LiClO_4 / DMSO electrolyte in Li cells with KB cathodes.

To demonstrate the necessity of the design principles, the control group molecules that only partially meet the requirements were tested. In contrast with Ph-C6, lacking an alkene linker between R_F and benzene (*i.e.* perfluorohexyl benzene, with the R_F directly substituting the H on benzene), negligible activities can be observed on discharge (**Figure 5-3a**). Similarly, if there's no conjugated system, *i.e.* only the alkene group + R_F , the reactant is also electrochemically inactive (**Figure 5-3b**). In addition, even with benzonitrile added as the “external” aromatic group, the system (which contains both the aromatic and the alkene group, but not in the same molecule), still exhibits negligible activity (**Figure 5-3c**). This indicates that the synthesis process that combines these functional groups together as a whole molecule, is essential to unlocking the electrochemical activity of the R_F .

5.3.2 Intrinsic electroactivity and products of fluoro-aromatic discharge

Given their best discharge performances (in terms of voltages and capacities), *o*- NO_2 -Ph-C6, *o*- NO_2 -Ph-C8, and *p*-CN-Ph-C8 were utilized to further investigate the reduction reaction mechanism. To demonstrate that the C–F bonds were successfully reduced during discharge, we

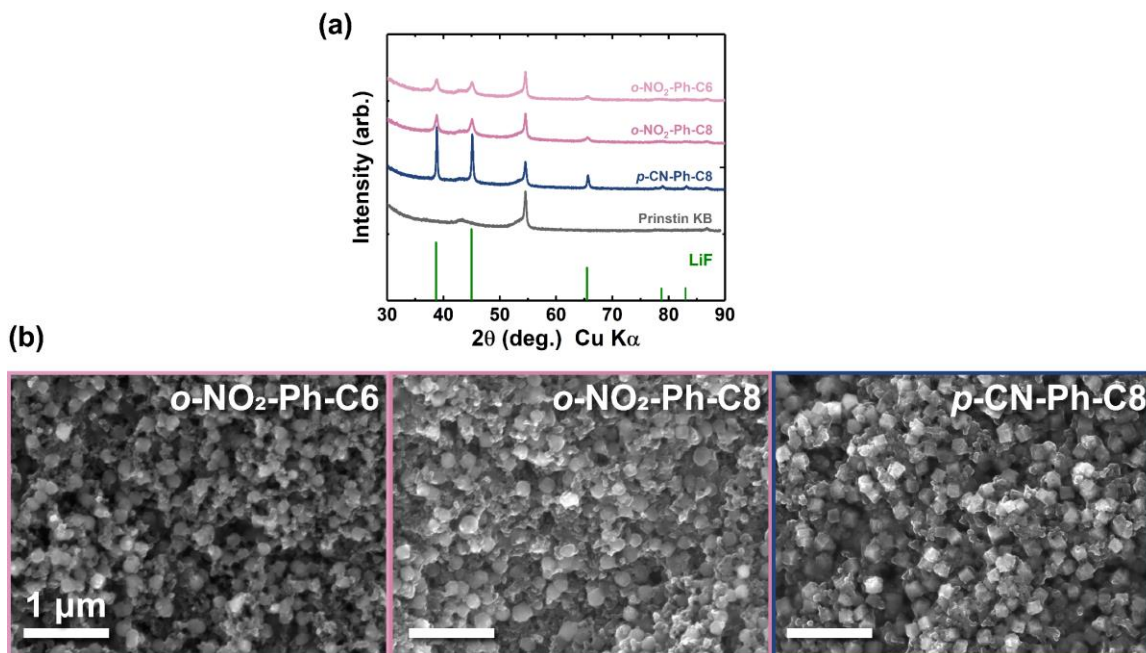


Figure 5-4 (a) XRD and (b) SEM of discharged cathodes from Li–fluoro-aromatics cells with 0.1 M reactant, discharged at 0.3 mA/cm² and 50 °C. Cell discharge capacities: 1.1, 1.5, and 1.5 mAh/cm², for *o*-NO₂-Ph-C6, *o*-NO₂-Ph-C8, and *p*-CN-Ph-C8, respectively.

characterized the solid discharge products formed on carbon cathodes. Note that non-fluorinated salt (LiClO₄) was used to avoid additional fluorine sources, thus the only fluorine sources are fluoro-aromatics and the binder (PVDF), the latter of which is well-known to be stable within the operating voltage window (1.9 – 3.0 V vs. Li/Li⁺). Therefore, the formation of LiF will directly indicate the C–F bond-breaking process for the fluoro-aromatics. As is shown in **Figure 5-4a**, LiF is the only crystallized products that can be detected from XRD after discharge for all three fluoro-aromatics. The slightly lower peak intensity obtained with *o*-NO₂-Ph-C8 than *p*-Ph-CN–C8, despite the similar discharge capacities, might be attributed to the lower LiF crystallinity – rounded LiF particles were observed from SEM after discharge of nitro-substituted molecules, while that observed from *p*-Ph-CN–C8 cells are more cubic (**Figure 5-4b**). This indicates that the *R*

functionality might affect LiF nucleation and growth process. The rate-dependent LiF morphology are shown in **Figure 5-5**, using Li-*p*-CN-Ph-C8 cell as an example. As the current density increased from 40 to 500 $\mu\text{A}/\text{cm}^2$, the average LiF particles sizes decreased significantly from $\sim 257 \pm 47$ to $\sim 93 \pm 17$ nm. Similarly, decreased LiF particle sizes at higher current densities was also observed in Li-SF₆ cells in **Chapter 2**. Combining these results, we can conclude that C-F bond cleavage was successfully triggered during discharge of Li-fluoro-aromatic cells.

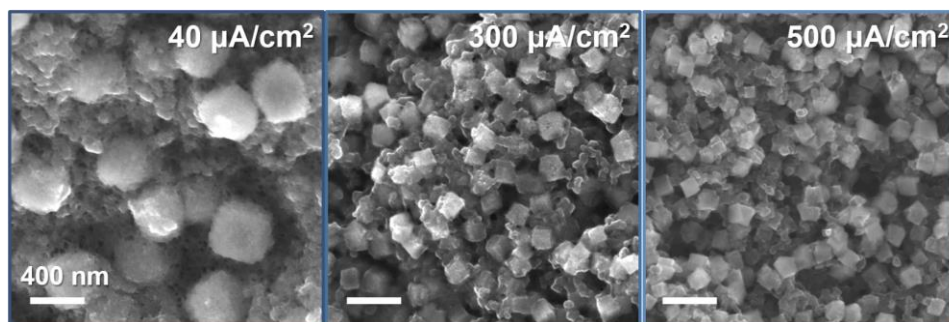


Figure 5-5 SEM images of the KB electrodes after fully discharged in the Li-*p*-Ph-CN-C8 cells at 0.04, 0.3 and 0.5 mA/cm^2 (as indicated). All the cells were discharged at 50 °C.

The rate performance of the three different fluoro-aromatic reactants were next examined. The discharge profiles of 0.1 M fluoro-aromatic reactants at 50 °C are shown in **Figure 5-6**, with the corresponding performance quantifications listed in **Table 5-2**. The gravimetric attainable capacities of *o*-NO₂-Ph-C6, *o*-NO₂-Ph-C8, and *p*-CN-Ph-C8 are 642, 681, and 748 $\text{mAh}/\text{g}_{\text{reactant}}$, respectively (at 0.04 mA/cm^2), very close to the theoretical value assuming 11 or 15 $e^-/\text{molecule}$ for C6 or C8 reactants. All three reactants showed good capacity retention as the current density increased from 0.04 to 1.0 mA/cm^2 , with capacities of $> 1 \text{ mAh}/\text{cm}^2$ obtained at high rate. The voltage drop of *p*-CN-Ph-C8 reduction at high current densities, however, is much severe than that observed from the -NO₂ substituted reactants. At 1.0 mA/cm^2 , the discharge of *p*-CN-Ph-C8 exhibits a sloping voltage profile at $< 2.3 \text{ V}$ vs. Li/Li⁺, while a relatively well-defined voltage

plateau initiating at ~ 2.5 V vs. Li/Li⁺ can be observed for *o*-NO₂-Ph-C6 and *o*-NO₂-Ph-C8. Among all three reactants, *o*-NO₂-Ph-C6 exhibits the best rate capability, with ~ 0.6 mAh/cm² capacity attained at a high rate of 3.0 mA/cm². As for the attained gravimetric energies (normalized to the weight of liquid reactant only), the two C8 molecules deliver slightly higher specific energies (1700 and 1785 Wh/kg_{reactant} for *o*-NO₂-Ph-C8 and *p*-CN-Ph-C8, respectively) than that of the C6 molecule (1600 Wh/kg_{reactant} for *o*-NO₂-Ph-C6) at low rate (0.04 mA/cm²), owing to the better C–F utilization. However, such advantages got lost at high rates: at 1.0 mA/cm², *o*-NO₂-Ph-C6 exhibited the highest energy density of 1165 Wh/kg_{reactant}, while that for the two C8 molecules

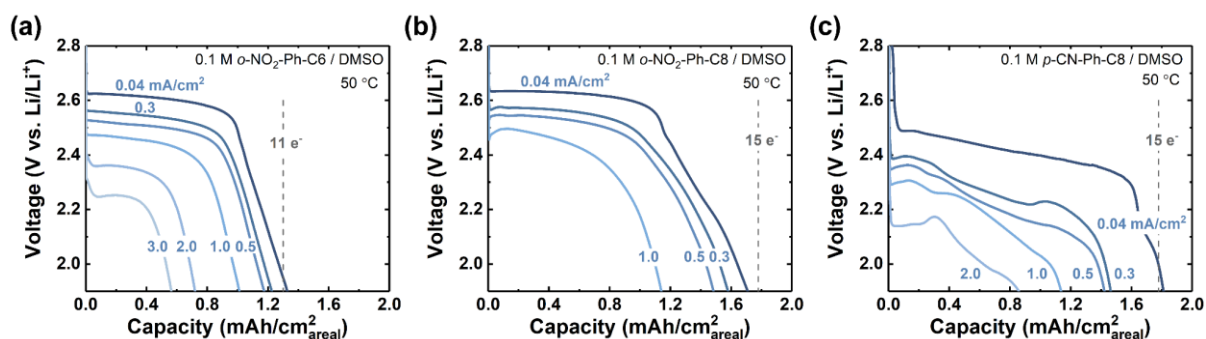


Figure 5-6 Galvanostatic discharge profiles of Li cells with 0.1 M fluoro-aromatic reactants: (a) *o*-NO₂-Ph-C6, (b) *o*-NO₂-Ph-C8, and (c) *p*-CN-Ph-C8 in 0.1 M LiClO₄ / DMSO supporting electrolyte, with KB cathode substrate at 50 °C.

Table 5-2. Attained discharge performances of *o*-NO₂-Ph-C6, *o*-NO₂-Ph-C8, and *p*-CN-Ph-C8*

	<i>o</i> -NO ₂ -Ph-C6	<i>o</i> -NO ₂ -Ph-C8	<i>p</i> -CN-Ph-C8
Capacity (mAh/g _{reactant})	642	681	748
Average Voltage (V vs. Li/Li ⁺)	2.5	2.5	2.4
Energy Density (Wh/g _{reactant})	1600	1700	1785
# e⁻ /molecule	11	15	15
Solubility Limit (M)	2	2	0.8

*At reactant concentration of 0.1 M and 50 °C. Calculated from discharge profiles in Figure 5-6.

were both less than $1100 \text{ Wh/kg}_{\text{reactant}}$. This suggests that the batteries for high power or high energy needs should be designed separately, with long alkyl chain molecules more suitable for low rate-high energy applications, and short chain reactants being preferred when power requirement is stringent.

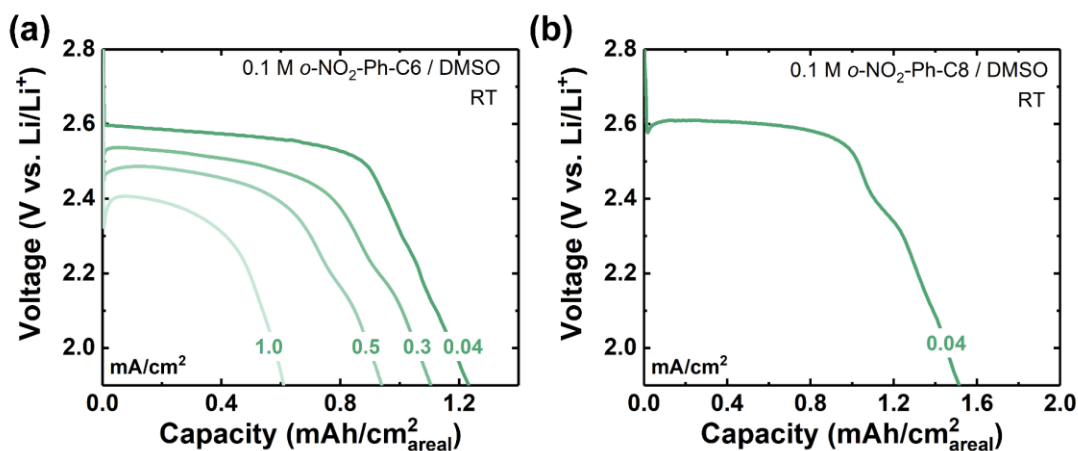


Figure 5-7 Galvanostatic discharge profile of Li cells with 0.1 M fluoro-aromatic reactants: (a) *o*-NO₂-Ph-C6 and (b) *o*-NO₂-Ph-C8 in 0.1 M LiClO₄/DMSO electrolyte, using KB electrodes at room temperature.

Given the limited solubility of *p*-CN-Ph-C8 in DMSO at room temperature (RT), the RT rate performances were tested only for the two nitro group substituted reactants, and the results are shown in **Figure 5-7**. At 0.04 mA/cm², both reactants exhibited slightly lower capacities than that obtained at 50 °C, with capacities of 10.4 and 12.8 e⁻ per molecule obtained for *o*-NO₂-Ph-C6 and *o*-NO₂-Ph-C8, respectively. The less significant capacity decrease at lower temperature for *o*-NO₂-Ph-C6 suggests that those reactants with shorter R_F chain, although with lower theoretical capacities, might be more suitable for room temperature applications, possibly due to their improved solubility/miscibility with DMSO. The achievable specific energy densities at room temperature for *o*-NO₂-Ph-C6 and *o*-NO₂-Ph-C8 are 1470 and 1490 Wh/kg_{reactant}, respectively,

higher than the theoretical specific energy of SOCl_2 ($\sim 1470 \text{ Wh/kg}_{\text{reactant}}$). However, it is important to note that SOCl_2 -based batteries operate with neat SOCl_2 (*i.e.* without supporting electrolyte solvents, such as DMSO used in this study), and thus this improved active material-level metrics might not be directly carried over to cell-level performances. Therefore, we next investigated the fluoro-aromatic discharge at closer to practical conditions, that is, at higher reactant concentrations where the DMSO volume is diminished.

5.3.3 Concentration effect on *o*-NO₂-Ph-C6 discharge

Given its high solubility, *o*-NO₂-Ph-C6 was used as an exemplar system to investigate the effect of reactant concentration on fluoro-aromatic reduction, with “*o*” henceforth omitted. To accommodate the increased amount of LiF formed at high concentrations, carbon foam (with high carbon loading: 5 mg/cm^2) were used as cathode substrate. **Figure 5-8a** shows the galvanostatic

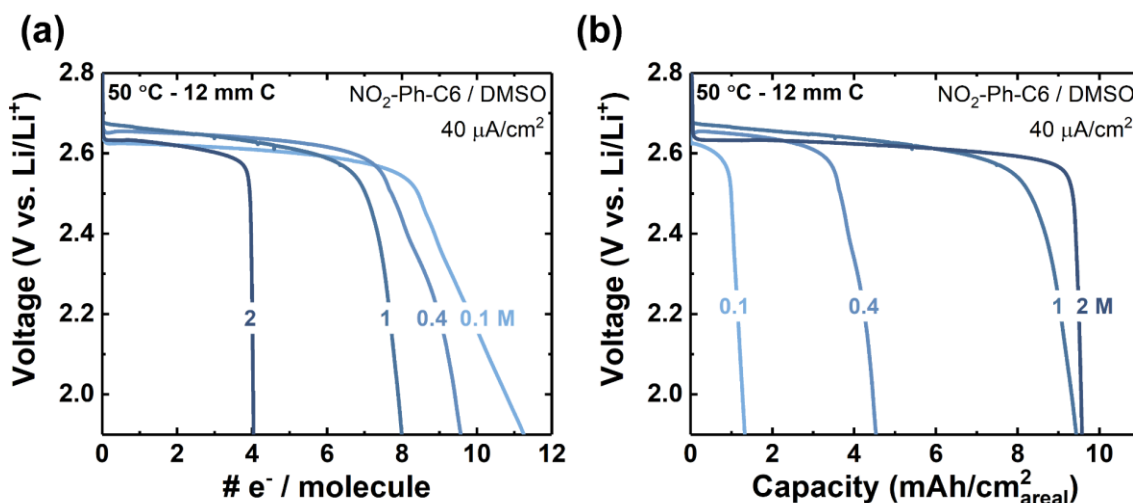


Figure 5-8 Galvanostatic discharge of Li-NO₂-Ph-C6 cells as a function of NO₂-Ph-C6 concentration in 0.1 M LiClO₄ / DMSO supporting electrolyte at $40 \mu\text{A/cm}^2$ and $50 \text{ }^\circ\text{C}$, with capacities normalized to (a) number of electron transfer per molecule, and (b) geometric area of carbon cathodes.

discharge profiles of NO₂-Ph-C6 as a function of reactant concentration, with capacities normalized to the average electron transfer per NO₂-Ph-C6. The C-F utilization saw a monotonic decrease as concentration increased, reduced from 11 e⁻/NO₂-Ph-C6 at 0.1 M to 4 e⁻/NO₂-Ph-C6 at 2.0 M. In spite of lower per-molecule utilization, the concentration enables improved cell-level metrics. **Figure 5-8b** plots the same set of data as in **Figure 5-8a**, but with capacities normalized to geometric area of carbon substrate. Increasing concentration from 0.1 to 1.0 M led to a significant increase in attainable capacity from 1.3 to 9.4 mAh/cm². Further increasing concentration to 2.0 M, however, induced negligible change in the total attained capacity (9.6 mAh/cm² at 2.0 M), which might be attributed to the extensive LiF formation at high concentrations that passivates the carbon surface.

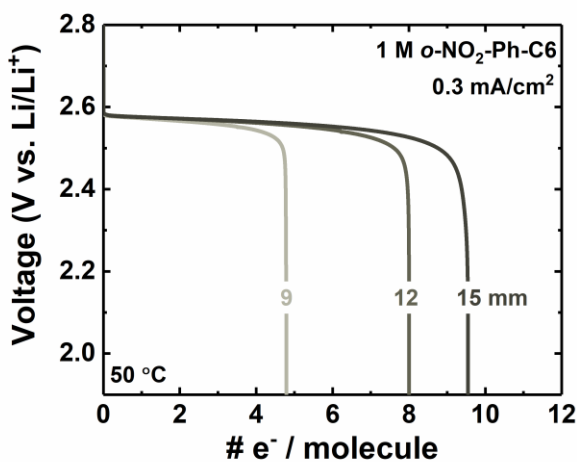


Figure 5-9 Galvanostatic discharge of Li-NO₂-Ph-C6 cells with 1 M NO₂-Ph-C6 in 0.1 M LiClO₄ / DMSO supporting electrolyte at 0.3 mA/cm² and 50 °C, with three different sizes of carbon substrates: with 9, 12, and 15 mm diameter (total C: 3.2, 5.7, and 8.9 mg, respectively).

To test this hypothesis, three different sizes of carbon cathodes (with 9, 12 and 15 mm diameter, **Figure 5-8** utilized 12 mm carbon cathodes) were used for 1 M NO₂-Ph-C6 cells, and

the corresponding discharge performances are shown in **Figure 5-9**. All the cells utilized 15 mm-diameter Li disk as anode, and were discharged at same areal current densities (0.3 mA/cm^2), which also corresponds to the same rate per weight of carbon (60 mA/g_C). Increasing carbon cathode diameter from 9 to 15 mm, *i.e.* increased the total carbon loading from 3.2 to 8.9 mg, successfully improved the C–F utilization from 4.8 to $9.5 \text{ e}^-/\text{NO}_2\text{-Ph-C6}$ with negligible change in discharge voltages, despite that the gravimetric current increased by nearly three times (from 8.2 to $22.7 \text{ mA/g}_{\text{NO}_2\text{-Ph-C6}}$). This suggests that one of the major limiting factors at high reactant concentrations ($\geq 1 \text{ M}$), which causes premature cell termination, is carbon cathode passivation by LiF. In fact, with large (15 mm) carbon cathodes, $11 \text{ e}^-/\text{NO}_2\text{-Ph-C6}$ is achievable at 1 M reactant concentration (at $40 \text{ }\mu\text{A/cm}^2$, **Figure 5-10a**), identical to that observed at 0.1 M, confirmed again that the limitation mainly originates from carbon. Further increase the reactant concentration from

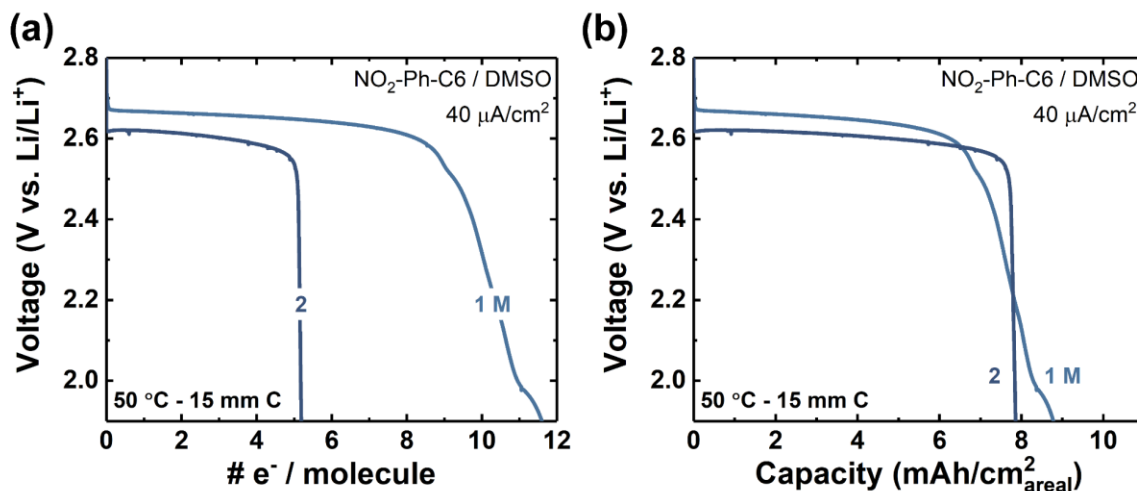


Figure 5-10 Galvanostatic discharge of Li–NO₂–Ph–C6 cells with 15 mm diameter carbon foam cathodes and 1 or 2 M NO₂–Ph–C6 in 0.1 M LiClO₄ / DMSO catholytes, at $40 \text{ }\mu\text{A/cm}^2$ and $50 \text{ }^\circ\text{C}$, with capacities normalized to (a) number of electron transfer per molecule, and (b) geometric area of carbon cathodes.

1 to 2 M resulted in similar areal capacity (8–9 mAh/cm²), but decreased C–F bond utilization (5 e⁻/NO₂-Ph-C6). Notably, the LiF passivation effect is likely to be more severe at higher reactant concentrations, given that the diminishing of supporting solvent DMSO (~62 wt% at 1 M vs. ~31 wt% at 2 M) could significantly decrease the ability to solubilize LiF.

To project the cell-level performances, we consider the “sub-stack” level energy, defined as cathode (fluoro-aromatics or CF_x) + carbon + electrolyte + consumed Li (see details in **Chapter 3**). Assuming 11 e⁻/molecule is achievable at 2 M for NO₂-Ph-C6, then the sub-stack level energy density of Li–NO₂-Ph-C6 cell could reach 915 Wh/kg_{sub-stack}. Given the better C–F bond utilization, the projected sub-stack level energy at 2 M for Li–NO₂-Ph-C8 cell is even higher (1160 Wh/kg_{sub-stack}, assuming 15 e⁻/NO₂-Ph-C8), exceeding that obtained from the state-of-the-art Li–CF_x systems (~1000 Wh/kg_{sub-stack}). Therefore, to achieve the intrinsically high energy density of fluoro-aromatics, future work could focus on developing high surface area carbon cathodes with proper pore size and distribution, tuning the *R* functionality to enable better solubility in electrolyte and Li⁺ affinity, and/or optimizing supporting solvent species to achieve stronger LiF solvation.

5.4 Conclusion

This study demonstrates the design principles for a new class of high-energy catholytes, which enable close-to-full defluorination of R_F group. These fluoro-aromatic reactants comprise: a R_F tail, which is the major redox active component; a conjugated system, such as a phenyl or pyridine ring, which facilitates electron transfer to the molecule upon discharge; an alkene linker, connecting the R_F with the ring structure, which assists the reductive transformation propagating along the R_F tail; and a *R* functionality on the ring component, which provides an additional handle to tune the R_F redox properties (*e.g.* reduction potential) as well as the reactant solubility. High degree of R_F defluorination has been achieved (11/13 total available F, or 15/17 total available F),

corresponding to $>1.8 e^-$ per carbon redox, and high gravimetric energy densities (1600, 1700 and 1785 Wh/kg_{fluoro-aromatic} for *o*-NO₂-Ph-C6, *o*-NO₂-Ph-C8 and *p*-CN-Ph-C8, respectively). The nitro group substituted fluoro-aromatics, with the highest discharge potential (~ 2.6 V vs. Li/Li⁺), exhibit good solubility/miscibility in DMSO (up to 2 M), and thus might be more suitable for practical applications where high active material loadings are favored. It is reasonable to assume that, with optimized carbon cathode substrates to address the LiF passivation challenge at high reactant concentrations, excellent cell-level performance metrics are attainable. Overall, this study provides a new platform for the molecular design of fluorinated materials, for increasing energy densities in primary batteries, or potentially, for improved cyclability in rechargeable systems, where LiF formation is beneficial for stabilizing reactive interfaces.

Chapter 6: Tailoring Fluoride Morphology to Facilitate Electrochemical Fluoridation of MnO for Li-ion Cathodes

Reproduced in part with permission from Gao, H., He, M., Guo, R., & Gallant, B. M. (2021). Electrochemical Fluoridation of Manganese Oxide by Perfluorinated-Gas Conversion for Li-ion Cathodes. *Batteries Supercaps*, 4, 1771. Copyright 2021.

6.1 Introduction

Sustained demand for higher-energy rechargeable Li/Li-ion batteries that can reach U.S. Department of Energy targets of 500 Wh/kg and 750 Wh/L motivates continued improvement beyond today's cathode materials, which limit cell performance.^{47,269} As introduced in **Section 1.3**, commercialized Li-ion battery cathodes belong mainly to oxide-based materials, with current focus on lithium nickel-manganese-cobalt oxides (NMC) that have capacities of ~200 mAh/g.⁴ Many oxides currently under development that can attain higher capacities, such as Li-rich cathodes (*e.g.* Li-rich NMC, >280 mAh/g)⁵¹ or Li-rich disordered rock-salt phases (>300 mAh/g),⁵² rely on anionic redox, which triggers oxygen release along with transition metal dissolution during cycling, plaguing cell stability.^{54,55,270} In this context, there has been great interest in identifying strategies to improve cyclability of oxide parent phases, of which fluorination/fluoridation methods have received focus in recent years. The high electronegativity of fluorine (F) and exceptionally high free energy of formation of fluorides imparts strong metal–F bonds,¹¹ stabilizing transition metal species from migration and improving lattice stability. Bulk-phase F-substitution for oxygen (O) has so far been conducted in oxides with various structures (spinel LiMn₂O₄, layered NMC, and Nb-based disordered rock-salt), yielding improved cyclability, higher discharge voltage, and increased capacity.^{65,67,68,271,272} In addition to bulk substitution, surface F-modification, such as nanoscopic LiF coatings, can protect the oxides against the

electrolyte under highly oxidizing conditions, helping to suppress side reactions while sustaining prolonged cycle life.⁸¹

More recently, LiF surface modification has been reported to support bulk-like fluoridation of oxide phases upon electrochemical activation at high potentials, as introduced in **Section 1.3.2.3**. Kang and co-workers, using composites composed of LiF and non-lithiated transition metal oxides synthesized by high energy ball milling, demonstrated that the initial charge step induces an LiF “splitting” (activation) reaction upon oxidation of a nearby transition metal site, *viz.*: $\text{MO} + \text{LiF} \leftrightarrow \text{MOF} + \text{Li}^+ + \text{e}^-$ ($\text{M} = \text{Mn}, \text{Fe}, \text{or Co}$).⁸³⁻⁸⁵ When used with a non-Li-containing oxide like the monoxide class MO, LiF acts as both an F and a Li source, with Li^+ migration to the anode as F^- is incorporated into the cathode to balance oxidation of M, and thus has an additional benefit of providing Li to the cathode and cell. Following activation, the resulting M-O-F phase, which reportedly has a disordered structure with an F-rich amorphous shell and an O-rich core, then cycles as a conversion cathode with reversible capacities up to 240 mAh/g_{MnO+LiF} (or ~345 mAh/g_{MnO}). Achieving these capacities previously required very small oxide/LiF particle sizes (< 10 nm for MO), which were reported as necessary to achieve meaningful degrees of fluoridation. This occurs because, upon first charge, F largely concentrates in the MnO surface region; consequently, large surface areas are needed to facilitate high MnO utilization.^{84,273} In contrast to mechanical milling, Tarascon and co-workers proposed a distinct approach for *in situ* fluoridation of oxides through LiPF₆ salt decomposition, attaining a capacity of ~250 mAh/g_{MnO}.^{86,87} However, the decomposition of salt demands excess electrolyte and will inevitably lead to other parasitic reactions. Finally, thin-film methods, such as pulse laser deposition (PLD), have recently been explored to form LiF/Fe/Cu or LiF/NiFe₂O₄ films with small domain sizes for both LiF and M/MO phases (< 10 nm) and improved contact between LiF and transition metal species.^{274,275} Scalability

of the thin film processing methods requires further development. Consequently, methodologies of F incorporation need further exploration and improvement to broaden applicability to practical battery materials, especially where high tap densities require larger particle sizes (up to ~several μm)²⁷⁶ and where parasitic salt consumption is untenable.

We hypothesized, given extensive reliance on ball-milling in previous work and known difficulty in LiF processing to form well-controlled interfaces, that poor physical/electrical contact between the MO substrate and LiF could limit attainable degrees of fluoridation below what may be achievable, contributing to stringent particle-size requirements seen previously. To test this hypothesis, and to examine another possible fluoridation methodology with potential to help elucidate the limitations of those used so far, this study investigated whether higher degrees of fluoridation, as evidenced by higher discharge capacities, are achievable using an electrochemically-sourced LiF formed by reduction of perfluorinated gases. As mentioned in **Section 1.4.3**, full reduction of SF_6 ($\text{SF}_6 + 8\text{e}^- + 8\text{Li}^+ \rightarrow \text{Li}_2\text{S} + 6\text{LiF}$)¹⁴ and NF_3 ($\text{NF}_3 + 3\text{e}^- + 3\text{Li}^+ \rightarrow 3\text{LiF} + \frac{1}{2}\text{N}_2$)¹⁶ occurs on carbon cathodes at potentials of $\sim 2\text{--}3$ V vs. Li/Li^+ , thus the gases act as a highly-F-dense and electroactive molecular LiF source. Moreover, in **0**, we showed that the morphology of the electrochemically-formed LiF, which nucleates and grows as nanoscale particles (with diameters ranging from 20 nm to >400 nm) on the cathode substrate, was highly versatile and could be tailored by modulating conditions such as electrolyte, discharge rate, and capacity.¹⁵ Herein, we examine the electrochemical nucleation and growth of LiF from these perfluorinated gases to form an intimate coating on an electronically-conductive oxide for the first time (**Figure 6-1**). Owing to the good contact with MnO and the nano-crystallinity of LiF, we find that the electrochemically-formed, LiF-coated MnO exhibits higher utilization ($\sim 0.9 \text{ e}^-/\text{MnO}$) with larger particles (~ 400 nm), consistent with a higher degree of fluoridation, compared to the ball-

milled composites (~ 40 nm, <0.7 e⁻/MnO) and those fluoridated from salt-based reactions previously reported with similar particle sizes (~ 0.6 e⁻/MnO).^{86,87}

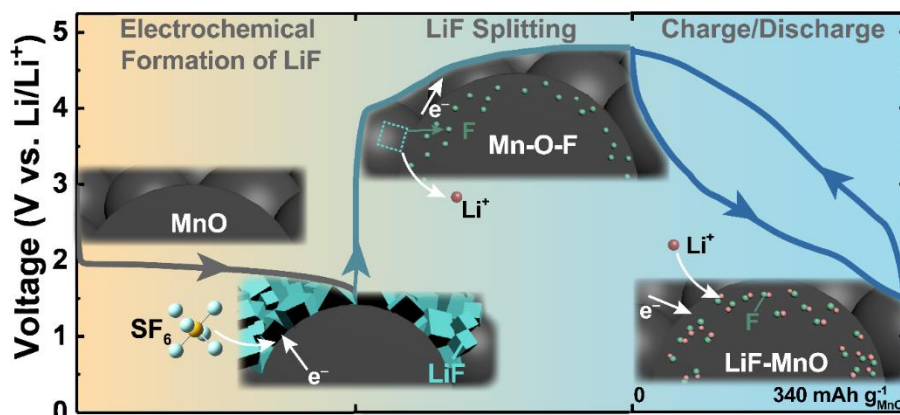


Figure 6-1 Schematic depicting electrochemical fluoridation of MnO cathodes using SF₆ gas as an exemplar fluorination source. Step 1: Electrochemical nucleation and growth of LiF occurs on MnO upon cathodic SF₆ reduction. Step 2: MnO/LiF electrodes are charged to induce electrochemical splitting of LiF and concurrent MnO fluoridation; as depicted, this process initiates at the surface of MnO particles and can continue into the bulk as charging proceeds. Step 3: Subsequent cycling occurs between the nominal end phases Mn-O-F ↔ LiF-MnO.

6.2 Experimental Methods

Chemicals and Materials. All chemicals, electrodes and cell-making materials were thoroughly dried and stored in an argon-filled glovebox (MBRAUN). LiClO₄ (99.99% trace metals basis, Sigma-Aldrich) and the Whatman filter paper (Grade QM-A, 2.2 μm pore size, 450 μm in thickness, Sigma Aldrich) were dried under active vacuum for 24 hours at 120 °C in a Buchi glass oven. Tetraethylene glycol dimethyl ether (TEGDME, 99%, Sigma-Aldrich), propylene carbonate (PC, 99.7%, Sigma-Aldrich), ethylene carbonate (EC, 99%, Sigma-Aldrich), and dimethyl carbonate (DMC, > 99.9%, Sigma-Aldrich) were stored inside the glovebox at room temperature.

Cathode Preparation. The as-received MnO particles (99%, Sigma-Aldrich, ~0.25 mm) were combined with Vulcan carbon (VC) (XC-72, Cabot Corporation) (MnO:VC=7:2 w/w), sealed in the glovebox, and ball-milled by a SPEX ball mill for 3 h. The ball-milled MnO/LiF composites were prepared by mixing the MnO with LiF (MnO:LiF = 1:1.2 m/m), as well as VC (20 wt% of total MnO/LiF composite) for 48 h using planetary milling at 400 r.p.m. (Retsch GmbH, Germany). The MnO/VC, and ball-milled MnO/LiF cathodes were fabricated in-house by uniformly coating sonicated inks composed of the as-prepared MnO composites, additional VC, N-Methyl-2-pyrrolidone (NMP), and polyvinylidene difluoride (PVDF) (with a weight ratio of PVDF:VC:MnO = 10:20:70) onto a sheet of Toray paper (TGP-H-030, Fuel cell earth). The final weight ratio of PVDF:VC:MnO = 10:35:55. The obtained coated Toray paper was dried at room temperature prior to being punched into circular disks (12 mm diameter), with a typical MnO loading of $1.12 \pm 0.17 \text{ mg}_{\text{MnO}} \text{ cm}^{-2}$ (error bar represents five measurements). The MnO cathodes were subsequently dried under active vacuum in a glass oven (Buchi) overnight at 90 °C.

Galvanostatic Discharge for LiF Formation. Two-electrode Swagelok-type Li–perfluorinated gas cells were constructed in an argon glovebox, with MnO cathode and a 9 mm diameter disk of Li metal as anode (0.75 mm thick, 99.9% metals basis, Alfa Aesar), which was prestabilized by soaking in 0.1 M LiClO₄ in PC for more than three days before use.¹²⁸ The separator (13 mm diameter glass fiber filter paper) was impregnated with 150 μL electrolyte solution (0.1 M LiClO₄ in TEGDME). SF₆ (Airgas, 99.999% purity) or NF₃ (Airgas, 99.999% purity) gas was introduced into cells following their assembly by purging the gas into the cell headspace within the glovebox for approximately 3 min, pressurizing it to ~1.6 bar, and then sealing the cell that contains excess amounts of SF₆ or NF₃ gas for subsequent discharge outside the glovebox. The cells were rested at open circuit voltage (OCV) for 15 h before the galvanostatic

discharge process, which were carried out (BioLogic VMP3 potentiostat or MPG2 workstation) at the specified current density with a voltage window ranging from OCV to a lower cutoff voltage of 1.6 V vs Li/Li⁺. The discharged cathodes were extracted from the cell, rinsed with dimethoxyethane (DME), dried and stored inside the glovebox.

Electrochemical Characterization: Two-electrode Swagelok-type Li-ion cells were constructed and sealed in an argon glovebox, with the Li metal as the anode and the LiF-coated or pristine MnO electrode (as indicated) as the cathode. The cells were cycled on a BioLogic VMP3 with 150 μ L 1 M LiClO₄ in EC/DMC (1:1 v/v) electrolyte impregnated into a glass fiber separator. Unless otherwise indicated, the cells were first constant current (CC) charged to 4.8 V, then constant voltage (CV) charged until the current dropped to half of the current used for CC charge. After the first charge process, the cells were galvanostatically cycled at the same rate as that for the first CC charge between 1.5 and 4.8 V.

Spectroscopic Measurements. ¹⁹F Nuclear Magnetic Resonance (NMR) measurements were performed using a Bruker Advance Neo 400 MHz NMR spectrometer. Samples were dissolved in deuterated D₂O (Sigma-Aldrich) with 2,2,2-trifluoroethanol (TFE, Sigma-Aldrich) as an internal reference. The solutions were then transferred into capped NMR tubes (Wilmad, 528-PP-7) for NMR analysis. The binding energies were calibrated by the adventitious carbon peak at 284.80 eV. Electron energy loss spectroscopy (EELS) was carried out on a JEOL 2010 FEG analytical electron microscope equipped with a Gatan image filter for EELS, operating at 200 kV in the parallel beam mode. The samples were quickly transferred into the TEM chamber for the measurement with minimum exposure to ambient.

Note that experimental details for all other testing and analysis techniques used in this chapter have already been provided in earlier chapters. Experimental procedures for SEM and XRD characterizations can be found in **0**, whereas those for Raman and XPS measurements can be found in **Chapter 3**.

6.3 Results and discussions

6.3.1 Electrochemical formation and characterization of LiF coating on MnO

MnO was chosen as a model substrate for fluorination in this work because it has been used in prior LiF splitting studies,^{84,86,87} providing sufficient data for comparison across methodologies, whereas few reports have investigated pre-lithiated Mn-containing compounds. The understanding gained from this study is expected to help with developing fluorinated practical oxide cathodes both without and with intrinsic Li sites. Due to the large particle size of the as-received MnO (~0.25 mm), a short ball-mill of 3 h was conducted on MnO/Vulcan carbon (VC, ~50 nm) mixture (MnO:VC=7:2 w/w) to reduce the particle size to $\sim 400 \pm 300$ nm (**Figure 6-2**). The resulting powder was then mixed with VC and polyvinylidene fluoride (PVDF) binder to form cathode materials (with a weight ratio of MnO:VC:PVDF = 55:35:10) and was coated onto Toray paper (5 wt% Teflon treated). In this work, 0.1 M lithium perchlorate (LiClO₄) was used as the salt to eliminate additional F sources in the electrolyte other than the fluorinated gas. For the first discharge (LiF formation step), tetraethylene glycol dimethyl ether (TEGDME) was used as the solvent given its ability to promote more film-like LiF upon SF₆ reduction (typical LiF particle sizes of ~30 nm with conformal coating on carbon) with better electrical contact with the underlying substrate, as opposed to larger discrete LiF particles (~100 nm) with exposed carbon surfaces as observed with higher-donor-number solvents like DMSO.¹⁵ In addition, SF₆ exhibits

higher discharge capacity in ethers than in carbonate solvents¹⁵ allowing more versatility for tailoring and studying electrochemically-formed LiF on MnO. Swagelok-type cells were assembled with Li anodes, the indicated cathode and electrolyte, and were purged with SF₆ or NF₃, pressurized to ~1 bar (typical gas solubilities ~1–5 mM)^{14,16} and sealed for testing.

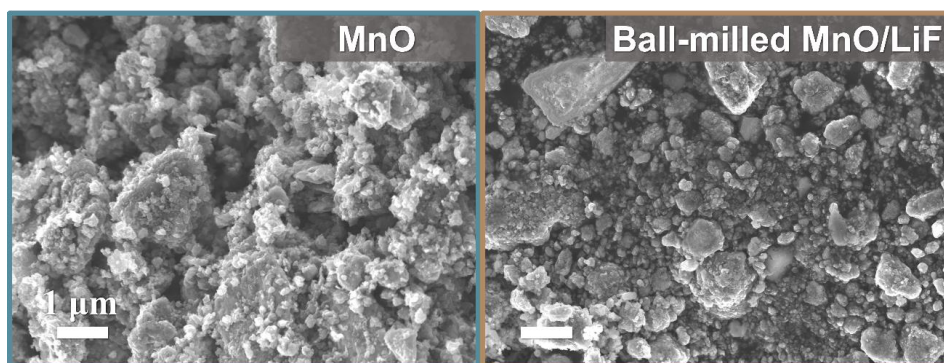


Figure 6-2 SEM of the ball-milled MnO and MnO/LiF powders (as indicated). Due to the large particle size of the as-received MnO (~0.25 mm), a short ball-mill of 3 h was conducted on MnO/Vulcan carbon (VC) mixture (MnO:VC=7:2 w/w) to reduce the particle size. The MnO/LiF composite (MnO:LiF = 1:1.2 m/m) contains 20 wt% of VC and was ball-milled for 48 h.

Typical first-discharge profiles under galvanostatic conditions are shown in **Figure 6-3a**. Without any fluorinated gas, MnO electrodes exhibited negligible capacity upon discharge (~30 mAh/g_{MnO}) as expected for Mn²⁺ which is inactive in this voltage window.²⁷⁷ In contrast, cells containing fluorinated gas exhibited electrochemical activity corresponding to gas reduction. The discharge potential of NF₃-containing cells (~2.1 V) at 75 mA/g_C (~48 mA/g_{MnO}) was similar to that on VC cathodes as measured previously,¹⁶ indicating that the inclusion of MnO does not significantly affect the reduction behavior of NF₃. Typical discharge capacities of Li–NF₃ cells on MnO/VC cathodes are 1100 mAh/g_{MnO} (~1700 mAh/g_C), corresponding to an NF₃ (consumed, assuming 3 e⁻ transfer per NF₃ molecule) to MnO molar ratio of 1:1. X-ray diffraction (XRD) in **Figure 6-3b** shows that LiF is the only crystalline phase formed following NF₃ reduction. From

scanning electron microscopy (SEM), a LiF layer was observed which covers the composite cathode, including the MnO particles, uniformly (**Figure 6-3c**).

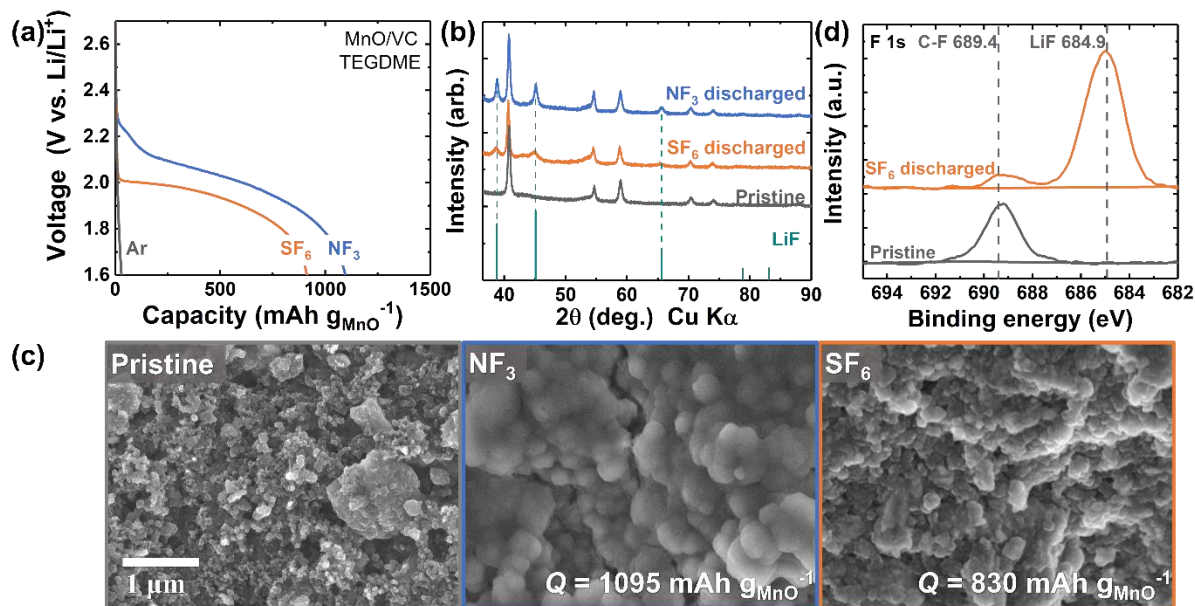


Figure 6-3 (a) Galvanostatic discharge profiles of Li-SF₆ and Li-NF₃ cells using MnO/VC cathodes as the substrate at 100 mA/g_c (~65 mA/g_{MnO}) and 75 mA/g_c (~48 mA/g_{MnO}), respectively. (b) X-ray diffraction of a discharged electrode in the Li-NF₃ ($Q = 1180 \text{ mAh/g}_{\text{MnO}}$) and Li-SF₆ ($Q = 830 \text{ mAh/g}_{\text{MnO}}$) cells. (c) SEM images of pristine electrodes and of electrodes discharged to full capacity using fluorinated gas as indicated. (d) High-resolution F 1s XPS spectra of the discharged electrode of a Li-SF₆ cell. To avoid binder-induced F signal, a non-fluorinated binder, polyacrylonitrile (PAN), was used in the cathode instead of PVDF, thus the capacity (~310 mAh/g_{MnO}) is lower than in (a) for this particular cell. The C-F peak at 689.4 eV is from Toray paper.

In comparison, discharge of MnO/VC electrodes with SF₆ gas at 100 mA/g_c (~65 mA/g_{MnO}) occurred ~100 mV below NF₃ throughout discharge, which is similar to previous discharge voltages of SF₆ on VC electrodes in TEGDME.¹⁵ Typical discharge capacities for SF₆ cells with

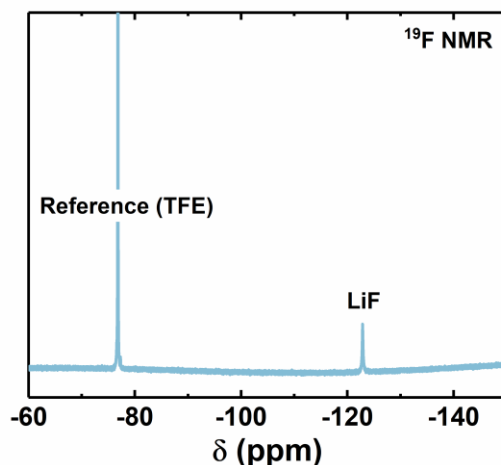


Figure 6-4 ^{19}F Nuclear Magnetic Resonance (NMR) spectra of the discharged MnO cathode (under SF_6) after soaking in D_2O . 2, 2, 2-trifluoroethanol was added into the solvent as reference.

MnO/VC electrodes are 900 $\text{mAh/g}_{\text{MnO}}$ ($\sim 1400 \text{ mAh/g}_\text{C}$), corresponding to a SF_6 (consumed, assuming 8 e^- transfer per SF_6 molecule) to MnO molar ratio of 0.3:1. In contrast to reduction of NF_3 , only very broad and weak LiF diffraction peaks were detected by XRD after reduction of SF_6 (**Figure 6-3b**), which indicates a substantially lower crystallinity and smaller particle sizes for the discharge product. Instead, X-ray photoelectron spectroscopy (XPS) was used to identify the composition of the formed phases. From the F 1s high-resolution scan (**Figure 6-3d**), a strong LiF peak at 684.9 eV was observed.²³² The existence of LiF was further confirmed from liquid ^{19}F nuclear magnetic resonance (NMR) spectroscopy (**Figure 6-4**) upon reacting discharged cathodes with water (D_2O) to solubilize the LiF, which yielded a strong peak at -122 ppm attributed to LiF.²⁷⁸ A negligible amount of S was detected in the discharged cathode from XPS (**Figure 6-5**). This is consistent with previous results that showed a tendency of reduced-S phases such as polysulfides to solubilize in the electrolyte upon discharge during SF_6 reduction. Therefore, both cathodes are

predominantly LiF-coated MnO with differing degrees of LiF crystallinity. From the SEM image in **Figure 6-3c**, the LiF layer formed using SF₆ was similarly uniform and conformal.

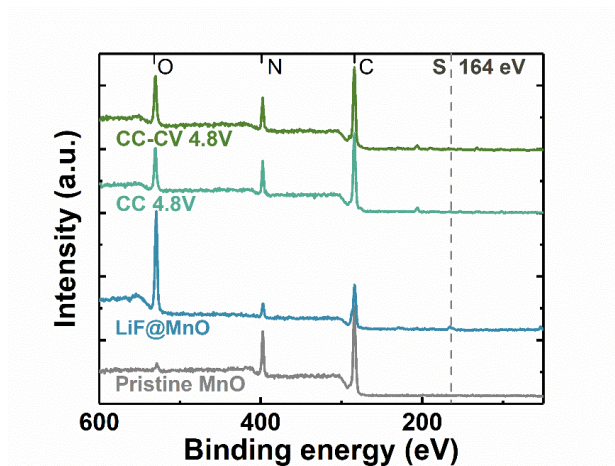


Figure 6-5. XPS survey scans of a pristine MnO/VC electrode, of LiF@MnO before first charge, and of LiF@MnO after first charge (LiF splitting) following either a constant current (CC) or constant current-constant voltage (CC-CV) protocol.

6.3.2 LiF splitting, MnO fluoridation and subsequent lithiation capacity

The MnO activation (charge) process was next investigated using 1 M LiClO₄ in ethylene carbonate and dimethyl carbonate (EC/DMC, v:v = 1:1) as electrolyte, which is more amenable to tolerate the high potentials required upon subsequent charging and LiF splitting when MnO is the substrate. Cells consisted of fresh Li anodes and MnO-containing cathodes, *i.e.* previously-discharged MnO/VC cathodes under NF₃ or SF₆. In these first experiments, the re-assembled cells in carbonate electrolyte contained no fluorinated gas. Except where otherwise noted, the first charge of the MnO, with or without LiF present, consisted of a constant current (CC) process at 20 mA/g_{MnO} (~0.05 C) to a cutoff of 4.8 V vs. Li/Li⁺, followed by a constant voltage (CV) hold until the current decreased below 10 mA/g_{MnO}.^{84,86} Henceforth, discharge rates are normalized to

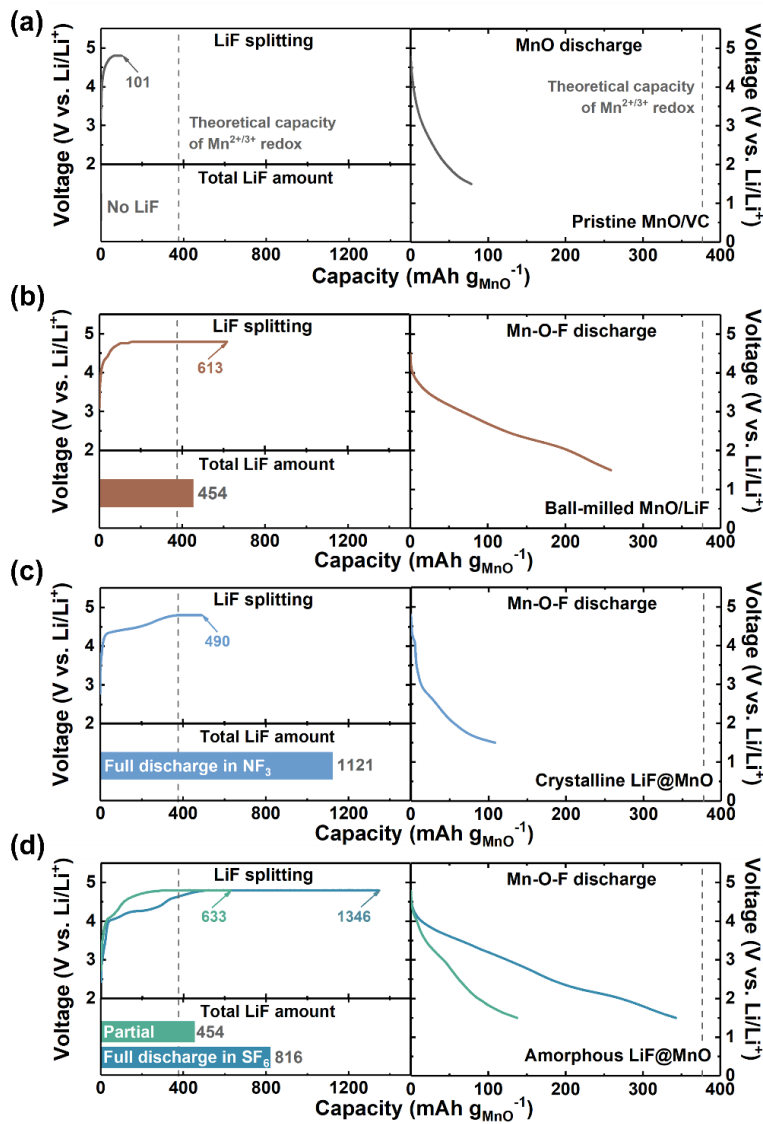


Figure 6-6 Electrochemical profiles of the first charge (LiF splitting) and the subsequent first discharge of the (a) pristine MnO, (b) ball-milled MnO/LiF, (c) LiF@MnO (from fully-discharged Li–NF₃ cells), and (d) LiF@MnO (from partially and fully-discharged Li–SF₆ cells) with 1 M LiClO₄ EC/DMC electrolyte. All the cells were CC charged at 20 mA/g_{MnO} (~0.05 C) to 4.8 V, then CV charged with a cutoff of 10 mA/g_{MnO}, then CC discharged at 20 mA/g_{MnO} to 1.5 V. The total LiF amount relative to MnO are indicated in each panel, which was calculated based on either the LiF added (for ball-milled sample in part b, assuming 1 e⁻/LiF), or the discharge capacity of Li–SF₆ or NF₃ cell (for c and d). For the latter, each electron was assumed to produce 1 LiF for NF₃, or 6/8 LiF for SF₆. The theoretical capacity of MnO assuming Mn^{2+/3+} redox, 378 mAh/g_{MnO}, is indicated as a grey dashed line.

the weight of MnO instead of carbon as Mn redox is the major contributor of reversible capacity. The theoretical capacity of Mn-O-F, assuming $\text{Mn}^{2+}/\text{Mn}^{3+}$ redox, is 378 mAh/g_{MnO}. For MnO/VC without LiF, the charge capacity was limited (101 mAh/g_{MnO}, **Figure 6-6a**) and reflected only capacitive-like behavior, likely dominated by the carbon particles (*i.e.* no voltage plateau was observed). During the following discharge, small capacity of <80 mAh/g_{MnO} was observed, which is ~2x of that observed before with Ar discharge (**Figure 6-3a**) given the larger voltage window (~2x, 4.8 V –1.5 V vs. ~3.1 V–1.6 V). This indicates no significant change to the MnO phase, which remained electrochemically inactive.

A mechanically ball-milled MnO/LiF composite was prepared for comparison, with an MnO/LiF molar ratio of 1:1.2 with 20% LiF excess, and 20 wt% of VC, comparable to that used previously.⁸⁴ The average particle size of the obtained MnO/LiF is $\sim 40 \pm 25$ nm as measured from SEM (**Figure 6-2**), substantially smaller than that used for electrochemical fluoridation used herein. Given the amount of LiF present in the as-prepared ball-milled cathode, full splitting of LiF would correspond to a capacity of 454 mAh/g_{MnO}, which is in excess of the theoretical capacity of MnO (378 mAh/g_{MnO}) owing to excess LiF. Experimentally, an initial charge capacity even higher, at 613 mAh/g_{MnO}, was observed (**Figure 6-6b**). Excess charge capacity beyond that used to fluorinate MnO is attributed to a combination of capacitive contributions and possibly to side reactions such as electrolyte oxidation, fluorination, or carbon oxidation.^{118,279} We note that a capacity higher than the theoretical does not imply full conversion of MnO to MnOF. The following discharge/lithiation of the ball-milled MnO/LiF system exhibits a higher capacity of 259 mAh/g_{MnO} than that of pristine MnO/VC without LiF, proving successful activation of MnO to the Mn-O-F phase which then serves as a conversion Li-ion cathode. However, the lower capacity compared to the theoretical (378 mAh/g_{MnO}) confirms the fact that not all MnO was accessed by

fluoridation in this system. The lower capacity than reported elsewhere for ball-milled samples ($\sim 345 \text{ mAh/g}_{\text{MnO}}$) is attributed to the larger particle size ($\sim 40 \pm 25 \text{ nm}$) used here, vs. 8 nm in literature, since the fluoridation process is mainly surface-controlled and increased particle size reduces the total active surface area for F incorporation.^{84,273}

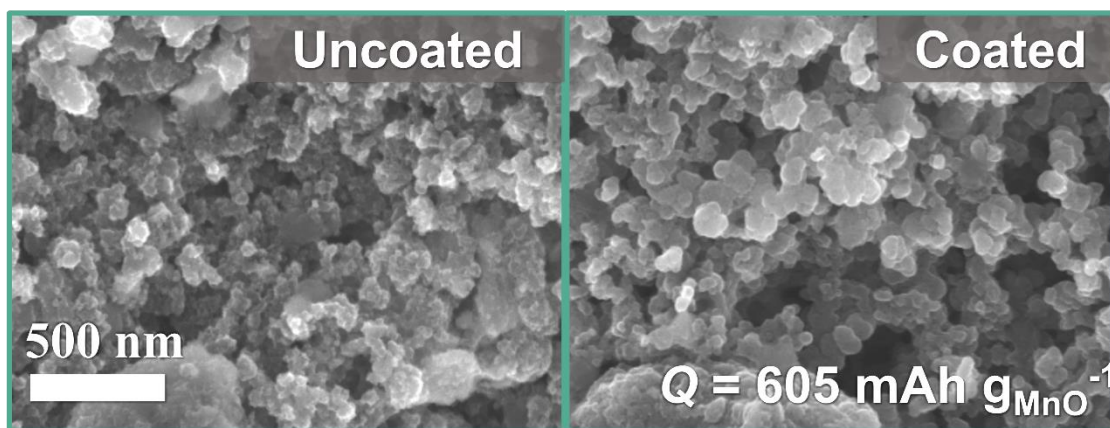


Figure 6-7 SEM of MnO/VC cathodes in partially discharged Li-SF₆ cell, with a capacity of $\sim 605 \text{ mAh/g}_{\text{MnO}}$ (corresponding to LiF amount of $454 \text{ mAh/g}_{\text{MnO}}$). Two different morphologies were observed: the one on the left shows small discrete particles, which is the pristine (uncoated) morphology; while the one on the right shows larger particle sizes with film-like structure, indicating the presence of the coating layer.

Electrochemically LiF-coated MnO cathodes (henceforth ‘LiF@MnO’) formed from SF₆ or NF₃ reduction were next compared. For LiF@MnO formed from fully-discharged Li-NF₃ reduction (**Figure 6-6c**), a relatively limited charge (LiF splitting) capacity of $490 \text{ mAh/g}_{\text{MnO}}$ was observed despite the large amount of LiF ($>1100 \text{ mAh/g}_{\text{MnO}}$ or 1.9x excess), implying not all LiF was electronically or electrochemically accessible for subsequent splitting. As a result, only limited capacity ($\sim 108 \text{ mAh/g}_{\text{MnO}}$) was delivered during the subsequent discharge/lithiation of MnO-F, reflecting a low degree of MnO fluoridation/activation. The insufficient LiF splitting and MnO activation may be attributed to the large particle size of the crystallized LiF formed. Next,

to form similar amount of LiF as that in the ball-milled MnO/LiF system, an SF₆ cell was partially discharged (LiF amount of 454 mAh/g_{MnO}). The obtained LiF@MnO yielded a similar capacity upon charge/activation (633 mAh/g_{MnO}) as that for ball-milled MnO/LiF (**Figure 6-6d**), indicating that the charge capacity is proportional to the total LiF quantity. The subsequent discharge/lithiation capacity of this LiF@MnO from the partially-discharged SF₆ cell was, however, only 137 mAh/g_{MnO}. We hypothesize that this low lithiation capacity is caused by the low degree of coating of MnO by LiF, recalling that LiF forms both on MnO and on VC (with the latter not contributing to reversible capacity) as was further supported by SEM images (**Figure 6-7**). Thus, to test this hypothesis, LiF@MnO electrodes were formed with even higher LiF amounts by discharging Li-SF₆ cells to completion. As is shown in **Figure 6-6d**, a larger capacity (> 1300 mAh g_{MnO}⁻¹) was attained from the first charge of the higher-LiF-loading LiF@MnO (typical resulting CV charge hold times were ~40 h). This increased capacity can be attributed to the increased amount of LiF, which, if fully decomposed, can contribute a capacity of ~820 mAh/g_{MnO}. The LiF@MnO from the fully-discharged SF₆ cell yielded a much higher lithiation capacity of ~340 mAh/g_{MnO}, equivalent to 0.9 e⁻/MnO, comparable to the highest MnO utilization reported to date.⁸⁴ Additional evaluation of the electrochemical behavior difference of ball-milled MnO/LiF and LiF@MnO (from SF₆ and NF₃ discharge) is shown *via* differential capacity plots in **Figure 6-8**. During first charge, the LiF@MnO from the fully or partially discharged Li-SF₆ cells exhibit lower onset potential (~4.0 V) than that of the ball-milled MnO/LiF and NF₃-formed LiF@MnO (~4.2 V), indicating clearly that the former two cathodes are more favorable for LiF splitting. During discharge, LiF@MnO from NF₃ discharge and partial SF₆ discharge exhibited negligible activity. In contrast, the LiF@MnO from full SF₆ discharge and the ball-milled MnO/LiF showed similar profiles with two cathodic peaks, in agreement with that observed in a

previous study where two peaks located at 2.5 V and 3.75 V were observed and attributed to Mn redox.⁸⁴ Therefore, LiF@MnO from fully discharged SF₆ cells was used in all following experiments.

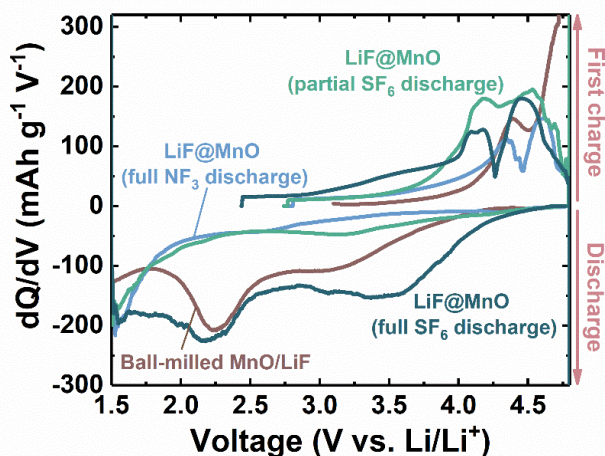


Figure 6-8 Differential capacity plot derived from the galvanostatic discharge profiles in Figure 6-6.

We next investigated the potential dependence of F-incorporation in MnO during the LiF splitting process on first charge in greater detail. LiF@MnO was charged following two additional procedures: CC–CV charge up to 4.7 V, and 4.8 V CC charge without a CV hold. Both charge protocols yielded significantly smaller LiF splitting capacity (~ 300 vs. > 900 mAh/g_{MnO} for a CC–CV charge up to 4.8 V), and only limited capacity (~ 100 mAh/g_{MnO}) upon subsequent discharge (**Figure 6-9a**), indicating insufficient MnO activation. The results reveal that CV charge at 4.8 V is crucial for the activation of bulk MnO to Mn–O–F. This was further confirmed by examination of the bulk Mn valence state by electron energy loss spectroscopy (EELS), focusing on the two charging protocols up to 4.8 V. In **Figure 6-9b**, the Mn L-edge showed negligible change after only CC charge, however, inclusion of the CV step at 4.8 V resulted in a Mn L₃ peak shifted to higher energy (from 640.2 eV to 641.3 eV), with a significant decrease in the ratio of L₃/L₂ peak

areas, corresponding to oxidation of Mn. Raman spectroscopy was further used to probe the MnO bonding environment change (**Figure 6-9c**). The vibrational band at 645 cm^{-1} (stretching A_{1g} modes of Mn–O bonds in MnO_6 octahedra) and low frequencies ($<360\text{ cm}^{-1}$, skeletal vibrations)

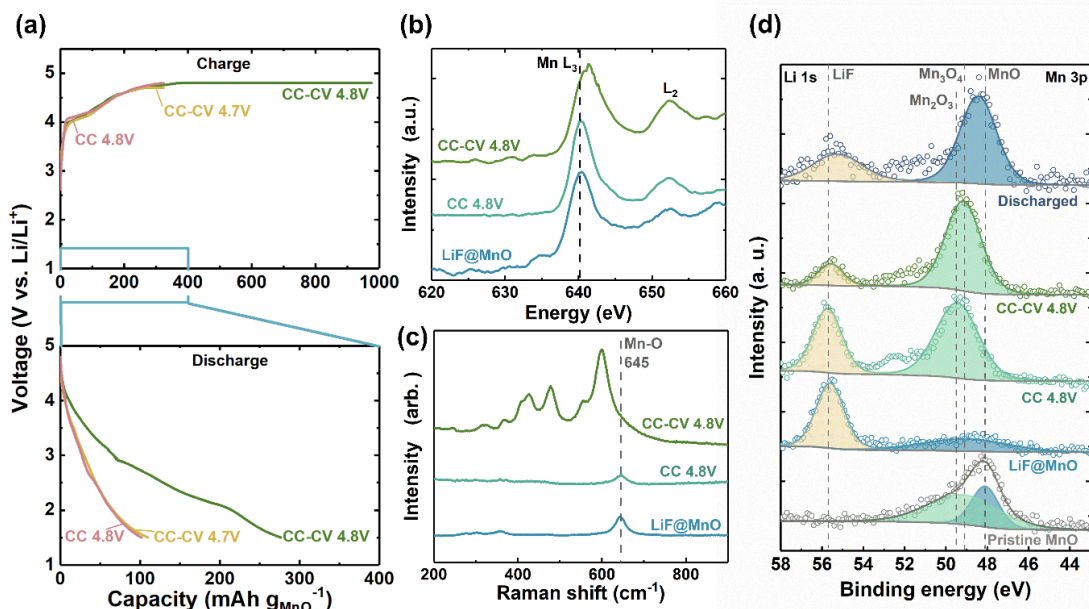


Figure 6-9 (a) First charge (LiF splitting) and discharge (lithiation) profiles of LiF@MnO (from fully discharged Li–SF₆ cells; also used for part b–d) at 20 mA/g_{MnO} with different charge procedures: CC-CV charged to 4.8 V, CC-CV charged to 4.7 V, or CC charged to 4.8 V. Both CV charges were cut off at 10 mA/g_{MnO}. The lower voltage cutoff upon discharge was 1.5 V. (b) EELS of Mn L-edge and (c) Raman spectra for LiF@MnO before charge, and after CC or CC-CV charge as indicated. (d) High-resolution Li 1s and Mn 3p XPS spectra of the pristine MnO electrode and LiF@MnO at different charge/discharge states. The XPS profile for pristine MnO, CC charged, CC-CV charged, and discharged electrodes are normalized by the Mn 3p peak integrated area. Binding energy reference peaks: LiF 55.7 eV, Mn₂O₃ 49.5 eV, Mn₃O₄ 49.1 eV, and MnO 48.1 eV.²³² To avoid binder-induced fluoridation, PAN binder was used in the cathode instead of PVDF.

belong to Mn_3O_4 instead of MnO ,²⁸⁰ given that, as was found from previous studies, MnO is easily transformed to Mn_3O_4 due to beam irradiation during Raman measurement.²⁸¹⁻²⁸³ Consistently, the band located at 645 cm^{-1} corresponding to the initial MnO phase showed negligible change when CC charged to 4.8 V. In contrast, CV charge resulting in a significant red shift of the Mn-O stretch (to $\sim 600\text{ cm}^{-1}$) along with the appearance of multiple small-intensity bands at lower frequencies, which cannot be assigned to any single manganese oxide phase.²⁸⁴ The decreased frequency is reflective of the increased Mn-O bond length,²⁸⁵ while the different band positions indicate a more complex Mn bonding environment induced by incorporation of F^- ions into the MnO lattice, resulting in more defect sites, and potential lattice distortion due to the Jahn-Teller effect of Mn^{3+} .⁶⁸ These findings are consistent with those observed in previous studies on MnO/LiF , where a defective Mn-O-F spinel-like phase was observed after first charge.^{84,87} Notably, such lattice structure change cannot be triggered without LiF : for pristine MnO without LiF coating, negligible change in Raman spectra can be observed after being CC-CV charged to 4.8 V (**Figure 6-10**).

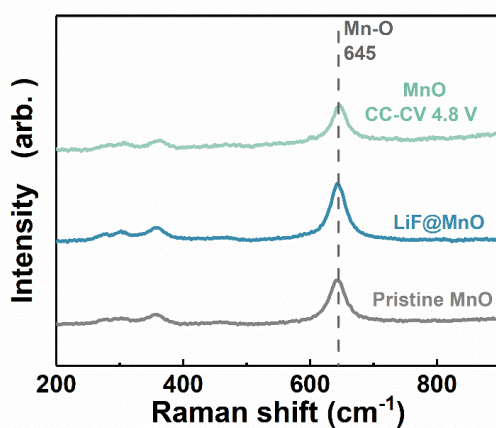


Figure 6-10 Raman spectra of the pristine MnO/VC electrode, $\text{LiF}@MnO$ (uncharged), and CC-CV charged MnO/VC (without LiF presence). Negligible change in Mn bonding environment can be observed.

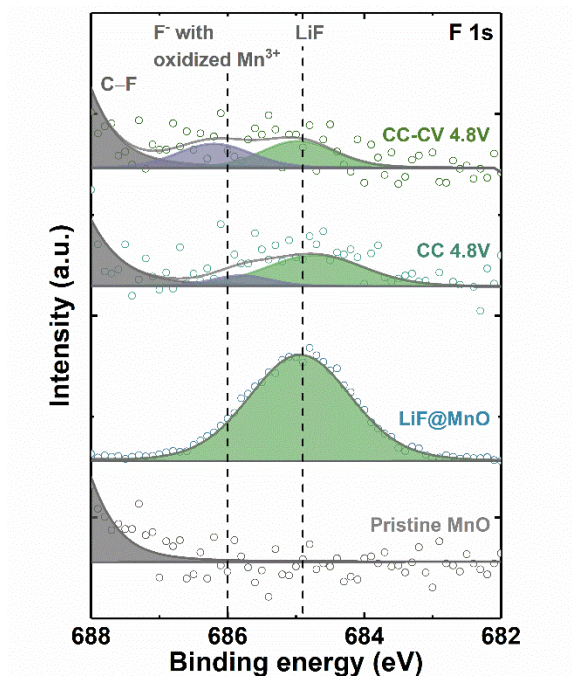


Figure 6-11 High-resolution F 1s XPS spectra of the pristine MnO electrode and LiF@MnO at different charge states. Binding energy reference peaks: LiF 684.9 eV, covalent C–F 689.4 eV,²³² and F[−] with oxidized Mn³⁺ 686.0 eV.⁸⁴ To avoid binder-induced fluoridation, PAN binder was used in the cathode instead of PVDF. The covalent C–F signal were from substrate Toray paper. Due to the weaker adhesion of PAN, some electrode powder was detached from the substrate after long cell testing and the underlying Toray paper became exposed, resulting in strong C–F signal. As a result, the ionic F signal is relatively weak.

The redox process on the MnO surface was also investigated using XPS. From F 1s XPS (**Figure 6-11**), the decrease in integrated LiF peak intensity, centered at 684.9 eV, after CV charge is consistent with electrochemical LiF splitting initiation at 4.8 V. The increased contribution from the peak at 686.0 eV, which corresponds to the F[−] ion bonding with the Mn ion,⁸⁴ also supports the enhanced depth of LiF splitting and F-incorporation upon CC-CV charge. In addition, Li 1s and Mn 3p, which have closely-located binding energies, were examined to provide a clearer observation of the correlated Li and Mn peak evolution (**Figure 6-9d**). All spectra are normalized

by Mn 3p peak integrated area, except for the uncharged LiF@MnO, in which the Mn signal is strongly blocked by the LiF layer on the surface. After the CC charge, the MnO surface was oxidized to a phase resembling Mn₃O₄ (Mn^{2+/3+}) or Mn₂O₃ (Mn³⁺), and retained its oxidation state after further CV charge, suggesting that Mn₃O₄/Mn₂O₃-like phases precede significant fluoridation. Correspondingly, the Li 1s peak intensity decreased significantly after CV charge, indicating LiF decomposition. Upon subsequent discharge/lithiation, the Li 1s peak recovered and the Mn valence state reverted to be close to Mn²⁺, consistent with reversible redox.

6.3.3 Rate capability of Mn-O-F derived from different fluorination sources

We next investigated the attainable rate performance of the first Mn-O-F discharge/lithiation (**Figure 6-12a**), with the derived Ragone plot and comparison with other MnO/LiF methodologies shown in **Figure 6-12b**. The MnO utilization (#e⁻/MnO) is calculated based on the discharge/lithiation capacity. The highest MnO utilization were achieved at low rate (<30 mA/g_{MnO}) in all systems. The LiF@MnO (~400 nm) exhibits high MnO utilization (~0.9 e⁻/MnO), comparable to the nano-scale (~8 nm) ball-milled MnO/LiF composites reported previously,⁸⁴ and much higher than that of ball-milled MnO/LiF with ~40 nm particle size (<0.7 e⁻/MnO). This indicates that the stringent particle size limitation of MnO in previous studies is no longer critical when LiF is nano-crystallized and in intimate contact with MnO. In addition, the MnO/LiPF₆ system reported elsewhere, where LiF is formed *in situ* from LiPF₆ decomposition,⁸⁷ used MnO particles with size ~50 nm – 2 μm, similar to that of LiF@MnO, but only exhibits ~0.5 e⁻/MnO utilization at ~25 mA/g_{MnO}. As for the rate capability, LiF@MnO demonstrated the highest MnO utilization among all MnO/LiF systems with particle sizes ≥ 40 nm. Notably, a relatively steep capacity decrease, from 343 mAh/g_{MnO} to 184 mAh/g_{MnO}, was observed for the LiF@MnO as the

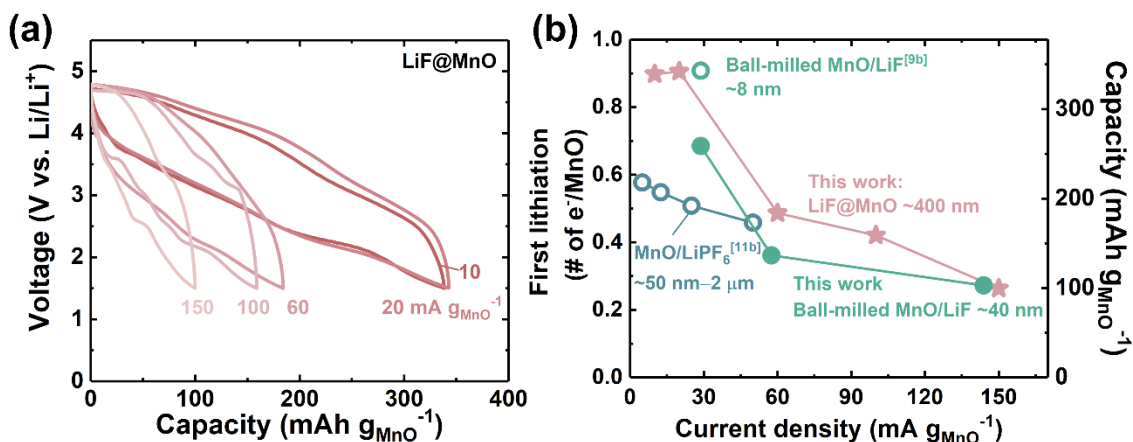


Figure 6-12 (a) Rate capability of Mn-O-F. The discharge rate of 10, 20, 60, 100, 150 mA/g_{MnO} correspond to 0.025, 0.05, 0.15, 0.25, and 0.40 C, respectively. The Mn-O-F were derived from LiF@MnO (from fully discharged Li-SF₆ cells; also used for part b) by first CC charge at the corresponding rates to 4.8 V and then CV hold till current drop to half of the initial current. (b) Ragone plot comparing the electrochemical performance of LiF-MnO systems as Li-ion cathodes: Ball-milled MnO/LiF composite with an average particle size of ~8 nm (data from Ref. 84) or ~40 ± 25 nm (synthesized and measured in this study); LiF formed *via* LiPF₆ decomposition (data from Ref. 87); and electrochemically-formed LiF@MnO (this study).

current density increased from 20 mA/g_{MnO} (~0.05 C) to 60 mA/g_{MnO} (~0.15 C). Further increasing the current density to up to 150 mA g_{MnO}⁻¹ results in capacity drop to ~100 mAh/g_{MnO}. It is noted that, when cycled at low rates (≤ 20 mA/g_{MnO}), although the attainable capacities are similar, lowering the current density is helpful for reducing voltage hysteresis of LiF@MnO between charge and discharge (**Figure 6-12a**). A similar trend was also observed for ball-milled MnO/LiF prepared in this work, where the capacity decreased from 259 mAh/g_{MnO} to 136 mAh/g_{MnO} as the rate increased to ~60 mA/g_{MnO}, and was comparable to that of LiF@MnO at the highest current density of ~150 mA/g_{MnO}. Therefore, this suggests that the conversion reaction between Mn-O-F

and MnO-LiF is kinetically limited, regardless of the LiF morphology, which may be caused by slow diffusion in the solid phase.

6.3.4 Trace SF₆ as additive for improved cyclability

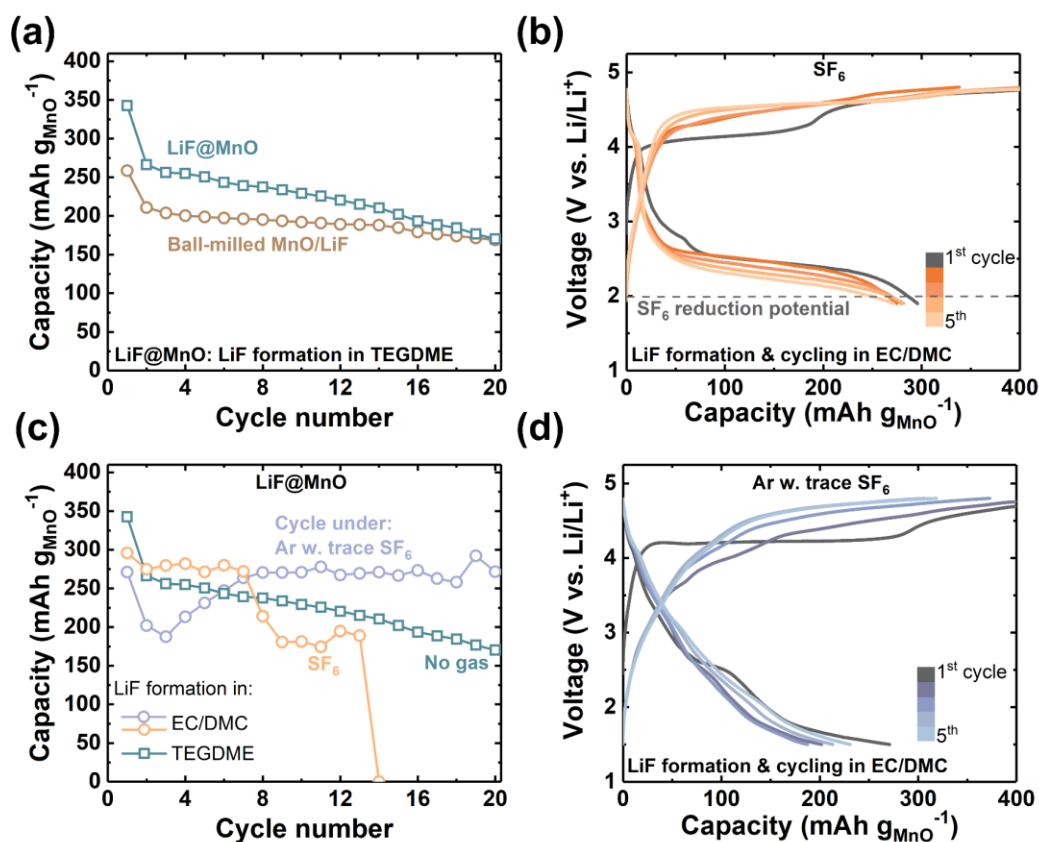


Figure 6-13 (a) Discharge capacities as a function of cycle number of ball-milled MnO/LiF (~40 nm) cathodes and LiF@MnO cathodes (LiF formed from SF₆ discharge in 0.1 M LiClO₄ TEGDME electrolyte). (b) and (c) Electrochemical profiles of the first five cycles of LiF@MnO (LiF formed from SF₆ reduction in 1 M LiClO₄ EC/DMC electrolyte). After LiF formation, (b) the cell was directly cycled under SF₆, or (c) purged with Ar, then cycled. (d) Discharge capacities as a function of cycle number of LiF@MnO cathodes in b and c, compared with the LiF@MnO with LiF formed in TEGDME electrolyte and cycled with no gas present (same data as LiF@MnO in part a). All cells were cycled with 1 M LiClO₄ in EC/DMC electrolyte at 20 mA/g_{MnO} (~0.05 C).

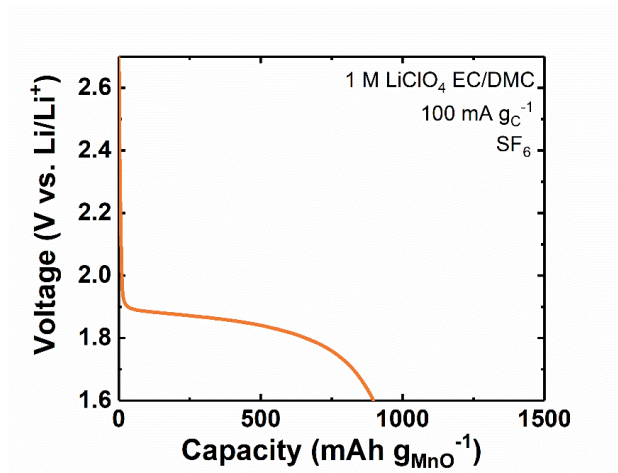


Figure 6-14 Galvanostatic discharge profile of Li–SF₆ cell with MnO/VC as cathode substrate and 1 M LiClO₄ EC/DMC as electrolyte at a rate of 100 mA/g_C.

When cycled at 20 mA/g_{MnO} (~0.05 C) with 1 M LiClO₄ EC/DMC electrolyte, both LiF@MnO and ball-milled MnO/LiF (~40 ± 25 nm) showed capacity fade from ~340 and 259 mAh/g_{MnO} respectively to ~170 mAh/g_{MnO} after 20 cycles (**Figure 6-13a**). The capacity fade can be attributed in part to the severe morphological changes upon repeated lithiation/delithiation and corresponding conversion of Mn-O-F to LiF-MnO, leading to gradual electronic disconnection and loss of active F for re-incorporation into the parent MnO phase.⁸⁶ Therefore, instead of fluorinated salts as used previously to resupply F to the MnO phase,^{86,87} we here demonstrate that regulated amounts of dissolved SF₆ (SF₆ solubility in organic solvents: ~ 2 mM)¹⁴ can function as an effective electrolyte additive and F source. These experiments also allowed examination of the potential for LiF formation and cycling to occur in the same cell, *i.e.* avoiding the need to change electrolyte to remove residual gas as before. The initial high-capacity LiF formation step was therefore conducted first in a Li–SF₆ cell discharged to full capacity in 1 M LiClO₄ EC/DMC electrolyte (**Figure 6-14**). Following charge activation and direct cycling with an SF₆ gas headspace present, a long discharge plateau (~250 mAh/g_{MnO}) at ~2.5 V was observed upon

subsequent discharge, the features of which are similar to that observed in Li-SF₆ cells with a characteristic “sudden death” (voltage drop) in the end of discharge (**Figure 6-13b**). These features indicate that the discharge activity upon cycling remains governed by SF₆ reduction when there is a large reservoir of SF₆ in the cell. The slightly increased SF₆ discharge potential at ~2.4 V (discharge potential of SF₆ cell at the same rate with pristine MnO/VC is ~2.0 V, **Figure 6-15**) is unclear at present, but could be attributed to a cathode morphology change caused by MnO fluoridation. Though good capacity retention (>270 mAh/g_{MnO}) was attained for the first five cycles, the cell discharge capacity dropped rapidly to ~180 mAh/g_{MnO} by the 9th cycle and became unstable (exhibited significant voltage fluctuation) at the 14th cycle causing cell termination (**Figure 6-13c**). We hypothesize that the instability observed from extended cycling can be attributed to the accumulation of excessive LiF/F⁻ in the cathode, which is detrimental given passivating qualities of LiF.

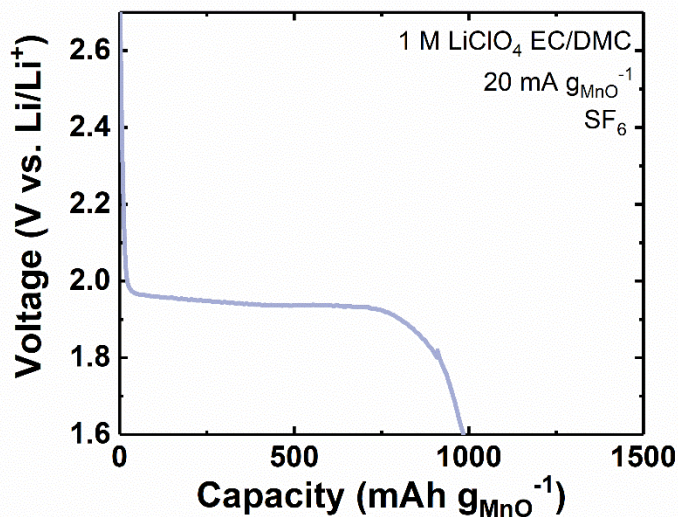


Figure 6-15 Galvanostatic discharge profile of Li-SF₆ cell with MnO/VC as cathode substrate and 1 M LiClO₄ EC/DMC as electrolyte at a rate of 20 mA/g_{MnO}.

To test this hypothesis and to further improve the cyclability, following the LiF-forming discharge step in 1 M LiClO₄ EC/DMC, cells were then briefly purged with Ar prior to continued cycling to remove excessive SF₆ in the headspace. A discharge profile similar to that of LiF@MnO without SF₆ (**Figure 6-6d**) is obtained, with the exception of a slightly extended tail at the end of discharge at ~1.5 V (**Figure 6-13d**). This is likely caused by the trace amount of SF₆ left in the cell that was not removed by Ar purging due to the high molecular weight of SF₆. The lower SF₆ reduction voltage than that observed with extra SF₆ present (**Figure 6-13b**) can be attributed to the concentration overpotential. Despite the lower capacity (271 mAh/g_{MnO} vs. 340 mAh/g_{MnO} for LiF@MnO formed with TEGDME electrolyte) at the beginning of cycling, which might be caused by the solvent-induced LiF crystallinity and particle size difference, this cell exhibits an improved cyclability with capacity higher than 270 mAh/g_{MnO} retained after 20 cycles (**Figure 6-13c**). The detailed mechanism of continued SF₆ reactivity over cycling will be investigated in future studies. However, these findings overall indicate the potential to explore future electroactive F additives to dynamically repair oxide phases as they become F-depleted. In particular, reduction of perfluorinated gases as studied herein occurs well within the electrochemical stability window of the electrolyte, providing a potentially softer fluorination route than those currently reported. The overall fluorination methodology is, however, currently limited by aggressive high voltages and charge protocols demanded by the intrinsic oxide redox states, which are too high for MnO to likely be feasible for practical cells. We anticipate potential for this methodology of LiF coating and dynamic fluoridation to be adaptable to future oxide substrates with lower oxidation potentials and more complex structures beyond that of the simpler binary phases.

6.4 Conclusions

Activation of the binary oxide MnO to Mn-O-F in the presence of LiF was demonstrated using electrochemically-formed LiF grown by the reduction of perfluorinated gas. The small feature size of LiF, which grows directly onto the electronically conductive surfaces of MnO and is therefore in intimate contact with the substrate, allows for effective LiF splitting upon subsequent charge and a high degree of fluoridation, as indicated by high capacities (up to 340 mAh/g_{MnO}) subsequently accessible upon Li⁺ cycling. These capacities correspond to high MnO utilization (~0.9 e⁻/MnO) and are obtained with moderate particle sizes (~400 nm), demonstrating that the stringent particle size requirement for high MnO utilization observed in previous studies (<10 nm) is not necessary as long as LiF is nano-crystallized and in intimate contact with MnO. The LiF@MnO exhibits improved rate capability compared to other methodologies used to source LiF into a MnO cathode with particle sizes ≥ 40 nm. Additionally, SF₆ was shown to be an effective electrolyte additive to support an F-enriched environment near MnO during cycling, leading to stable cycling with capacities ~270 mAh/g_{MnO} at 20 mA/g_{MnO} over at least 20 cycles. This study indicates that previously-reported limits on oxide fluoridation can be overcome by methodologies that allow for improved control over LiF quantity, particle sizes, and overall morphology, which can further contribute to the development of other high-performance cell cathode materials with F substitution (*e.g.* Li-containing oxides with disordered rock-salt or layered structures) in future work.

Chapter 7: Conclusions and Outlook

7.1 Conclusions

In summary, this thesis explored the governing parameters for fluoride/fluorine bond redox activities, including both intrinsic (*e.g.* molecular structures) and extrinsic (*e.g.* electrolyte solvent properties, reaction rates) factors, and their implications in Li and Li-ion batteries. These understandings present multiple tools for tuning the fluoride redox to the desired voltage and rate, or to form F-containing precipitates with ideal morphologies, and thus will expand the design landscape of fluoride-based battery materials, such as cathodes, electrolytes, and additives. In particular, three different bonds were examined in detail: sulfur–fluorine (S–F, **Chapter 2 and 3**) carbon–fluorine (C–F, **Chapter 4 and 5**), and manganese–fluorine (Mn–F, **Chapter 6**) bonds.

In **Chapter 2**, the effect of solvent fluoride solvation property on the S–F bond conversion in lithium-sulfur hexafluoride (Li–SF₆) primary battery was investigated. We reported two viable strategies to improve the solvation of the passivating discharge product, lithium fluoride (LiF), which contributed to improved battery rate capability. Operating at moderately elevated temperatures, *e.g.* 50 °C, in DMSO dramatically improves LiF solubility and promotes sparser and larger LiF nuclei on gas diffusion layer (GDL) electrodes, leading to capacity improvements of ~10x at 120 μA/cm². More aggressive chemical modification of the electrolyte by including a tris(pentafluorophenyl)borane (TPFPB) anion receptor further promotes LiF solubilization; capacity increased even at room temperature by a factor of 25 at 120 μA/cm², with attainable capacities up to 3 mAh/cm². This work shows that bulk fluoride-forming conversion reactions can be strongly manipulated by tuning the electrolyte environment to be solvating towards F⁻, and that significantly improved rate capability can be achieved.

Chapter 3 examined the molecular design strategies to facilitate S–F bond reduction in pentafluorosulfanyl ($-\text{SF}_5$)-containing reactants, where one of the F in SF_6 is substituted by aromatic groups. We reported a family of fluorinated reactants based on pentafluorosulfanyl arenes ($R\text{-Ph-SF}_5$), where the aromatic structure (Ph) improves the molecular polarity and facilitate electron transfer, while the ring substitution group (R) provides additional handles to tune the reduction potential by affecting the electron distribution on $-\text{SF}_5$ group. These $R\text{-Ph-SF}_5$ reactants allow for high electron-transfer numbers (up to $8\text{-e}^-/\text{reactant}$) by exploiting multiple coupled redox processes including extensive S–F bond breaking, yielding capacities of $861\text{ mAh/g}_{\text{reactant}}$ and voltages up to $\sim 2.9\text{ V}$ when used as catholytes in primary Li cells. At a cell level, gravimetric energies of 1085 Wh/kg are attained at moderate temperatures of $50\text{ }^\circ\text{C}$, with 853 Wh/kg delivered at $>100\text{ W/kg}$, exceeding all leading primary batteries based on electrode + electrolyte (sub-stack) mass. Voltage compatibility of $R\text{-Ph-SF}_5$ reactants and carbon monofluoride (CF_x) conversion cathodes further enabled investigation of a hybrid battery containing both fluorinated catholyte and cathode. The hybrid cells reach extraordinarily high cell active mass loading ($\sim 80\%$) and allow for significant boosting of sub-stack gravimetric energy of Li-CF_x cells by at least 20% while exhibiting good shelf life and safety characteristics.

In **Chapter 4**, we turned our focus to C–F bonds and scrutinized the affecting parameters for C–F redox in high F-content materials. We examined the possibility to conduct multi-electron carbon reduction using a candidate class of liquid CF_x analogues, perfluoroalkyl iodides ($\text{C}_n\text{F}_{2n+1}\text{I}$, with F/C ratios of $x > 2$), in supporting electrolyte as catholytes for Li cells. The large, polarizable iodine supports electrochemical reduction with concerted F^- ligand expulsion, forming LiF as the main solid discharge product. Under initial conditions (1 M reactant and 0.3 mA/cm^2 in dimethylsulfoxide), only limited defluorination ($1.5\text{ e}^-/\text{molecule}$) is accessed. Governing factors

for C–F bond redox are further investigated, including reactant concentration, discharge rate, temperature, and solvent properties including catholyte viscosity. A maximum of 8 e⁻/C₆F₁₃I, or 8/13 available F, is accessible in the voltage range 2.8–1.9 V vs. Li/Li⁺ with low reactant concentrations (0.1 M) and rates (20 μA/cm²). The data indicate that multiple handles exist to tailor extended C–F bond activation in these reactants. However, premature reaction termination caused by deactivation of intermediates, which is particularly exacerbated at higher concentrations and/or rates, is likely to be a persistent challenge for practical applications.

To address those challenges, in **Chapter 5**, molecular structural design for perfluoroalkyl group (R_F)-containing reactants was conducted, aiming to unlock full defluorination of R_F. We reported a novel class of fluorinated reactants based on fluoro-aromatics, where the I-ligand in perfluoroalkyl iodide is replaced with an aromatic structure. Close-to-full defluorination of R_F group was achieved, yielding up to 15 (or 11) e⁻ per molecule, *i.e.* 15/17 (or 11/13) available F at voltages up to 2.6 V vs. Li/Li⁺. In consistent to that observed with *R-Ph-SF₅*, the ring structure is beneficial for charge transfer, and the electron withdrawing strength of the *R* functionality is positively correlates to the defluorination potential. In contrast, the alkene linker, which is absent in *R-Ph-SF₅* molecules, was found to be essential here for the electron propagating along the R_F tail. The fluoro-aromatics exhibits attractive active-material-level energies of up to 1785 Wh/kg_{*R-Ph-C8*}, while the practical cell-level performance, where high reactant concentrations are needed, are still yet to be optimized. This is because high concentration exacerbates the LiF passivation effects, requiring future research efforts to optimize the carbon substrate structures to accommodate the extensive LiF formation.

In **Chapter 6**, we probed the electrochemical fluoridation process of transition metal oxide (MO), aiming to provide insights for the design of fluoridated cathodes for rechargeable Li-ion

batteries. We investigated an electrochemical methodology to grow LiF by reduction of perfluorinated gas onto MO, which then forms M-O-F by splitting of LiF upon charge, using MnO as an example target phase. Unlike current methods where particle size <10 nm is necessary for high MnO utilization (subsequent discharge/lithiation capacity), owing to the nano-crystallinity and intimate contact of electrochemically-grown LiF, high MnO utilization ($\sim 0.9 e^-/\text{MnO}$, 340 mAh/g_{MnO}) is achieved with large MnO particle size (~ 400 nm), exceeding comparable MnO/LiF systems reported to date. Additionally, incorporation of perfluorinated-gas additive benefits cycling, with capacity of ~ 270 mAh/g_{MnO} retained after 20 cycles. This work demonstrates the opportunity for electrochemically-driven fluoridation to achieve high capacities with larger particle sizes needed to bring oxyfluorides closer to practical reality.

7.2 Outlook

Looking forward, the design focuses for advanced fluorinated conversion cathodes are different for primary and rechargeable batteries. For primary batteries, where high energy densities are critical, multiple bond cleavage in one molecule is favored given its ability to minimize the weight requirement per charge transfer. Therefore, the perfluorinated reactants investigated in **Chapter 2–5**, where 8 to 15 e^- transfer per molecule has been obtained, are promising candidates for high-energy primary battery cathodes, once the challenges at high reactant concentrations being addressed. The complex bond-breaking mechanism, however, may not be favorable for the design of rechargeable systems, as it makes the re-construction of those bonds extremely difficult. As a result, to achieve reversible fluoride conversion, single or double electron transfer redox may be more favored, and thus the selection of redox center will be critical, as it needs to form a relatively weak bond with F ligands and also serve as a stable F^- host. These design considerations, which may guide future research directions, are elaborated below.

For primary batteries:

- **Understanding the voltage determining factor in the conversion of fluorinated reactants** – All of the fluorinated cathodes mentioned before, including: SF₆, NF₃, CF_x, *R-Ph-SF₅*, perfluoroalkyl iodides (CFI), and R_F containing fluoro-aromatics, exhibit very similar discharge potentials between 2.3 –2.9 V vs. Li/Li⁺. However, for SF₆, NF₃ and CF_x, the thermodynamic data of which are available, the calculated theoretical potentials are much higher than that obtained experimentally from two electrode cells (3.69, 5.70, and 4.6 V vs. Li/Li⁺ for SF₆, NF₃ and CF_x, respectively),^{17,33} suggesting the existence of large overpotentials, which might be induced by the intermediate reaction steps (*e.g.* the solvent-mediated mechanism in Li–CF_x systems, see **Section 1.2.2**).^{11,35} In addition, the cell voltages for SF₆, CF_x and CFI, were all proven to be highly dependent on electrolyte solvent properties (Chapter 2 and 4).^{36,37} Therefore, understanding the origin of the overpotential or the similar discharge potentials in these Li–fluorinated reactant cells will provide valuable insights for improving cell voltages and attainable energy densities. Future work could utilize computation tools like density functional theory (DFT) and ab initio molecular dynamics (AIMD) to probe intermediates that are hard to detect from experimental characterizations, due to their small quantity or low stability. Experimental tools, such as galvanostatic intermittent titration technique (GITT) and cyclic voltammetry (CV), allows the measure of cell voltages at closer to equilibrium conditions, and comparing the results across different solvent environment would help to better understand the effect of solvation environments.

- **Exploring molecular structures with functionalities to improve the reactant solubility and Li⁺ affinity** – One of the challenges for the liquid fluorinated cathodes developed in **Chapter 3–5** is the performances at high reactant concentrations. This is because the high active material loading yielding increased amount of discharge products (*e.g.* LiF, or lithium polysulfides), but the diminishing of supporting solvent resulting in less solubility of those products, exacerbating the electrode passivation. One promising pathway to address this challenge is to incorporate functionalities (for example, the *R* group in *R-Ph-SF₅*) with strong affinities to solvent molecules or Li⁺ ions, and thus increasing the portion of free solvent molecules available for solvating discharge intermediates and products. Ideally, fluorinated reactants with good Li salt solubility are desirable, where the supporting solvent is no longer needed (this will be similar to Li–thionyl chloride cells,²⁷ see cell mechanisms and limitations in **Section 1.2.1**). In this case, the cell-level energy density could be maximized by reducing the “dead weight” in cell, and the reactant might also allow some extent of solubility for discharge products.
- **Identifying solvent species that enable strong fluoride solvation and good stability against Li** – Another pathway to address the challenge at high reactant concentrations is to optimize the solvent properties, to achieve high LiF solubility while maintaining good stability with Li metal anode. For strong fluoride solvation, as discussed in **Chapter 2**, solvents with high donor number (DN) or acceptor number are favored. Notably, some of the high DN solvents, such as N,N-dimethylacetamide (DMA, DN=27.8),¹⁸ exhibit poor interface stability when coupled with Li metal. However, at high fluorinated-reactant concentrations, such reactivity might be reduced due to the formation of LiF passivation layer on Li surface, making experimental efforts necessary to determine the actual stability

of those solvents in high reactant concentration cells. Other solvent properties, such as dielectric constant and viscosity, are also worth considering, since they could affect the reactant solubility and transport properties (as discussed in **Chapter 4**). Therefore, future work screening the effect of different solvent species, or binary (even ternary) solvent mixtures, are critical for the optimization of more practical cell-level performances at high reactant concentrations.

For rechargeable batteries:

Reproduced in part with permission from Gao, H., & Gallant, B. M. (2020). Advances in the chemistry and applications of alkali-metal–gas batteries. Nat. Rev. Chem., 4, 566–583. Copyright 2020.

Design strategy for rechargeable fluoride conversion cathodes diverges from that for primary cathodes, given the trade-off between specific energy and the reversibility: multiple bond-breaking enables multi-electron transfer reactions and is usually facilitated by high stability of the formed products (*e.g.* LiF); however, this simultaneously increases the complexity for the backward reaction. To elaborate on this, we use oxide and fluoride gas cathodes as examples, because their molecular structures are simpler and relatively easier to model.

One factor relating to reversibility of gas reactants is the hardness of the reactant-state molecule, which determines to what extent reduction is favored as well as the ensuing electronic reconfiguration as the gas reacts to the solid phase. The definition of absolute hardness (η) given by Parr and Pearson is:²⁸⁶

$$\eta = \frac{1}{2} \left(\frac{\partial^2 E}{\partial N^2} \right) \sim \frac{I - A}{2}$$

where E is the energy, N is the total number of electrons, I is the ionization potential and A is the electron affinity (EA). I is related to the energy level of the highest occupied molecular orbital

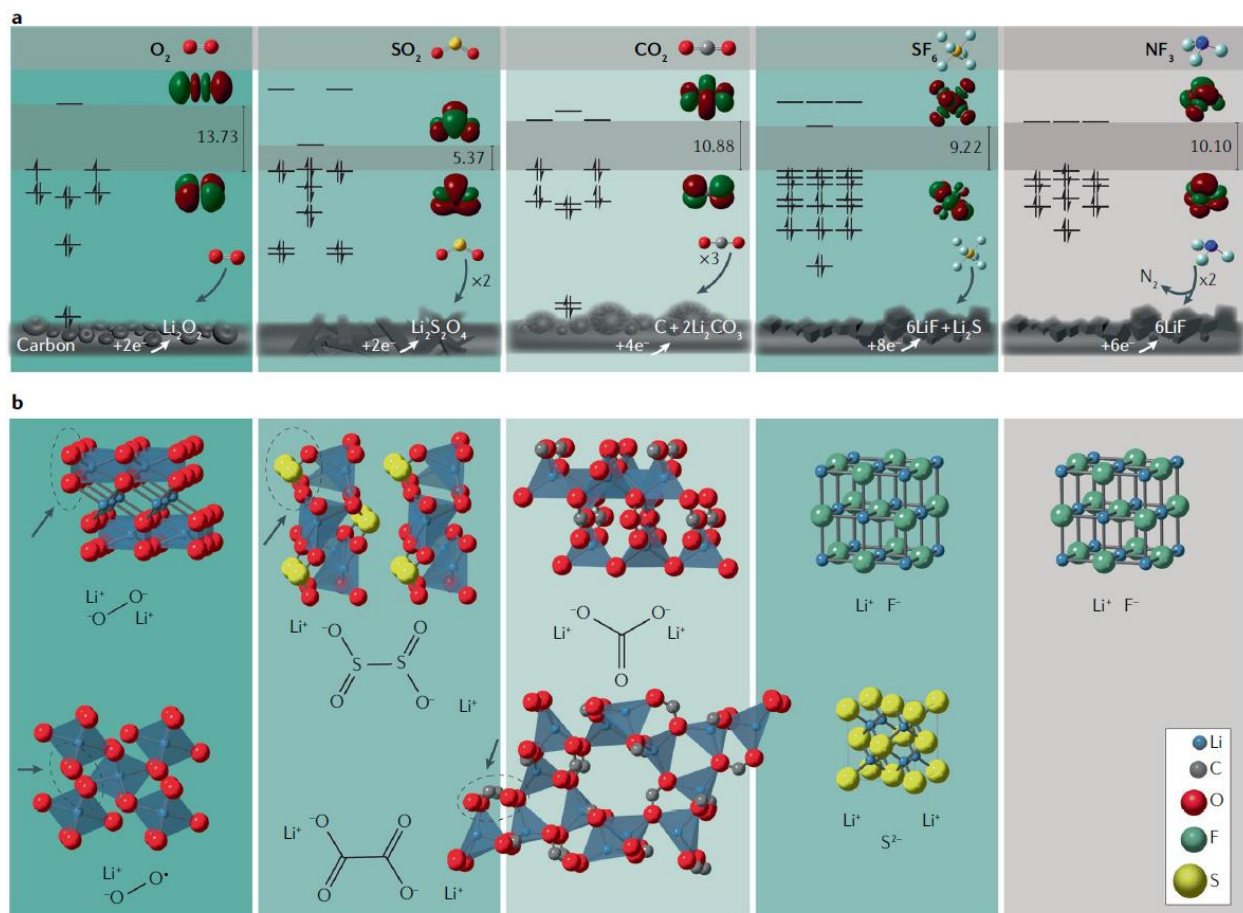


Figure 7-1 Motifs underlying molecular and solid-state reversibility. (a) Comparison of reactant gas cathode molecules, including electronic structures: molecular orbital (MO) diagram; highest occupied MO (HOMO)–lowest unoccupied MO (LUMO) gap. (b) Lattice structure of Li_2O_2 , Li_2CO_3 , $Li_2C_2O_4$, $Li_2S_2O_4$ (adapted from $Na_2S_2O_4$), LiF and LiS . Circles/arrows indicate moieties within the solid phases (O–O pairing in Li_2O_2 and LiO_2 , SO_2 motifs within $Li_2S_2O_4$, and CO_2 motifs within $Li_2C_2O_4$) predictive of reversibility. Note that LiO_2 is rarely observed as a stable discharge phase but is included here for comparison. Likewise, $Li_2C_2O_4$ is not commonly observed in Li– CO_2 batteries where the primary product is the less-reversible Li_2CO_3 , but is included here for comparison.

(HOMO) or the singly occupied molecular orbital (SOMO), such that $I = -\epsilon_{\text{HOMO(SOMO)}}$. For molecules with a fully-filled HOMO, the electron affinity is related to the energy of the lowest unoccupied molecular orbital (LUMO): $A = -\epsilon_{\text{LUMO}}$, thus the hardness is the energy difference between HOMO and LUMO. The larger the HOMO/LUMO gap ($\sim 2\eta$), the higher the molecule hardness η . In contrast, for molecules with unpaired electrons, the hardness is determined by the electron repulsion energy in the SOMO (the LUMO energy becomes irrelevant).²⁸⁷

Based on the hard-soft (Lewis) acid-base (HSAB) theory, electron-transfer events favor soft/soft interactions²⁸⁸ in which the electronic structure of the molecule can gently re-configure to accommodate the added charge into available molecular orbitals without drastic restructuring, the latter of which includes reduction of bond orders down to 0. This indicates that soft gas molecules will be more likely to support a reversible electron transfer. As is shown in **Figure 7-1a**, except for O₂ which has unpaired electrons, the HOMO of the remaining molecules are all filled, such that the first electron enters above a significant HOMO/LUMO gap. Among these, SO₂ exhibits the smallest HOMO/LUMO gap of 5.37 eV, and is thus softest. As for O₂, the EA is ~ 0.45 eV,²⁸⁹ resulting in $2\eta \approx 7.93$ eV, which is the second-lowest among the five molecules.²⁶⁴ O₂ can also accommodate two electrons in the π^* orbitals; the bond order reduces by 1 but is not fully broken. This reasoning agrees with experimental observations in which SO₂ and O₂ exhibit facile discharge behavior compared to the theoretical voltages (see discussions in **Section 1.4**) and relatively minor structural reconfiguration upon incorporation into the solid phase—O—O bonds or S—O bonds are still retained (**Figure 7-1b**). In contrast, the three “hard” molecules, CO₂, SF₆, and NF₃, are less favored for electron transfer: Li—CO₂ batteries exhibit relatively limited rate performance and catalysts are usually needed, while Li—SF₆ and Li—NF₃ batteries still burdened by large discharge overpotentials which might be attributed to sluggish kinetics of the first electron

transfer. In addition, for SF₆ and NF₃, all S–F or N–F bonds are broken during reduction to accommodate the large number of electrons per molecule. The extensive bond-breaking process makes it nearly impossible to reconstruct the gas molecules from the highly stable products (Li₂S, LiF, or N₂). Similar is true for Li–CO₂ batteries; though the detailed reaction mechanism remains unclear, the formation of C indicates some extent of C–O bond breaking; meanwhile the formation of the highly stable Li₂CO₃ makes recharge highly challenging.

Therefore, to develop rechargeable fluoride-based conversion cathodes, several design criteria needs to be considered:

- (1) Breaking only small number of bonds (or ideally, no bond cleavage) during reduction while retaining mass-efficiency (light weight per charge transfer);
- (2) Forming only moderately stable solid phases (less stable than LiF) that are more amenable to recharge.
- (3) Gaining improved control over electrochemical pathway to avoid parasitic chemistry of radicals and unlock long cycle life.

We note that meeting those requirements will inevitably require a long-term, more drastic evolution in the fluoride redox chemistries, such as new redox center with light weight per charge transfer and is also stable upon accepting/donating F ligands; and coupling with non-Li anode species (*e.g.* sodium or potassium), to form reduction products with weaker metal–fluorine bonds. In a short-term, the understanding of governing parameters for fluoride redox will be helpful for the design of fluorinated electrolytes or additives. For example, fluoroethylene carbonate (FEC), methyl 2,2,2-trifluoroethyl carbonate (FEMC), and liquefied CH₃F) were shown to be able to effectively increase Li cyclability by forming LiF-rich solid electrolyte interphase (SEI) on Li.¹⁹ The molecular design and fluoride morphology control strategies demonstrated in this thesis are

very likely to be applicable to the development of new fluorinated electrolyte components, to form a thin, protective LiF layer at desired voltage range, and thus enabling high cycle stabilities.

References

- 1 Whittingham, M. S. Ultimate limits to intercalation reactions for lithium batteries. *Chem. Rev.* **114**, 11414-11443 (2014).
- 2 Liu, J. *et al.* Pathways for practical high-energy long-cycling lithium metal batteries. *Nat. Energy* **4**, 180-186 (2019).
- 3 Drive, U. Electrochemical energy storage technical team roadmap. *US Department of Energy* (2013).
- 4 Schmuch, R., Wagner, R., Hörpel, G., Placke, T. & Winter, M. Performance and cost of materials for lithium-based rechargeable automotive batteries. *Nat. Energy* **3**, 267-278 (2018).
- 5 Reddy, T. B. & Linden, D. Lithium primary batteries in *Linden's handbook of batteries (4th Edition)* 14.11-14.87 (McGraw-Hill 2010).
- 6 Dell, R. Batteries: fifty years of materials development. *Solid State Ionics* **134**, 139-158 (2000).
- 7 Reddy, M. V., Mauger, A., Julien, C. M., Paoletta, A. & Zaghbi, K. Brief history of early lithium-battery development. *Materials* **13**, 1884 (2020).
- 8 Kwak, W.-J. *et al.* Lithium–oxygen batteries and related systems: potential, status, and future. *Chem. Rev.* (2020).
- 9 Liu, T. *et al.* Current challenges and routes forward for nonaqueous lithium–air batteries. *Chem. Rev.* (2020).
- 10 Qiao, Y. *et al.* Li-CO₂ electrochemistry: a new strategy for CO₂ fixation and energy storage. *Joule* **1**, 359-370 (2017).

- 11 Amatucci, G. G. & Pereira, N. Fluoride based electrode materials for advanced energy storage devices. *J. Fluorine Chem.* **128**, 243-262, doi:10.1016/j.jfluchem.2006.11.016 (2007).
- 12 Fuchigami, T. Electrochemical reactions of fluoro organic compounds in *Electrochemistry V* 1-37 (Springer, 1994).
- 13 Wu, F. & Yushin, G. Conversion cathodes for rechargeable lithium and lithium-ion batteries. *Energy Environ. Sci.* **10**, 435-459 (2017).
- 14 Li, Y., Khurram, A. & Gallant, B. M. A high-capacity lithium–gas battery based on sulfur fluoride conversion. *J. Phys. Chem. C* **122**, 7128-7138 (2018).
- 15 Gao, H., Li, Y., Guo, R. & Gallant, B. M. Controlling fluoride-forming reactions for improved rate capability in lithium-perfluorinated gas conversion batteries. *Adv. Energy Mater.*, 1900393 (2019).
- 16 He, M., Li, Y., Guo, R. & Gallant, B. M. Electrochemical conversion of nitrogen trifluoride as a gas-to-solid cathode in Li batteries. *J. Phys. Chem. Lett.* **9**, 4700-4706 (2018).
- 17 Gao, H. & Gallant, B. M. Advances in the chemistry and applications of alkali-metal–gas batteries. *Nat. Rev. Chem.* **4**, 566–583, doi:10.1038/s41570-020-00224-7 (2020).
- 18 Gutmann, V. Empirical parameters for donor and acceptor properties of solvents. *Electrochim. Acta* **21**, 661-670 (1976).
- 19 Hobold, G. M. *et al.* Moving beyond 99.9% Coulombic efficiency for lithium anodes in liquid electrolytes. *Nat. Energy* **6**, 951-960 (2021).
- 20 Meyers, W. F. & Simmons, J. W. Electric current-producing cell with anhydrous organic liquid electrolyte. U.S. patent No. 3,423,242 (1969).

- 21 Blurton, K. F. & Sammells, A. F. Metal/air batteries: their status and potential—a review. *J. Power Sources* **4**, 263-279 (1979).
- 22 Abraham, K. & Jiang, Z. A polymer electrolyte-based rechargeable lithium/oxygen battery. *J. Electrochem. Soc.* **143**, 1-5 (1996).
- 23 Lim, H. D. *et al.* A new perspective on Li–SO₂ batteries for rechargeable systems. *Angew. Chem., Int. Ed.* **54**, 9663-9667 (2015).
- 24 Zhao, Y. *et al.* A Review on Battery Market Trends, Second-Life Reuse, and Recycling. *Sustain. Chem.* **2**, 167-205 (2021).
- 25 Sarakonsri, T. & Kumar, R. V. Primary Batteries in *High Energy Density Lithium Batteries: Materials, Engineering, Applications* (eds Katerina E. Aifantis, Stephen A. Hackney, & R. Vasant Kumar) 27-52 (2010).
- 26 Xing, H. *et al.* Ambient lithium–SO₂ batteries with ionic liquids as electrolytes. *Angew. Chem., Int. Ed.* **53**, 2099-2103 (2014).
- 27 Hills, A. & Hampson, N. The Li-SOCl₂ cell—a review. *J. Power Sources* **24**, 253-271 (1988).
- 28 Sharma, N., Dubois, M., Guérin, K., Pischedda, V. & Radescu, S. Fluorinated (Nano) Carbons: CF_x Electrodes and CF_x-Based Batteries. *Energy Technol.* **9**, 2000605 (2021).
- 29 Zhang, S. S., Foster, D., Wolfenstine, J. & Read, J. Electrochemical characteristic and discharge mechanism of a primary Li/CF_x cell. *J. Power Sources* **187**, 233-237 (2009).
- 30 Bock, D. C., Marschilok, A. C., Takeuchi, K. J. & Takeuchi, E. S. Batteries used to power implantable biomedical devices. *Electrochim. Acta* **84**, 155-164 (2012).
- 31 Yazami, R. & Hamwi, A. A new graphite fluoride compound as electrode material for lithium intercalation in solid state cells. *Solid State Ionics* **28**, 1756-1761 (1988).

- 32 Hagiwara, R., Nakajima, T. & Watanabe, N. Kinetic Study of Discharge Reaction of Lithium-Graphite Fluoride Cell. *J. Electrochem. Soc.* **135**, 2128 (1988).
- 33 Wood, J. L., Valerga, A. J., Badachhape, R. B. & Margrave, J. L. Thermodynamic, Electrochemical and Synthetic Studies of the Graphite-Fluorine Compounds CF and C₄F. *National Technical Information Service*, 755, 934 (1972).
- 34 Nickol, A. *et al.* GITT analysis of lithium insertion cathodes for determining the lithium diffusion coefficient at low temperature: challenges and pitfalls. *J. Electrochem. Soc.* **167**, 090546 (2020).
- 35 Nakajima, T. Carbon-fluorine compounds as battery materials. *J. Fluorine Chem.* **100**, 57-61 (1999).
- 36 Zhang, Q., Takeuchi, K. J., Takeuchi, E. S. & Marschilok, A. C. Progress towards high-power Li/CF_x batteries: electrode architectures using carbon nanotubes with CF_x. *Phys. Chem. Chem. Phys.* **17**, 22504-22518 (2015).
- 37 Fu, A. *et al.* Boosting the Energy Density of Li||CF_x Primary Batteries Using a 1, 3-Dimethyl-2-imidazolidinone-Based Electrolyte. *ACS Appl. Mater. Interfaces* **13**, 57470-57480 (2021).
- 38 Leung, K. *et al.* Edge-Propagation Discharge Mechanism in CF_x Batteries—A First-Principles and Experimental Study. *Chem. Mater.* **33**, 1760-1770 (2021).
- 39 Sayahpour, B. *et al.* Revisiting Discharge Mechanism of CF_x as a High Energy Density Cathode Material for Lithium Primary Battery. *Adv. Energy Mater.* **12**, 2103196 (2022).
- 40 Wang, J. *et al.* Unraveling nanoscale electrochemical dynamics of graphite fluoride by in situ electron microscopy: key difference between lithiation and sodiation. *J. Mater. Chem. A* **8**, 6105-6111 (2020).

- 41 Fan, R. *et al.* First-principles study of the adsorption behaviors of Li atoms and LiF on the CF_x ($x= 1.0, 0.9, 0.8, 0.5, \sim 0.0$) surface. *RSC Adv.* **10**, 31881-31888 (2020).
- 42 Lagow, R., Badachhape, R., Wood, J. & Margrave, J. Synthesis of superstoichiometric poly (carbon monofluoride). *J. Am. Chem. Soc.* **96**, 2628-2629 (1974).
- 43 Zhang, W. *et al.* Effect of curvature on C–F bonding in fluorinated carbons: from fullerene and derivatives to graphite. *Phys. Chem. Chem. Phys.* **12**, 1388-1398 (2010).
- 44 Lam, P. & Yazami, R. Physical characteristics and rate performance of $(\text{CF}_x)_n$ ($0.33 < x < 0.66$) in lithium batteries. *J. Power Sources* **153**, 354-359 (2006).
- 45 Mizushima, K., Jones, P., Wiseman, P. & Goodenough, J. B. Li_xCoO_2 ($0 < x < 1$): A new cathode material for batteries of high energy density. *Mater. Res. Bull.* **15**, 783-789 (1980).
- 46 Nitta, N., Wu, F., Lee, J. T. & Yushin, G. Li-ion battery materials: present and future. *Mater. Today* **18**, 252-264 (2015).
- 47 Armand, M. & Tarascon, J. M. Issues and challenges facing rechargeable batteries. *Nature* **414**, 359-367 (2001).
- 48 Ji, H. *et al.* Hidden structural and chemical order controls lithium transport in cation-disordered oxides for rechargeable batteries. *Nat. Commun.* **10**, 1-9 (2019).
- 49 Xu, B., Qian, D., Wang, Z. & Meng, Y. S. Recent progress in cathode materials research for advanced lithium ion batteries. *Mater. Sci. Eng. R Rep* **73**, 51-65 (2012).
- 50 Kim, M.-H., Shin, H.-S., Shin, D. & Sun, Y.-K. Synthesis and electrochemical properties of $\text{Li}[\text{Ni}_{0.8}\text{Co}_{0.1}\text{Mn}_{0.1}]\text{O}_2$ and $\text{Li}[\text{Ni}_{0.8}\text{Co}_{0.2}]\text{O}_2$ via co-precipitation. *J. Power Sources* **159**, 1328-1333 (2006).

- 51 Rozier, P. & Tarascon, J. M. Li-rich layered oxide cathodes for next-generation Li-ion batteries: chances and challenges. *J. Electrochem. Soc.* **162**, A2490 (2015).
- 52 Clément, R., Lun, Z. & Ceder, G. Cation-disordered rocksalt transition metal oxides and oxyfluorides for high energy lithium-ion cathodes. *Energy Environ. Sci.* **13**, 345-373 (2020).
- 53 Lee, K.-S., Myung, S.-T., Amine, K., Yashiro, H. & Sun, Y.-K. Structural and Electrochemical Properties of Layered Li $[\text{Ni}_{1-2x}\text{Co}_x\text{Mn}_x]\text{O}_2$ ($x= 0.1-0.3$) Positive Electrode Materials for Li-Ion Batteries. *J. Electrochem. Soc.* **154**, A971 (2007).
- 54 Yang, J. *et al.* Understanding Voltage Decay in Lithium-Rich Manganese-Based Layered Cathode Materials by Limiting Cutoff Voltage. *ACS Appl. Mater. Interfaces* **8**, 18867-18877, doi:10.1021/acsami.6b04849 (2016).
- 55 Seo, D. H. *et al.* The Structural and Chemical Origin of the Oxygen Redox Activity in Layered and Cation-disordered Li-excess Cathode Materials. *Nat. Chem.* **8**, 692 (2016).
- 56 Cabana, J., Monconduit, L., Larcher, D. & Palacin, M. R. Beyond intercalation-based Li-ion batteries: the state of the art and challenges of electrode materials reacting through conversion reactions. *Adv. Mater.* **22**, E170-E192 (2010).
- 57 Bruce, P. G., Freunberger, S. A., Hardwick, L. J. & Tarascon, J.-M. Li-O₂ and Li-S batteries with high energy storage. *Nat. Mater.* **11**, 19-29 (2012).
- 58 Pang, Q., Liang, X., Kwok, C. Y. & Nazar, L. Advances in lithium-sulfur batteries based on multifunctional cathodes and electrolytes. *Nat. Energy* **1**, 1-11 (2016).
- 59 Manthiram, A., Chung, S. H. & Zu, C. Lithium-sulfur batteries: progress and prospects. *Adv. Mater.* **27**, 1980-2006 (2015).

- 60 Luo, Q. & Manthiram, A. Effect of Low-Temperature Fluorine Doping on the Properties of Spinel $\text{LiMn}_{2-2y}\text{Li}_y\text{M}_y\text{O}_{4-\eta}\text{F}_\eta$ (M= Fe, Co, and Zn) Cathodes. *J. Electrochem. Soc.* **156**, A84 (2008).
- 61 Takeda, N. *et al.* Reversible Li storage for nanosize cation/anion-disordered rocksalt-type oxyfluorides: $\text{LiMoO}_{2-x}\text{LiF}$ ($0 \leq x \leq 2$) binary system. *J. Power Sources* **367**, 122-129 (2017).
- 62 Clément, R. J., Kitchaev, D., Lee, J. & Ceder, G. Short-range order and unusual modes of nickel redox in a fluorine-substituted disordered rocksalt oxide lithium-ion cathode. *Chem. Mater.* **30**, 6945-6956 (2018).
- 63 Okumura, T. *et al.* Role of local and electronic structural changes with partially anion substitution Lithium manganese spinel oxides on their electrochemical properties: X-ray absorption spectroscopy study. *Dalton Trans.* **40**, 9752-9764 (2011).
- 64 Windmüller, A. *et al.* Enhancing the performance of high-voltage LiCoMnO_4 spinel electrodes by fluorination. *J. Power Sources* **341**, 122-129 (2017).
- 65 Yue, P. *et al.* Effect of Fluorine on the Electrochemical Performance of Spherical $\text{LiNi}_{0.8}\text{Co}_{0.1}\text{Mn}_{0.1}\text{O}_2$ Cathode Materials via a Low Temperature Method. *Powder Technol.* **237**, 623-626, doi:10.1016/j.powtec.2012.12.061 (2013).
- 66 Wang, J. *et al.* Role of fluorine surface modification in improving electrochemical cyclability of concentration gradient $\text{Li}[\text{Ni}_{0.73}\text{Co}_{0.12}\text{Mn}_{0.15}]\text{O}_2$ cathode material for Li-ion batteries. *RSC Adv.* **6**, 26307-26316 (2016).
- 67 Kang, S.-H. & Amine, K. Layered $\text{Li}(\text{Li}_{0.2}\text{Ni}_{0.15+0.5z}\text{Co}_{0.10}\text{Mn}_{0.55-0.5z})\text{O}_{2-z}\text{F}_z$ cathode materials for Li-ion secondary batteries. *J. Power Sources* **146**, 654-657 (2005).

- 68 Wang, Y. *et al.* Suppressing Mn Reduction of Li-Rich Mn-Based Cathodes by F-Doping for Advanced Lithium-Ion Batteries. *J. Phys. Chem. C* **122**, 27836-27842, doi:10.1021/acs.jpcc.8b08669 (2018).
- 69 Lee, J. *et al.* Unlocking the potential of cation-disordered oxides for rechargeable lithium batteries. *Science* **343**, 519-522 (2014).
- 70 Richards, W. D., Dacek, S. T., Kitchaev, D. A. & Ceder, G. Fluorination of lithium-excess transition metal oxide cathode materials. *Adv. Energy Mater.* **8**, 1701533 (2018).
- 71 Chen, R. *et al.* Disordered lithium-rich oxyfluoride as a stable host for enhanced Li⁺ intercalation storage. *Adv. Energy Mater.* **5**, 1401814 (2015).
- 72 House, R. A. *et al.* Lithium manganese oxyfluoride as a new cathode material exhibiting oxygen redox. *Energy Environ. Sci.* **11**, 926-932 (2018).
- 73 Deng, D. Transition Metal Oxyfluorides for Next-Generation Rechargeable Batteries. *ChemNanoMat* **3**, 146-159 (2017).
- 74 Chen, R. *et al.* Lithiation-driven structural transition of VO₂F into disordered rock-salt Li_xVO₂F. *RSC Adv.* **6**, 65112-65118 (2016).
- 75 Tong, W. & Amatucci, G. Synthesis, Structure, and Electrochemistry of Silver Niobium Oxyfluorides for Lithium Batteries. *Electrochem. Solid-State Lett.* **12**, A219 (2009).
- 76 Opra, D. *et al.* Fluorine substituted molybdenum oxide as cathode material for Li-ion battery. *Mater. Lett.* **160**, 175-178 (2015).
- 77 Pereira, N., Badway, F., Wartelsky, M., Gunn, S. & Amatucci, G. Iron oxyfluorides as high capacity cathode materials for lithium batteries. *J. Electrochem. Soc.* **156**, A407 (2009).

- 78 Kim, S.-W. *et al.* Structure stabilization by mixed anions in oxyfluoride cathodes for high-energy lithium batteries. *ACS Nano* **9**, 10076-10084 (2015).
- 79 Richards, W. D., Miara, L. J., Wang, Y., Kim, J. C. & Ceder, G. Interface stability in solid-state batteries. *Chem. Mater.* **28**, 266-273 (2016).
- 80 Ménétrier, M. *et al.* NMR evidence of LiF coating rather than fluorine substitution in Li (Ni_{0.425}Mn_{0.425}Co_{0.15})O₂. *J. Solid State Chem.* **181**, 3303-3307 (2008).
- 81 Xiong, X., Wang, Z., Yin, X., Guo, H. & Li, X. A modified LiF coating process to enhance the electrochemical performance characteristics of LiNi_{0.8}Co_{0.1}Mn_{0.1}O₂ cathode materials. *Mater. Lett.* **110**, 4-9 (2013).
- 82 Kim, S.-W. *et al.* Energy storage in composites of a redox couple host and a lithium ion host. *Nano Today* **7**, 168-173 (2012).
- 83 Dimov, N., Kitajou, A., Hori, H., Kobayashi, E. & Okada, S. Electrochemical splitting of LiF: a new approach to lithium-ion battery materials. *ECS Trans.* **58**, 87-99 (2014).
- 84 Jung, S. K. *et al.* Lithium-free Transition Metal Monoxides for Positive Electrodes in Lithium-ion Batteries. *Nat. Energy* **2**, 16208, doi:10.1038/nenergy.2016.208 (2017).
- 85 Jung, S.-K. *et al.* New iron-based intercalation host for lithium-ion batteries. *Chem. Mater.* **30**, 1956-1964 (2018).
- 86 Zhang, L., Chen, G., Berg, E. J. & Tarascon, J. M. Triggering the in situ Electrochemical Formation of High Capacity Cathode Material From MnO. *Adv. Energy Mater.* **7**, 1602200 (2017).
- 87 Zhang, L. *et al.* Origin of the High Capacity Manganese-Based Oxyfluoride Electrodes for Rechargeable Batteries. *Chem. Mater.* **30**, 5362-5372, doi:10.1021/acs.chemmater.8b02182 (2018).

- 88 Zhang, L., Batuk, D., Chen, G. & Tarascon, J.-M. Electrochemically activated MnO as a cathode material for sodium-ion batteries. *Electrochem. Commun.* **77**, 81-84 (2017).
- 89 Lu, Y.-C. *et al.* Lithium–oxygen batteries: bridging mechanistic understanding and battery performance. *Energy Environ. Sci.* **6**, 750-768 (2013).
- 90 Ogasawara, T., Débart, A., Holzapfel, M., Novák, P. & Bruce, P. G. Rechargeable Li₂O₂ electrode for lithium batteries. *J. Am. Chem. Soc.* **128**, 1390-1393 (2006).
- 91 Débart, A., Paterson, A. J., Bao, J. & Bruce, P. G. α -MnO₂ nanowires: A catalyst for the O₂ electrode in rechargeable lithium batteries. *Angew. Chem., Int. Ed.* **47**, 4521-4524 (2008).
- 92 Lu, Y.-C. *et al.* Platinum–gold nanoparticles: a highly active bifunctional electrocatalyst for rechargeable lithium–air batteries. *J. Am. Chem. Soc.* **132**, 12170-12171 (2010).
- 93 Read, J. *et al.* Oxygen transport properties of organic electrolytes and performance of lithium/oxygen battery. *J. Electrochem. Soc.* **150**, A1351 (2003).
- 94 Lu, Y.-C. *et al.* The discharge rate capability of rechargeable Li–O₂ batteries. *Energy Environ. Sci.* **4**, 2999-3007 (2011).
- 95 Freunberger, S. A. *et al.* Reactions in the rechargeable lithium–O₂ battery with alkyl carbonate electrolytes. *J. Am. Chem. Soc.* **133**, 8040-8047 (2011).
- 96 McCloskey, B. D., Bethune, D. S., Shelby, R. M., Girishkumar, G. & Luntz, A. C. Solvents' critical role in nonaqueous lithium–oxygen battery electrochemistry. *J. Phys. Chem. Lett.* **2**, 1161-1166 (2011).
- 97 McCloskey, B. D. *et al.* On the efficacy of electrocatalysis in nonaqueous Li–O₂ batteries. *J. Am. Chem. Soc.* **133**, 18038-18041 (2011).

- 98 Aurbach, D., McCloskey, B. D., Nazar, L. F. & Bruce, P. G. Advances in understanding mechanisms underpinning lithium–air batteries. *Nat. Energy* **1**, 16128 (2016).
- 99 Johnson, L. *et al.* The role of LiO₂ solubility in O₂ reduction in aprotic solvents and its consequences for Li–O₂ batteries. *Nat. Chem.* **6**, 1091 (2014).
- 100 Peng, Z. *et al.* Oxygen reactions in a non-aqueous Li⁺ electrolyte. *Angew. Chem., Int. Ed.* **50**, 6351-6355 (2011).
- 101 Yu, Q. & Ye, S. In situ study of oxygen reduction in dimethyl sulfoxide (DMSO) solution: a fundamental study for development of the lithium–oxygen battery. *J. Phys. Chem. C* **119**, 12236-12250 (2015).
- 102 Galloway, T. A. & Hardwick, L. J. Utilizing in situ electrochemical SHINERS for oxygen reduction reaction studies in aprotic electrolytes. *J. Phys. Chem. Lett.* **7**, 2119-2124 (2016).
- 103 Viswanathan, V. *et al.* Electrical conductivity in Li₂O₂ and its role in determining capacity limitations in non-aqueous Li–O₂ batteries. *J. Chem. Phys.* **135**, 214704 (2011).
- 104 Gallant, B. M. *et al.* Influence of Li₂O₂ morphology on oxygen reduction and evolution kinetics in Li–O₂ batteries. *Energy Environ. Sci.* **6**, 2518-2528 (2013).
- 105 Laoire, C. O., Mukerjee, S., Abraham, K., Plichta, E. J. & Hendrickson, M. A. Influence of nonaqueous solvents on the electrochemistry of oxygen in the rechargeable lithium–air battery. *J. Phys. Chem. C* **114**, 9178-9186 (2010).
- 106 Burke, C. M., Pande, V., Khetan, A., Viswanathan, V. & McCloskey, B. D. Enhancing electrochemical intermediate solvation through electrolyte anion selection to increase nonaqueous Li–O₂ battery capacity. *Proc. Natl. Acad. Sci.* **112**, 9293-9298 (2015).

- 107 Aetukuri, N. B. *et al.* Solvating additives drive solution-mediated electrochemistry and enhance toroid growth in non-aqueous Li–O₂ batteries. *Nat. Chem.* **7**, 50 (2015).
- 108 Schwenke, K. U., Metzger, M., Restle, T., Piana, M. & Gasteiger, H. A. The influence of water and protons on Li₂O₂ crystal growth in aprotic Li–O₂ cells. *J. Electrochem. Soc.* **162**, A573–A584 (2015).
- 109 Park, J. B., Lee, S. H., Jung, H. G., Aurbach, D. & Sun, Y. K. Redox mediators for Li–O₂ batteries: status and perspectives. *Adv. Mater.* **30**, 1704162 (2018).
- 110 Gao, X., Chen, Y., Johnson, L. & Bruce, P. G. Promoting solution phase discharge in Li–O₂ batteries containing weakly solvating electrolyte solutions. *Nat. Mater.* **15**, 882 (2016).
- 111 Lee, D. *et al.* Direct observation of redox mediator-assisted solution-phase discharging of Li–O₂ battery by liquid-phase transmission electron microscopy. *J. Am. Chem. Soc.* **141**, 8047–8052 (2019).
- 112 Liu, T. *et al.* The effect of water on quinone redox mediators in nonaqueous Li–O₂ batteries. *J. Am. Chem. Soc.* **140**, 1428–1437 (2018).
- 113 Peng, Z., Chen, Y., Bruce, P. G. & Xu, Y. Direct detection of the superoxide anion as a stable intermediate in the electroreduction of oxygen in a non-aqueous electrolyte containing phenol as a proton source. *Angew. Chem., Int. Ed.* **54**, 8165–8168 (2015).
- 114 Gao, X., Jovanov, Z. P., Chen, Y., Johnson, L. R. & Bruce, P. G. Phenol-catalyzed discharge in the aprotic lithium–oxygen battery. *Angew. Chem.* **129**, 6639–6643 (2017).
- 115 Liang, Z., Zhou, Y. & Lu, Y.-C. Dynamic oxygen shield eliminates cathode degradation in lithium–oxygen batteries. *Energy Environ. Sci.* **11**, 3500–3510 (2018).

- 116 Khetan, A., Luntz, A. & Viswanathan, V. Trade-offs in capacity and rechargeability in nonaqueous Li–O₂ batteries: solution-driven growth versus nucleophilic stability. *J. Phys. Chem. Lett.* **6**, 1254-1259 (2015).
- 117 Wang, Y. *et al.* A solvent-controlled oxidation mechanism of Li₂O₂ in lithium-oxygen batteries. *Joule* **2**, 2364-2380 (2018).
- 118 Ottakam Thotiyl, M. M., Freunberger, S. A., Peng, Z. & Bruce, P. G. The carbon electrode in nonaqueous Li–O₂ cells. *J. Am. Chem. Soc.* **135**, 494-500 (2012).
- 119 Black, R. *et al.* Screening for superoxide reactivity in Li–O₂ batteries: effect on Li₂O₂/LiOH crystallization. *J. Am. Chem. Soc.* **134**, 2902-2905 (2012).
- 120 Zhang, X. *et al.* LiO₂: cryosynthesis and chemical/electrochemical reactivities. *J. Phys. Chem. Lett.* **8**, 2334-2338 (2017).
- 121 Wandt, J., Jakes, P., Granwehr, J., Gasteiger, H. A. & Eichel, R. A. Singlet oxygen formation during the charging process of an aprotic lithium–oxygen battery. *Angew. Chem., Int. Ed.* **55**, 6892-6895 (2016).
- 122 Mahne, N. *et al.* Singlet oxygen generation as a major cause for parasitic reactions during cycling of aprotic lithium–oxygen batteries. *Nat. Energy* **2**, 1-9 (2017).
- 123 Mourad, E. *et al.* Singlet oxygen from cation driven superoxide disproportionation and consequences for aprotic metal–O₂ batteries. *Energy Environ. Sci.* **12**, 2559-2568 (2019).
- 124 Mahne, N., Renfrew, S. E., McCloskey, B. D. & Freunberger, S. A. Electrochemical oxidation of lithium carbonate generates singlet oxygen. *Angew. Chem., Int. Ed.* **57**, 5529-5533 (2018).
- 125 Sharon, D. *et al.* Oxidation of dimethyl sulfoxide solutions by electrochemical reduction of oxygen. *J. Phys. Chem. Lett.* **4**, 3115-3119 (2013).

- 126 McCloskey, B. D. *et al.* Twin problems of interfacial carbonate formation in nonaqueous Li–O₂ batteries. *J. Phys. Chem. Lett.* **3**, 997-1001 (2012).
- 127 Lu, Y.-C. & Shao-Horn, Y. Probing the reaction kinetics of the charge reactions of nonaqueous Li–O₂ batteries. *J. Phys. Chem. Lett.* **4**, 93-99 (2013).
- 128 Peng, Z., Freunberger, S. A., Chen, Y. & Bruce, P. G. A reversible and higher-rate Li–O₂ battery. *Science* **337**, 563-566 (2012).
- 129 Thotiyl, M. M. O. *et al.* A stable cathode for the aprotic Li–O₂ battery. *Nat. Mater.* **12**, 1050 (2013).
- 130 Adams, B. D. *et al.* The importance of nanometric passivating films on cathodes for Li–air batteries. *ACS Nano* **8**, 12483-12493 (2014).
- 131 Kundu, D., Black, R., Berg, E. J. & Nazar, L. F. A highly active nanostructured metallic oxide cathode for aprotic Li–O₂ batteries. *Energy Environ. Sci.* **8**, 1292-1298 (2015).
- 132 Lu, J. *et al.* Aprotic and aqueous Li–O₂ batteries. *Chem. Rev.* **114**, 5611-5640 (2014).
- 133 Liang, Z. & Lu, Y.-C. Critical role of redox mediator in suppressing charging instabilities of lithium–oxygen batteries. *J. Am. Chem. Soc.* **138**, 7574-7583 (2016).
- 134 Chen, Y., Freunberger, S. A., Peng, Z., Fontaine, O. & Bruce, P. G. Charging a Li–O₂ battery using a redox mediator. *Nat. Chem.* **5**, 489 (2013).
- 135 Lim, H. D. *et al.* Superior rechargeability and efficiency of lithium–oxygen batteries: hierarchical air electrode architecture combined with a soluble catalyst. *Angew. Chem., Int. Ed.* **53**, 3926-3931 (2014).
- 136 Lim, H.-D. *et al.* Rational design of redox mediators for advanced Li–O₂ batteries. *Nat. Energy* **1**, 16066 (2016).

- 137 Chen, Y., Gao, X., Johnson, L. R. & Bruce, P. G. Kinetics of lithium peroxide oxidation by redox mediators and consequences for the lithium–oxygen cell. *Nat. Commun.* **9**, 767 (2018).
- 138 McCloskey, B. D. & Addison, D. A viewpoint on heterogeneous electrocatalysis and redox mediation in nonaqueous Li–O₂ batteries. *ACS Catal.* **7**, 772–778 (2017).
- 139 Wang, Y., Liang, Z., Zou, Q., Cong, G. & Lu, Y.-C. Mechanistic insights into catalyst-assisted nonaqueous oxygen evolution reaction in lithium–oxygen batteries. *J. Phys. Chem. C* **120**, 6459-6466 (2016).
- 140 Lopez, N. *et al.* Reversible reduction of oxygen to peroxide facilitated by molecular recognition. *Science* **335**, 450-453 (2012).
- 141 Lu, J. *et al.* A lithium–oxygen battery based on lithium superoxide. *Nature* **529**, 377 (2016).
- 142 Kwak, W.-J., Park, J.-B., Jung, H.-G. & Sun, Y.-K. Controversial topics on lithium superoxide in Li–O₂ batteries. *ACS Energy Lett.* **2**, 2756-2760 (2017).
- 143 Papp, J. K. *et al.* Poly (vinylidene fluoride)(PVDF) binder degradation in Li–O₂ batteries: a consideration for the characterization of lithium superoxide. *J. Phys. Chem. Lett.* **8**, 1169-1174 (2017).
- 144 Giordani, V. *et al.* A molten salt lithium–oxygen battery. *J. Am. Chem. Soc.* **138**, 2656-2663 (2016).
- 145 Xia, C., Kwok, C. & Nazar, L. F. A high-energy-density lithium-oxygen battery based on a reversible four-electron conversion to lithium oxide. *Science* **361**, 777-781 (2018).
- 146 Maricle, D. L. & Mohns, J. P. Electrochemical cell containing sulfur dioxide as the cathode depolarizer. No. 3,567,515. 2 (1971).

- 147 Dey, A., Kuo, H., Piliero, P. & Kallianidis, M. Inorganic electrolyte Li/SO₂ rechargeable system: development of a prototype hermetic C cell and evaluation of its performance and safety characteristics. *J. Electrochem. Soc.* **135**, 2115 (1988).
- 148 Fey, G.-K. Li/SO₂ rechargeable batteries. *J. Power Sources* **35**, 153-162 (1991).
- 149 Park, H. *et al.* High-efficiency and high-power rechargeable lithium–sulfur dioxide batteries exploiting conventional carbonate-based electrolytes. *Nat. Commun.* **8**, 14989 (2017).
- 150 Xu, S., Das, S. K. & Archer, L. A. The Li–CO₂ battery: A novel method for CO₂ capture and utilization. *RSC Adv.* **3**, 6656-6660 (2013).
- 151 Xie, J. & Wang, Y. Recent Development of CO₂ Electrochemistry from Li–CO₂ Batteries to Zn–CO₂ Batteries. *Acc. Chem. Res.* (2019).
- 152 Hou, Y. *et al.* Mo₂C/CNT: an efficient catalyst for rechargeable Li–CO₂ batteries. *Adv. Funct. Mater.* **27**, 1700564 (2017).
- 153 Khurram, A., Yin, Y., Yan, L., Zhao, L. & Gallant, B. M. Governing role of solvent on discharge activity in lithium–CO₂ batteries. *J. Phys. Chem. Lett.* **10**, 6679-6687 (2019).
- 154 Takechi, K., Shiga, T. & Asaoka, T. A Li–O₂/CO₂ battery. *Chem. Commun.* **47**, 3463-3465 (2011).
- 155 Yin, W., Grimaud, A., Lepoivre, F., Yang, C. & Tarascon, J. M. Chemical vs electrochemical formation of Li₂CO₃ as a discharge product in Li–O₂/CO₂ batteries by controlling the superoxide intermediate. *J. Phys. Chem. Lett.* **8**, 214-222 (2017).
- 156 Gowda, S. R., Brunet, A., Wallraff, G. & McCloskey, B. D. Implications of CO₂ contamination in rechargeable nonaqueous Li–O₂ batteries. *J. Phys. Chem. Lett.* **4**, 276-279 (2013).

- 157 Lim, H.-K. *et al.* Toward a lithium–“air” battery: the effect of CO₂ on the chemistry of a lithium–oxygen cell. *J. Am. Chem. Soc.* **135**, 9733-9742 (2013).
- 158 Zhao, Z., Su, Y. & Peng, Z. Probing lithium carbonate formation in Trace-O₂-assisted aprotic Li-CO₂ batteries using in situ surface-enhanced raman spectroscopy. *J. Phys. Chem. Lett.* **10**, 322-328 (2019).
- 159 Khurram, A., He, M. & Gallant, B. M. Tailoring the discharge reaction in Li-CO₂ batteries through incorporation of CO₂ capture chemistry. *Joule* **2**, 2649-2666 (2018).
- 160 Yang, S. *et al.* A reversible lithium–CO₂ battery with Ru nanoparticles as a cathode catalyst. *Energy Environ. Sci.* **10**, 972-978 (2017).
- 161 Liu, B. *et al.* Recent advances in understanding Li–CO₂ electrochemistry. *Energy Environ. Sci.* **12**, 887-922 (2019).
- 162 Garcia-Lastra, J. M., Myrdal, J. S., Christensen, R., Thygesen, K. S. & Vegge, T. DFT+U study of polaronic conduction in Li₂O₂ and Li₂CO₃: implications for Li–Air batteries. *J. Phys. Chem. C* **117**, 5568-5577 (2013).
- 163 Ling, C., Zhang, R., Takechi, K. & Mizuno, F. Intrinsic barrier to electrochemically decompose Li₂CO₃ and LiOH. *J. Phys. Chem. C* **118**, 26591-26598 (2014).
- 164 Zhang, Z. *et al.* Verifying the rechargeability of Li–CO₂ batteries on working cathodes of Ni nanoparticles highly dispersed on N-doped graphene. *Adv. Sci.* **5**, 1700567 (2018).
- 165 Ma, W., Lu, S., Lei, X., Liu, X. & Ding, Y. J. J. o. M. C. A. Porous Mn₂O₃ cathode for highly durable Li–CO₂ batteries. *J. Mater. Chem. A* **6**, 20829-20835 (2018).
- 166 Hughes, T., Smith, R. & Kiely, D. Stored chemical energy propulsion system for underwater applications. *J. Energy* **7**, 128-133 (1983).

- 167 Kwabi, D. G. *et al.* Experimental and computational analysis of the solvent-dependent $\text{O}_2/\text{Li}^+-\text{O}^{2-}$ redox couple: standard potentials, coupling strength, and implications for lithium–oxygen Batteries. *Angew. Chem., Int. Ed.* **55**, 3129-3134 (2016).
- 168 Zámostná, L. & Braun, T. Catalytic degradation of sulfur hexafluoride by rhodium complexes. *Angew. Chem.* **127**, 10798-10802 (2015).
- 169 He, H. *et al.* Highly-efficient conversion of SF_6 via an eight-electron transfer process in lithium batteries. *Nano Energy*, 104679 (2020).
- 170 Braun, T., Noveski, D., Neumann, B. & Stammler, H. G. Conversion of hexafluoropropene into 1, 1, 1-trifluoropropane by rhodium-mediated C-F activation. *Angew. Chem., Int. Ed.* **41**, 2745-2748 (2002).
- 171 Zámostná, L. & Braun, T. Catalytic degradation of sulfur hexafluoride by rhodium complexes. *Angew. Chem., Int. Ed.* **55**, 15072–15075 (2015).
- 172 Kim, J., Kim, H. & Kang, K. Conversion-Based Cathode Materials for Rechargeable Sodium Batteries. *Adv. Energy Mater.* **8**, 1702646 (2018).
- 173 Ma, L. *et al.* Fundamental understanding and material challenges in rechargeable nonaqueous $\text{Li}-\text{O}_2$ batteries: recent progress and perspective. *Adv. Energy Mater.* **8**, 1800348 (2018).
- 174 Seppelt, K. Molecular hexafluorides. *Chem. Rev.* **115**, 1296-1306 (2015).
- 175 Ren, X. *et al.* Understanding side reactions in $\text{K}-\text{O}_2$ batteries for improved cycle life. *ACS Appl. Mater. Interfaces* **6**, 19299-19307 (2014).
- 176 Bender, C. L., Hartmann, P., Vračar, M., Adelhalm, P. & Janek, J. On the thermodynamics, the role of the carbon cathode, and the cycle life of the sodium superoxide (NaO_2) battery. *Adv. Energy Mater.* **4**, 1301863 (2014).

- 177 McCloskey, B. D., Scheffler, R., Speidel, A., Girishkumar, G. & Luntz, A. C. On the mechanism of nonaqueous Li–O₂ electrochemistry on C and its kinetic overpotentials: some implications for Li–air batteries. *J. Phys. Chem. C* **116**, 23897-23905 (2012).
- 178 Lyu, Z. *et al.* Recent advances in understanding of the mechanism and control of Li₂O₂ formation in aprotic Li–O₂ batteries. *Chem. Soc. Rev.* **46**, 6046-6072 (2017).
- 179 Yu, W. *et al.* Molecular Sieve Induced Solution Growth of Li₂O₂ in the Li–O₂ Battery with Largely Enhanced Discharge Capacity. *ACS Appl. Mater. Interfaces* **10**, 7989-7995 (2018).
- 180 Liu, Z., Ma, L., Guo, L. & Peng, Z. Promoting solution discharge of Li–O₂ batteries with immobilized redox mediators. *J. Phys. Chem. Lett.* **9**, 5915-5920 (2018).
- 181 Lu, Y.-C., Gasteiger, H. A. & Shao-Horn, Y. Method development to evaluate the oxygen reduction activity of high-surface-area catalysts for Li-air batteries. *Electrochim. Solid-State Lett.* **14**, A70 (2011).
- 182 Gao, J., Lowe, M. A., Kiya, Y. & Abruna, H. D. Effects of liquid electrolytes on the charge–discharge performance of rechargeable lithium/sulfur batteries: electrochemical and in-situ X-ray absorption spectroscopic studies. *J. Phys. Chem. C* **115**, 25132-25137 (2011).
- 183 Yim, T. *et al.* Effect of chemical reactivity of polysulfide toward carbonate-based electrolyte on the electrochemical performance of Li–S batteries. *Electrochim. Acta* **107**, 454-460 (2013).
- 184 Hartmann, P. *et al.* A rechargeable room-temperature sodium superoxide (NaO₂) battery. *Nat. Mater.* **12**, 228 (2013).

- 185 Mayer, U., Gutmann, V. & Gerger, W. The acceptor number—A quantitative empirical parameter for the electrophilic properties of solvents. *Monatshefte für Chemie/Chemical Monthly* **106**, 1235-1257 (1975).
- 186 Jones, J., Anouti, M., Caillon-Caravanier, M., Willmann, P. & Lemordant, D. Thermodynamic of LiF dissolution in alkylcarbonates and some of their mixtures with water. *Fluid Phase Equilib.* **285**, 62-68 (2009).
- 187 Jones, J. *et al.* Solubilization of SEI lithium salts in alkylcarbonate solvents. *Fluid Phase Equilib.* **305**, 121-126 (2011).
- 188 Lutz, L. *et al.* High capacity Na-O₂ batteries: key parameters for solution-mediated discharge. *J. Phys. Chem. C* **120**, 20068-20076 (2016).
- 189 Abraham, K. Rechargeable batteries for the 300-mile electric vehicle and beyond. *ECS Trans.* **41**, 27 (2012).
- 190 Xin, N., Sun, Y., He, M., Radke, C. J. & Prausnitz, J. M. Solubilities of six lithium salts in five non-aqueous solvents and in a few of their binary mixtures. *Fluid Phase Equilib.* **461**, 1-7 (2018).
- 191 Stubblefield, C. B. & Bach, R. O. Solubility of lithium fluoride in water. *J. Chem. Eng. Data* **17**, 491-492 (1972).
- 192 Wynn, D. A., Roth, M. M. & Pollard, B. D. The solubility of alkali-metal fluorides in non-aqueous solvents with and without crown ethers, as determined by flame emission spectrometry. *Talanta* **31**, 1036-1040 (1984).
- 193 Abraham, K. Electrolyte-directed reactions of the oxygen electrode in lithium-air batteries. *J. Electrochem. Soc.* **162**, A3021-A3031 (2015).

- 194 Rauh, R., Shuker, F., Marston, J. & Brummer, S. Formation of lithium polysulfides in aprotic media. *J. Inorg. Nucl. Chem.* **39**, 1761-1766 (1977).
- 195 Lau, S. & Archer, L. A. Nucleation and growth of lithium peroxide in the Li–O₂ battery. *Nano Lett.* **15**, 5995-6002 (2015).
- 196 Liu, B. *et al.* Temperature dependence of the oxygen reduction mechanism in nonaqueous Li–O₂ batteries. *ACS Energy Lett.* **2**, 2525-2530 (2017).
- 197 Erker, G. Tris (pentafluorophenyl) borane: a special boron Lewis acid for special reactions. *Dalton Trans.*, 1883-1890 (2005).
- 198 Döring, S., Erker, G., Fröhlich, R., Meyer, O. & Bergander, K. Reaction of the Lewis acid tris (pentafluorophenyl) borane with a phosphorus ylide: competition between adduct formation and electrophilic and nucleophilic aromatic substitution pathways. *Organometallics* **17**, 2183-2187 (1998).
- 199 Li, L. *et al.* New electrolytes for lithium ion batteries using LiF salt and boron based anion receptors. *J. Power Sources* **184**, 517-521 (2008).
- 200 Sun, X., Lee, H., Yang, X. & McBreen, J. Improved Elevated Temperature Cycling of LiMn₂O₄ Spinel Through the Use of a Composite LiF-Based Electrolyte. *Electrochem. Solid-State Lett.* **4**, A184 (2001).
- 201 Chen, Z. & Amine, K. Tris (pentafluorophenyl) borane as an additive to improve the power capabilities of lithium-ion batteries. *J. Electrochem. Soc.* **153**, A1221 (2006).
- 202 Sun, X., Lee, H., Yang, X.-Q. & McBreen, J. Using a boron-based anion receptor additive to improve the thermal stability of LiPF₆-based electrolyte for lithium batteries. *Electrochem. Solid-State Lett.* **5**, A248 (2002).

- 203 Han, G.-B., Lee, J.-N., Choi, J. W. & Park, J.-K. Tris (pentafluorophenyl) borane as an electrolyte additive for high performance silicon thin film electrodes in lithium ion batteries. *Electrochim. Acta* **56**, 8997-9003 (2011).
- 204 Herstedt, M., Stjerndahl, M., Gustafsson, T. & Edström, K. Anion receptor for enhanced thermal stability of the graphite anode interface in a Li-ion battery. *Electrochem. Commun.* **5**, 467-472 (2003).
- 205 Zheng, D., Wang, Q., Lee, H. S., Yang, X. Q. & Qu, D. Catalytic disproportionation of the superoxide intermediate from electrochemical O₂ reduction in nonaqueous electrolytes. *Chemistry* **19**, 8679-8683 (2013).
- 206 Wang, Q., Zheng, D., McKinnon, M. E., Yang, X.-Q. & Qu, D. Kinetic investigation of catalytic disproportionation of superoxide ions in the non-aqueous electrolyte used in Li-air batteries. *J. Power Sources* **274**, 1005-1008 (2015).
- 207 Abraham, K. & Chaudhri, S. The lithium surface film in the Li/SO₂ cell. *J. Electrochem. Soc.* **133**, 1307 (1986).
- 208 Abraham, K. Chemical and electrochemical processes in some lithium-liquid cathode batteries. *J. Power Sources* **34**, 81-101 (1991).
- 209 Sheppard, W. A. Arylsulfur pentafluorides. *J. Am. Chem. Soc.* **84**, 3064-3072 (1962).
- 210 Savoie, P. R. & Welch, J. T. Preparation and utility of organic pentafluorosulfanyl-containing compounds. *Chem. Rev.* **115**, 1130-1190 (2015).
- 211 Frisch, M. J. *et al.* Gaussian 03 Revision B.05. *Gaussian 03, Revision B.05*, Gaussian, Inc., Pittsburgh PA (2003).

- 212 Thom, A. J., Sundstrom, E. J. & Head-Gordon, M. LOBA: a localized orbital bonding analysis to calculate oxidation states, with application to a model water oxidation catalyst. *Phys. Chem. Chem. Phys.* **11**, 11297-11304 (2009).
- 213 Lu, T. & Chen, F. Multiwfn: a multifunctional wavefunction analyzer. *J. Comp. Chem.* **33**, 580-592 (2012).
- 214 Safety data sheet of thionyl chloride. (Sigma-Aldrich, <https://www.nwmissouri.edu/naturalsciences/sds/t/Thionyl%20chloride.pdf>, 2014).
- 215 Safety data sheet for Lithium Hexafluorophosphate in EC/EMC 3:7. (MTI, https://www.mtixtl.com/sds/LiPF6_SDS.pdf, 2018).
- 216 Safety data sheet 5671301 - Phenylsulfur pentafluoride. (Synquest Laboratories, <http://www.synquestlabs.com/msds/5600/5671-3-01.pdf>, 2018).
- 217 Safety data sheet 5671K01 - 4-Iodophenylsulfur pentafluoride. (Synquest Laboratories, <http://www.synquestlabs.com/msds/5600/5671-K-01.pdf>, 2018).
- 218 Safety data sheet 86623X0 - 3-Nitrophenylsulfur pentafluoride. (Synquest Laboratories, <http://www.synquestlabs.com/msds/8600/8662-3-X0.pdf>, 2017).
- 219 Safety data sheet 86623X3 - 4-Nitrophenylsulfur pentafluoride. (Synquest Laboratories, <http://www.synquestlabs.com/msds/8600/8662-3-X3.pdf>, 2017).
- 220 Safety data sheet of lithium tetrafluoroborate, anhydrous. (ThermoFisher Scientific, <https://www.fishersci.com/store/msds?partNumber=AC223770100&productDescription=LITHIUM+TETRAFLUOROBORAT+10GR&vendorId=VN00032119&countryCode=US&language=en>, 2018).
- 221 Safety data sheet of ethylene glycol dimethyl ether. (ThermoFisher Scientific, <https://www.fishersci.com/store/msds?partNumber=O24304&productDescription=1%2C>

2-

- [DIMETHOXYETHANE+CERT+4L&vendorId=VN00033897&countryCode=US&language=en](https://www.sigmaaldrich.com/US/en/sds/aldrich/746738), 2018).
- 222 Safety data sheet of lithium hexafluorophosphate solution. (Sigma-Aldrich, <https://www.sigmaaldrich.com/US/en/sds/aldrich/746738>, 2021).
- 223 Safety data sheet of CF_x hybrid lithium battery. (EaglePicher Technologies, <https://www.eaglepicher.com/sites/default/files/EHS-AIS-1008%20CFx%20hybrid%20lithium%20battery%20rev%20D%201-19-21.pdf>, 2021).
- 224 Safety data sheet of ENERGY+ brand lithium (metal) battery-lithium carbon monofluoride (Li-CF_x). (Fedco Electronics Inc, <https://www.shorepowerinc.com/media/wysiwyg/files/fc-br-ccf2th.pdf>, 2013).
- 225 Pressure-Temperature Nomograph Interactive Tool. (MilliporeSigma, <https://www.sigmaaldrich.com/US/en/support/calculators-and-apps/pressure-temperature-nomograph-interactive-tool>).
- 226 Safety data sheet of dimethyl sulfoxide. (Sigma-Aldrich, <https://louisville.edu/micronano/files/documents/safety-data-sheets-sds/DimethylSulfoxide.pdf>, 2018).
- 227 Hansch, C., Leo, A. & Taft, R. A survey of Hammett substituent constants and resonance and field parameters. *Chem. Rev.* **91**, 165-195 (1991).
- 228 Zou, Q. & Lu, Y.-C. Solvent-dictated lithium sulfur redox reactions: an operando UV-vis spectroscopic study. *J. Phys. Chem. Lett.* **7**, 1518-1525 (2016).
- 229 Bonnaterre, R. & Cauquis, G. Spectrophotometric study of the electrochemical reduction of sulphur in organic media. *J. Chem. Soc., Chem. Commun.*, 293-294 (1972).

- 230 Liang, X. *et al.* A highly efficient polysulfide mediator for lithium–sulfur batteries. *Nat. Commun.* **6**, 1-8 (2015).
- 231 Wild, M. *et al.* Lithium sulfur batteries, a mechanistic review. *Energy Environ. Sci.* **8**, 3477-3494 (2015).
- 232 *The NIST x-ray photoelectron spectroscopy database.* 20899 (National Institute of Standards and Technology, 2000).
- 233 Aurbach, D. *et al.* On the surface chemical aspects of very high energy density, rechargeable Li–sulfur batteries. *J. Electrochem. Soc.* **156**, A694 (2009).
- 234 Siow, K. S., Britcher, L., Kumar, S. & Griesser, H. J. XPS study of sulfur and phosphorus compounds with different oxidation states. *Sains Malaysiana* **47**, 1913-1922 (2018).
- 235 Wood, K. N. & Teeter, G. XPS on Li-battery-related compounds: analysis of inorganic SEI phases and a methodology for charge correction. *ACS Appl. Mater. Interfaces* **1**, 4493-4504 (2018).
- 236 Gittleson, F. S. *et al.* Raman spectroscopy in lithium–oxygen battery systems. *ChemElectroChem* **2**, 1446-1457 (2015).
- 237 Zerbi, G. *et al.* Molecular mechanics for phase transition and melting of n-alkanes: A spectroscopic study of molecular mobility of solid n-nonadecane. *J. Chem. Phys.* **75**, 3175-3194 (1981).
- 238 Ferrari, A. & Robertson, J. J. P. r. B. Origin of the 1150–cm⁻¹ Raman mode in nanocrystalline diamond. *Phys. Rev. B* **63**, 121405 (2001).
- 239 Kornblum, N. & Widmer, J. Substitution reactions which proceed via radical anion intermediates. 19. Direct conversion of nitro compounds to thiols. *J. Am. Chem. Soc.* **100**, 7086-7088 (1978).

- 240 Betz, J. *et al.* Theoretical versus practical energy: a plea for more transparency in the energy calculation of different rechargeable battery systems. *Adv. Energy Mater.* **9**, 1803170 (2019).
- 241 Muffoletto, B. C. & Kuwik, R. J. Internal electrode and assembly method for electrochemical cells. U.S. Patent No. 5,250,373 patent No. 5,250,373 (1993).
- 242 Probst, J., Takeuchi, E. S. & Smesko, S. A. Enhanced capacity Li/CF_x electrochemical cell. U.S. Patent No. 6,451,483 patent No. 6,451,483 (2002).
- 243 Zhang, X. & Wang, X. High Capacity and High Rate Lithium Cells with CF_x-MnO₂ Hybrid Cathode. U.S. patent (2009).
- 244 Marple, J. Performance characteristics of Li/MnO₂-CF_x hybrid cathode jellyroll cells. *J. Power Sources* **19**, 325-335 (1987).
- 245 Hansen, L. D. & Frank, H. Kinetics and thermodynamics of chemical reactions in Li/SOCl₂ cells. *J. Electrochem. Soc.* **134**, 1 (1987).
- 246 Gimferrer, M., Van der Mynsbrugge, J., Bell, A. T., Salvador, P. & Head-Gordon, M. Facing the challenges of borderline oxidation state assignments using state-of-the-art computational methods. *Inorg. Chem.* **59**, 15410-15420 (2020).
- 247 Greatbatch, W., Holmes, C., Takeuchi, E. & Ebel, S. Lithium/carbon monofluoride (Li/CF_x): a new pacemaker battery. *Pacing Clinical Electrophysiology* **19**, 1836-1840 (1996).
- 248 Guérin, K. *et al.* Synthesis and characterization of highly fluorinated graphite containing sp² and sp³ carbon. *Chem. Mater.* **16**, 1786-1792 (2004).

- 249 Mitkin, V., Asanov, I. & Mazalov, L. X-Ray Photoelectron- and Auger-Spectroscopic Study of Superstoichiometric Fluorographite-Like Materials. *J. Struct. Chem.* **43**, 843-855 (2002).
- 250 Watanabe, N. & Fukuda, M. Primary cell for electric batteries. US patent 3536532 (1970).
- 251 Kopilov, J. & Evans, D. H. Electrochemical reduction of some α -haloacetanilides. *J. Electroanal. Chem. Interfacial Electrochem.* **280**, 435-438 (1990).
- 252 Barker, D., Brewin, D., Dahm, R. & Hoy, L. The electrochemical reduction of polytetrafluoroethylene. *Electrochim. Acta* **23**, 1107-1110 (1978).
- 253 Zhang, X. Q., Cheng, X. B., Chen, X., Yan, C. & Zhang, Q. Fluoroethylene carbonate additives to render uniform Li deposits in lithium metal batteries. *Adv. Funct. Mater.* **27**, 1605989 (2017).
- 254 Liu, X., Zhou, J., Xu, Z. & Wang, Y. Atomic thermodynamics and microkinetics of the reduction mechanism of electrolyte additives to facilitate the formation of solid electrolyte interphases in lithium-ion batteries. *RSC Adv.* **10**, 16302-16312 (2020).
- 255 Murphy, P. M., Baldwin, C. S. & Buck, R. C. Syntheses utilizing n-perfluoroalkyl iodides [RFI, C_nF_{2n+1}-I] 2000–2010. *J. Fluorine Chem.* **138**, 3-23 (2012).
- 256 Andrieux, C. P., Gelis, L., Medebielle, M., Pinson, J. & Saveant, J. M. Outer-sphere dissociative electron transfer to organic molecules: a source of radicals or carbanions? Direct and indirect electrochemistry of perfluoroalkyl bromides and iodides. *J. Am. Chem. Soc.* **112**, 3509-3520 (1990).

- 257 Médebielle, M., Pinson, J. & Savéant, J.-M. Electrochemically Induced Nucleophilic Substitution of Perfluoroalkyl Halides. An Example of a Dissociative Electron-Transfer-Induced Chemical Reaction. *J. Am. Chem. Soc.* **113**, 6872-6879 (1991).
- 258 Wakselman, C. Single electron-transfer processes in perfluoroalkyl halides reactions. *J. Fluorine Chem.* **59**, 367-378 (1992).
- 259 Xu, J., Ma, J., Fan, Q., Guo, S. & Dou, S. Recent progress in the design of advanced cathode materials and battery models for high-performance lithium-X (X= O₂, S, Se, Te, I₂, Br₂) batteries. *Adv. Mater.* **29**, 1606454 (2017).
- 260 Brace, N. O. Syntheses with perfluoroalkyl radicals from perfluoroalkyl iodides. A rapid survey of synthetic possibilities with emphasis on practical applications. Part one: alkenes, alkynes and allylic compounds. *J. Fluorine Chem.* **93**, 1-25 (1999).
- 261 Pavlishchuk, V. V. & Addison, A. W. J. I. C. A. Conversion constants for redox potentials measured versus different reference electrodes in acetonitrile solutions at 25°C. *Inorg. Chim. Acta* **298**, 97-102 (2000).
- 262 Frisch, M. J. *et al.* Gaussian09. *Gaussian 09, Revision C.01*, Gaussian, Inc., Wallingford CT (2010).
- 263 Castro, L. & Bühl, M. Calculations of one-electron redox potentials of oxoiron (IV) porphyrin complexes. *J. Chem. Theory Comput.* **10**, 243-251 (2014).
- 264 Johnson III, R. D. *NIST computational chemistry comparison and benchmark database*. (NIST Standard Reference Database Number 101, 2019).
- 265 Fan, X. *et al.* Non-flammable electrolyte enables Li-metal batteries with aggressive cathode chemistries. *Nat. Nanotechnol.* **13**, 715-722 (2018).

- 266 Michelsen, P. J. *Relationship between chromatographic retention and donor and acceptor numbers* Master of Science thesis, Rochester Institute of Technology, (1990).
- 267 Yoshinaga, K. & Swager, T. M. Revisiting the Heck Reaction for Fluorous Materials Applications. *Synlett* **32**, 1725-1729 (2021).
- 268 Jaffé, H. H. A reexamination of the Hammett equation. *Chem. Rev.* **53**, 191-261 (1953).
- 269 Kang, K., Meng, Y. S., Bréger, J., Grey, C. P. & Ceder, G. Electrodes with High Power and High Capacity for Rechargeable Lithium Batteries. *Science* **311**, 977-980 (2006).
- 270 Lee, K. S., Myung, S. T., Amine, K., Yashiro, H. & Sun, Y. K. Structural and Electrochemical Properties of Layered $\text{Li}[\text{Ni}_{1-2x}\text{Co}_x\text{Mn}_x]\text{O}_2$ ($x=0.1-0.3$) Positive Electrode Materials for Li-Ion Batteries. *J. Electrochem. Soc.* **154**, A971-A977 (2007).
- 271 Lee, J. *et al.* Reversible $\text{Mn}^{2+}/\text{Mn}^{4+}$ double redox in lithium-excess cathode materials. *Nature* **556**, 185 (2018).
- 272 Ko, J. K. *et al.* Transport, Phase Reactions, and Hysteresis of Iron Fluoride and Oxyfluoride Conversion Electrode Materials for Lithium Batteries. *ACS Appl. Mater. Interfaces* **6**, 10858-10869, doi:10.1021/am500538b (2014).
- 273 Jung, S. K. *et al.* Chemical Origins of Electrochemical Overpotential in Surface-Conversion Nanocomposite Cathodes. *Adv. Energy Mater.* **9**, 1900503 (2019).
- 274 Zhao, Y. *et al.* LiF splitting catalyzed by dual metal nanodomains for an efficient fluoride conversion cathode. *ACS Nano* **13**, 2490-2500 (2019).
- 275 Wei, K. *et al.* Low-Overpotential LiF Splitting in Lithiated Fluoride Conversion Cathode Catalyzed by Spinel Oxide. *Adv. Funct. Mater.*, 2009133 (2021).

- 276 Jiang, F. & Peng, P. Elucidating the performance limitations of lithium-ion batteries due to species and charge transport through five characteristic parameters. *Sci. Rep.* **6**, 1-18 (2016).
- 277 Poizot, P., Laruelle, S., Grugeon, S., Dupont, L. & Tarascon, J. Nano-sized transition-metal oxides as negative-electrode materials for lithium-ion batteries. *Nature* **407**, 496-499 (2000).
- 278 SDBSWeb. (National Institute of Advanced Industrial Science and Technology).
- 279 Imhof, R. & Novák, P. Oxidative electrolyte solvent degradation in lithium-ion batteries: an In Situ differential electrochemical mass spectrometry investigation. *J. Electrochem. Soc.* **146**, 1702 (1999).
- 280 Bernardini, S., Bellatreccia, F., Casanova Municchia, A., Della Ventura, G. & Sodo, A. Raman spectra of natural manganese oxides. *J. Raman Spectrosc.* **50**, 873-888 (2019).
- 281 Mai, Y. *et al.* MnO/reduced graphene oxide sheet hybrid as an anode for Li-ion batteries with enhanced lithium storage performance. *J. Power Sources* **216**, 201-207 (2012).
- 282 Rusakova, I. *et al.* Nanoparticle shape conservation in the conversion of MnO nanocrosses into Mn₃O₄. *Chem. Mater.* **19**, 1369-1375 (2007).
- 283 Li, X., Zhu, Y., Zhang, X., Liang, J. & Qian, Y. MnO@ 1-D carbon composites from the precursor C₄H₄MnO₆ and their high-performance in lithium batteries. *RSC Adv.* **3**, 10001-10006 (2013).
- 284 Zahn, D. T. Vibrational spectroscopy of bulk and supported manganese oxides. *Phys. Chem. Chem. Phys.* **1**, 185-190 (1999).
- 285 Julien, C., Massot, M. & Poinignon, C. Lattice vibrations of manganese oxides: Part I. Periodic structures. *Spectrochim. Acta A* **60**, 689-700 (2004).

- 286 Parr, R. G. & Pearson, R. G. Absolute hardness: companion parameter to absolute electronegativity. *J. Am. Chem. Soc.* **105**, 7512-7516 (1983).
- 287 Pearson, R. G. Absolute electronegativity and hardness correlated with molecular orbital theory. *Proc. Natl. Acad. Sci.* **83**, 8440-8441 (1986).
- 288 Pearson, R. G. Hard and soft acids and bases. *J. Am. Chem. Soc.* **85**, 3533-3539 (1963).
- 289 Travers, M. J., Cowles, D. C. & Ellison, G. B. Reinvestigation of the electron affinities of O₂ and NO. *Chem. Phys. Lett.* **164**, 449-455 (1989).